SPARSE RECONSTRUCTION AND ANALYSIS OF GUIDED WAVEFIELDS FOR DAMAGE DETECTION AND QUANTIFICATION

A Thesis
Presented to
The Academic Faculty

by

Olivier Mesnil

In Partial Fulfillment
of the Requirements for the Degree
Doctor of Philosophy in the
D. Guggenheim School of Aerospace Engineering

Georgia Institute of Technology
August 2016

SPARSE RECONSTRUCTION AND ANALYSIS OF GUIDED WAVEFIELDS FOR DAMAGE DETECTION AND QUANTIFICATION

Approved by:

Dr. Massimo Ruzzene, Advisor
D. Guggenheim School of Aerospace Engineering
Georgia Institute of Technology

Dr. Krish Ahuja
D. Guggenheim School of Aerospace Engineering
Georgia Institute of Technology

Dr. George Kardomateas
D. Guggenheim School of Aerospace Engineering
Georgia Institute of Technology

Dr. Kamran Paynabar
H. Milton Stewart School of Industrial and Systems Engineering
Georgia Institute of Technology

Dr. Jennifer Michaels
School of Electrical and Computer Engineering
Georgia Institute of Technology

Date Approved: May 20^{th}, 2016

ACKNOWLEDGEMENTS

I want to thank my advisor Dr. Massimo Ruzzene for his guidance. His advice, review, comments and help have greatly contributed to my professional and personal development.

I also want to thank my committee members Dr. Krish Ahuja, Dr. George Kardomateas, Dr. Kamran Paynabar and Dr. Jennifer Michaels for their interest in my research and the time they dedicated to me. For their guidance during our collaborative work, I also thank Dr. Steven Danyluk, Dr. Jianjun Shi, Dr. Cara Leckey and Dr. Michael Stewart. In addition, I want to thank Rajaguruprasath Raveendran and Hao Yan for their flexibility and efficiency in our collaborative work along with Westin Williams for his help with the C-Scans.

A special thank goes to Rachel & Marshall for their friendship and hospitality. I also want to acknowledge Aaron and Marshall (again): it is easier to stay on track when you can share your daily struggles with friends, I believe we successfully created some knowledge from our mutual ignorance. Out of order I would also like to thanks, Matteo, William, Giuseppe, Hannah, Chen, Guglielmo, Raj, Yongqiang, Phuc. Last but not least, I want to thank my family for their constant support and understanding and of course Charlotte for her love, support, patience and sacrifices

TABLE OF CONTENTS

LIST OF TABLES

LIST OF FIGURES

SUMMARY

This thesis presents the study of novel guided wave-based techniques that locate, quantify and analyze defects in composite materials and metals. These techniques find themselves at the intersection of Structural Health Monitoring (SHM) and Non Destructive Evaluation (NDE) due to their use of both guided wave methods and Guided Wavefield Imaging (GWI) techniques. The primary goals of NDE are limited to the local detection and the evaluation of damages. NDE is often characterized by off-line inspection requiring a cumbersome equipment. On the other hand, SHM generally aims at monitoring the condition of the structure during its regular operating cycle, ideally with embedded sensors. Guided wave methods are commonly considered to be part of SHM methodologies and are widely used for the detection of flaws in plate-like structures. Guided Wavefield Imaging is a technique that relies on the detection of images corresponding to the time evolution guided waves propagation in the structure. Due to the high sensibility of guided waves to internal defects and the amount of information they include, wavefields have the potential to provide extensive information regarding the structural component under consideration. However the main limitation of GWI is the time consuming guided wavefield acquisition process.

The objectives of this dissertation is to develop novel GWI techniques able to detect, locate and quantify defects in metals and composite materials while reducing the acquisition time. In addition, the work attempts to link guided wave signatures to damage parameters in order to provide strength estimates. Two complimentary techniques are developed to achieve the objectives. The first technique, namely the Sparse Wavefield Reconstruction (SWR) reduces the acquisition time required to detect a wavefield. The approach employs sparse measurements, i.e., fewer measurements than required by the traditional sampling criteria, scattered within the region of inspection. The SWR technique is applied for the reconstruction of various experimental wavefields with compression ratios of about 90%, where compression ratio denotes the reduction of point measurement with the SWR technique with respect to traditional sampling criteria. The second technique, namely the Frequency Domain Instantaneous Wavenumber (FDIW), focuses on the quantification of a defect through local measurement of the wavenumber. The FDIW is applied to multiple defects and provides and estimation of the three-dimensional shape of the defects. . The combination of these two techniques provides an inspection methodology that reduces the inspection time and provides detailed defect quantification. Finally, a novel methodology bridging guided wave measurements and residual life prediction is presented. This study measures the constitutive damage parameters of composite panels in order to obtain residual properties estimates through damage mechanics numerical models. This methodology is used to measure the constitutive damage variable of a numerically simulated damage and show promising results for an experimental application.

CHAPTER I

INTRODUCTION

1.1 Chapter overview

The goal of this thesis is to investigate guided wave-based techniques to locate, quantify and analyze defects in composite materials. The techniques rely on Guided Wavefield Imaging (GWI), which enables a number of methodologies that belong to the intersection of Non-Destructive Evaluation (NDE) and Structural Health Monitoring (SHM). This chapter first discusses the context for the development of the techniques investigated herein. The motivations and the objectives of this work are then detailed. Finally, the contributions of this thesis to the literature and the organization of this document are presented.

1.2 Non Destructive Evaluation and Structural Health Monitoring

The common goal of Non-Destructive Evaluation (NDE) and Structural Health Monitoring (SHM) is to assess the health of an engineering structure not only to prevent the catastrophic failure of vital structures, but also to anticipate and reduce maintenance costs. While the primary goals of NDE are limited to the local detection and the evaluation of damages, SHM aims at monitoring the condition of the structure during its regular operating cycle by incorporating multiple NDE methods [1]. For comprehensive reviews on SHM and NDE, the reader is invited to refer to [2, 3, 4].

Structural inspections in both SHM and NDE contexts rely on the measurement of a physical quantity directly affected by the presence of damage or flaws in the structure. NDE inspection methodologies include, but are not restricted to: visual inspection, magnetic testing, liquid penetrant testing, eddy current, radiography and ultrasonic testing. All these techniques have intrinsic sets of pros and cons that are related to the observed measured physical phenomena.

Among the various existing NDE techniques, Ultrasonic Testing (UT) is the most relevant to this thesis. Ultrasonic Testing relies on the measurement of the propagation of ultrasonic waves through a specimen in order to deduce information regarding potential defects along the path of the propagating waves. There exist multiple methodologies for structural inspection using UT. In pulse-echo and through-transmission UT for example, ultrasonic waves are sent through the thickness of a specimen [5]. A schematic of the pulse-echo and the through-transmission methods is shown in Figure 1.1a. In pulse-echo mode, the waves are generated and received by the same device. The time instant at which wave reflections are measured is related to the depth of the reflecting object through the speed of the wave in the material. In through-transmission mode, the receiver and the emitter are two distinct devices placed on the opposite sides of the inspected structure. The quantity of energy measured by the receiver indicates the presence of flaws between the two devices. Pitch-catch is another UT method sending ultrasonic waves in the inspected structure with a fixed angle with respect to the surface [5], as displayed in Figure 1.1b. The strength of the received signal then indicates the presence of a flaw in the path of the waves.

Generally, UT techniques are capable of detecting and quantifying subsurface features with less depth limitation than other NDE methodologies. Secondly, UT can detect small defects due to the sensitivity of the ultrasonic waves to the flaws of the material they are propagating in. Finally, UT can be automated and has no negative influence on its direct environment (no safety hazard, no noise etc...). Among the set of disadvantages, the duration of inspection and the limited inspected area are main drawbacks.

The techniques developed in this thesis belong to the UT family because they

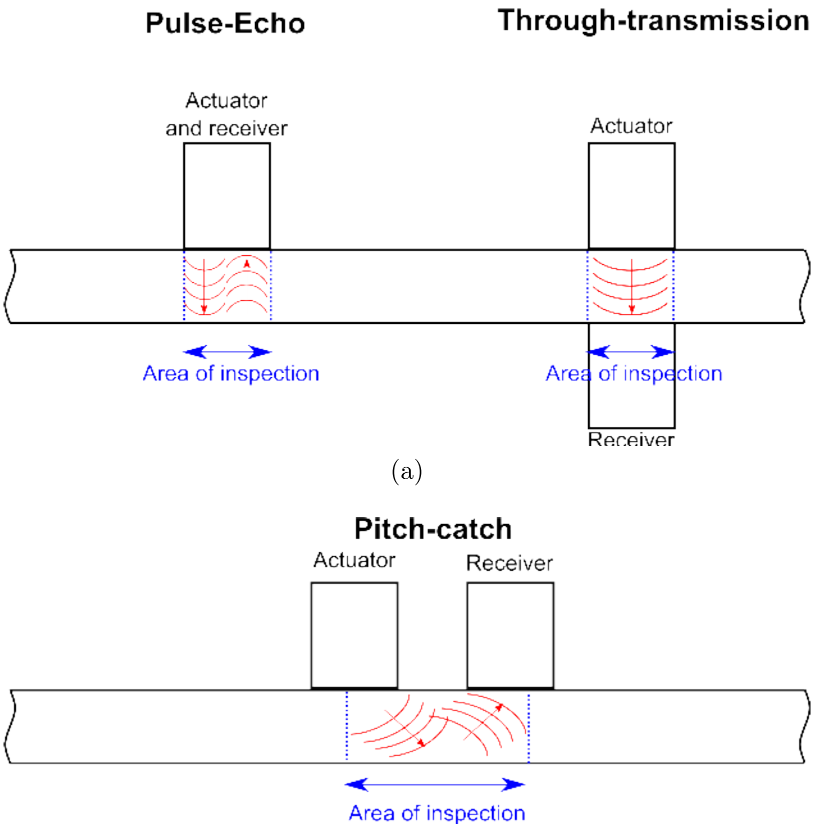

(a)

(b)

Figure 1.1: Schematic of some ultrasonic testing methodologies. The ultrasonic waves (red) travel from the actuator to the receiver (a): Pulse-echo and through-transmission and (b): Pitch-catch

rely on the use of the propagation of ultrasonic waves. However the propagation of the waves does not occur through the thickness of the specimen but by using waves guided by the specimen to utilize the long range propagation of guided waves.

1.3 Guided waves for damage detection

Guided waves are elastic waves whose wavelengths are comparable or greater than the thickness of the structure (waveguide) they propagate in. Unlike most UT techniques, Guided Wave Ultrasonic Testing (GWUT) uses the specimen as a waveguide and rely on the interaction with both surface and subsurface defects. The frequency of excitation in GWUT is typically of the order of hundreds of kilo-hertz, while UT commonly uses frequencies of the order of the mega-hertz. A schematic of the

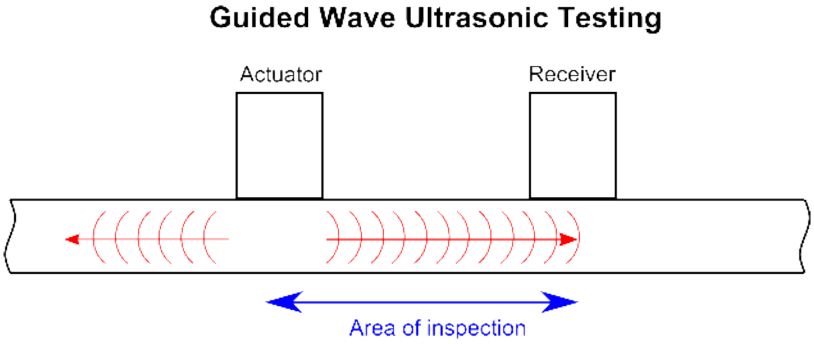

Figure 1.2: Schematic of the Guided Wave Ultrasonic Testing. The ultrasonic waves (red) travel from the actuator to the receiver along the thickness of the specimen

overall concept of GWUT is shown in Figure 1.2. In this schematic, guided waves are generated by the actuator and measured by the receiver. The signal measured by the receiver consists of the dispersed waves scattered by all the features between the transducer and the receiver [6]. The main advantage of GWUT compared to UT is the large area of inspection [7]. Indeed, guided waves propagate over long distances with little attenuation, hence a fixed transducer has the potential ability to interrogate large areas. For example in [8], propagation of guided waves over two meters is achieved with a single actuator, and artificial flaws of the order of 1 cm^2 are detected in a composite beam specimen with a single actuator-receiver pair. Similarly, [9] demonstrates the ability of guided waves to detect flaws such as a delamination or a crack using a single actuator-receiver pair.

Another important advantage of GWUT is that, as the interrogated specimen acts as a waveguide, it is not required for the region between the transducer and receiver to be accessible to an operator. This enables the applications of GWUT for buried pipe inspection for example [10]. However, a major difficulty in GWUT is the interpretation of the measurements. Indeed, guided waves are multi-modal, dispersive and highly sensitive to the boundary conditions, i.e., a minor change in the boundary conditions of an inspected structure may induce a significant change of the guided wave behavior. Hence extracting the part of the measurements corresponding to the defect of interest is a difficult task involving significant signal processing such as mode separation [11, 12] and dispersion compensation [13].

Commonly, GWUT rely on the measurement of the waves at a few punctual locations in space. Measurements are typically conducted by single-point fixed transducers, such as piezoelectric transducers glued on the surface of the specimen. Each measurement contains information on the path between the excitation and the measurement point and is corrupted by the multiple reflected wavefronts from all the features of the specimen (edges, defects, stiffeners...). Even though GWUT methodologies are often affordable and simple to implement, they only provide limited amount of information regarding the health of the specimen. Furthermore, due to the limited quantity of available information and the complexity of the measured signal, baseline signals, i.e., a measure of the wave propagation in the pristine specimen, are often necessary to interpret the measurements [14]. Among the more recent progress in GWUT, embedded arrays of transducer to detect and locate damage in isotropic plates are used as in [15] as well as to evaluate the damage detection ability of sparse arrays in complex structure under different environmental conditions [16]. Techniques using phase arrays to detect defects located outside the array are presented in [17], [18]. Overall, these techniques successfully locate defects but are not able to quantify them in details.

1.4 Guided wavefield imaging

A wavefield denotes a series of images representing to the time evolution of a propagating wave. Guided Wavefield Imaging (GWI) is an inspection technique relying on the collection of large amounts of information provided by the detection of guided wavefield to identify surface and subsurface defects. Guided wavefields have the ability to detect delaminations [19], repair patches [20] or fatigue cracks [21, 22, 23].

Complete damage size quantification and detection through GWI techniques are presented in [24, 25, 26] and [27, 28]. Note that, even though multiple GWI techniques have the ability to map the size and the shape of a defect, none has the ability to estimate the depth at which a defect is located.

Guided wavefields are measured by point-by-point measurement devices such as a Scanning Laser Doppler Vibrometer (SLDV) [29]. The quantity of information in the wavefield is directly connected to the number of points at which the wave propagation is measured. Increasing the number of points leads to a better wave resolution and better defect detection and mapping abilities. The main downside of a guided wavefield measurement is the extended acquisition time required. Even though guided waves propagation is a fast phenomenon of the order of the micro-second, full field acquisition duration is often of the order of several hours. This is due to the need for a high number of point-measurements, the need to measure multiple times a single point to compensate a low signal-to-noise ratio and the need to wait between each measurement to ensure that the initial conditions are identical for each point-measurement. The long acquisition time of the guided wavefield based techniques is the main barrier to the implementation of these techniques in industry. Indeed, the inspected structure must be off-line, i.e., not operating, during the inspection. Therefore there is a strong need of shortening the acquisition time of GWI while obtaining a detailed defect detection and quantification.

1.5 Motivations and objectives

Guided Wavefield Imaging has received a lot of attention for damage detection and quantification in the past decade and promising results have been obtained. However, the main downside of GWI is the long acquisition time. It is widely recognized today by the GWI community that the lengthy acquisition duration is the bottleneck on the path of applying GWI techniques in a practical environment. Moreover, GWI techniques are currently limited in terms of defect depth quantification. Indeed, even though in-plane defect shape estimation has been achieved with GWI techniques, no technique aiming at quantifying the depth of defects using GWI has been successfully implemented yet. The through-the-thickness location of a defect is however an important piece of information to assess the health of a structure as a defect might be more or less critical in function of its depth. Finally, to the author's knowledge, no work aiming at estimating the residual structural properties of a damaged specimen from GWI has been achieved yet. Bridging GWI and the residual properties estimate of a non-pristine structure would however be very valuable as it would enable customized residual life predictions.

Based on the current limitations of GWI techniques, the purpose of this dissertation is to develop novel guided wave-based techniques for the localization, quantification and analysis of defects in composite materials with the following requirements:

1. Detect, locate and quantify defects in plates from wavefields;
2. Reduce the acquisition time required for guided wavefield detection;
3. Provide a three-dimensional defect visualization;
4. Establish a link between GWI and residual properties estimate.

Effort will be put into making the techniques proposed in this work applicable outside the laboratory experimental conditions as well as applying the methods to different structural materials, including aluminum, glass fiber composites and carbon fiber composites. To validate the results obtained, other NDE inspection techniques such as thermography and through-transmission UT are presented and applied to the studied specimens.

1.6 Contributions

Based on the list of objectives of Section 1.5, the following contributions are made:

1. Development of the Sparse Wavefield Reconstruction (SWR) technique. This techniques aims at reconstructing wavefields in order to reduce the number of point-measurements required to be measured to know a wavefield and estimate defect locations. The SWR is a baseline-free scalable technique with the ability to detect and coarsely locate defects in large specimens that requires the knowledge of the structural properties of the inspected specimen.

2. Development of the Frequency Domain Instantaneous Wavenumber (FDIW). The goal of this technique is to fully quantify the three-dimensional spatial extents of a defect along with its through-the-thickness location from a guided wavefield. The FDIW is a baseline-free technique and has the ability to quantify damage with an accuracy of the order of the millimeter. This approach has the ability to quantify the depth of defects from steady state Lamb waves measurement.

3. SWR and FDIW integration and comparison against NDE techniques. The monitoring of large structures is enabled by the SWR process while the local defect assessment and quantification are achieved by the FDIW. The integrated methodologies is compared to existing NDE techniques.

4. Constitutive damage parameters detection and analysis. This study aims at measuring damage constitutive parameters in order to obtain residual properties estimate is conducted. This study bridges GWI and residual structural life forecasts.

1.7 Organization of this research

This document is organized as follows. First, the background on GWI necessary to fulfill the objectives of Section 1.5 is given in Chapter 2. Chapter 3 describes the development of the Sparse Wavefield Reconstruction (SWR) process, a methodology using

Compressed Sensing to reconstruct wavefields from sparse measurements. Chapter 4 presents the Frequency Domain Instantaneous Wavenumber (FDIW) technique, a GWI technique able to estimate the three-dimensional extent of a defect along with its through-the-thickness location. The SWR process and the FDIW techniques are both applied to multiple materials with various defects to ensure their reliability and encompass their overall abilities. The implementation of the integrated process is then described in Chapter 5. This process is applied to impact defects in composites and the results are compared to NDE references techniques. The study of constitutive damage variable measurement from GWI for residual strengths estimate is then presented in Chapter 6. Finally, Chapter 7 draws the conclusion of this research and make suggestions regarding the future directions of this research.

CHAPTER II

GUIDED WAVEFIELD DETECTION

2.1 Chapter overview

This chapter provides an introduction to the methodologies for guided wavefield detection, which then enable the development of GWI techniques. The fundamentals of guided waves are first described, followed by a presentation of the common practices for actuation and sensing of guided waves. Finally, the experimental setup used for the accomplishment of this work is presented, along with an example of a measured wavefield and the description of the information it can provide.

2.2 Fundamentals of Lamb waves

A guided wave is a mechanical wave whose direction of propagation is parallel to the boundaries of the waveguide it is propagating in [30]. In general, guided waves are dispersive, meaning that their phase velocities depend on the frequency. Lamb waves, Rayleigh waves and Stoneley waves are guided waves propagating in free plates, semi-infinite plates and at the interface between two mediums, respectively. Reviews of damage identification techniques by guided waves are available in [31, 32, 33]. Since this work concerns primarily the inspection of plate-like structures, the presentation of key features of Lamb waves propagation is provided next.

Lamb waves were initially described by Lamb in [34] and observed by Worlton in [35]. Lamb waves propagate in parallel to the edges of plates and through the entire thickness, making them suitable for in-depth defect inspection. Lamb waves are multi-modal, meaning that multiple wave modes exist in the specimen, where a mode is defined as a solution to the wave equation with a unique displacement

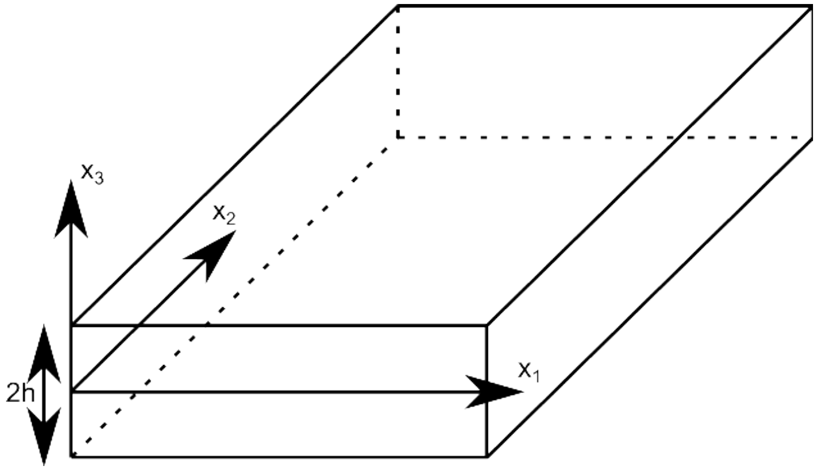

Figure 2.1: Schematic of the free-free plate. The plate is infinite in the direction 1 and 2

profile through the thickness. Lamb waves are also dispersive, meaning that the phase velocity is a function of frequency. Because of these properties, the analysis of Lamb waves is complicated and requires the use of signal processing techniques such as dispersion compensation [13] and mode filtering [11, 12].

Lamb wave solutions are derived from the theory of elasticity [30]. The system of interest is the free-free infinite plate displayed in figure 2.1. Assuming that the displacements are infinitesimal, the medium is isotropic, and that there is no external forcing applied to the system, the following equation holds:

$$(\lambda + \mu)\nabla(\nabla \cdot \boldsymbol{u}) + \mu\nabla^2\boldsymbol{u} = \rho\frac{\partial^2\boldsymbol{u}}{\partial t^2} \tag{2.1}$$

where $\boldsymbol{u} = u(x, y, z)$ is the displacement vector of a material point, ∇^2 is the Laplacian operator, λ and μ are the Lamé coefficients and ρ is the density. Equation (2.1) is known as the elastodynamic wave equation. The Helmholtz decomposition of Equation (2.1) applied to the free plate whose geometry is shown in Figure 2.1 leads to two uncoupled wave equations:

$$\frac{1}{c_L^2}\frac{\partial^2\phi}{\partial t^2} = \frac{\partial^2\phi}{\partial x_1^2} + \frac{\partial^2\phi}{\partial x_3^2} \tag{2.2}$$

$$\frac{1}{c_T^2}\frac{\partial^2\psi}{\partial t^2} = \frac{\partial^2\psi}{\partial x_1^2} + \frac{\partial^2\psi}{\partial x_3^2} \tag{2.3}$$

where ϕ and ψ are scalar potentials and c_L^2 and c_T^2 are the longitudinal and the transverse speed respectively with:

$$c_L^2 = \frac{\lambda + 2\mu}{\rho} \tag{2.4}$$

$$c_T^2 = \frac{\mu}{\rho} \tag{2.5}$$

Equation (2.2) governs the propagation of the longitudinal waves while Equation (2.3) governs the shear waves. The plain strain assumption in the free plate depicted in Figure 2.1 leads to the following displacement functions:

$$u_1 = \frac{\partial\phi}{\partial x_1} + \frac{\partial\psi}{\partial x_3} \tag{2.6}$$

$$u_2 = 0 \tag{2.7}$$

$$u_3 = \frac{\partial\phi}{\partial x_3} - \frac{\partial\psi}{\partial x_1} \tag{2.8}$$

The stresses can then be deduced by using the constitutive equations of the studied material. For a linear elasticity isotropic material:

$$\boldsymbol{\sigma} = \lambda\boldsymbol{\epsilon}\boldsymbol{I} + 2\mu\boldsymbol{\epsilon} \tag{2.9}$$

where $\boldsymbol{\sigma}$ is the stress tensor, $\boldsymbol{I}$ is the identity tensor and $\boldsymbol{\epsilon}$ is the strain tensor given by:

$$\boldsymbol{\epsilon} = \frac{1}{2}\left(\boldsymbol{\nabla u} + (\boldsymbol{\nabla u})^T\right) \tag{2.10}$$

The solutions of Equations (2.2) and (2.3) are assumed in the form of

$$\phi(x_1, x_3, t) = \phi(x_3)e^{i(kx_1-\omega t)} \tag{2.11}$$

$$\psi(x_1, x_3, t) = \psi(x_3)e^{i(kx_1-\omega t)} \tag{2.12}$$

where k is the wavenumber, ω is the angular frequency and t represents the time variable. The solutions are separated in two sets: symmetric and antisymmetric. Here the word symmetry denotes the symmetry of the displacement components with respect to the middle-thickness plane of the plate, i.e., the axis x_1 in Figure 2.1.

The solution for the symmetric modes is:

$$u_{1,S} = ikA_2cos(px_3) + qB_1cos(qx_3) \tag{2.13}$$

$$u_{3,S} = -pA_2sin(px_3) - ikB_1sin(qx_3) \tag{2.14}$$

where A_2 and B_1 are arbitrary amplitudes scalars and

$$p^2 = \left(\frac{\omega}{c_L}\right) - k^2 \tag{2.15}$$

$$q^2 = \left(\frac{\omega}{c_T}\right) - k^2 \tag{2.16}$$

while the solution for the antisymmetric modes is the following:

$$u_{1,A} = ikA_1sin(px_3) + qB_2sin(qx_3) \tag{2.17}$$

$$u_{3,A} = pA_1cos(px_3) - ikB_2cos(qx_3) \tag{2.18}$$

By imposing that the edges of the plates are free:

$$\sigma_{13} = \sigma_{33} = 0 \text{ at } x_3 = \pm h \tag{2.19}$$

the following characteristic equations are obtained:

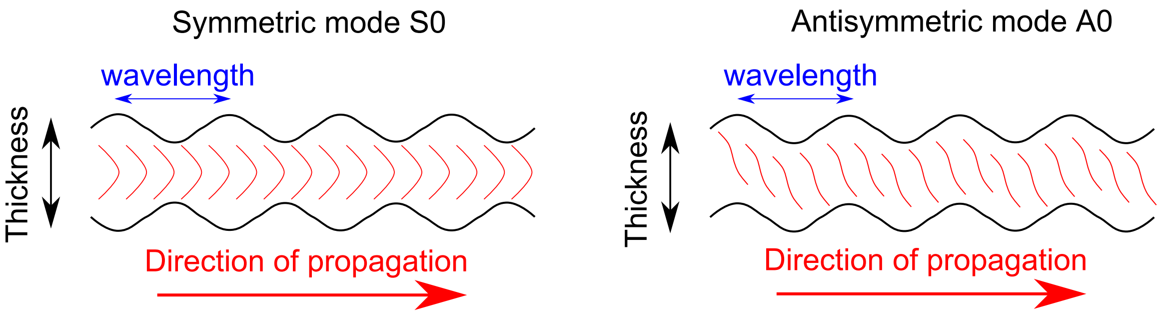

Figure 2.2: Schematic of the symmetric and antisymmetric modes of zeroth order propagating in an elastic plate.

$$\frac{tan(qh)}{tan(ph)} = -\frac{4k^2pq}{(q^2-k^2)^2} \tag{2.20}$$

$$\frac{tan(qh)}{tan(ph)} = -\frac{(q^2-k^2)^2}{4k^2pq} \tag{2.21}$$

Equations (2.20) and (2.21) are transcendental equations known as Rayleigh-Lamb equations [36]. The solutions of these equations provide a non-unique relationship between the frequency ω and the wavenumber k. Each independent solution of Equations (2.20) and (2.21) identifies a wave mode. The dispersion relation of a given mode μ is the relation between the wavenumber and the frequency and is denoted $k_\mu(\omega)$.

There exist an infinite number of antisymmetric and symmetric modes, i.e., an infinite number of solutions to Equations (2.20) and (2.21), but only the zeroth order symmetric and antisymmetric modes, denoted $S0$ and $A0$ respectively, exist at every frequency. The higher order modes, denoted $S1, A1, S2, A2, ...$ only appear at higher frequencies, called cutoff frequencies. A schematic of the shape of the in-plane deformation u_1 in the cross section of the plate induced by the $A0$ and $S0$ Lamb waves modes are represented in Figure 2.2. As indicated by its name, the deformation induced by the $A0$ mode is antisymmetric with respect to the mid-plane of the plate and the deformation induced by the $S0$ mode is symmetric. The wavelength λ represented by the blue arrow in Figure 2.2 is the spatial period of the deformation along the direction of propagation. Note that even though the out-of-plane and in-plane deformation are infinitesimal due to the linear elasticity assumption, wavelengths are typically of the order of several millimeters or centimeters.

Due to the complexity of the dispersive behavior of Lamb waves, knowing the dispersion relations is critical to the analysis of the measurements. There exist a number of techniques to experimentally measure the dispersion relations of a media such as the one presented in [37], which uses mathematical tools to extract the dispersion relations from Laser vibrometer measurement data. However, in a general case, it is required to know the dispersion relations prior to guided waves measurement in order to tune the acquisition parameters to the expected wave speeds and wavelengths. More specifically in this document, the dispersion relations are used to formulate models necessary for the achievements of the objectives listed in Section 1.5.

The Semi-Analytical Finite Element (SAFE) technique is a widely used and accepted technique to compute the dispersion relations of plates. SAFE was initially developed by Nelson et al. in [38] and Dong et al in [39]. The technique has been refined by several research groups and is now a commonly accepted method to compute the dispersion relations of multilayer anisotropic laminates [40], viscoelastic materials [41] and other waveguides. The outputs of SAFE contains the following interdependent physical quantities as functions of the frequency: group speed, phase speed, wavenumber and wavelength.

2.3 Sensing and actuation of guided waves

There exist numerous devices capable to generate or measure guided waves. This section presents a non-exhaustive list of actuating and sensing devices commonly used within the GWUT community. The main advantages and disadvantages of the guided wave generation and sensing techniques in the context of this research are

Table 2.1: Main advantages and disadvantages of some guided wave transducer as actuator in the context of this research

Actuator	Advantages	Disadvantages
PZT transducer	Low price, light and small Broadband	Low energy Permanently bounded
Power transducer	High energy Non-permanent mounting	Narrow band Contact
EMAT	Non-contact	Magnetic/ferromagnetic specimens
Air coupled	Non-contact	Low energy
Pulsed Laser	Non-contact High energy	Hazard to environment Damage to specimen

Table 2.2: Main advantages and disadvantages of some guided wave transducer as receivers in the context of this research

Receiver	Advantages	Disadvantages
PZT transducer	Low price, light and small	Permanently bounded Point measurement
EMAT	Area measurement	Magnetic/ferromagnetic specimens
Air coupled	Area measurement	Low signal-to-noise ratio
SLDV	Area measurement Distance to specimen	Reflective surface OR Low signal-to-noise ratio

presented in Tables 2.1 and 2.2 respectively. More details on each of these techniques are presented in the following subsections.

2.3.1 Piezoelectric transducer

The most common practice to generate and measure Lamb waves is to use a Piezoelectric (PZT) transducer bonded to a specimen [42, 43]. A PZT transducer can be used either as a sensor or an actuator [44, 45]. A PZT transducer can operate along one of these three deformation modes in function of its design: transverse, longitudinal and shear. By imposing the dimensions of the PZT, the operating frequency of a PZT transducer can be easily tuned for the desired application. As it is necessary to hold the transducer in contact with the specimen for both emission and reception modes, PZTs are often permanently bonded to the inspected specimen.

2.3.2 High power piezoelectric transducer

High power piezoelectric transducers, shortened *power transducers* in this document, are high quality PZT transducers designed to generate guided waves of much greater amplitude than regular PZT transducers by operating at their resonant frequency. They found application in ultrasonic cleaning, cell disruption or ultrasonic mixing [46].

Power transducers are typically made of several stacked circular layers of ceramic material [47]. The stack is pre-stressed with a screw at a given load in order to tune the resonant frequency of the assembly to a desired range of use. For the detailed characteristics of pre-stressed sandwich ultrasonic transducer, the reader is referred to [48, 49]. The typical dimensions of a power transducer is $40 \times 40 \times 60$ mm for a mass of about 0.3 kilograms and a cost of about $100, making it suitable for testing, but too heavy for the applications in which it is necessary to have an actuator permanently bonded to the inspected structure. A detailed design of a power transducer is available in [50]. Power transducers can be bonded to the specimen, but due to their sizes, alternative mounting technique are generally used. The non-permanent mounting of a power transducer on a specimen used in this research will be described in Section 5.2. Since power transducers focus on generating high amplitude guided waves at a single frequency, they are not suited to act as sensors.

2.3.3 Electromagnetic transducer

The Electro MAgnetic Transducer, or EMAT, is a type transducer using the electromagnetic effect to generate or receive ultrasonic waves. EMAT typically operates in a frequency range from 20 kHz to 10 MHz. EMAT is a contact free transducer but its application is limited by the fact that it can only interact with metallic or ferromagnetic materials [51].

EMATs are made of two parts: a permanent or electromagnet and an electric coil are kept at a given standoff distance (typically a few millimeters) of the specimen. Two fundamentally different mechanisms can then occur in the specimen in function of its physical properties. If the material is ferromagnetic, the EMAT generate or receive guided waves through magnetostriction, an effect initially observed by Joule in [52]. Magnetostriction is observed when a time dependent magnetic field is applied to a ferromagnetic material, causing motion and deformation of the material. Reversely, measuring the evolution of the magnetic field generated by the ferromagnetic specimen is a way to measure guided wave. However if the material is only conductive, eddy currents are generated or measured by the magnetic coil on the surface of the material, thus relating motion to the electrical signal associated with Lorentz forces.

The fact that EMAT can only be used with magnetic and ferromagnetic specimen is the main downside of this transducer in the context of this research. Solution to use EMAT with composite material have been explored in [53], but they require some sort of contact with the specimen, for example adding an adhesive aluminum layer on the composite. Thus, defeats the main advantage of EMAT which is to be a contact and couplant-free transducer.

2.3.4 Air-coupled transducers

An air-coupled transducer is a transducer interacting with a specimen through a thin layer of air and was first used to generate waves in [54]. Due to the great difference of impedance between the air and the commonly studied specimens (either metals or composites), guided waves generated by air coupled transducer are often of low amplitude [55, 56]. In [57], defects are located in a aluminum plate using PZT transducers as guided wave actuators and an air coupled transducer to measure the propagating waves. Recently, a new system of air coupled transducer has been designed to generate higher amplitude guided waves in composites from a standoff distance up to 6 cm in [58], but still requires a heavy experimental setup because it requires multiple independently controlled transducers. Air-coupled transducers are truly non-contact and can be the only solution to excite or measure guided waves when being in contact with the specimen and using a pulsed Laser are not valid options.

2.3.5 Pulsed Laser

Pulsed Laser is a device whose goal is to generate guided waves by sending a short and intense pulse of energy to a waveguide using a Laser beam. This technique has the advantage to be entirely contact free. Initially developed in [59], pulsed Laser relies on the generation of elastic waves by an intense local heating of the specimen.

Two main mechanisms can be used for guided wave generation by pulsed Laser for GWUT use: ablation and thermoelasticity [60, 61]. The process of ablation consists in striking the surface with a very high energy pulse, thus vaporizing locally a thin layer of material. Even though very high amplitude waves can be generated by this process, the damage induced to the specimen is often not acceptable. Finally thermoelasticity is the process of sending a pulse of lower energy compared to the ablation process. The specimen is locally heated by the pulse and the resulting mechanical deformation generates guided waves. Thermoelasticity is the only pulsed Laser process capable of generating guided waves of sufficient amplitude for GWUT purposes without damaging the specimen [62]. The excitation by a pulse laser is usually broadband [63]. A technique using a Laser to remotely excite a PZT transducer placed on the inspected surface thus creating a non-contact technique with no risk of damaging the specimen is presented in [61].

In theory, pulsed Laser is the most multipurpose of all the guided wave generation techniques since any type of guided waves can be generated, in any material and from an arbitrary distance to the specimen, without the need to have complete access to the inspected surface. In practice however, the setup is expensive and can be a threat to the operator's eye. Moreover, the thermoelastic process can damage the inspected structures if not used properly.

2.3.6 Laser Doppler Vibrometry

A Laser Doppler Vibrometer (LDV) is a device that employs a Laser beam and the Doppler effect to measure the motion of the surface. The Doppler effect states that the frequency of a wave changes if the observer is in motion with respect to the source [64]. A LDV is essentially made of a two-beam Laser interferometer measuring the frequency shift between a baseline and a test Laser beam. The baseline Laser beam is kept unchanged while the test beam is sent to the specimen. The test beam is then reflected back by the specimen to the LDV to interfere with the baseline beam. The difference in frequency between the two beams, measured by an interferometer, carries information on the velocity of the motion of the surface of the specimen. The output of a single point LDV measurement is the velocity of the measured point as a function of time. The range of application of Laser vibrometer is very large, from waves and vibrations measurement to remote listening system.

A LDV with a unique beam direction is said to be a 1D LDV as only a single point measurement can be acquired for a given experimental configuration. However if the Laser beam can target multiple points through an automated scanning mechanism, the Laser is said to be a 2D LDV or a Scanning Laser Doppler Vibrometer (SLDV). This can be achieved either by using a system of mirror or by physically moving a 1D LDV on a plane. Several companies sell fully integrated SLDV made of a 1D LDV plus a system of rotating mirrors, thus allowing non-contact inspection of large structures from any distance.

The major downside of the LDV is the fact that the test Laser beam must be reflected by the specimen. Low signal-to-noise ratio of the measurements is indeed a problem if the reflection coefficient of the inspected surface is low. To solve this issue, it is commonly accepted by the research community to add a reflective surface to the inspected specimen which can be either reflective tape of reflective paint. This is, of course, a limitation in practical applications. Furthermore, even if the surface is highly reflective, it is required to have a Laser beam nearly orthogonal to the inspected surface in order to obtain a sufficient signal-to-noise ratio [65]. In order to ensure that the angle between the Laser beam and the scanned structure is nearly orthogonal, it is valuable to place the SLDV as far as possible from the structure. However for high amplitude excitation, such as an excitation by a power PZT transducer or a pulsed Laser, the orthogonality of the Laser beam to the specimen and the presence of an additional reflective surface on the specimen may not be required.

SLDV is a versatile guided wave measurement device since it is purely non-contact, can inspect very large areas and can operate from a wide range of distances with respect to the specimen.

2.4 Experimental setup for guided wavefield detection

The experimental setup used to acquire wavefields in this research is shown in Figure 2.3. The excitation function, typically but not necessarily a harmonic function, is generated by a signal generator. The signal generator is an Agilent 33220A which can generate any arbitrary waveform with a frequency up to 20 MHz. The excitation is then amplified by a Broadband Power Amplifier 1040L that operates from 10 kHz to 5 MHz with a gain of at least 55 dB with a maximum output power of 500 Watts. The high voltage excitation is then sent to a transducer in contact with the specimen. In this research, unless otherwise specified, the transducer is a single broadband low energy PZT disk bonded to the surface of the specimen operating in thickness vibration mode. The out-of-plane velocity of the specimen is measured on a grid of points by the SLDV Polytec PSV-400-M2 and then sent to the Polytec integrated software for vibration measurement version 8.2. Measurement at one location can

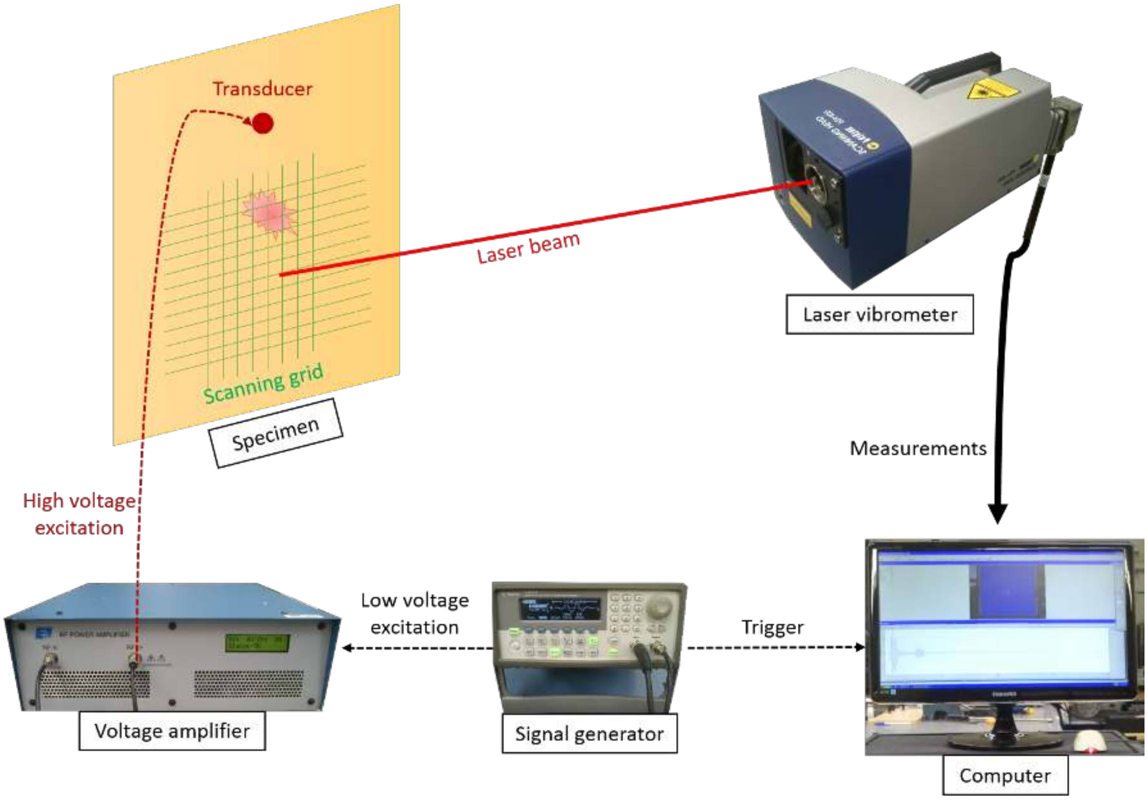

Figure 2.3: Experimental setup to generate and measure guided wave

be repeated an arbitrary number of times for averaging purposes. This SLDV has an angular opening of 20 degrees so can measure an area of 1.5 × 1.5 m^2 from a standoff distance of 2 meters, which is an approximate distance used in practice. The SLDV uses a class 2 Laser and therefore does not require safety glass while operating. Due to the inertia of the mirrors that direct the Laser beam, the SLDV can only measure up to 30 points per seconds. The signal generator and the computer are synchronized so each measurement is started when a trigger is received from the signal generator. Unless otherwise specified, reflective tape or paint is present on the surface of the specimen in order to increase the signal-to-noise ratio of the measurement, especially if the Laser beam is not orthogonal to the specimen, as this is always the case when scanning large surfaces. Table 2.3 summarizes the range of the experimental parameters that can be achieved with the system available, as well as the device limiting the range of the corresponding parameter.

Table 2.3: Range of experimental parameters

Parameter	Range	Limiting device
Excitation frequency	10 kHz to 5 MHz	Amplifier
Excitation power	$< 2 - 3$ Watts	PZT transducers
Sample frequency	2.56 MHz	SLDV
Point-measurement per second	30	SLDV
Area of inspection	1.5×1.5 m^2	SLDV
Max number of points	$40,000$	Software

2.5 Experimental parameters

The choice of each of the parameters described in the previous section is crucial to the detection of guided wavefields. There exist some criteria such as Nyquist-Shannon sampling theorem [66] imposing lower bounds on some parameters, but for some, the choice is arbitrary and based on experience.

Nyquist theorem states that the sampling rate must be at least twice greater than the inverse of the period of the signal to measure:

$$\frac{F_s}{2} \geq f \tag{2.22}$$

where F_s is the sample frequency and $f = 1/T$ is the frequency to be measured. If this criteria is not respected, aliasing is observed. In guided wave acquisition, Nyquist theorem must be applied in both time and space. The application of Nyquist theorem in the time domain requires that the sampling frequency is at least two times the highest frequency of the waves propagating in the specimen. In the spatial domain, Nyquist theorem's provides an upper bound to the spacing between every measurement point. This requires the estimation of the smallest wavelength propagating in the media, which is done by studying the dispersion relations of the specimens computed by SAFE.

The typical process to choose the experimental parameters is the following:

1. Compute the dispersion relations of the studied specimen with SAFE;

2. Select an interrogating frequency below the first cutoff frequency. For a broadband transducer, the frequency can be chosen arbitrarily while for a narrowband transducer, the excitation frequency must be a resonant frequency fixed by the transducer;
3. Select the corresponding sampling frequency using Equation (2.22);
4. Using the dispersion relations and the excitation frequency, estimate the smallest propagating wavelength in the media within the frequency range;
5. Deduce the maximal point spacing using Nyquist's theorem;
6. Define the region of interest including the features to be measured;
7. Define the duration of the inspection in function of the size of the inspected area and the group speed given by the dispersion relations.

2.6 Example of guided wavefield

This section presents a guided wavefield measured with the experimental setup detailed in Figure 2.3. The goal is to provide an intuitive understanding of wavefield measurements and the information they provide.

The studied specimen is a glass fiber quasi-isotropic composite plate of dimensions $600 \times 600 \times 1.6$ mm and layup $[0, 90, +45, -45]_s$. A 25.4 mm diameter Teflon disk was inserted between the second and the third ply during the manufacturing of the plate to simulate a delamination. This specimen will be used in this entire research for illustration purposes. The front size of the plate is chosen to be the side on which the delamination is 2 layers deep. The plate is covered with reflective tape on both sides and a PZT disc is bonded at the center of the plate on the back side. The delamination is located 100 mm away from the center of the plate in the direction corresponding to a fiber angle of 0°. The excitation is a four-cycle Tone Burst (abbreviated TB4) of center frequency 200 kHz. The frequency of excitation is chosen using the dispersion relations calculated by SAFE so that only the $A0$ and $S0$ modes propagate in the specimen. The area of inspection is 473×445 mm, discretized in $178 \times 178 = 31,684$ points. A duration of 3.2 ms is waited between each measurement so that the energy of the tone burst of the previous measurement completely vanishes due to dissipation and attenuation so it does not interfere with the following measurement. Furthermore, each measurement is averaged 10 times to increase the signal-to-noise ratio, so that 300 measurements are taken every second corresponding to the 30 points per seconds limit of the SLDV. Furthermore, the sample frequency is 2.56 MHz and the duration of each measurement is 400 μs. Two time snapshots of the wavefield are shown in Figure 2.4a and 2.4b. The first picture is the wavefield at $t = 50$ μs after the excitation. Two waves corresponding to the two propagating modes are visible. Note that the disturbance of the faster mode ($S0$) shows the location of the defect. The second picture is the wavefield at $t = 70$ μs and shows the standing waves in the delaminated area and the $A0$ wave which is about to interact with the defect.

Given the experimental parameters, the theoretical acquisition time is 18 minutes while the actual measurement time is nearly 2 hours. The difference is due to the lag induced by the computer recording and averaging the data. The amplitude represented by the color scale of the wavefields presented in this thesis are not shown, this is because only the relative values of the displacements are meaningful, while the absolute values, which are functions of the parameters used for the acquisition by the SLDV, are not useful to the methods presented herein. This is also due to the fact that the measurement by the SLDV is actually the out-of-plane velocity instead of the displacement. However as guided waves are represented by harmonic functions, no distinction will be made between measured displacement and measured velocity.

The dispersion relations of the wavefield are then presented in Figure 2.5a and 2.5b. The dash lines present the theoretical dispersion relations estimated by SAFE.

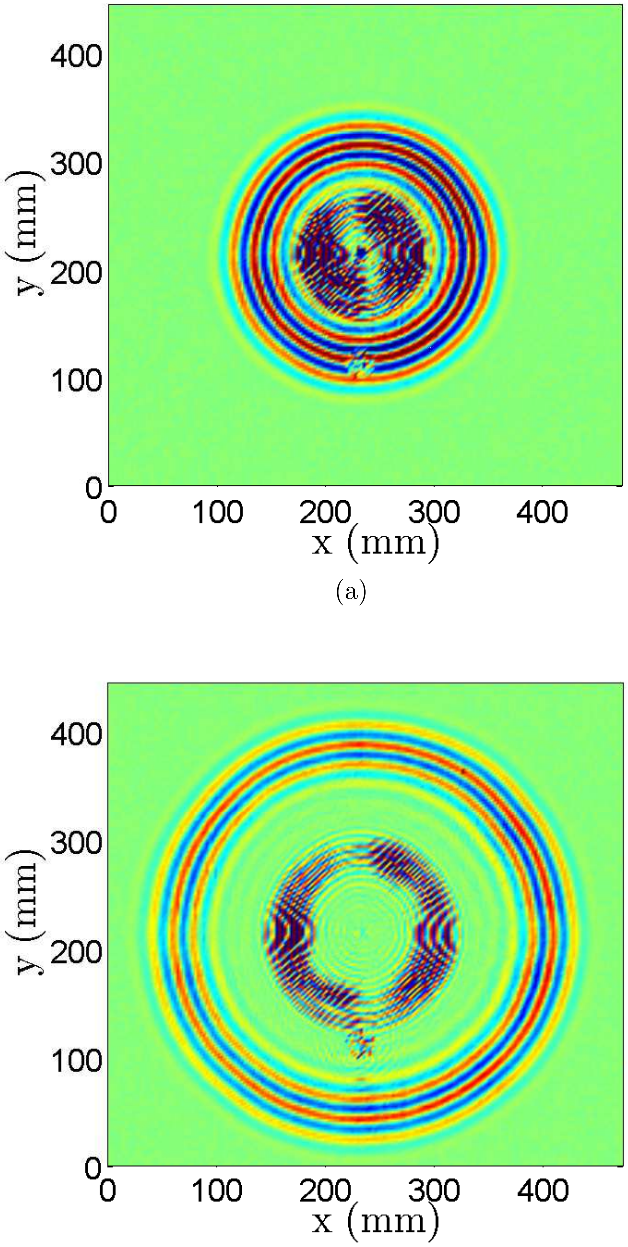

(a)

(b)

Figure 2.4: Two snapshots of the example wavefield at (a): $t = 50\ \mu\text{s}$ and (b): $t = 70\ \mu\text{s}$

Figure 2.5a shows the two wavenumbers at the excitation frequency 200 kHz and was obtained by applying a 3D Fast-Fourier Transform (FFT) [67] to the wavefield and extracting the frequency slice corresponding to the excitation frequency. Note that in this case the greatest wavenumber is associated to the slower mode ($A0$) while the smaller value is the $S0$ mode. Figure 2.5b shows the dispersion relations as a function of frequency along a single direction and was obtained by applying the FFT to the line of the wavefield of direction 0^0.

2.7 Conclusions

This chapter presented an introduction to GWI. Fundamentals of guided waves were first summarized along with the calculation of the dispersion relations. The common practices of the GWI community for the actuation and the sensing of guided waves were presented next. The experimental setup used in this research for guided wavefield measurement was presented, followed by guidelines regarding the choice of the experimental parameters. An illustration of guided wavefield detection was given. Based on this introduction, the following chapter will attempt to fulfill the first and the second objective defined in Section 1.5, namely the guided wavefield acquisition time reduction and defect detection.

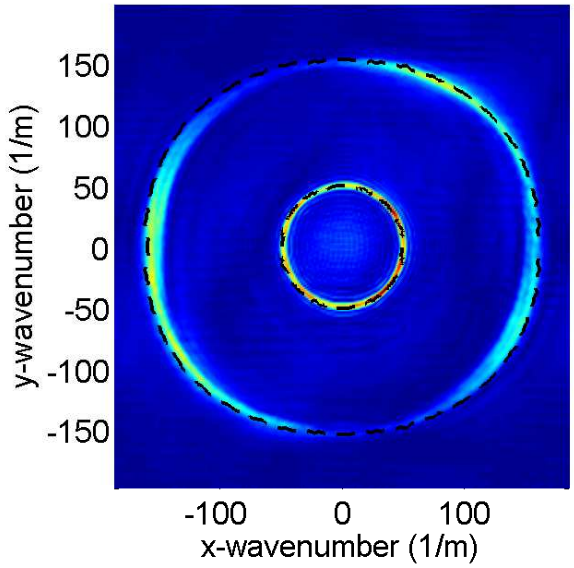

(a)

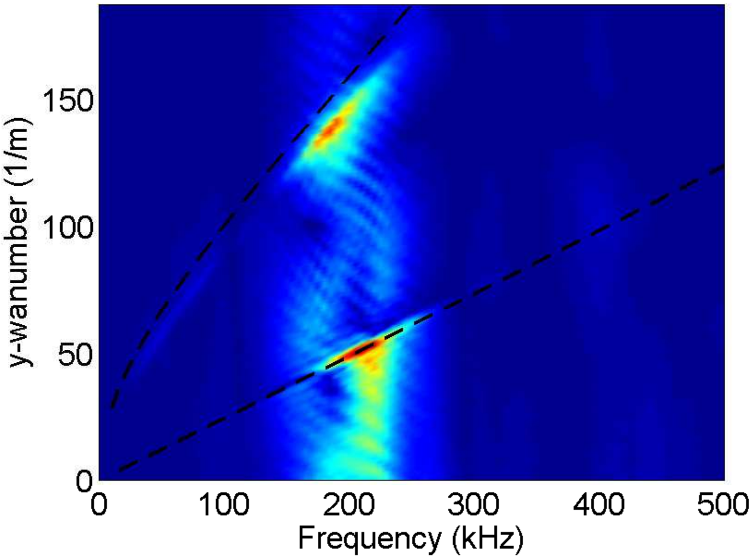

(b)

Figure 2.5: (a): Frequency slice at 200 kHz of the dispersion relation of the example wavefield, dash lines: SAFE predictions and (b): Dispersion relation in the direction 0^o as a function of frequency, dash lines: SAFE predictions

CHAPTER III

SPARSE WAVEFIELD RECONSTRUCTION

3.1 Chapter overview

Wavefield acquisition is a time consuming process due to the need for multiple averages at each measurement location to mitigate the effects of low signal-to-noise ratios, the waiting time between each measurement and the measurement density required to avoid spatial aliasing. There is therefore a recognized need to reduce wavefield acquisition time by reducing the number of point-acquisition. This is the focus of recent papers in which the use of dedicated equipment is explored to speed up acquisitions by increasing the number of measurements per unit of time. Examples include the use of a multi-point Laser Doppler Vibrometer (LDV) [68, 69], and of a galvanometer mirror system acting as a continuously moving LDV [70].

This chapter contributes to this objective by developing a process that reduces the number of required point-measurements below the limits imposed by Nyquist sampling theorem. The proposed process is based on the hypothesis that the time response recorded at one point of the surface of a plate structure can be employed to infer the response at any other point assuming prior knowledge of dispersion relations, plate geometry, and location of the excitation. When this knowledge is incomplete due to the presence of defects for example, this extrapolation is not straightforward and tools such as Compressed Sensing (CS) must be used [71, 72, 73]. A novel Sparse Wavefield Reconstruction (SWR) technique, presented in this section implements the interpolation of sparse guided wavefield measurements to reconstruct a wavefield. As a by-product, features inside or outside the area of inspection can be also identified. The SWR uses CS and the dispersion relations of the specimen for interpolation. A short background on CS is first provided, followed by an overview of the use of sparse measurements in GWI. The model used to interpret the sparse measurements is then presented. The matrix formulation, the implementation of the SWR process and the choice of the parameters are detailed next. Finally, results of wavefield reconstructions on anisotropic specimens are presented.

3.2 Introduction to Compressed Sensing

3.2.1 Fundamentals

Compressed Sensing (CS) is a mathematical theory commonly used as a reconstruction process for data sampled below the Nyquist frequency [66]. Compressed sensing deals with *sparse* or *compressible* signals randomly sampled within the domain of interest, either time or space. A *sparse* signal is here intended as a signal with only a few nonzero coefficients, whereas a signal is *compressible* if there exist a basis in which the signal has a sparse representation. Applications of CS include image processing [74], magnetic resonance imaging [75, 76], radars [77] or single point cameras [74].

The fundamental mathematical result of CS states that if a signal $\boldsymbol{x} \in \mathbb{R}^{N\times 1}$ is K $(K << N)$ *sparse*, i.e., only K components of x are non-zero, it can be exactly reconstructed with an overwhelming probability from few measurements randomly chosen [71, 72]. The same result holds for *compressible* signals, which are signals well approximated by a small number of coefficients in a given basis. The basis in which a compressible signal is sparse is called a *sparsifying basis.*

The general under-sampling problem can be expressed as:

$$\boldsymbol{y} = \boldsymbol{\Phi}\boldsymbol{x} \tag{3.1}$$

where $\boldsymbol{y} \in \mathbb{R}^{M\times 1}$ is the measurement vector, $\boldsymbol{\Phi} \in \mathbb{R}^{M\times N}$ is the down-sampling measurement matrix and $\boldsymbol{x} \in \mathbb{R}^{N\times 1}$ is the unknown vector to reconstruct. It is assumed that $M << N$, so that $\mathbf{\Phi}$ is a *short and large* type of matrix. In other words, the number of measurements is smaller than the number of unknown variables in $\boldsymbol{x}$.

For a compressible signal, the problem in Equation (3.1) can be rewritten through a change of basis as follows:

$$\boldsymbol{y} = \mathbf{\Phi}\boldsymbol{B}\boldsymbol{\alpha} = \boldsymbol{A}\boldsymbol{\alpha} \tag{3.2}$$

where $\boldsymbol{\alpha} \in \mathbb{R}^{P\times 1}$ is the sparse representation of $\boldsymbol{x}$ in the basis defined by $\boldsymbol{B} \in \mathbb{R}^{N\times P}$, i.e., $\boldsymbol{A} = \mathbf{\Phi}\boldsymbol{B}$, where $\boldsymbol{A} \in \mathbb{R}^{M\times P}$ is called the *sensing matrix*. Thus:

$$\boldsymbol{x} = \boldsymbol{B}\boldsymbol{\alpha} \tag{3.3}$$

with P denoting the number of vectors forming the basis $\boldsymbol{B}$.

Equation (3.2) defines a CS problem. The objective is the estimation of the basis coefficients $\boldsymbol{\alpha}$ that provide the best reconstruction of the unknown set of physical variables $\boldsymbol{x}$ represented through $\boldsymbol{B}$. Inputs to the problem are the measurements $\boldsymbol{y}$. It is important to note that the definition of the *sensing matrix* is a crucial step in CS, as it must properly describe the signal to reconstruct [78, 79]

3.2.2 Solutions of Compressed Sensing problems

Several methods have been proposed for the solution of under-determined linear CS problems as expressed by Equation (3.2). The methods can be separated in three groups [80]: greedy algorithms, $l1$-minimizers (or Basis Pursuit), and total variation algorithms. First, greedy algorithms minimize the $l0$-norm of the sparse signal. Greedy algorithms are iterative techniques choosing the best local minimum at each iteration and are expected to find a satisfying approximation of the global optimum after several iterations. Even though conceptually simple and quickly converging, greedy algorithms are unstable and not robust to measurement noise. Specifically, the solution may not converge if the results of the first iterations are incorrect. The most famous greedy algorithm is the Orthogonal Matching Pursuit algorithm proposed in [81, 82, 83], which is most robust than most greedy algorithms [84].

Second, $l1$-minimization algorithms also called Basis Pursuit (BP) [85, 86], aim at minimizing the $l1$-norm of the sparse signal by solving the following minimization problem:

$$\text{minimize } \|\boldsymbol{\alpha}\|_1 \text{ subject to } \boldsymbol{y} = \boldsymbol{A}\boldsymbol{\alpha} \tag{3.4}$$

In addition to be more stable and more robust to noise than greedy algorithms, Basis Pursuit algorithms are able to reconstruct not truly sparse signals. Because noise is expected in the experimental Lamb wave measurements, BP algorithm are considered good choices for this research.

Finally, Total Variation (TV) algorithms are methods similar to $l1$-minimization techniques but assume that the sparse property is carried by the gradient of the signal instead of the signal itself. Total Variation algorithms are therefore very efficient when the signal to reconstruct is piecewise constant [87, 88].

3.2.3 Basis Pursuit for Compressed Sensing

Because the Basis Pursuit (BP) methods are commonly robust to measurement noise and capable of estimating non-truly sparse signals [89], only BP techniques will be used in this work. The application of BP methods require that the sensing matrix $\boldsymbol{A}$ verifies the Restricted Isometry Property (RIP) with a RIP constant δ_s smaller than unity [89]. This constant is defined for a matrix $\boldsymbol{A}$ by the smallest scalar verifying the following inequality for all $\boldsymbol{y}$ and for all sub-matrices of $\boldsymbol{A}$, denoted $\boldsymbol{A}_s$:

$$(1-\delta_s)\,\|\boldsymbol{y}\|_2^2 \leq \|\boldsymbol{A}_s\boldsymbol{y}\|_2^2 \leq (1+\delta_s)\,\|\boldsymbol{y}\|_2^2$$

The δ_s constant is a characterization of the nearly orthogonal matrices operating on sparse vectors. The case $\delta_s \approx 0$ corresponds to a nearly orthonormal matrix, while $\delta_s \approx 1$ indicates that some of the vectors forming the matrix $\boldsymbol{A}$ are nearly identical or redundant. This requirement guarantees that the CS problem can be inverted with an overwhelming probability through BP. There exists a list of candidate matrices $\boldsymbol{A}$ obeying this property. These include the random Gaussian, the Bernoulli and the partial Fourier matrices [86]. However, computing these RIP constants is a non-deterministic polynomial-time hard (NP-hard) problem and is not possible for most matrices [90], meaning that this requirement can not be verified in general. In practice, this requirement is often replaced by ensuring that matrices $\boldsymbol{B}$ and $\boldsymbol{\Phi}$ in Equation (3.2) are incoherent [91, 89]. This is mathematically verified by checking that the mutual coherence is smaller than a constant defined in [92], which is equivalent to checking that the matrix $\boldsymbol{A}$ is nearly orthonormal. The mutual coherence M_C of a matrix A is given by the maximum value of the scalar product between all the columns of the $\boldsymbol{A}$ matrix:

$$M_C(\boldsymbol{A}) = \max_{1 \leq i \neq j \leq m} |a_i^H a_j| \tag{3.5}$$

where the column of the matrix $\boldsymbol{A}$ are denoted a_i for $i = 1$ to m, while $(\ )^H$ denotes the conjugate transpose operator.

The Basis Pursuit Denoising (BPDN) algorithm [85, 86] is a BP algorithm that guarantees exact reconstruction [93] by solving the following problem

$$\text{minimize } \left\|\boldsymbol{\alpha}\right\|_1 \text{ subject to } \left\|\boldsymbol{y} - \boldsymbol{A}\boldsymbol{\alpha}\right\|_2^2 \leq \sigma \tag{3.6}$$

where σ is a constant related to the noise level in the measurements, with $\sigma = 0$ in the absence of noise. The BPDN algorithm used is this work is a Spectral Projected-Gradient for $l1$ minimization called SGPL1, which is a solver for large scale sparse reconstruction that employs convex optimization to find a sparse representation of $\boldsymbol{\alpha}$ even when $\boldsymbol{B}$ is an over-complete dictionary of basis functions [94, 95], this is achieved by solving the Lasso problem [96]:

$$\text{minimize } \|\boldsymbol{y} - \boldsymbol{A}\boldsymbol{\alpha}\|_2 \text{ subject to } \|\boldsymbol{\alpha}\|_1 \leq \sigma \tag{3.7}$$

Accordingly, an estimation of the sparse optimum can be found even if the vectors in $\boldsymbol{B}$ are coherent with one another. As many of the BPDN solvers, SPGL1 is robust to measurement noise and takes σ as the only input parameter. The solver SPGL1 is implemented in Matlab [94, 95] and can be executed with three arguments by the following command:

$$\boldsymbol{\alpha} = spgl1(\boldsymbol{A}, \boldsymbol{y}, \sigma) \tag{3.8}$$

The solver SPGL1 can handle additional options such as starting point for the minimization or a maximum number of iterations. As the expected solution is sparse (i.e., few values are non-zero), the starting point of the SPGL1 minimizer is the zero vector in this research.

3.3 Current developments in wavefield reconstruction

Techniques to efficiently extract relevant information or reconstruct wavefields from sparse measurements have been explored by several research groups. For example, a noisy flaw signal can be reconstructed using Bayesian learning as in [97]. Sparse single mode measurement and baseline subtraction are used in [98] to locate a transducer in isotropic material. Dispersion compensation techniques, initially developed in [99], and later in [13, 100, 101, 102, 103] aim at compensating for the effect of the wave dispersion and have the ability to detect impact locations, relying on the sparse representation of waves. In practice, dispersion compensation techniques reconstruct an excitation and its location from the measurement of the dispersed waves. It would however be of interest to reconstruct guided waves from sparse measurements with an arbitrary number of modes and without using baseline signals. To this end, prior work focused on reducing the number of point-measurements to estimate a wavefield

[104]. In contrast to the work presented here, the methodology presented in [104] requires no prior knowledge of the physical properties of the medium as described by the dispersion relations. More recently in [105], a wavefield reconstruction technique similar to the one presented herein, employs analytical basis functions such as wavelets [106], Fourier functions or Gabor atoms as bases for wavefield reconstruction. Another series of papers develops a technique called sparse *wavenumber analysis* [107, 108] for reconstructing the dispersion relations of a plate through sparse measurements. This technique has also been recently applied to pristine wavefield reconstruction [109]. Without attempting to reconstruct wavefields, a technique to locate defects relying on a sparse representation of the wavefield and dictionary learning is proposed in [110]. Finally, an approach to overcome aliasing due to under-sampled measurements by using an iterative interpolation scheme is presented in [111].

This chapter presents a process to reconstruct a wavefield on an oversampled grid. This work differentiates itself from prior work by performing the reconstruction upon locating the non-pristine material points interacting with the wavefronts. The estimated dispersion relations of the medium are then used to extrapolate the wavefield onto a grid of points of arbitrary size and density. The estimated dispersion relations form the basis that sparsifies the wavefield, and allows wavefield reconstruction. Furthermore, this basis locates the features within the specimen that interact or affect the wavefield, including sources or scatterers such as defects. The process also reconstructs an arbitrary number of Lamb wave modes. The number of measurements required for the reconstruction is significantly smaller than the number of measurements required by common sampling requirements. This work was published in [112].

3.4 Model: the propagation equation

Reconstruction of compressible signals by CS relies on the definition of a sparsifying basis. The goal of this section is to establish a model that can be used to obtain a sparse representation of any wavefield. The model relies on the out-of-plane displacement measured at a distance d from a point source of unit amplitude in an elastic plate [113, 114]:

$$\widehat{U}^{(\mu)}(d, \omega) \propto \frac{e^{-ik^{(\mu)}(\omega)d}}{\sqrt{d}} \tag{3.9}$$

where $U^{(\mu)}(d, \omega)$ is the out-of-plane displacement of an elastic plate due to the Lamb wave mode (μ), at frequency ω, at a distance d from a point source of unit amplitude and $k^{(\mu)}$ denotes the wavenumber of mode (μ). This equation means that the amplitude received at a distance d from a source evolves with the term $1/\sqrt{d}$, which represents the 2D geometric spreading, while the phase is given by the product $k^{(\mu)}(\omega)d$. Similar equations were used in [115, 116, 117].

By superposition, the displacement received at a distance d_s from a source s of arbitrary excitation function $\widehat{V}_s^{(\mu)}(\omega)$ for mode (μ) is given by:

$$\widehat{U}^{(\mu)}(d_s, \omega) = \widehat{V}_s^{(\mu)}(\omega)\frac{e^{-ik^{(\mu)}(\omega)d_s}}{\sqrt{d_s}} \tag{3.10}$$

In practice, a point-measurement at location m, denoted $\widehat{Y}_m(\omega)$, is the superposition of the displacements from multiple sources and multiple modes. Let S be the total number of sources contributing to the displacement received at location m and $N^{(\mu)}$ be the number of Lamb wave modes. By superposition from all the sources and all the modes, the displacement at location m is given by:

$$\widehat{Y}_m(\omega) = \sum_{\mu=1}^{N^{(\mu)}} \sum_{s=1}^{S} \frac{e^{-ik^{(\mu)}(\omega)d_{m,s}}}{\sqrt{d_{m,s}}} \widehat{V}_s^{(\mu)}(\omega) \tag{3.11}$$

where $d_{m,s}$ denotes the distance from the source s to the measurement m.

For an anisotropic material, the wavenumber $k^{(\mu)}(\omega)$ is a function of the direction of propagation defined by the line between the measurement and the source, hence is denoted $k^{(\mu)}_{m,s}(\omega)$ from now on. Application of inverse Fourier Transform leads to the time evolution at the measurement point y_m with $m = 1$ to M:

$$y_m(t) = \sum_{\mu=1}^{N^{(\mu)}} \sum_{s=1}^{S} \frac{1}{\sqrt{d_{m,s}}} \mathcal{F}^{-1} \left(\mathcal{F} \left(v_s^{(\mu)}(t) \right) e^{-ik^{(\mu)}_{m,s}(\omega) d_{m,s}} \right) \tag{3.12}$$

Here S is the number of sources emitting wavefronts, $d_{m,s}$ is the distance between the source s and the measurement point m, while $\mathcal{F}$ and $\mathcal{F}^{-1}$ denote the Fourier Transform and its inverse, respectively. Furthermore, $v_s^{(\mu)}(t)$ is the excitation function for mode (μ) at source s, $\omega = 2\pi f$ is the angular frequency, and $k^{(\mu)}_{m,s}(\omega)$ is the wavenumber of mode (μ) along the line joining the source s to the measurement point m. Equation (3.12) assumes that amplitude decays solely due to geometrical spreading, and therefore material dissipation is neglected.

The objective of this chapter is to reconstruct the wavefield with a limited number of measurements and without prior knowledge of all sources that contribute to the propagation of guided waves within the plate-like structure under consideration. Surface mounted transducers, boundaries, structural features such as holes, interfaces, stiffeners, and defects are considered as potential sources. Since their numbers and locations are initially unknown, all points belonging to the discretized region of interest are treated as potential source locations. In general, the grid of potential sources is defined to at least satisfy Nyquist criterion for proper sampling of the wavefield, i.e., two per wavelength.

3.5 Compressed Sensing matrix formulation

Assuming multi-modal wave propagation, Equation (3.11) can be expressed in matrix form as follows:

$$\widehat{\boldsymbol{y}}(f) = \sum_{\mu=1}^{N^{(\mu)}} \boldsymbol{H}^{(\mu)}(f) \widehat{\boldsymbol{v}}^{(\mu)}(f) \tag{3.13}$$

where $\widehat{\boldsymbol{y}}(f) \in \mathbb{R}^{M\times 1}$ is the vector containing the M measurements in the frequency domain:

$$\widehat{\boldsymbol{y}}(f) = [\widehat{Y_1}(f), \cdots, \widehat{Y_M}(f)]^T$$

Also, $N^{(\mu)}$ is the number of propagating modes, while $\boldsymbol{H}^{(\mu)}(f)$ is the matrix of basis functions whose m, s term is:

$$\widehat{h}^{(\mu)}_{m,s}(f) = \frac{e^{-ik^{(\mu)}_{m,s}(f)d_{m,s}}}{\sqrt{d_{m,s}}} \tag{3.14}$$

where s is the index of the source with $s \in [1, S]$. Furthermore, vector $\widehat{\boldsymbol{v}}^{(\mu)}(f) \in \mathbb{R}^{S\times 1}$ is given by:

$$\widehat{\boldsymbol{v}}^{(\mu)}(f) = [\widehat{v_1}^{(\mu)}(f), \cdots, \widehat{v_S}^{(\mu)}(f)]^T$$

and contains unknown amplitude and phase information for source s at frequency f.

The basis functions are selected upon assumption of the dispersion relations of the structure, which is based on knowledge of thickness and material properties. Specifically, the wavenumbers $k^{(\mu)}_{m,s}(f)$ are estimated using SAFE (Section 2.2). Hence, for every measurement-sources pair, the only unknown in Equation (3.11) is $\widehat{v_s}^{(\mu)}(f)$. It is understood that the assumption of the dispersion properties is a source of uncertainty and potential errors, the influence of the usage of inexact dispersion relations will be studied in Section 3.8.1.

In most of the wavefields investigated in this research, frequencies are below the $A1$ and $S1$ mode cut-off frequencies so that only the $A0$ and $S0$ modes propagate in the specimen. While this choice is made for convenience of experimentation and computation, it is noted that the formulation can be extended to include a higher number of modes. Accordingly, for $N^{(\mu)} = 2$, Equation (3.13) can be rewritten as:

$$\widehat{\boldsymbol{y}}(f) = \boldsymbol{H}^{S0}(f)\widehat{\boldsymbol{v}}^{S0}(f) + \boldsymbol{H}^{A0}(f)\widehat{\boldsymbol{v}}^{A0}(f) = \boldsymbol{H}(f)\widehat{\boldsymbol{v}}(f) \tag{3.15}$$

where $\boldsymbol{H}(f)$ and $\widehat{\boldsymbol{v}}(f)$ are obtained respectively by horizontal and vertical concatenations of the corresponding matrices and vectors. The dimensions of $\boldsymbol{H}(f)$ are

$M \times SN^{(\mu)}$, where S is the number of potential sources, M the number of measurement and $N^{(\mu)} = 2$ for $A0$ and $S0$ only.

Equation (3.15) is in the same form of Equation (3.2), so that the following CS problem can be solved at a given frequency f:

$$\text{minimize } \|\widehat{\boldsymbol{v}}(f)\|_1 \text{ subject to } \|\widehat{\boldsymbol{y}}(f) - \boldsymbol{H}(f)\widehat{\boldsymbol{v}}(f)\|_2^2 \leq \sigma \tag{3.16}$$

The $l1$-minimization described in Equation (3.16) estimates amplitude and phase of each component of the source vector $\widehat{\boldsymbol{v}}(f)$, and therefore defines the contribution of the potential sources to the measured wavefield. It is worthwhile emphasizing that this source vector includes excitation provided by transducers employed to originate the wavefield along with any source of scattering resulting from both known structural features and unknown defects. Of note is also the fact that the contribution to each mode is evaluated separately. This accounts for the fact that excitation through surface mounted transducers such as piezoelectric disc and scattering occurs with different efficiency for each participating mode. Finally, it is noted that the basis functions (Equation (3.14)) are independent on the direction, meaning that every source is omni-directional.

The sparsity of the formulation exploited herein relies on the fact that vector $\widehat{\boldsymbol{v}}(f)$ is sparse in space, which is based on the reasonable assumption that the number of actual sources, either known or unknown, can be considered small compared to the number of potential sources in the region of interest. Therefore only a few components of $\widehat{\boldsymbol{v}}(f)$ are expected to be non-zero.

3.6 Wavefield reconstruction methodology

3.6.1 Implementation

The wavefield reconstruction process can be described by the two steps process depicted in Figure 3.1. The first step consists in the estimation of the excitation function spectra for each potential sources and each mode through $l1$-minimization. The inputs of this step are the M measurements and the sensing matrix $\boldsymbol{H}(f)$, created using the dispersion relations of the media, the location of measurements and potential sources. The measurements are selected in the region of interest following a predefined distribution. The measurement distribution can be regular, semi random or fully random. For more details on measurement distribution, refer to section 3.6.3. The Compression Ratio (CR) of the reconstructed wavefield with respect to Nyquist theorem is defined by:

$$CR(\%) = 100 \times (1 - \frac{M}{M_{Nyq}}) \tag{3.17}$$

where M_{Nyq} is the number of measurements required by Nyquist theorem to fully know a wavefield:

$$M_{Nyq} = \frac{2(max(x) - min(x))}{\lambda^x_{min}} \times \frac{2(max(y) - min(y))}{\lambda^y_{min}} \tag{3.18}$$

where x and y are the spatial extend of the inspected window and λ^x_{min} and λ^y_{min} are the smallest propagating wavelength along the x and the y dimensions respectively. Equation (3.18) is equivalent to measuring two points per wavelength along each dimension, as required by Nyquist sampling theorem. The CR expresses the reduction of the number of measurements to acquire with respect to the full capture of the wavefield based on sampling criteria. Note that Nyquist theorem only provides the theoretical lower bound on the number of measurement, in general, it is common practice to oversample and take more measurements that what is required in order to ensure the best possible result quality.

Critical to the CS problem solution is the choice of the stopping criteria σ in Equation (3.6). In practice, relating σ to the norm of the measurement has been proven to be efficient in [118]. Section 3.6.4 presents more details on the choice of the parameter σ.

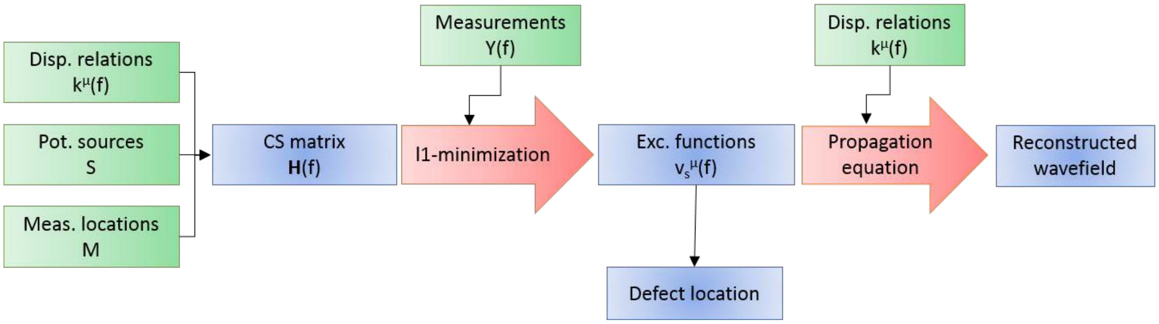

Figure 3.1: Schematic of the two steps wavefield reconstruction process.

The first step provides as an output the vector $\widehat{\boldsymbol{v}}(f)$. This is performed by employing the Basis Pursuit solver SPGL1 [95] which is used to invert Equation (3.15) through $l1$-minimization of Equation (3.6). The vector $\widehat{\boldsymbol{v}}(f)$ contains information on the location of the sources as well as on their amplitudes and phases for each mode and frequency. As such, $\widehat{\boldsymbol{v}}(f)$ may be used to detect and locate defects. Since the problem is solved at each frequency, and in order to have a visual representation of the location of the sources that are active contributors to the wavefield, the following quantity is monitored:

$$\mid v_s^{(\mu)} \mid = \frac{1}{\Delta f} \int_f \widehat{v_s}^{(\mu)}(f) df \tag{3.19}$$

where Δf defines the considered frequency bandwidth selected for the reconstruction. Mapping of the resulting vector $\mid \boldsymbol{v}^{(\mu)} \mid = [\mid v_1^{(\mu)} \mid, \cdots, \mid v_S^{(\mu)} \mid]$ over the entire discretized region provides a map of active sources including defects. The points for which vector $\mid \boldsymbol{v}^{(\mu)} \mid$ is greater than zero represent the active sources of mode (μ) and identifies a feature that contributes to the considered modal component of the wavefield.

The second step consists in the reconstruction of the wavefield, which involves the forward application of Equation (3.15), by employing the estimated $\widehat{\boldsymbol{v}}(f)$ into the propagation equation (Equation (3.11)). The wavefield is extrapolated to a desired set of points that may be of arbitrary size and density. In words, the second step is efficiently an extrapolation of the excitation functions and sources over the region of interest using the basis functions. Since the basis functions are valid as long as the geometry of the specimen does not vary, the wavefields can be reconstructed on a grid of points of arbitrary size and density. Unless otherwise specified, for comparison purposes, wavefields will be reconstructed on the grid of the full measurement.

The quality of the reconstruction is evaluated by the magnitude squared coherence defined as

$$\mathcal{C}(\boldsymbol{r}, f) = \frac{|S_{Ms,Rc}(\boldsymbol{r}, f)|^2}{S_{Ms}(\boldsymbol{r}, f) S_{Rc}(\boldsymbol{r}, f)} \tag{3.20}$$

where S_{Ms} and S_{Rc} are the auto-spectral densities of the fully measured and of the reconstructed wavefield respectively, while $S_{Ms,Rc}(\boldsymbol{r}, f)$ is the cross-spectral density between the two wavefields. The coherence at the excitation frequency f_0 may be averaged over the spatial extent of the region of interest to evaluate the effect of the number of measurement points M and is denoted $< \mathcal{C}(f_0) >$. Alternatively, the average coherence is estimated as a function of frequency $< \mathcal{C}(f) >$ to evaluate the quality of the reconstruction over the excitation bandwidth. Finally, the spatial variation of the coherence at the excitation frequency $\mathcal{C}(\boldsymbol{r}, f_0)$ defines the quality of the reconstruction over the domain of interest. A coherence value of one means that the reconstructed wavefield is identical to the true measured wavefield. This is however not possible as the true measured wavefield contains measurement noise. In this chapter, a reconstruction coherence value greater than 0.9 is considered as satisfying. These various metrics are employed to illustrate the performance of the reconstruction process.

3.6.2 Example of reconstruction

This section presents an example of a reconstruction. The sole purpose of this section is illustrative, as the choice of parameters along with the discussion on the quality of the results will be conducted in the following sections. For simplicity, the wavefield to reconstruct was created using the propagation equation (Equation (3.12)) with the following excitation functions for the $A0$ and $S0$ modes:

$$\text{For t } \leq \frac{n}{f_0}:$$

$$v_s^{A0}(t) = v_s^{S0}(t) = \frac{1}{2}\left(1 - cos(2\pi\frac{f_0}{n}t)\right) \times sin(2\pi f_0 t) \times \delta(x - x_0) \times \delta(y - y_0) \tag{3.21}$$

corresponding to the four-cycle sine burst with a Hanning window at 200 kHz for $n = 4$ and $f_0 = 200,000$ Hz shown in Figure 3.2a and applied at $(x_0, y_0) = (50, 50)$ mm. The magnitude of the normalized spectrum of the tone burst is shown in Figure 3.2b, the black dash lines represent the frequency limits of the main lobe of the frequency spectrum, namely $f_{min} = 100$ and $f_{max} = 300$ kHz. It is assumed that the frequency content outside this band is negligible, therefore the reconstruction is only conducted within this range.

The dispersion relations used to create the data are those for a 2 mm thick aluminum plate. The reconstruction region is 200×200 mm. Note that for this frequency range, the smallest propagating wavelength is the one of the $A0$ mode at $f_{max} = 300$ kHz and is equal to 6.9 mm. Hence $M_{Nyq} = 3,403$ is the theoretical minimum number of measurements required to properly sample the wavefield according to Equation (3.18). A snapshot corresponding to the time frame $t = 39$ μs is shown in Figure 3.3a. Note how the two wavepackets with different wavenumbers are separated in space due to the different group velocities.

The reconstruction is first attempted with $M = 100$ measurements regularly distributed, as represented by the blue triangles in Figure 3.4. Figure 3.3b shows the Fourier interpolation obtained from the 100 measurements. The Fourier interpolation, or trigonometric interpolation, is an interpolation scheme using a sum of trigonometric functions to interpolate. As expected, this interpolation scheme fails to reconstruct the waves due to the under-sampling $M < M_{Nyq}$. The reconstruction is then attempted with the SWR process with 100 measurements at the locations

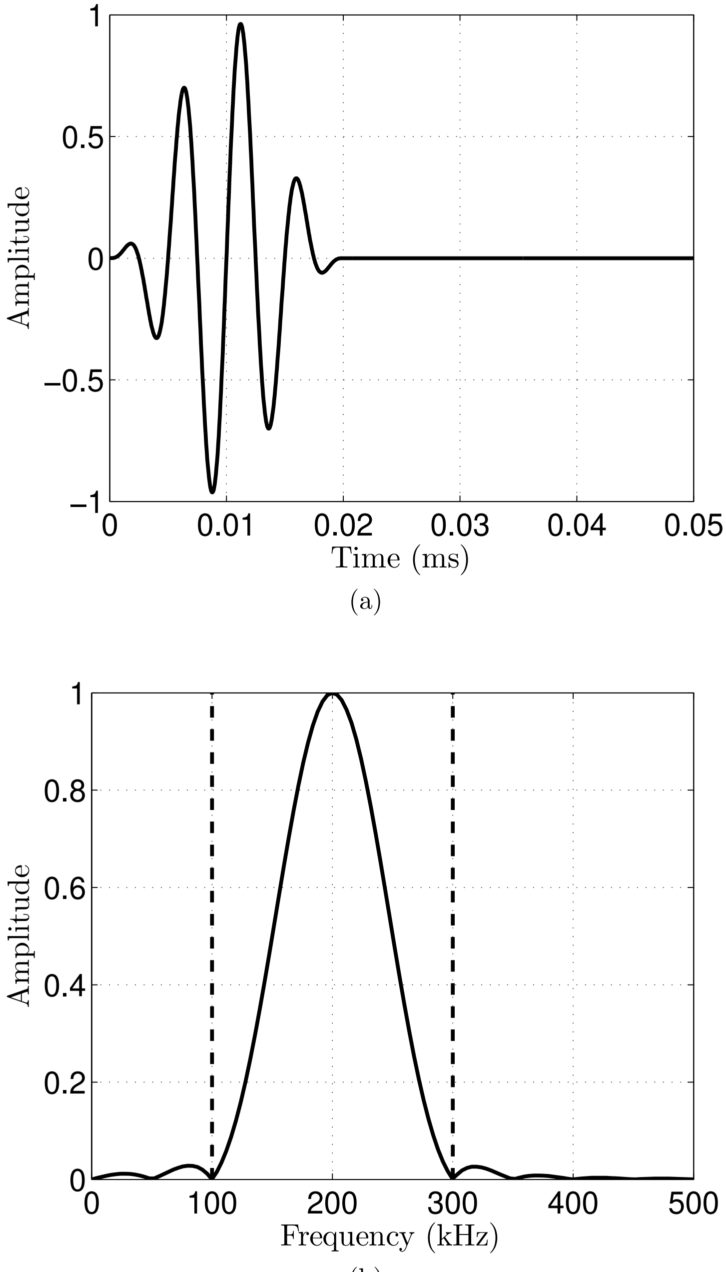

(a)

(b)

Figure 3.2: (a): 4-cycle 200 kHz tone burst and (b): Frequency domain of the 4-cycle 200 kHz tone burst, the dash lines represent the upper and lower frequency bounds for the reconstruction

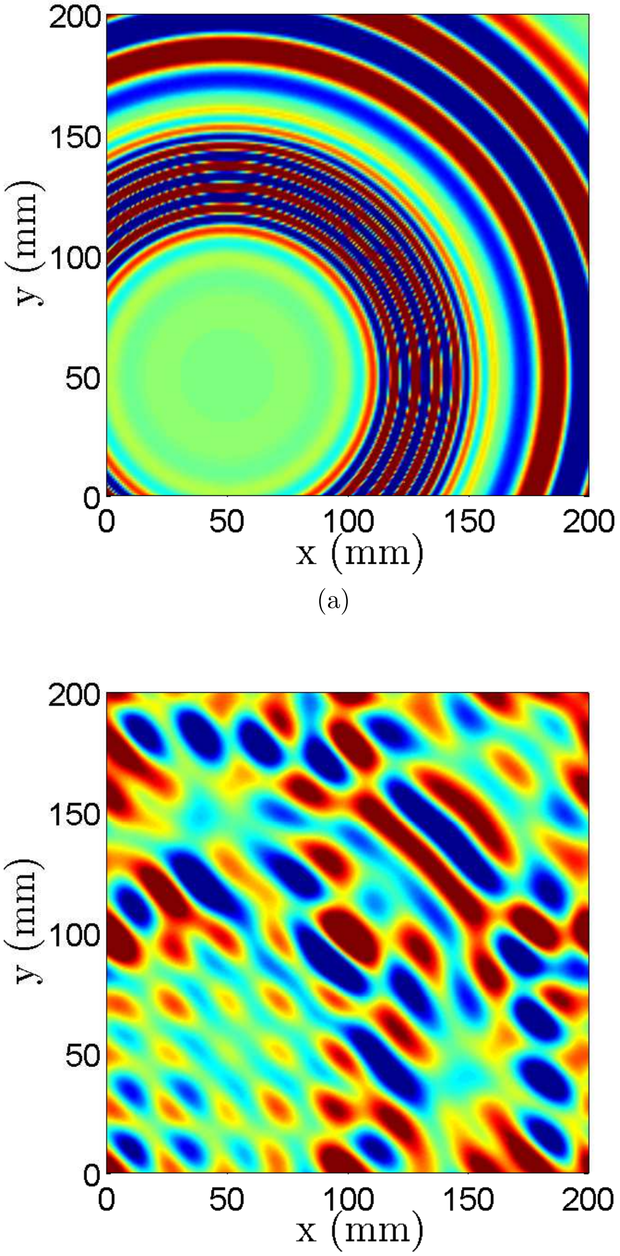

(a)

(b)

Figure 3.3: (a): Snapshot of the analytical wavefield representing a 4-cycle 200 kHz tone burst propagating in a 2 mm thick aluminum plate and (b): Fourier interpolation of 100 regular measurements taken from Figure 3.3a

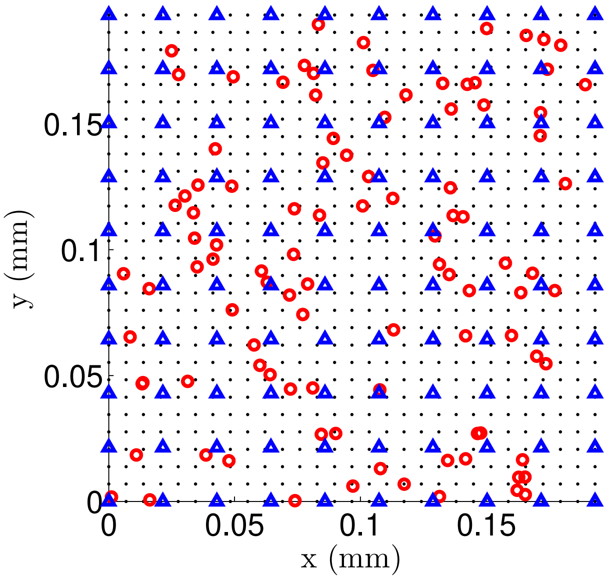

Figure 3.4: Distribution of sources and measurements used for the analytical wavefield. Black dots: Potential sources regularly distributed following Nyquist theorem. Blue triangles: 100 regular measurements used to generate Figure 3.3b. Red circles: 100 random measurements used for the SWR process.

represented by the blue circles in Figure 3.4, corresponding to a compression ratio of $CR(\%) = 97\%$ (Equation (3.17)). This time, the locations of the measurements were randomly chosen to meet the first CS requirement. A regular distribution of potential sources is then defined throughout the region of interest, as represented by the black dots of Figure 3.4. The distribution of potential sources is chosen to follow Nyquist theorem, i.e two potential sources per wavelength, or $S = 3,403$, with a spacing of $\Delta_x = \Delta_y = 3.45$ mm.

The location and the excitation value of each potential source is then estimated using Equation (3.16). According to [118], it is efficient to define the stopping criteria σ of the BP solver as a function of the norm of the measurement vector, thus $\sigma(f) = \|\widehat{\boldsymbol{y}}(f)\|/2$ is arbitrary chosen. In practice, and using the SPGL1 solver presented in Section 3.2.3, the problem is solved by using the SPGL1 Matlab implementation and running the following command:

$$\forall f \in [f_{min}, f_{max}],\ \widehat{\boldsymbol{v}}(f) = spgl1(\boldsymbol{H}(f), \widehat{\boldsymbol{y}}(f), \frac{\|\widehat{\boldsymbol{y}}(f)\|}{2}) \tag{3.22}$$

The resulting active sources distribution calculated using Equation (3.19) is show in Figure 3.5a and 3.5b for the $A0$ and $S0$ mode respectively. These two figures show that only the point the closer to the location $(x_0, y_0) = (50, 50)$ mm is an high amplitude active source, meaning that all the wavepackets propagating in the inspected area originate from this active source. Note that due to the discretization of the region of interest in potential source, the actual location of the active source is estimated to be at $(x_r, y_r) = (51.43, 51.43)$ mm, which is the closest potential source to $(x_0, y_0) = (50, 50)$ mm but is located at a distance of 2.02 mm to the actual source, which is roughly equal to one third of the smallest wavelength. This inexact estimation of the main active source location is automatically compensated by the solver during the minimization by the addition of several secondary sources to partially correct the wavepackets emitted from the main source to match the measurements. The reconstructed $A0$ and $S0$ excitation signals at the main source (x_r, y_r) are shown in Figures 3.6a and 3.6b respectively. Note that the 4-cycle 200 kHz sine burst is properly reconstructed for both modes, but is shifted in time. Moreover, non-negligible perturbations are visible in the excitation signal, especially for the $S0$ mode. These perturbations and the time shift are due to the distance between the estimated and the actual main source, that is being compensated by adding secondary sources throughout the area of inspection. Indeed, because the discretization of the region in potential sources does not allow the reconstruction of the true source at exactly (x_0, y_0), a cloud of potential sources is created as close as possible to (x_0, y_0) and their excitation functions are calculated by the minimizer to compensate for this non-exact localization. In this case, the perturbations are greater for the $S0$ mode because its wavelength is greater than the one of the $A0$ mode hence it is *easier for the minimizer* to compensate with secondary sources, while for the $A0$ mode,

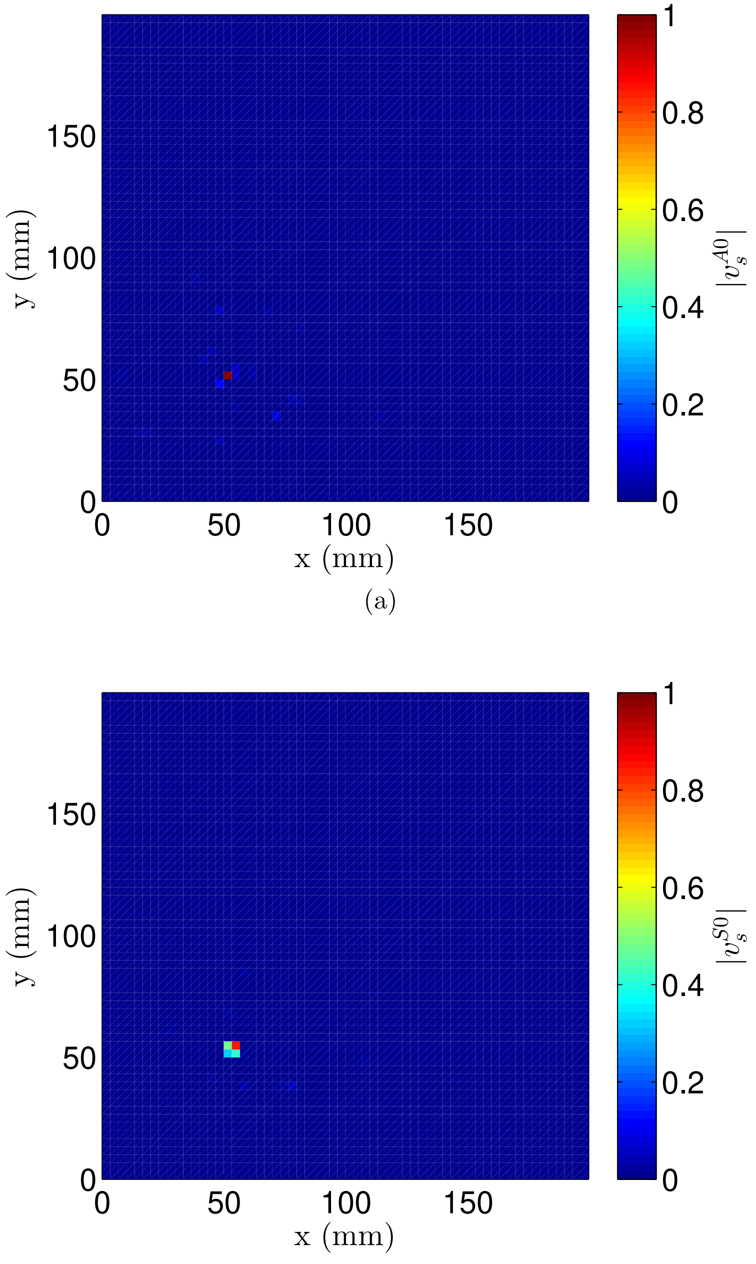

(a)

(b)

Figure 3.5: (a): Estimated potential source excitation for the $A0$ mode $\mid \widehat{v_s}^{S0} \mid$ and (b) $\mid \widehat{v_s}^{A0} \mid$. The true source is located at $(x_0, y_0) = (50, 50)$ mm.

the minimizer must find the a correct excitation signal estimation as it is harder to compensate using the secondary sources because of the smaller wavelength.

The reconstruction operation is then conducted using the estimated active source distributions and excitation functions previously presented. The reconstructed wavepackets are shown for the time frame $t = 39$ μs in Figures 3.7a and 3.7b for the $A0$ and $S0$ mode respectively. In these figures, both modes are properly reconstructed separately and the superposition of these two figures is visibly similar to Figure 3.3a, meaning that the reconstruction is effective.

In order to quantify the quality of the reconstruction, the coherence metric is studied. First, the coherence $C(x, y, f_0)$ (Equation (3.20)) computed in space at the dominant frequency f_0 is displayed in Figure 3.8a. It is visible in this figure that the coherence is close to unity throughout the window of interest except periodically nearby to the main source. This is essentially due to the fact that no potential source is exactly located at the (x_0, y_0) location. Indeed, as the main source is located at $(x_r, y_r) = (51.43, 51.43)$ mm instead of $(x_0, y_0) = (50, 50)$ mm, a periodic error is induced in the reconstruction, which leads to a periodic reduction of the coherence. Figure 3.8b then presents the value of the coherence of the reconstruction averaged in space as a function of frequency. Note that the coherence of the reconstruction is close to unity within the bound of the reconstruction, represented by the dash lines. Furthermore, it is visible in Figure 3.8b that the coherence decreases as the frequency increases within the boundary of the reconstruction. This is due to the fact that the wavelengths decrease as the frequency increases so the effect of the inexact main source location becomes more critical as the frequency increase.

Now that the process has been illustrated, the following sections will present the detailed choice of the parameters of the process, including the choice of the distributions for both the potential sources and the measurements along with the parameters of solver.

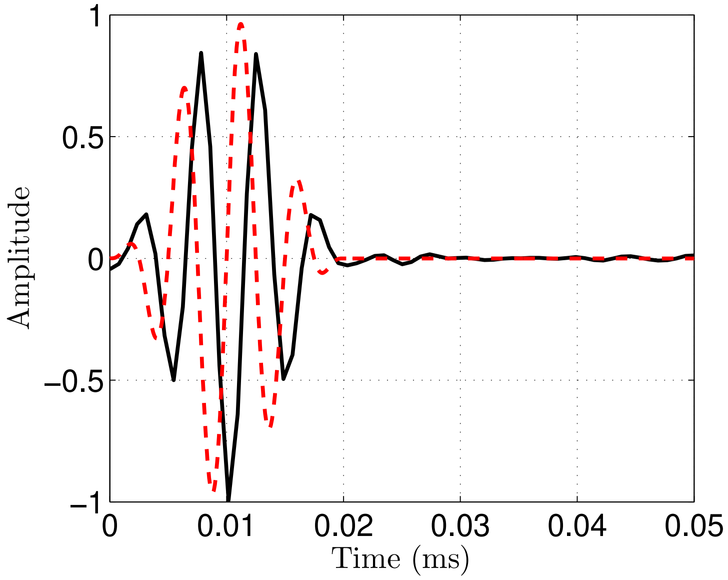

(a)

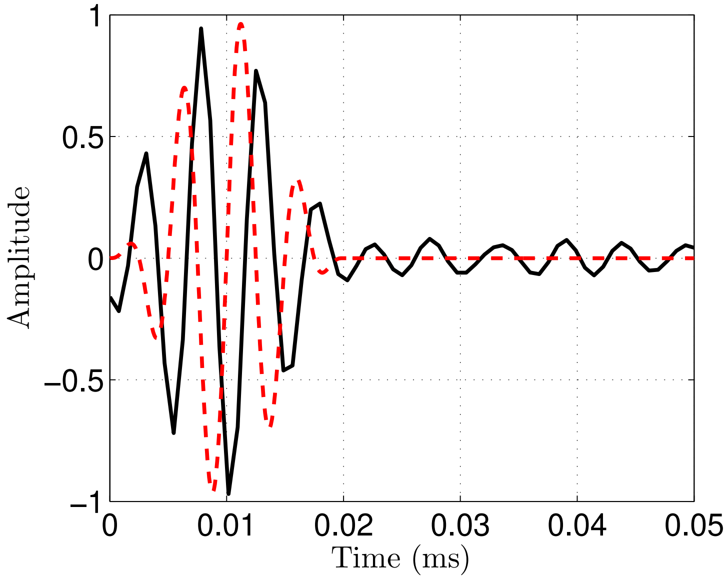

(b)

Figure 3.6: Reconstructed excitation signals at the main source location at $(x_r, y_r) = (51.43, 51.43)$ mm (black solid line) and truc excitation signal at $(x_0, y_0) = (50, 50)$ mm (red dashed line) for the (a): $A0$ mode and (b): $S0$ mode

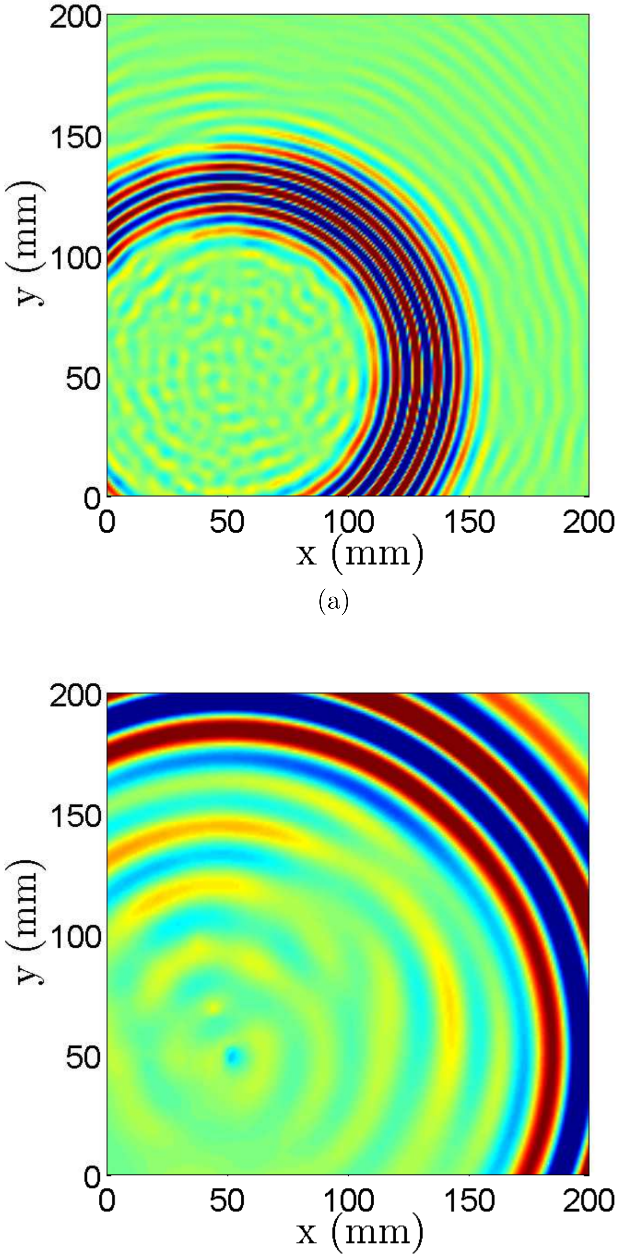

(a)

(b)

Figure 3.7: (a): Snapshot of the reconstructed $A0$-only wavefield from 100 measurements by SWR and (b) Snapshot of the reconstructed $S0$-only wavefield from 100 measurements by SWR

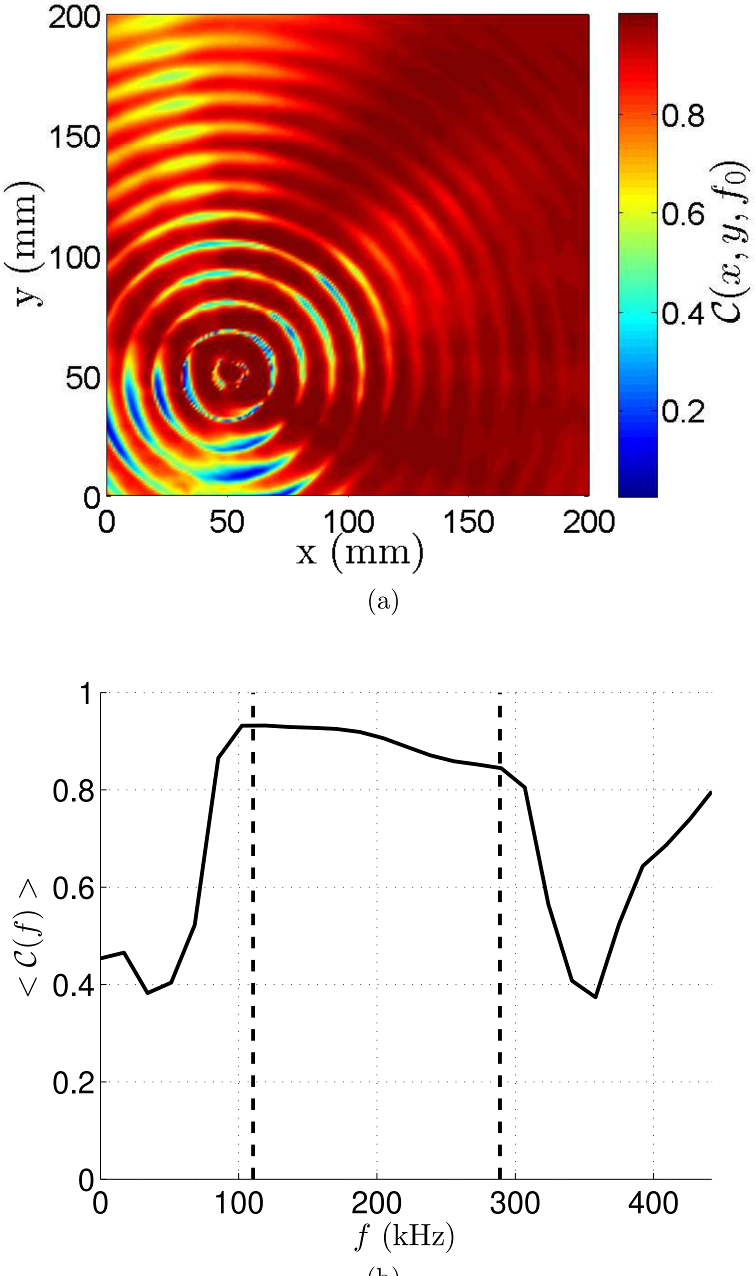

(a)

(b)

Figure 3.8: (a) Spatial coherence at $f_0 = 200$ kHz between the true wavefield and the sum of the $A0$ and $S0$ wavefields reconstructed from 100 measurements and (b) Space averaged coherence as a function of frequency for the same reconstruction

3.6.3 Choice of the measurement locations and the source distributions

This section presents the different sampling schemes for the measurements and the potential sources that have been considered in this research. The choice of the sampling scheme is a compromise between randomness to fulfill CS low mutual coherence (Equation (3.5)) requirement and the need to obtain the information necessary to properly reconstruct the wavefield. Moreover, the measurement distribution must obey the physical and practical constraints of guided wave measurement.

The different sampling schemes which can be used for the measurement and the potential source distributions will first be introduced. The distributions will then be summarized by Table 3.1.

3.6.3.1 Regular sampling

The first and most intuitive choice is to use a regular distribution as it was done for the potential sources in the example of Section 3.6.2. Regular distributions have the advantage to be deterministic, purely controlled by the operator and cover the entire region of interest. However, the randomness requirement of CS, i.e., the fact that the matrix $\boldsymbol{H}(f)$ must have a low coherence as explained in Section 3.2.3, may not be meet while using purely regular distributions. The default option of the SLDV is to scan region discretized on a regular grid, which makes this distribution practical for the measurements.

3.6.3.2 Random sampling

The other intuitive choice is to use a purely random distribution in order to ensure that the CS randomness requirement is met (see Section 3.2.3), as it was the case for the measurements in the example of Section 3.6.2. The downside of purely random sampling is that entire regions can be ignored by the sampling scheme and point-measurements can be nearly overlapping, resulting in a high matrix coherence for the CS matrix. In this context, two points are nearly overlapping if the distance between them is small compared to the smallest wavelength of interest. The SLDV does not provide the option to scan random points.

3.6.3.3 Jittered sampling

Jittered sampling [119] is a compromise between randomness and regularity. A *jittered* distribution is built when the region of interest is divided in rectangular cells and one point is placed randomly within each cell. Figure 3.9 illustrates a jittered sampling distribution. An important advantage of jittered sampling is that it is guaranteed that the distribution covers the entire area of interest, while ensuring some randomness in the process. The downside of this sampling scheme in the context of this research is that two points may end up arbitrary close. It is not directly possible to define a jittered distribution with the SLDV.

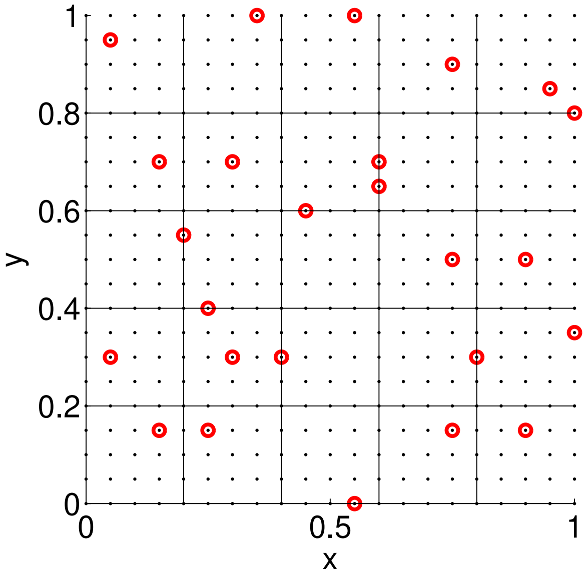

Figure 3.9: Jittered sampling of the measurement region: the region of interest is split in cells (black lines) and one measurement (red circles) is taken randomly within each cell. The black dots represent the points required for spatial discretization according to Nyquist criterion.

Table 3.1: Combination of potential sources and measurement distributions in term of randomness, minimal source distance control and practical feasibility

Source	Measurement	Random	Distance control	Practical feasibility
Regular	Regular	x	✓	✓
Regular	Random Jittered	✓	✓	x
Random Jittered	Regular	✓	x	✓

3.6.3.4 Other potential sources distributions

Other distributions such as Poisson disk [120] and Farthest point [121] samplings have been studied but will not be presented here. The reason is that these distributions are more complex and do not significantly improve the results.

3.6.3.5 Choice of distributions

The choice of the measurement and potential source distributions is a compromise between randomness, measurement distance control and feasibility: First, some degree of randomness is required to meet CS low matrix coherence requirement. Source distance control is required so that the basis functions created by each measurement-source pair is unique in order to create a low coherence matrix $\boldsymbol{H}(f)$. Indeed, as each column of $\boldsymbol{H}(f)$ is the contribution that would be received at all the measurements from one source, it is acceptable to have two nearby measurements. However, two nearly overlapping potential sources would create two nearly identical vectors in $\boldsymbol{H}(f)$, resulting in a high matrix coherence. Finally, the process should be feasible in practice. The SLDV is a fully integrated device with a predefined set of measurement patterns such as grids or circles. Taking measurements according to a random or semi-random distribution is not feasible as it would require to define every measurement-point individually.

The initial implementation of the process does not consider the practical feasibility, hence regular potential sources and jittered measurements distributions are used unless otherwise specified. It is important to note that in order to make the process feasible in practice, the randomness can be artificially embedded in the sources distribution by letting the measurements being regularly distributed in space and defining the potential sources using a jittered distribution.

3.6.4 Choice of numerical parameters

The dimension of the sensing matrix $\boldsymbol{H}(f)$ is $SN^{(\mu)} \times M$ where S is the number of potential sources, $N^{(\mu)}$ is the number of modes included in the model and M is the number of measurements. The minimization must be conducted L_f times, where L_f is the length of the frequency vector. The dimension of the sensing matrix is critical since it represents the size of the problem to solve hence is a representation of the computational time of the minimization operation. The goal of this section is to discuss how the computational time can be reduced by reducing the size of $\boldsymbol{H}(f)$ without influencing significantly the quality of the results.

3.6.4.1 Parameter $N^{(\mu)}$

The parameter $N^{(\mu)}$ is the number of modes composing the measurements. It is defined by the number of responding modes within the studied range of frequency, hence cannot be changed a priori. However, in some cases, the response of a mode is known to be negligible with respect to another and therefore $N^{(\mu)}$ can be reduced by neglecting a mode. For example when using a SLDV placed perfectly orthogonally with respect to a flat specimen, the measurements will be greatly dominated by the $A0$ response which is mainly out-of-plane, while the $S0$ response, mainly in-plane, will be negligible.

3.6.4.2 Parameter L_f

The parameter L_f is the number of discretized frequencies at which the Equation (3.15) is inverted. It is a function of the size of the frequency range of the reconstruction and the spacing between the frequency points. The bounds of the frequency spectrum are determined by the frequency response of the M measurements, or the bandwidth of the excitation if known. Because the last step of the reconstruction involve a Fourier Transform (see Figure 3.1), the spacing between the discrete values of the frequency vector is chosen according to Nyquist theorem to prevent aliasing.

The parameter L_f is therefore not a variable that can be changed in the process. However Equation (3.15) is solved for each frequency individually. Hence the $l1$-minimization is parallelizable with respect to the frequency parameter.

3.6.4.3 Parameter M

The parameter M is the number of measurements to acquire and to feed to the reconstruction process. This is the most critical parameter of the process since it influences both the acquisition and reconstruction time while driving the quantity of information fed to the system. As far as the author knows, there is no rigorous technique predicting the minimal value of M to ensure satisfying reconstruction. In this research, for each reconstruction, several M values, defined as fractions of M_{Nyq}, have been tested until satisfying reconstruction is obtained. The variable M can be the subject of convergence analyses to determine M_{Min}, the minimum number of measurements to ensure a reconstruction coherence of at least 0.9. However these convergence analyses require the knowledge of the wavefield to reconstruct, which can draw guidelines regarding the choice of this parameter.

3.6.4.4 Parameter S

The parameter S is the number of potential sources used for the reconstruction and is a purely virtual parameter. The number and the distribution of the potential sources are critical for both the quality of the reconstruction and the computational time. S defines the resolution of the discretization of the region of interest in potential sources and is a compromise since a value too high would result in a needlessly long computational time. Using too few sources would also result in potentially missing features and limit the quality of reconstruction. As shown in Section 3.6.2, not having a potential source at the exact location of the source impacts negatively the quality of the reconstruction. Note that for the reconstruction of experimental data, as no source is truly punctual, it is necessary to ensure that several potential sources are located inside the excited region to properly represent the area of excitation. Let the spacing between two sources, Δ_s, be given by:

$$\Delta_s = \frac{\lambda_{min}}{N_\lambda} \tag{3.23}$$

where N_λ is the number of potential sources per wavelength. The default value of the parameter N_λ is chosen such that the potential sources distribution follows Nyquist theorem in order to ensure that all the potential features of the specimen are included, meaning that $N_\lambda = 2$ unless otherwise specified.

Once this maximum spacing is fixed, several avenues can be considered to reduce the number of sources without threatening the reconstruction quality. First, potential sources can be pre-located, meaning that spatial regions are favored during the repartition of the sources. Source pre-location could be achieved by assuming which region of space contain defects and which one does not, but by doing so, potential defect locations are also removed from the problem. Source pre-location could also be achieved by solving the problem for a single frequency with a uniform source distribution and then use only the active sources resulting of this computation to define the potential sources of the entire problem. The shortcoming of this technique is that there is no guarantee that the true active sources will all be found by the single frequency solution. Furthermore, each frequency needs a different set of secondary active sources in order to compensate for the inexact localization of the main sources resulting of the discretization of the space, hence this technique would not allow the solver to compensate for the model mismatch using secondary sources. The other avenue to consider to reduce the number of potential sources is to define a custom number of potential sources for each frequency. Indeed, as the required number of potential sources is related to the smallest wavelength, itself a function of the frequency, potential source distribution can be recomputed for each frequency. Experimentally, these three processes were found to be ineffective, hence are not reported herein.

3.6.4.5 Parameter σ

The last parameter to choose is σ in Equation (3.16), which can be interpreted as a stopping criteria. On one hand, a σ parameter too high will result in a trivial or incomplete solution because the constraint of Equation (3.16) is verified by the zero solution. On the other hand, a low value of σ will give too much importance to the noise and will induce unnecessary computation. In general, it is a common practice to relate σ to the norm of the measurement vector $\widehat{\boldsymbol{y}}(f)$. In this research, σ is defined as a function of frequency using the following relationship:

$$\sigma(f) = \frac{\|\widehat{\boldsymbol{y}}(f)\|_2}{N_\sigma} \tag{3.24}$$

where N_σ is an scalar constant. N_σ must be calibrated in function of the noise and the quality of the model. In practice, σ is a quantification of the difference between the reconstructed and the measured signal. Because this difference increases if the noise increases, a low N_σ value (i.e., a high σ) is required for noisy measurement.

Finally, the $l1$-minimization of Equation (3.16) becomes:

$$\forall f,\ \text{minimize}\ \left\|\widehat{\boldsymbol{v}}(f)\right\|_1\ \text{subject to}\ \left\|\widehat{\boldsymbol{y}}(f) - \boldsymbol{H}(f)\widehat{\boldsymbol{v}}(f)\right\|_2^2 \leq \frac{\|\widehat{\boldsymbol{y}}(f)\|_2}{N_\sigma} \tag{3.25}$$

For low noise dataset well-described by their model, i.e., the dispersion relations used for the reconstruction, such a the analytical example of section 3.6.2, a high value of N_σ can be used, for example $N_\sigma = 1,000$. However if the measurements are noisy and/or if it is known that the dispersion relations do not match the experiment properly, smaller values of N_σ must be used such as $N_\sigma = 2$ or 10 to account for the expected difference between the measured and the reconstructed signals.

3.7 Results

This section presents results of the application of the SWR to various wavefields measured experimentally. For comparison purposes, full wavefields were recorded, out of which a subset of points is extracted and utilized for reconstruction. The purpose of this section is to demonstrate the robustness of the SWR process operating on several experimental datasets and its ability to identify potential defects as secondary sources. This section explores some of the limitations of the SWR process.

3.7.1 Aluminum plate with a single notch

For the first application of the SWR process to an experimental dataset, an isotropic aluminum plate is investigated. The results will be used to illustrate the effect of parameters $[M, N_\sigma, N_\lambda]$. Finally the reconstruction will be extrapolated to a region extending beyond the measured area. The dimension of the considered sample is $600 \times 600 \times 2$ mm. A 1.4 mm deep notch was created in the specimen. Guided waves are generated in the specimen by a PZT disk transducer bonded to surface of the plate 170 mm away from the notch, as represented in blue in Figure 3.11a. Wave measurement are taken over an area of 124×72 mm^2 on a grid of $163 \times 105 = 17,115$ points. The excitation is a $f_0 = 230$ kHz 4-cycle sine burst repeated every 2.3 ms. For each point the duration of the measurement is 120 μs and the sampling frequency 2.56 MHz. Two time snapshots of the fully measured wavefield at $t = 54$ μs and $t = 70$ μs are shown in Figures 3.10a and 3.10b respectively. In the first snapshot, interaction of the low amplitude $S0$ mode with the notch is visible while the disturbance of the $A0$ wavepackets by the notch is noticeable in the second snapshot. According to the dispersion relations computed with SAFE, the smallest propagating wavelength in this media and within the range of frequencies is 6.44 mm thus the limit number of measurement by Nyquist theorem is $M_{Nyq} = 1,181$.

The reconstruction is attempted in the frequency range between $f_{min} = 130$ kHz and $f_{max} = 340$ kHz with $M = 450$ measurements, corresponding to $M_{Nyq} = 62\%$. The potential sources are regularly distributed with $N_\lambda = 2$ potential sources per wavelength. The considered measurement distribution is jittered as represented in Figure 3.9. In order to ensure that the PZT transducer is included within the potential sources, which is necessary to reconstruct the incoming waves, the potential sources distribution is artificially extended to the coordinate $y = -200$ mm as displayed by the black dots in Figure 3.11a. This step is necessary as the PZT is located outside of the scanned area. The parameter σ is fixed at its default value with $N_\sigma = 2$. Note that this choice is arbitrary and the influence of this parameter will be studied in this section.

The sparse representation of the wavefield for the sum of the $A0$ and $S0$ excitations is shown in Figure 3.11b. This sparse representation shows the distribution of the quantity $\mid \widehat{v}_s^{A0} \mid + \mid \widehat{v}_s^{S0} \mid$ (Equation (3.19)), where $\widehat{v}_s^{A0}$ and $\widehat{v}_s^{A0}$ have been obtained by solving the $l1$-minimization of Equation (3.25) with the SPGL1 solver.

The sparse representation in Figure 3.11b shows two mains features: a line of sparse active sources approximately at the location of the transducer and a cluster of active sources at the location of the notch, efficiently locating both the transducer and the notch.

The reconstruction is then conducted on the grid on which the wavefield was initially measured, leading to the results of Figures 3.12a and 3.12b, representing the two times snapshots previously shown in Figures 3.10a and 3.10b. These two

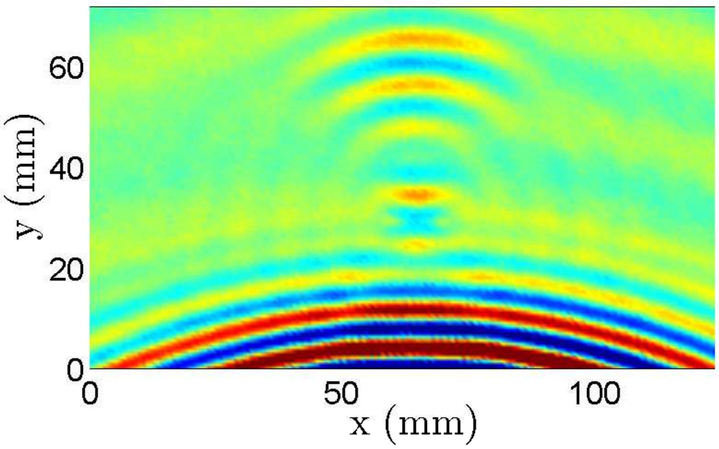

(a)

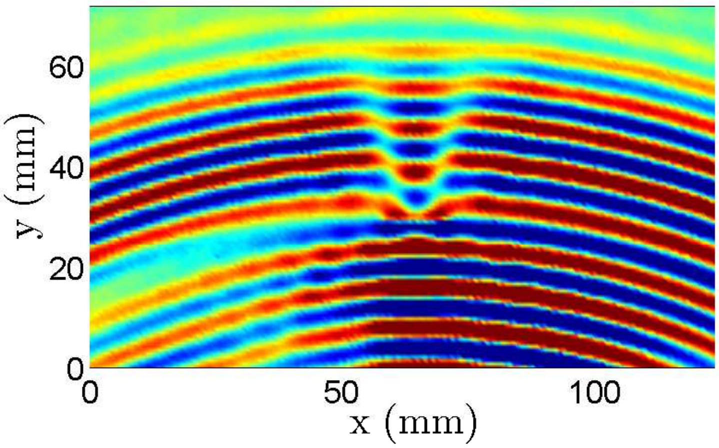

(b)

Figure 3.10: Snapshot of the wavefield representing a 4-cycle 230 kHz tone burst interacting with a notch in a 2 mm thick aluminum plate at (a): $t = 54$ μs and (b): $t = 70$ μs

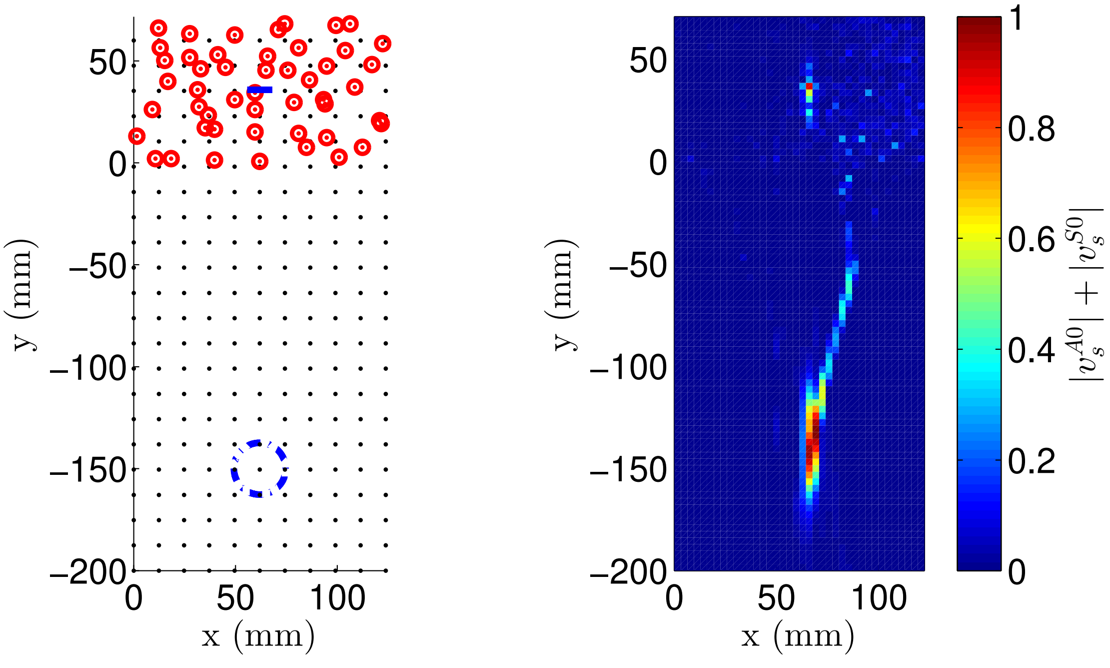

(a) (b)

Figure 3.11: (a): Discretization of the area of interest: black dots: potential sources (not all are represented), red circles: measurements used for reconstruction (not all are represented), blue line: notch, blue circle: PZT transducer and (b): Sparse representation of the wavefield $|\ \widehat{v_s}^{A0}\ | + |\ \widehat{v_s}^{S0}\ |$ obtained with the set of parameters $[M, N_\sigma, N_\lambda] = [450, 2, 2]$

snapshots show that the main wavepackets, as well as the interaction with the notch are reconstructed. The coherence between the fully measured and the reconstructed wavefields in the measurement region is then computed in order to assess the quality of the reconstruction. The coherence at the dominant frequency and as a function of space is shown in Figure 3.13a and the coherence averaged in space as a function of frequency is shown in Figure 3.13b. The spatial distribution of the coherence at f_0 in Figure 3.13a shows that the value of the coherence is equal to one (represented in red in Figure 3.13a) everywhere except in the vicinity of the notch. This shows that the scattering of the waves by the notch is difficult to reconstruct, which is due to the fact that the model assumes that every source is omni-directional. This is however not the case for a notch and for most defects in general. The frequency variation of the coherence in Figure 3.13b shows that the averaged coherence of the reconstruction is close to one within the frequency band of the excitation. This example demonstrates that the ability of the SWR process to operate with simple experimental measurements and to locate a notch along with a transducer located outside the measured region.

3.7.1.1 Influence of the parameters

In order to judge the influence of the parameters $[M, N_\sigma, N_\lambda]$ on the quality of the reconstruction and the computational time, a sensitivity study is conducted for each of these parameter for the same dataset. The metric to evaluate the quality of the reconstruction is the coherence at the dominant frequency averaged in space. The computational time is the duration of the minimization (Equation (3.16)) obtained with a single 3.40 GHz CPU and is provided in order to show the evolution of the complexity of the minimization.

First, $[N_\sigma, N_\lambda] = [2, 2]$ is fixed while the number of measurements M varies between $M_{min} = 10$ and $M_{max} = 900$. The corresponding coherence and computational

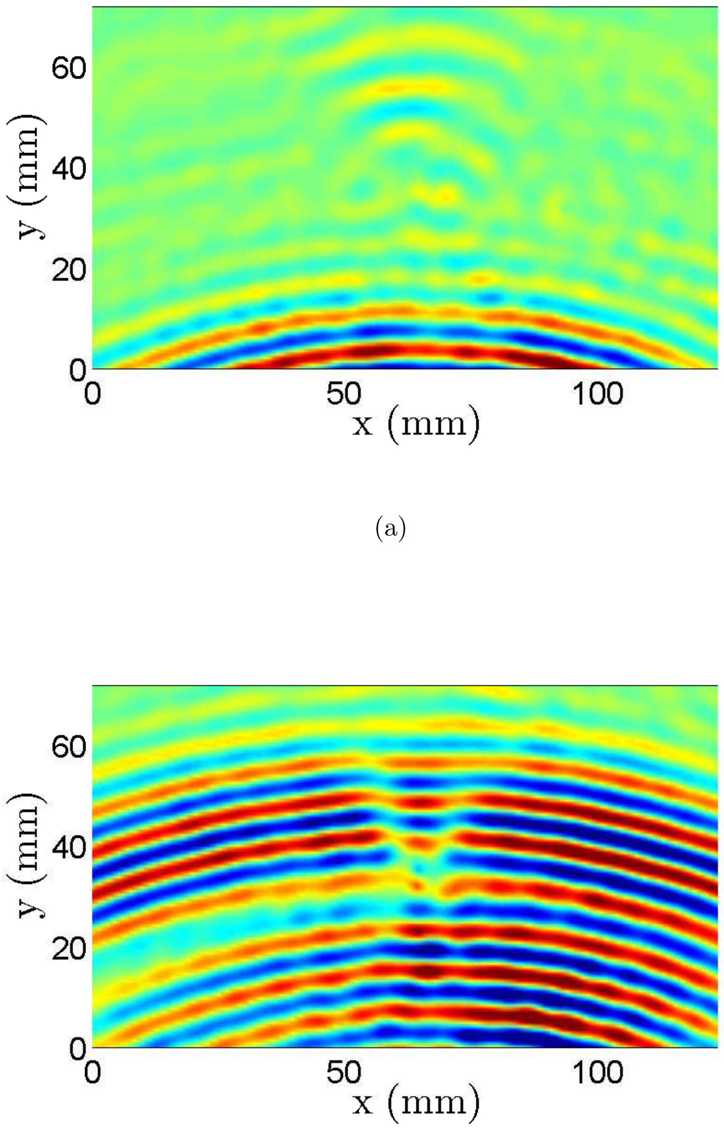

(a)

(b)

Figure 3.12: Snapshot of the reconstructed wavefield representing a 4-cycle 230 kHz tone burst interacting with a notch in a 2 mm thick aluminum plate with the set of parameters $[M, N_\sigma, N_\lambda] = [450, 2, 2]$ at (a): $t = 54$ μs and (b): $t = 70$ μs

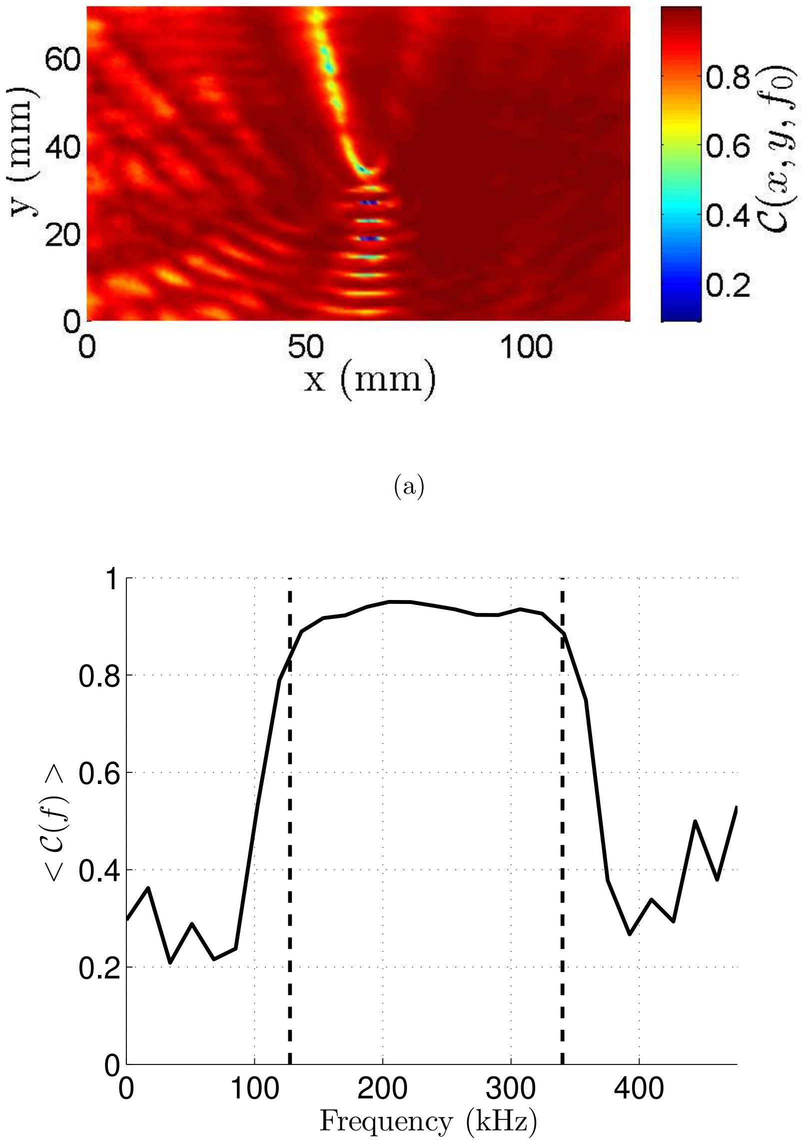

(a)

(b)

Figure 3.13: (a) Spatial coherence at $f_0 = 230$ kHz between the true wavefield and the wavefield reconstructed with the set $[M, N_\sigma, N_\lambda] = [450, 2, 2]$ and (b) Space averaged coherence as a function of frequency for the same reconstruction, black dashed line: frequency boundary of the reconstruction

time are displayed in Figures 3.14a and 3.14b. These figures show that the coherence reaches a plateau value for approximately $M > 100$ while the computational cost increases nearly linearly in logarithmic scale with the number of measurements, meaning that the optimal choice is to select M slightly greater than 100.

Secondly, the parameters M and N_λ are fixed to the values $[450, 2]$ while the parameter N_σ varies between 10^{-1} and 10^3. As a reminder, the parameter N_σ corresponds to the constraint of the minimization function and is defined by Equation (3.24). The coherence and the computational time of the reconstruction are then plotted in Figure 3.15a and 3.15b respectively. Note that for $N_\sigma = 0$, the zero vector is the trivial solution of Equation (3.25). Indeed, the constraint of Equation (3.25) is verified for any value of the vector $\widehat{\boldsymbol{v}}(f)$. It is therefore expected that the reconstruction quality will go down with N_σ. From the coherence plot in 3.15a, it is visible that the value $N_\sigma = 2$ previously used does not provide the best possible reconstruction. In particular $N_\sigma > 10$ leads to a reconstruction coherence close to unity while the computational time increases roughly linearly in logarithmic scale with N_σ. Note that the optimal value of N_σ is a function of the measurement noise and the inaccuracies of the model. Indeed as explained in 3.6.4, the parameter N_σ tunes the upper limit of the constraint $\|\widehat{\boldsymbol{y}}(f) - \boldsymbol{H}(f)\widehat{\boldsymbol{v}}(f)\|_2^2 \leq \frac{\|\widehat{\boldsymbol{y}}(f)\|_2}{N_\sigma}$.

Finally, the parameters M and N_σ are fixed to the values $[450, 2]$ while the parameter N_λ varies between 10^{-1} and 10^1. As a reminder, the parameter N_λ was defined in Equation (3.23) and drives the density of the potential sources distribution. The coherence and the computational time of the reconstruction are then plotted in Figure 3.16a and 3.16b respectively. The coherence plot shows that a plateau value of the coherence is achieved for $N_\lambda > 1$, meaning that there must be at least one potential source per wavelength in order to properly reconstruct the wavefield. The plot of the computational time only shows a linear increase in logarithmic scale in the region $N_\lambda > 1$, while a nearly flat region is observed for $N_\lambda < 1$. The computational time hits

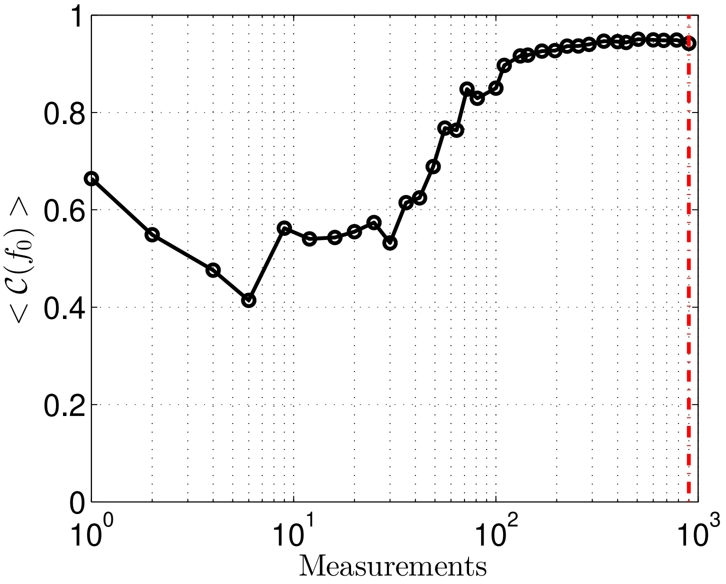

(a)

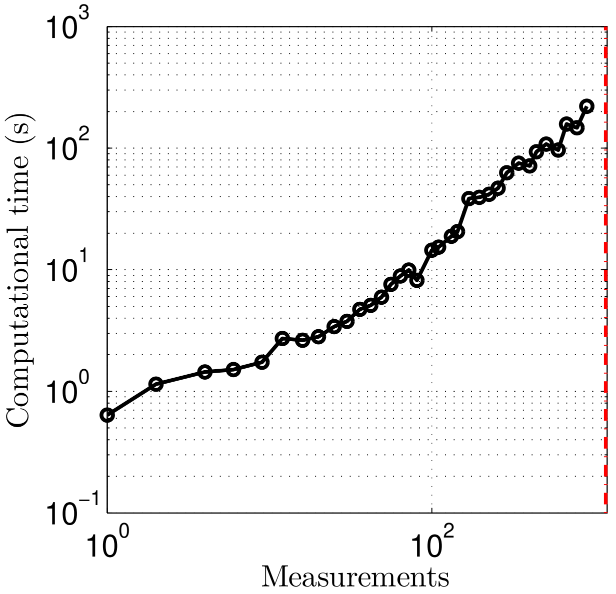

(b)

Figure 3.14: Convergence of the reconstruction as a function of the measurements for $[N_\sigma, N_\lambda] = [2, 2]$. The red dashed line represent the theoretical lower bound $M_{Nyq} = 1,181$. (a): Coherence averaged in space at the dominant frequency and (b): Computational time of the minimization

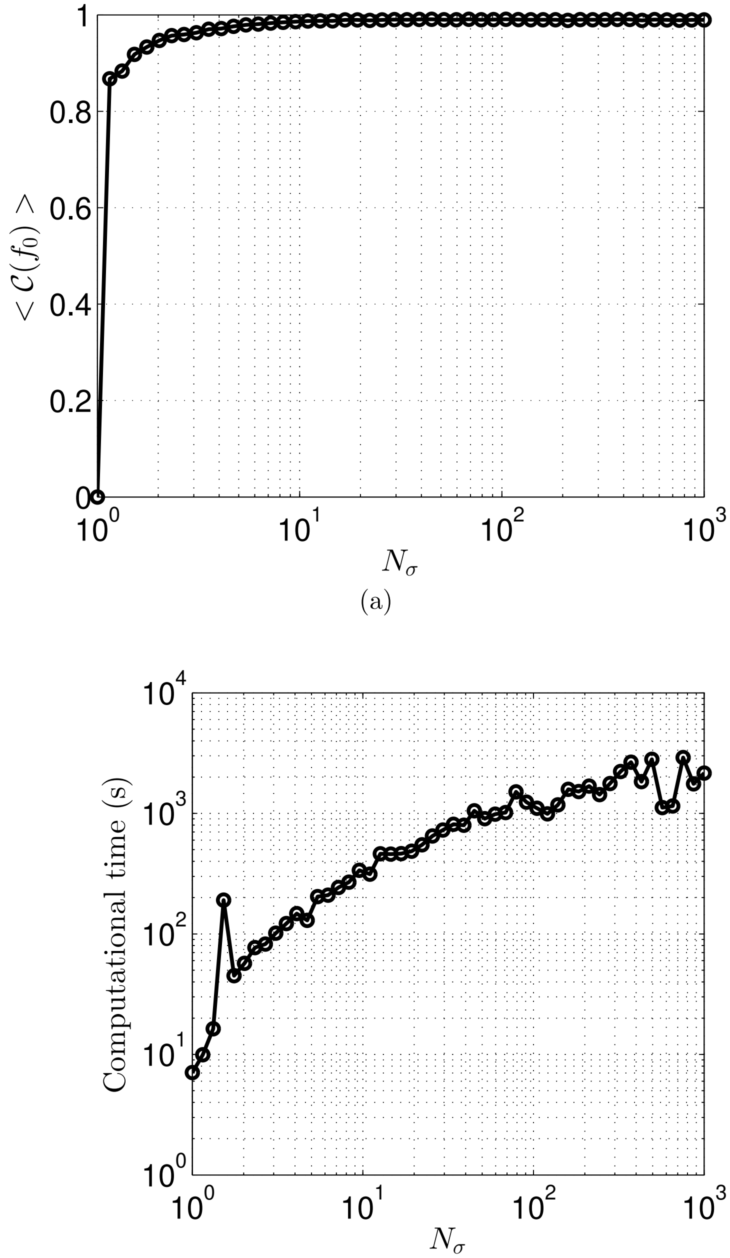

(a)

(b)

Figure 3.15: Convergence of the reconstruction as a function of N_σ for $[M, N_\lambda] = [450, 2]$. (a): Coherence averaged in space at the dominant frequency and (b): Computational time of the minimization

a minimum for $N_\lambda = 1$. The reason is that for $N_\lambda < 1$, there are not enough potential sources to accurately describe the physical system hence the optimization problem is ill-posed resulting in a difficult convergence. As N_λ increases, the dimensionality of the objective function increases dramatically resulting in the linear increase for $N_\lambda > 1$.

As a conclusion, for high enough values of each of the parameters $[M, N_\sigma, N_\lambda]$, the coherence of the reconstruction reaches a plateau value. Furthermore, computational time increases linearly with respect to these three parameters once the coherence plateau value is reached meaning that, in practice, the best compromise is to find the beginning of each plateau to define each parameter. As the sensitivity studies are computationally expensive, it is counterproductive to do these convergence analysis for every single reconstruction, hence the following lower bounds are chosen for each parameter:

$$M \geq \frac{M_{Nyq}}{10} \tag{3.26}$$

$$N_\sigma \geq 2 \tag{3.27}$$

$$N_\lambda \geq 1 \tag{3.28}$$

In practice, the parameters are initially fixed to the lower bounds and then gradually increased until satisfying reconstruction ($< \mathcal{C}(f_0) > \;\; > 0.9$) is achieved.

3.7.1.2 Reconstruction on a larger grid

So far, reconstructions were only conducted over the region covered by the initial measured grid of points. However, the second step of the SWR process can be conducted on a grid of larger size and density. As demonstrated with the ongoing aluminum notched plate example, active sources can be detected outside the window of inspection, as long as waves of non-negligible amplitude originating from outside the measurement region are measured within the inspection region. This section presents the

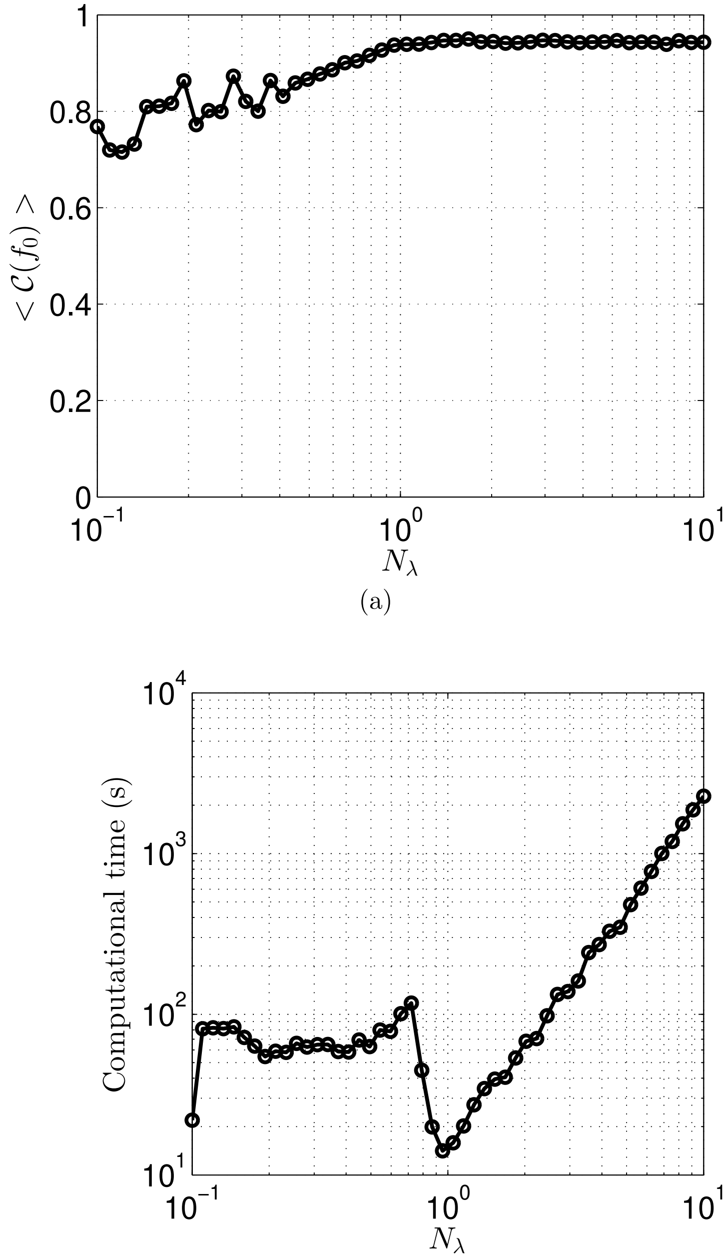

(a)

(b)

Figure 3.16: Convergence of the reconstruction as a function of N_λ for $[M, N_\sigma] = [450, 2]$. (a): Coherence averaged in space at the dominant frequency and (b): Computational time of the minimization

results of the reconstruction on a larger region than the measured region. More specifically the reconstruction is achieved in the region used to define the potential sources drawn in Figure 3.11a. Note that no measurements were taken in this extended area hence it is not possible to rigorously compare the results. However as the transducer is supposedly omni-directional and the media isotropic, it is safe to infer that at a given time step, the wavepackets should be regularly distributed in a circular pattern around the transducer. Figure 3.17a and 3.17a show the reconstructed extended wavefield at the same time steps as in Figure 3.12 obtained with the parameters set $[M, N_\sigma, N_\lambda] = [450, 2, 2]$. Note that in these figures, the area above $y > 0$ indicated by the black box is the one previously reconstructed. A first observation is that the wavepackets are not equally distributed around the transducer located approximately at $(50, -150)$ mm, more specifically, only the wavepackets directly traveling towards the region of inspection (black box), i.e., in the North direction, are reconstructed. It is however understood that the true wavefield should be omni-directional, i.e., the wavepackets should spread from the transducer in circle. However, as no measurement were taken in the directions East, West and South with respect to the transducer, there is no need for the minimizer to *build* wavepackets in these directions. The reconstructed wavefield presented in Figures 3.17a and 3.17a is not physically feasible, but is authorized by the model. This directional solution is selected by the $l1$-minimizer because it has a smaller objective function that the true solution. From this result, it can be concluded that there is no guarantee that the solver will properly reconstruct the wavefield in directions of propagation not covered by the region of inspection, it is therefore wise to take sparse measurements in all the directions with respect to the main source when reconstructing outside the region of inspection.

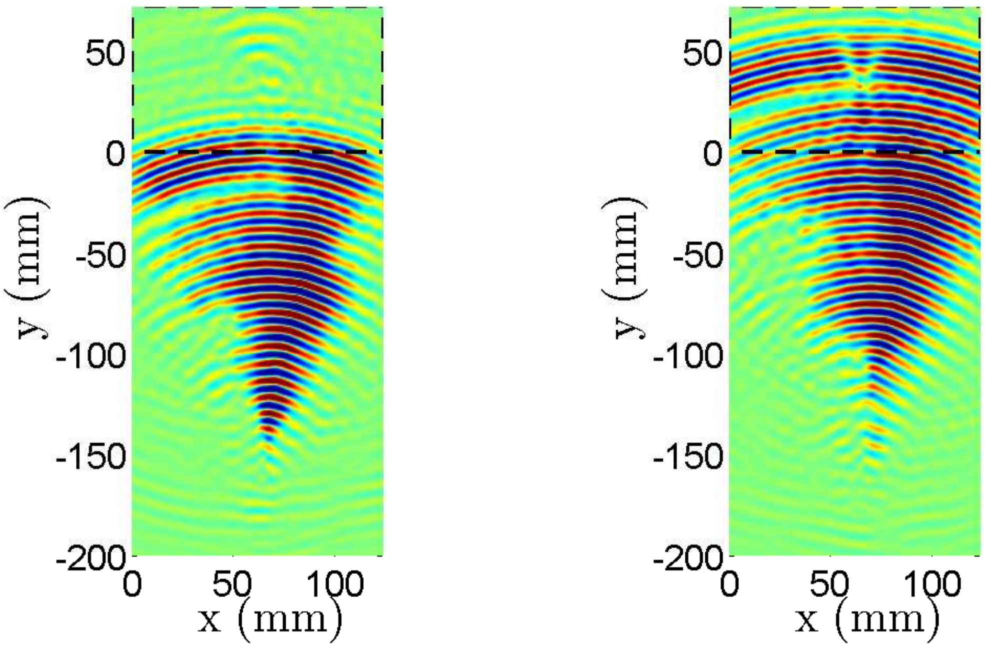

(a) (b)

Figure 3.17: Snapshot of the reconstructed wavefield on a large region including the transducer, representing a 4-cycle 230 kHz tone burst interacting with a notch in a 2 mm thick aluminum plate with the set of parameters $[M, N_\sigma, N_\lambda] = [450, 2, 2]$ at (a): $t = 54$ μs and (b): $t = 70$ μs. The black dashed box represent the region of inspection

3.7.2 Aluminum plate with multiple features

This section demonstrates the ability of the SWR to entirely map the geometry of a specimen containing multiple features. To this effect, an aluminum plate with multiple notches is studied. The specimen is a $600 \times 600 \times 2$ mm aluminum plate with four notches of depth $1.2, 1.4, 1.6$ and 1.8 mm whose geometry is depicted in Figure 3.18. The region of inspection is a 432×416 mm^2 region discretized in 193×191 points and includes the four notches. A PZT disk of 25 mm diameter is bonded at the center of the inspected region, 150 mm away from each notch. Note that the notches are not located at equal distance from the edges of the plate so that the transducer is not located at the center of the plate, as displayed in Figure 3.18. The transducer is excited by a four-cycle tone burst at 200 kHz. The duration of the measurement is 800 μs and the sampling frequency 2.56 MHz. The duration ensures that the wavepackets reflected from the edges are included in the measurements. The smallest propagating wavelength is 7.1 mm resulting in $M_{Nyq}^{region} = 15,165$ for the inspected region and $M_{Nyq}^{plate} = 28,566$ for the entire plate. Another PZT transducer is bonded outside the measurement region as shown in Figure 3.18. This transducer is not activated in the experiment and behaves as an added mass. The list of features to reconstruct is therefore the following: one active PZT transducer, four notches of different depths, one inactive PZT (added mass) and four edges at different distances from the transducer.

A time snapshot of the fully measured wavefield at $t = 62$ μs is shown in Figure 3.19a, where the interaction with three of the notches is clearly visible, while the interaction of the wavepackets with the shallowest notch is hardly noticeable. A second time snapshot of the wavefield at $t = 124$ μs shown in Figure 3.19b shows reflections from the edges of the plate. In order to ensure that all the features are included in the model, the active sources region is larger than the plate, as depicted in by the orange box in Figure 3.18. The reconstruction is then conducted with the set

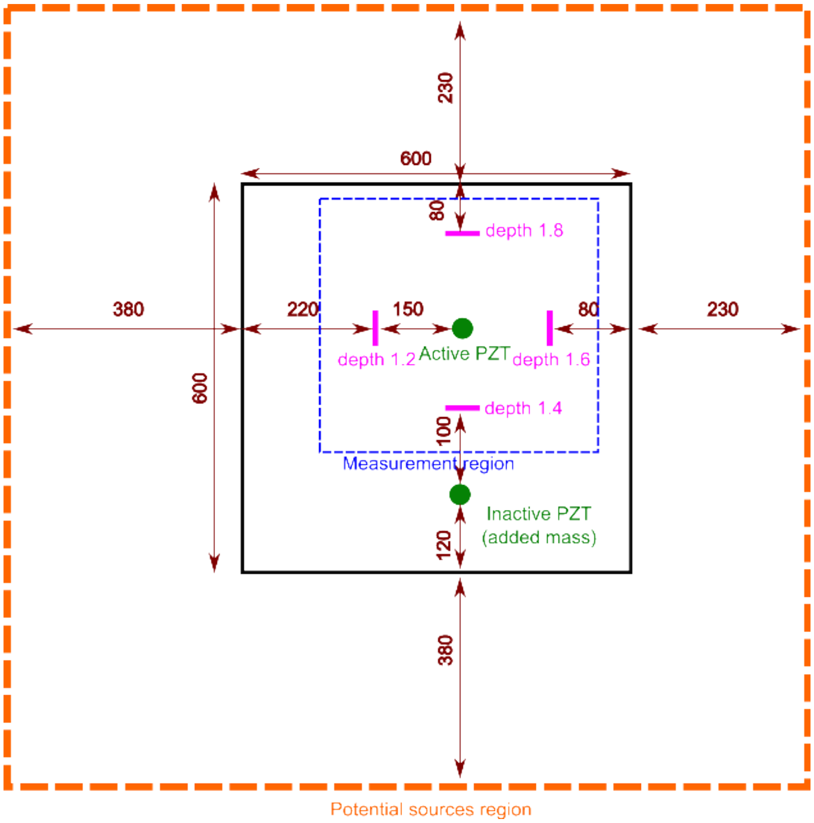

Figure 3.18: Schematic of an aluminum plate (black contour) with four notches (pink), two transducers (green, only one is activated), region of measurements (blue) and potential sources (orange). All dimensions are in millimeters

of parameters $[M, N_\sigma, N_\lambda] = [2000, 10, 2]$ in a frequency range from 110 to 290 kHz. The map of the active sources given by $\mid \widehat{v_s}^{A0} \mid + \mid \widehat{v_s}^{S0} \mid$ is shown in Figure 3.20 and exhibits numerous features that will be described in detail in the following. First, the principal source of the wavepackets, the active PZT transducer, is properly located at the center of the measurement region (inner black dashed square). The notches are also properly identified as active sources, with the shallowest notch that may easily be misinterpreted as noise due to its low intensity. The added mass of the inactive PZT, located approximately at $(220, -45)$ mm is also properly identified. Finally, instead of identifying the edges, the solver artificially created several clusters of active sources. Four of these clusters are the reflections of the transducer with respect to each edge, thus providing the wavepackets with the following travel history: active PZT-edge-measurement region, while the other clusters outside the measurement region model the wavepackets after two reflections, hence with the travel history active PZT-edge-edge-measurement region.

Using this active source map, the wavefield is then reconstructed on the entire plate, i.e., on a larger area than the measurement region. The resulting reconstructed wavefield is displayed in Figures 3.21a and 3.21b for the same two time snapshots previously presented. Due to the fact that the measurement region and the reconstructed region are not equal, it is not possible to compare the results directly using the coherence metric. This example illustrates the ability of the process to map the geometry of the inspected specimen even though some features and the physical boundaries of the specimen are not included within the measurement region.

3.7.3 Glass fiber composite with Teflon insert

Next, the SWR process is applied to an anisotropic panel containing a Teflon insert simulating a delamination. The goal of this example is to demonstrate the ability of the SWR process to operate on anisotropic specimen and to successfully reconstruct a

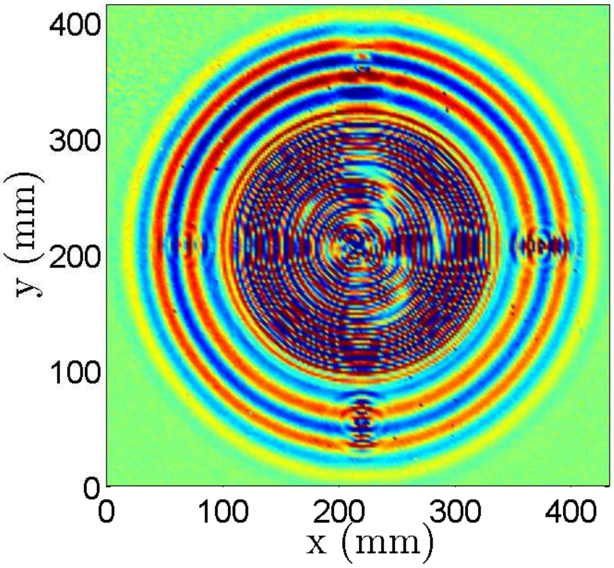

(a)

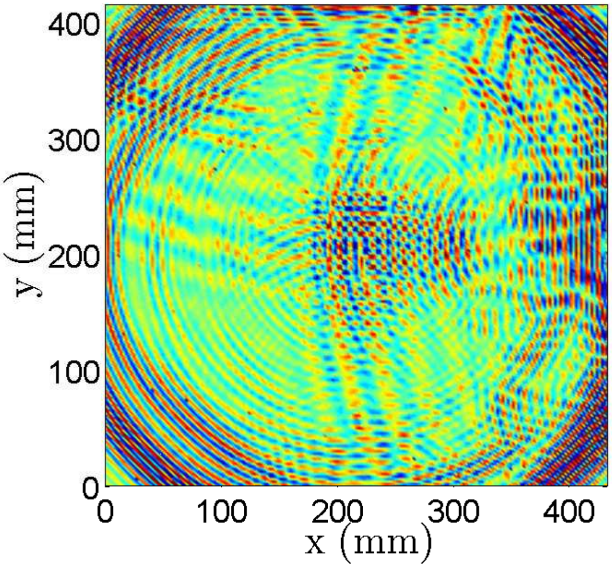

(b)

Figure 3.19: Snapshot of the wavefield representing a 4-cycle 200 kHz tone burst interacting with four notches in a 2 mm thick aluminum plate (a): at $t = 62$ μs and (b): at $t = 124$ μs

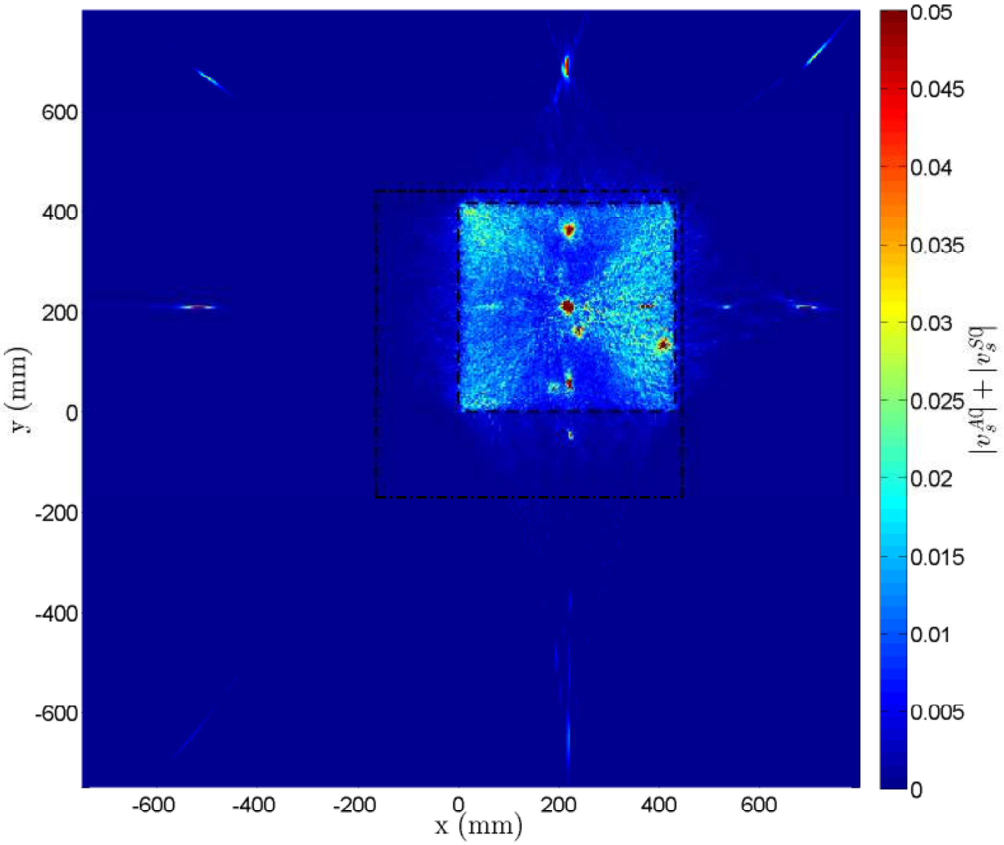

Figure 3.20: Sparse representation of the wavefield $\mid \widehat{v_s}^{A0} \mid + \mid \widehat{v_s}^{S0} \mid$ obtained with the set of parameters $[M, N_\sigma, N_\lambda] = [2000, 10, 2]$ showing the active transducer, the four notch, the added mass and the clusters of active sources emulating the four edges. The outside black represents the plate while the inner black box represents the region of inspection.

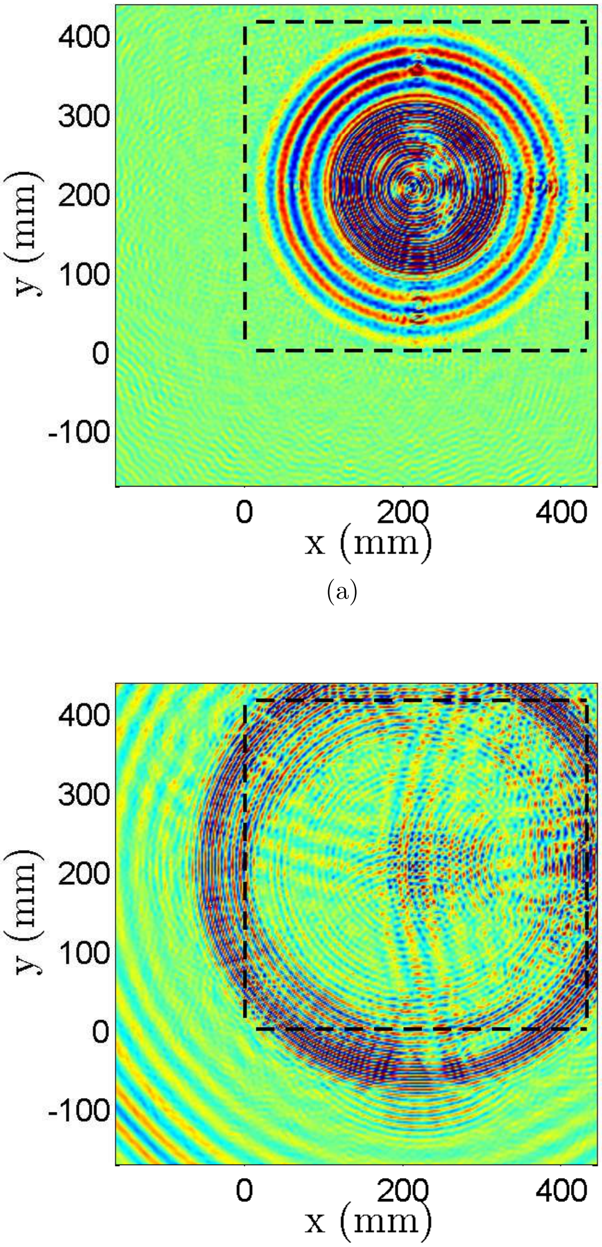

(a)

(b)

Figure 3.21: Snapshots of the reconstructed wavefield on the entire aluminum plate with the set of parameters $[M, N_\sigma, N_\lambda] = [2000, 10, 2]$ (a): at $t = 62$ μs and (b): at $t = 124$ μs

wavefield despite the presence of a larger defect. The specimen is the $600 \times 600 \times 1.6$ mm glass fiber plate first presented in Section 2.6. The defect is a circular Teflon insert of 25 mm diameter inserted between the 2^{nd} and the 3^{rd} ply. Guided waves are generated by a PZT disk transducer bonded at the center of the specimen, 100 mm away from the center of the defect. The transducer is excited by a four cycle tone burst at 300 kHz. The area of interest is 111×106 mm^2. The duration of the measurement is 120 μs and the sampling frequency 2.56 MHz. A time snapshot of the fully measured wavefield at $t = 50$ μs is shown in Figure 3.22a in which the interaction of the faster mode ($S0$) with the defect features standing waves and wavenumbers different than the one of the pristine regions. Given the geometry and the excitation, the lower measurement bound imposed by Nyquist theorem is $M_{Nyq} = 77 \times 74 = 5,698$.

The PZT transducer is located outside the measurement region, which requires a grid of potential sources to be defined over an 180×106 mm area. This ensures that the origin of the wave is determined from the CS problem solution. A representation of the area used to define the potential sources regions and the region in which the measurements are taken is shown in Figure 3.22b. In this case, the acquisition time is limited to avoid the inclusion of edge reflections. Thus, the need to add the boundaries of the specimen as potential sources is avoided. The $l1$-minimization is conducted for the set of parameters $[M, N_\sigma, N_\lambda] = [2000, 10, 2]$ ($CR = 65\%$). The resulting amplitude of source excitation normalized to unity is shown in Figures 3.23a and 3.23b, respectively for the $A0$ and $S0$ mode.

In both figures, two clusters of active sources are visible in correspondence to the location of the PZT at $y = 150$ mm, as well as in an area that outlines the shape of the delamination. The sparse representation of the PZT is a line approximately 15 mm long while the actual transducer is a 12 mm diameter disk. In this case, the sparse representation of the PZT is neither a circle nor a single point because the measurements are only taken below the transducer, i.e., for $y < 106$ mm, so that only

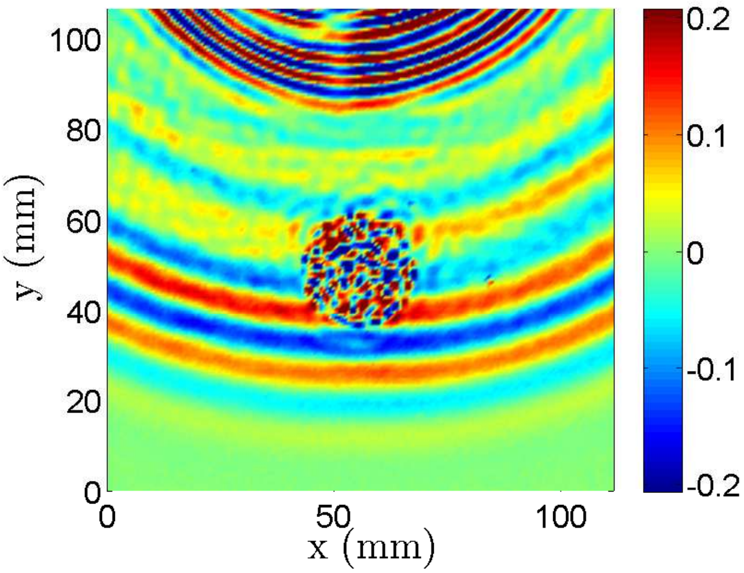

(a)

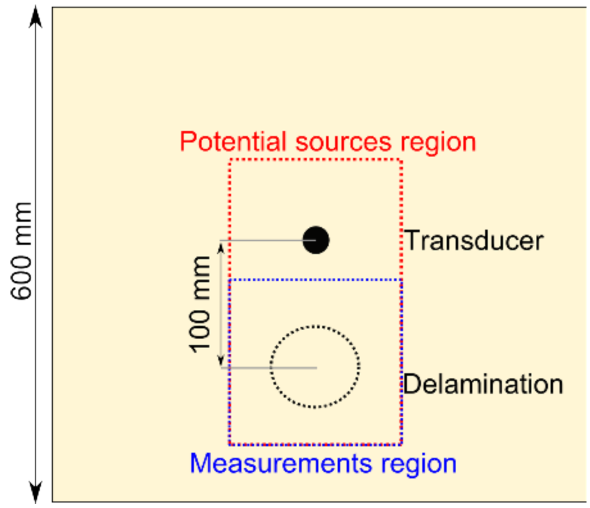

(b)

Figure 3.22: (a): Snapshot of the wavefield representing a 4-cycle 200 kHz tone burst interacting with a circular Teflon in glass fiber plate at $t = 62$ μs and (b): Schematic of the region of interest and the potential sources region (not to scale)

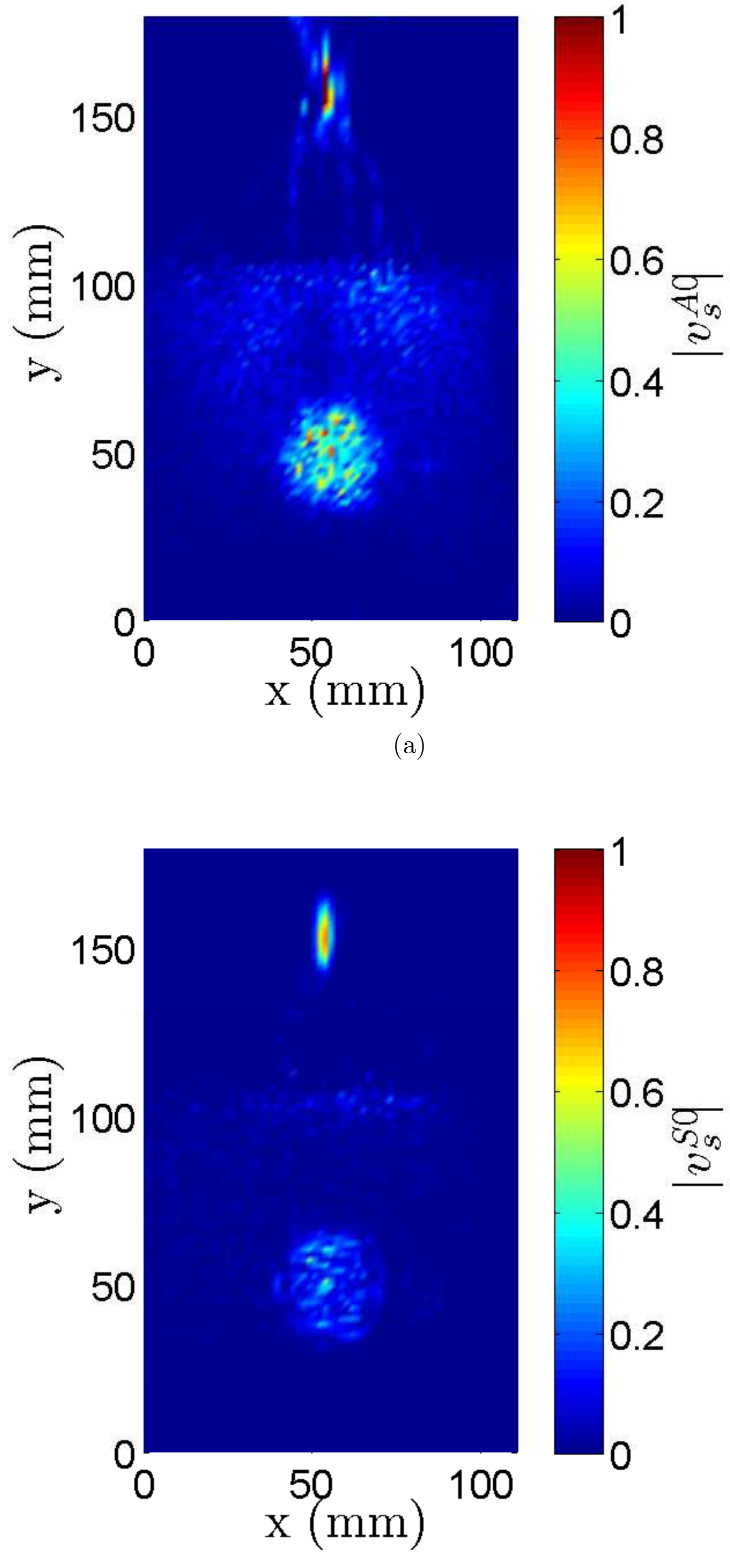

(a)

(b)

Figure 3.23: Sparse representation of the wavefield with the set of parameters $[M, N_\sigma, N_\lambda] = [2000, 10, 2]$ (a): $A0$ sources ($| \widehat{v_s}^{A0} |$) (b): $S0$ sources ($| \widehat{v_s}^{S0} |$)

the wavepackets resulting of the elongation of the transducer along the vertical axis are measured, as it was the case in Section 3.7.1.2. Two main differences between Figure 3.23a and 3.23b are observed. First, the location of the PZT transducer is sharply identified for the $S0$, while the identification for $A0$ appears less defined. This is attributed to a mismatch observed upon measurement between actual wavenumbers and those numerically predicted and used in the basis functions. Such mismatch is approximately 2% for the $A0$ mode, while it is less than 1% for $S0$ mode. The lower definition of the $A0$ source results from several active sources being identified by the $l1$-minimization, which compensates for the mismatch in wavenumber estimations. Secondly, the excitation amplitude of the active sources in the delaminated area appears to be much greater for the $A0$ mode than for the $S0$. This is due to the fact the $A0$ wavenumber is greater than the $S0$ one, and better matches the wavenumber observed within the delaminated region. In fact, the employed basis only includes the two modal components for the undamaged plate, and has therefore limited ability to fully reconstruct regions of different wavenumber content. In this case, as the wavenumber of the standing wave in the delaminated area is not present in the basis functions matrix $\boldsymbol{H}(f)$ (Equation (3.14)), there exist no sparse representation of the delamination, hence the delamination is represented by a full circle of active sources instead of a ring and the wavepackets are not successfully reconstructed in the delaminated region.

The estimated vector $\widehat{\boldsymbol{v}}(f)$ is then used for wavefield reconstruction. The result is shown for each individual mode in Figures 3.24a and 3.24b respectively, at the time instant ($t = 50\mu$s). The reconstructed wavefield matches quite well the measured one, with the exception of the delaminated region, where a lower wavenumber is observed. This is expected given the limited basis used, and its corresponding limited ability to resolve regions of high wavenumber content.

The coherence of the reconstructed wavefield, given by the sum of the $A0$ and $S0$

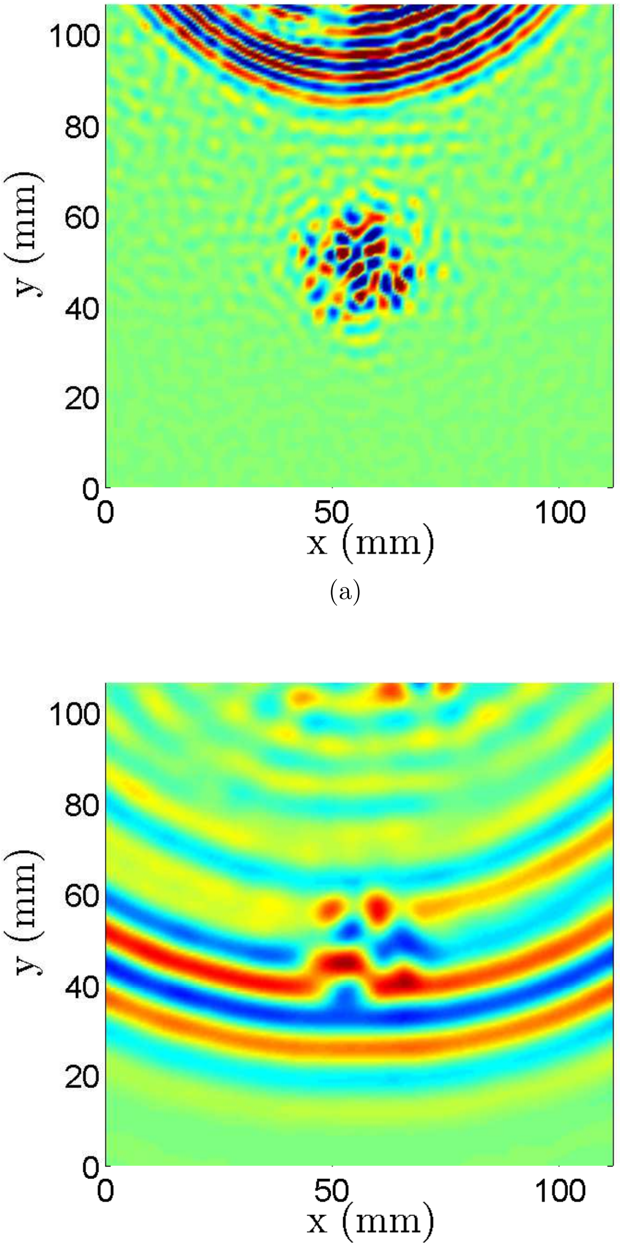

(a)

(b)

Figure 3.24: Snapshot of the reconstructed wavefield at $t = 62$ μs using the individual modes: (a): $A0$ mode and (b): $S0$ mode

wavefields, is then used to quantify the quality of the reconstruction process. The spatially averaged coherence as a function of frequency is shown in Figure 3.25a, where it can be seen that the coherence of the reconstruction is close to one within the limits of the reconstruction represented by the red dashed lines. Furthermore, the spatially averaged coherence at the excitation frequency (300 kHz) as a function of the number of measurements M is shown in Figure 3.25b. This highlights that the number of measurements required for a coherence $\mathcal{C} > 0.9$ is $M = 636$, corresponding to a compression ration $CR = 89\%$. Thus, the proposed sparse reconstruction technique is able to reconstruct this wavefield with a coherence greater than 0.9 from only $1/10^{th}$ the number of measurements required by Nyquist theorem, or only one measurement every 5 wavelengths. For reference, the coherence at the excitation frequency with $M = 2,000$ is $\mathcal{C} = 0.951$. The fact that the coherence does not reach unity can be explained by the presence of measurement noise in the true wavefield and the non-modeled standing wave in the delaminated area, which limits the ability to resolve the wavefield in the delaminated region which occupies 17% of the area of interest. This is illustrated by mapping the coherence over the measurement region at the dominant frequency for $M = 2000$ in Figure 3.26. This last plot shows a value of the coherence close to unity in the pristine area, while the value of the coherence is very low in the delaminated region.

3.7.4 Single frequency reconstruction

This section demonstrates the ability of the SWR process to reconstruct single frequency wavefields as defined in Section 4.3. To achieve this, the fundamental equation of the SWR process must be solved only at the frequency f_0 so that Equation (3.25) becomes:

$$\text{minimize } \|\boldsymbol{v}(f_0)\|_1 \text{ subject to } \|\boldsymbol{y}(f_0) - \boldsymbol{H}(f_0)\boldsymbol{v}(f_0)\|_2^2 \leq \frac{\|\boldsymbol{y}(f_0)\|_2}{N_\sigma} \tag{3.29}$$

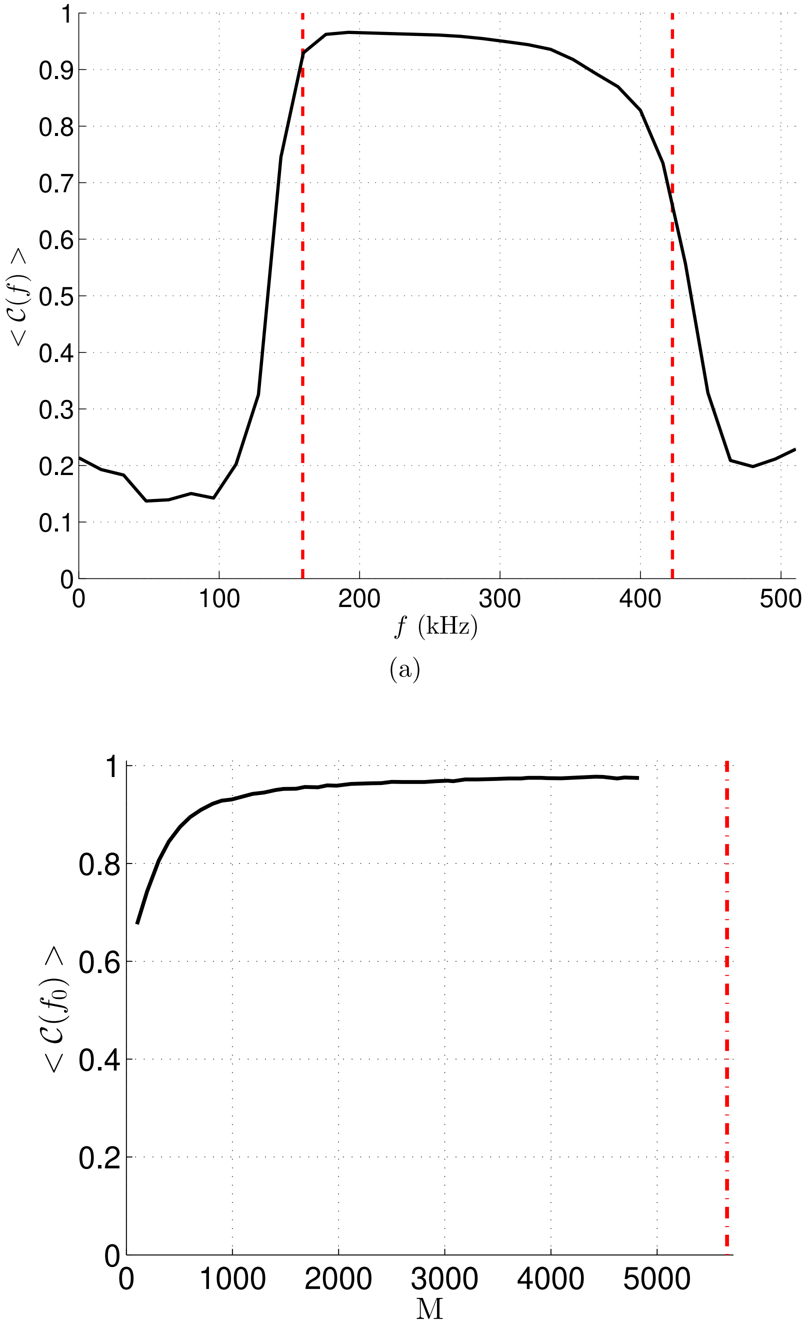

(a)

(b)

Figure 3.25: Coherence of the reconstructed wavefield (superposition of $A0$ and $S0$) (a): Coherence averaged in space as a function of frequency and (b): Evolution of the averaged coherence at the dominant frequency $f_0 = 300$ kHz as a function of the number of measurements M

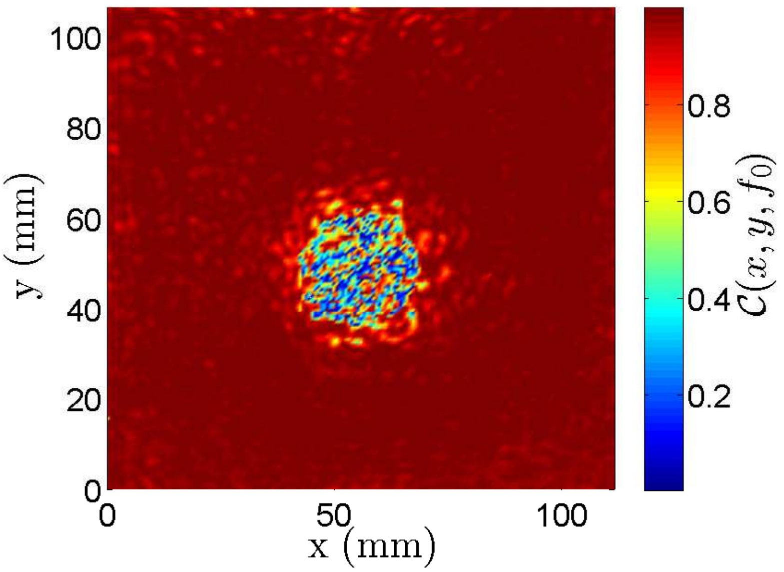

Figure 3.26: Coherence of the reconstructed wavefield at the dominant frequency

No further reformulation of the SWR process is required. In practice, instead of solving for a range of frequency, the problem is solved for a single frequency. The challenge is that by reconstructing a single frequency, the quantity of information fed to the solver is much less than when several frequencies are used, potentially leading to a low signal-to-noise ratio. For comparison, the SWR process was applied to 54 discrete frequency values in Section 3.7.3.

The single frequency wavefield obtained from the wavefield presented in the previous section is used to illustrate the process. The single frequency wavefield at the excitation frequency $f_0 = 300$ kHz obtained by the application of a one dimensional Fourier Transform to the time dependent wavefield of Section 3.7.3 is displayed in Figure 3.27.

The parameters of this reconstruction are kept similar to the one of the previous section. The potential sources are defined on a larger grid up to $y_{max} = 200$ mm in order to include the transducer and $[M, N_\sigma, N_\lambda] = [2000, 10, 2]$. The active source maps for both the $A0$ and $S0$ modes are shown in Figures 3.28a and 3.28b respectively.

As previously observed, the active sources map presents two main features: a

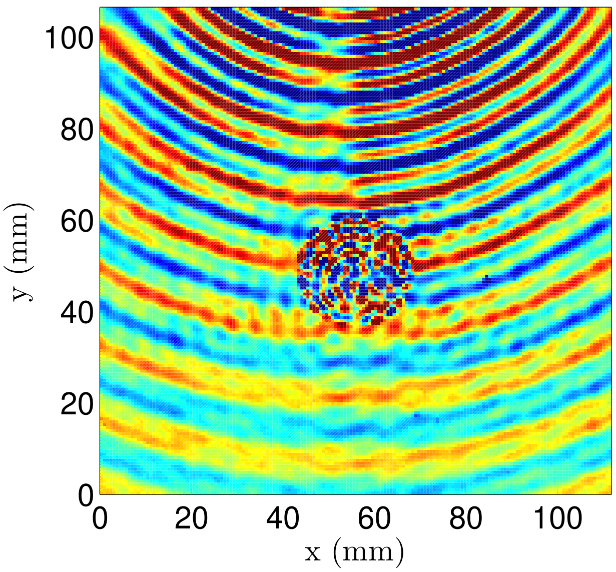

Figure 3.27: Single frequency wavefield at $f_0 = 300$ kHz

circular cluster of active sources corresponding to the delamination and a line of active sources for the transducer. The result of the reconstruction at f_0 is displayed in Figure 3.29. The single frequency wavefield is reconstructed and the delamination properly located.

3.8 Sources of model-experiment mismatches

Despite the successful application of the SWR process to several sets of data, the author believes that much greater compression ratios could be achieved with this technique. Furthermore, the reconstructed wavefields are often noisy and secondary low-amplitude sources are often scattered throughout the active sources maps. Intuitively, if the model was perfectly describing the measured physical phenomena, reconstruction would require fewer measurements. This section identifies five potential reasons to justify these imperfections. This are five potential avenues to further improve the performance of the SWR process. These weak points are associated with model-experiment mismatch. The sensitivity of the quality of reconstruction with respect to these sources of mismatch are discussed in the next subsections.

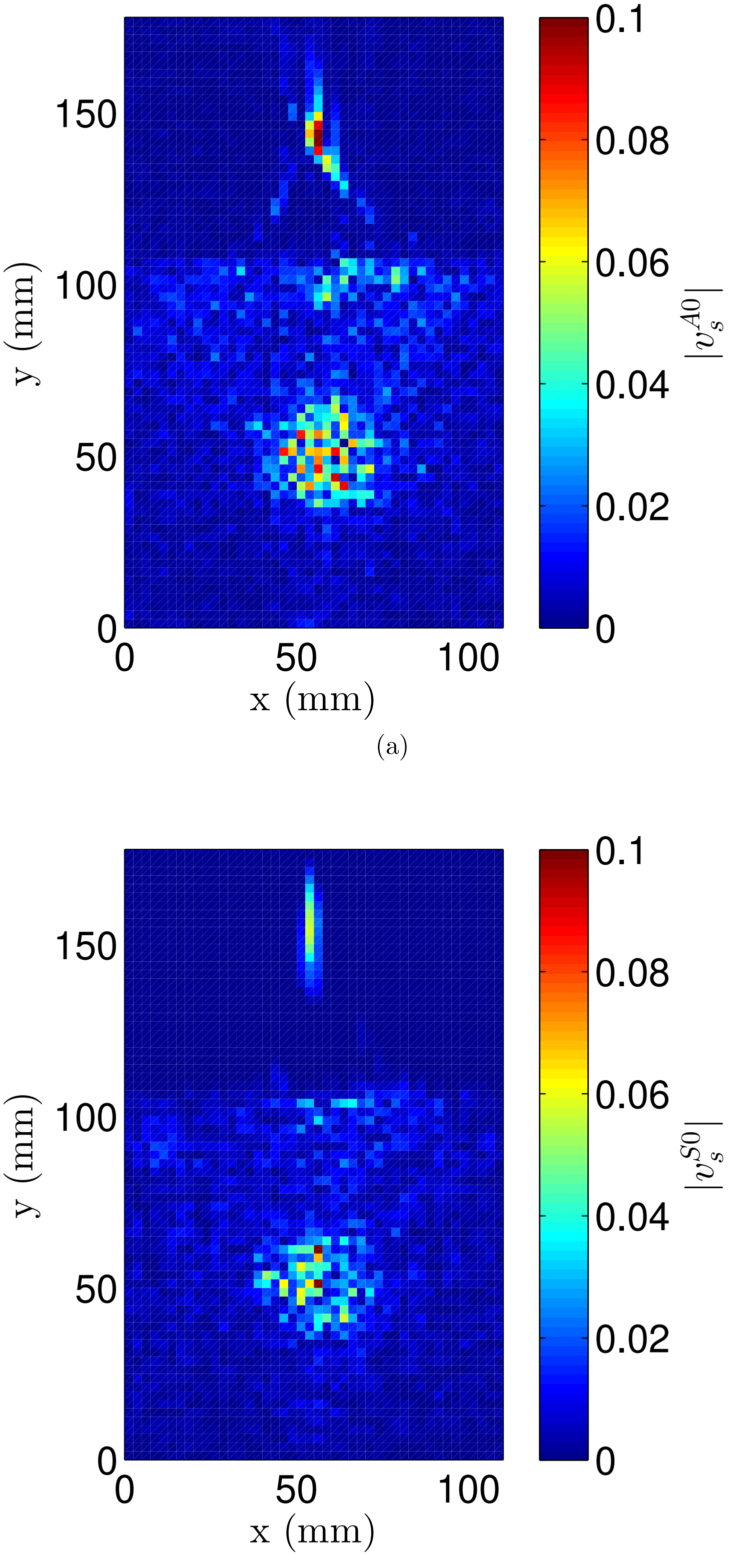

(a)

(b)

Figure 3.28: Sparse representation of the single frequency wavefield with the set of parameters $[M, N_\sigma, N_\lambda] = [2000, 10, 2]$ (a): $A0$ sources ($|\ \widehat{v}_s^{A0}\ |$) (b): $S0$ sources ($|\ \widehat{v}_s^{S0}\ |$)

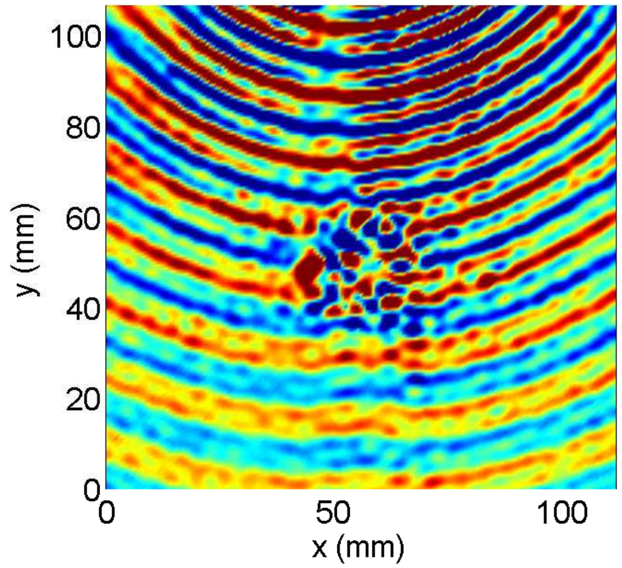

Figure 3.29: Reconstructed single frequency wavefield

3.8.1 Wavenumber mismatch

The first model-experiment mismatch comes from an inaccurate estimation of the wavenumber $k^{(\mu)}_{m,s}(f)$ used to generate the basis functions in Equation (3.14). There are several sources of experimental uncertainty that may lead to inexact dispersion relations estimation. Mainly, the physical and mechanical properties of the studied specimen are provided by the manufacturer instead of being directly measured. These properties uncertainties induce errors. This includes, but is not limited to: elasticity modulus, Poisson ratio, layer thickness and ply orientation of each layer. Another potentially source of inaccuracy comes from the measure of the grid of inspection by the operator through the SLDV software. This measure provides location of each point in space. Understanding that perfectly estimating wavenumbers is incompatible with scaling up the inspection technique to numerous specimens, this section quantifies the potential loss of reconstruction quality induced by an inexact wavenumber estimation. The reconstruction of the wavefield presented in Section 3.7.1 is investigated. This wavefield is chosen because an extensive analysis of the parameters was presented

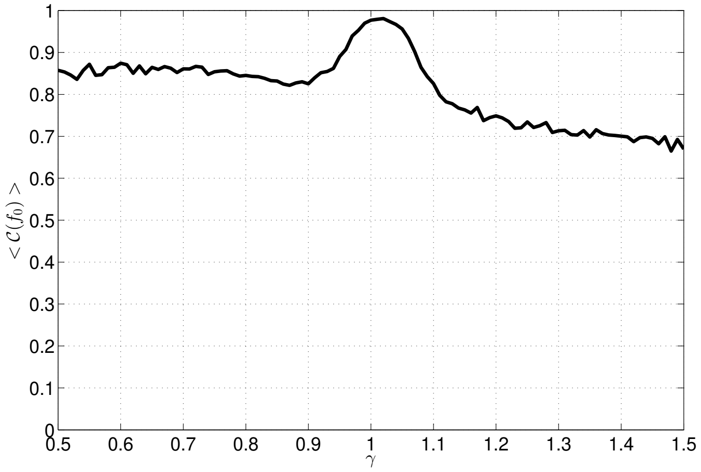

Figure 3.30: Sensitivity of the reconstruction coherence as a function of the wavenumber scaling parameter γ

in Section 3.7.1.1. Based on these results, the following set of parameters is used $[M, N_\sigma, N_\lambda] = [300, 10, 2]$. The reconstruction is conducted with the wavenumber scaled by a parameter γ according to the following equation:

$$\forall \mu,\ k_{m,s}^{(\mu),\gamma}(f) = \gamma k_{m,s}^{(\mu)}(f) \tag{3.30}$$

where γ varies between 0.5 and 1.5, representing inexact wavenumber estimation as important as 50%. The coherence of the reconstruction averaged in space at the dominant frequency $f_0 = 230\ kHz$ is recorded, leading to the Figure 3.30. From this plot, it can be concluded that the SWR process is sensitive to the accuracy of the wavenumber estimation within ±10% of the exact value of the wavenumber. Outside this range, the reconstruction decays slowly as γ evolves. In practice, it was observed that wavenumbers estimated by SAFE is usually 1 to 5% off the measured values, which bounds the negative consequences of this mismatch. Furthermore, this analysis shows that using the exact wavenumber can increase the reconstruction quality.

3.8.2 Amplitude decay mismatch

The second model-experiment mismatch comes from the theoretical energy decay used to generate the basis functions. In Equation (3.14), the energy decays with the inverse of the square root of the distance from the source, or $1/\sqrt{d_{m,s}}$. This assumes that the amplitude is driven by the geometric spreading only and all the energy dissipation phenomena [122] are neglected. Even though this assumption may be satisfying for low attenuation specimens such as aluminum, it may not be the case for glass fiber specimens for example. It is possible to modify this model by changing the exponent of the denominator in Equation (3.12). Empirical model or experimental calibration can be used to determine the value of this exponent. In order to judge the effect of this mismatch, the amplitude of the mode shapes used in the reconstruction of the analytical wavefield of Section 3.6.2 is modified according to the following equation:

$$h_{m,s}^{(\mu),\delta}(f) = \frac{e^{-ik_{m,s}^{(\mu)}(f)d_{m,s}}}{d_{m,s}^{\frac{1}{2}+\delta}} \tag{3.31}$$

where the parameter δ tunes the amplitude decay of the model. By default $\delta = 0$.

Figure 3.31 shows that the coherence of the reconstruction is also sensitive to the choice of the attenuation parameter, but the error induced by the choice of an inexact attenuation parameter is bounded in Figure 3.31.

3.8.3 Amplitude directionality

The third model-experiment mismatch comes from the amplitude directionality of the wavepackets. Amplitude directionality can originate from two physical phenomena: First, amplitude of wavepackets vary with the direction in anisotropic specimens [123]. Secondly, the transducer and its coupling with the specimen may induce directionality. It was indeed observed experimentally that the amplitude of wavepackets may be directional even in isotropic material due to an unequal thickness of the coupling layer between the specimen and the transducer or an uneven electric field in the

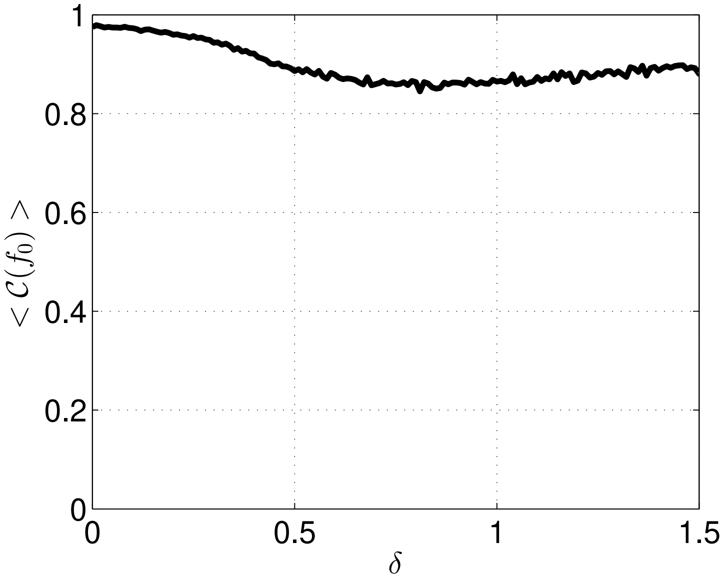

Figure 3.31: Sensitivity of the reconstruction coherence as a function of the amplitude decay parameter δ

transducer disk. Moreover, scatterers, interpreted in the model as omni-directional secondary sources are almost always directional [118]. Due to the fact that this effect is dependent on multiple parameters, no sensitivity study is conducted for this effect.

3.8.4 Source discretization

Source discretization can induce model-experiment mismatch as well. Indeed, no physical feature emitting, reflecting or scattering wave is truly punctual. Typically, the surface of contact between a PZT disk transducer and a specimen is a disk of 10 to 20 mm diameter (depending on the size of the transducer) which will result in about 1 to 100 potential sources (depending on the value of the ratio λ/N_λ defined in Equation (3.23)). Furthermore, even if a PZT could be described by a single source, it would require that this source is exactly located at the center of the transducer to avoid phase shifts. For example in the reconstruction of the analytical wavefield presented in section 3.6.2, the main source of error comes from the imperfectly located source.

3.8.5 Measurement noise

Finally, the measurement noise is not included in the model and can be a source of significant mismatch. In the context of this research, the electronic noise is mostly negligible as most of the noise comes from the quality of the reflection of the laser beam of the SLDV on the specimen, and can be mitigated through preparation of the specimen. For example covering the specimen with a reflective paint or tape will greatly reduce the measurement noise. Moreover, the measurement noise can be reduced by averaging the measured signal. For time scan, this means measuring multiple time each point and average the results. A short noise sensitivity study is conducted here with the analytical wavefield of Section 3.6.2. In order to emulate the noise, the measurements are artificially modified according to the following equation:

$$\forall m, \forall f, \boldsymbol{y}_m^{\zeta}(f) = \boldsymbol{y}_m(f) \times (1 + \zeta \cdot rand(-1, 1)) \tag{3.32}$$

where ζ is a scaling parameter of the random number included between -1 and 1 denoted $rand(-1, 1)$. The evolution of the coherence averaged in space at the dominant frequency is then displayed in Figure 3.32.

From this result, it can be observed that the reconstruction quality is not significantly decreased by the measurement noise as long as the noise is kept below 20% of the signal strength.

3.9 Conclusions

This chapter presented the Sparse Wavefield Reconstruction (SWR), a technique able to reconstruct wavefields and identify defect locations from sparse measurements and the knowledge of the dispersion relations of the specimen. The SWR technique has been applied to several datasets in order to evaluate its performance. Compression ratios of the order of 90% have been achieved. The influence of the numerical parameters has been discussed, as well as the sensitivity of the mismatches model-experiment on

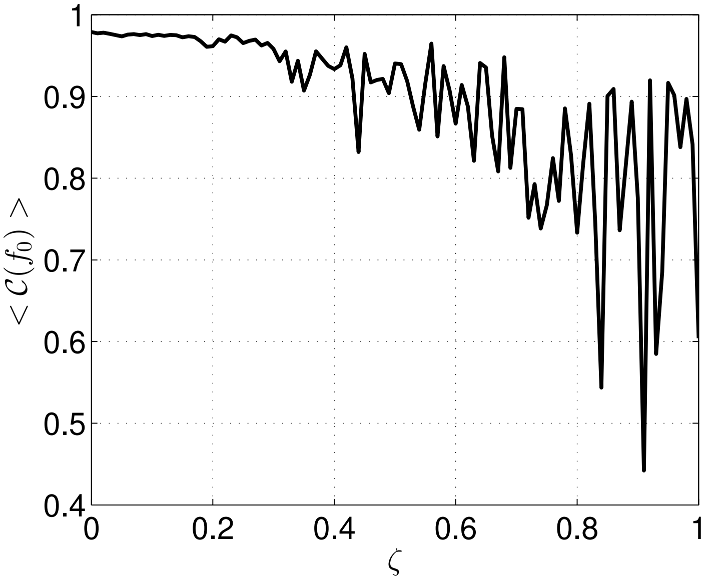

Figure 3.32: Sensitivity of the reconstruction coherence as a function of the noise scaling parameter ζ

the quality of the reconstruction. These sources of mismatch affect the basis functions used for the reconstruction. This technique fulfills the second objective and partially fulfills the first objective described in Section 1.5, namely defect detection and localization, as well as acquisition time reduction. The following chapter will present the approach for damage quantification which leads to three-dimensional maps of the detected defect.

CHAPTER IV

THE FREQUENCY DOMAIN INSTANTANEOUS WAVENUMBER

4.1 Chapter overview

Guided wavefields provide an abundance of information regarding the health of the waveguide. Especially, it has been proven in [124] that the value of the wavenumber of the Lamb waves changes locally in the presence of a defect. This information was later exploited in [24] to highlight the change of wavenumber over a delaminated area.

In this chapter, two techniques able to quantify a local wavenumber value, namely the Instantaneous Wavenumber (IW) and the Frequency Domain Instantaneous Wavenumber (FDIW), are investigated. The IW converts every time frame of a wavefield into the local quantification of the wavenumber, while the FDIW estimates the local wavenumber content at a single frequency. Since the FDIW is related to a single frequency, its result can be used to obtain a local quantitative value representing the depth of a defect in terms of an Effective Thickness (ET).

The IW technique is first presented along with the FDIW technique. Next, the process to quantify defect depth from a wavenumber map is presented. A section is then devoted to the validation of the ability of the FDIW to measure directional wavenumbers. Finally, results are shown to demonstrate the ability of the technique to detect and quantify defects.

4.2 Instantaneous Wavenumber

The IW technique relies on the instantaneous wave vector analysis [125]. The idea to apply the instantaneous wave vector analysis to quantify the wavenumber of wavefield was initially described in [126]. This section presents the development of the IW, shows its application to a multi-modal analytical wavefield and highlights its limitations.

4.2.1 Model

Given a wavefield function of time and space $w(x, y, t)$, the Instantaneous Wavenumber (IW) is computed by deriving the phase of the analytical signal of the wavefield. The analytical signal is computed using the Hilbert transform [127, 128]. The Hilbert transform is a linear operator acting on a function $f(x)$. It can be interpreted as the convolution between $f(x)$ and the function $h(x) = 1/\pi x$. As $h(x)$ is not integrable at zero, the Hilbert transform is defined as the Cauchy principal value (denoted $p.v.$) of the convolution of $f(x)$ and $h(x)$:

$$\mathcal{H}(f)(x) = p.v.\left(f * h\right)(x) = p.v. \int_{-\infty}^{\infty} f(x)h(x-\xi)d\xi = \frac{1}{\pi}p.v. \int_{-\infty}^{\infty} \frac{f(x)}{x-\xi}d\xi \tag{4.1}$$

The Hilbert transform efficiently shifts the phase of its input by $\pi/2$ in the complex plane. Similarly, the Hilbert transform can operate along three dimensions individually, as detailed in [129].

Next, the analytical signal of a wavefield $w(x, y, t)$ is defined by [130]:

$$g(x, y, t) = w(x, y, t) + i\mathcal{H}(w(x, y, t)) = A(x, y, t)e^{i\theta(x,y,t)} \tag{4.2}$$

where $A(x, y, t)$ and $\theta(x, y, t)$ are the instantaneous amplitude and the instantaneous phase, and are given by:

$$A(x,y,t) = \sqrt{w(x,y,t)^2 + \mathcal{H}(w(x,y,t))^2} \tag{4.3}$$

$$\tan(\theta(x,y,t)) = \frac{\mathcal{H}(w(x,y,t))}{w(x,y,t)} \tag{4.4}$$

In the case of a wavefield, $A(x,y,t)$ and $\theta(x,y,t)$ provide a local and an instantaneous value of the amplitude and the phase of the wavefield.

It is common practice to observe the absolute value of the analytical signal given by $\mid g(x,y,t) \mid = A(x,y,t)$, called envelope, to locate the energy of the wave in space and time, thus allowing easy measurement of the group speed of the guided waves [131]. For example, Figure 4.1a shows the envelope (dashed line) of a decaying harmonic signal (solid line), which is directly related to the location of the energy at a given time instant. Furthermore, by analogy between Equation (4.2) and Equation (2.11), it can be observed that the instantaneous phase is expressed as a function of the wavenumber $\boldsymbol{k}$ and the position vector $\boldsymbol{r}$ by:

$$\theta(x,y,t) = \boldsymbol{k} \cdot \boldsymbol{r} - \omega t = k_x x + k_y y - \omega t \tag{4.5}$$

where k_x and k_y denote the wavenumber in the direction x and y respectively. The wavenumbers can then be obtained by the first order derivative of $\theta(x,y,t)$:

$$k_x(x,y,t) = \frac{\partial \theta(x,y,t)}{\partial x} \tag{4.6}$$

$$k_y(x,y,t) = \frac{\partial \theta(x,y,t)}{\partial y} \tag{4.7}$$

Hence the first order spatial derivatives of the phase of the analytical signal provide the wavenumber in the Cartesian directions. The difficulty resides in calculating the instantaneous phase $\theta(x,y,t)$. Indeed, as the phase is defined by an arctangent function (Equation (4.4)), lies between $[-\pi, \pi]$ and is periodically discontinuous with discontinuities of amplitude 2π as shown by the solid line of Figure 4.1b.

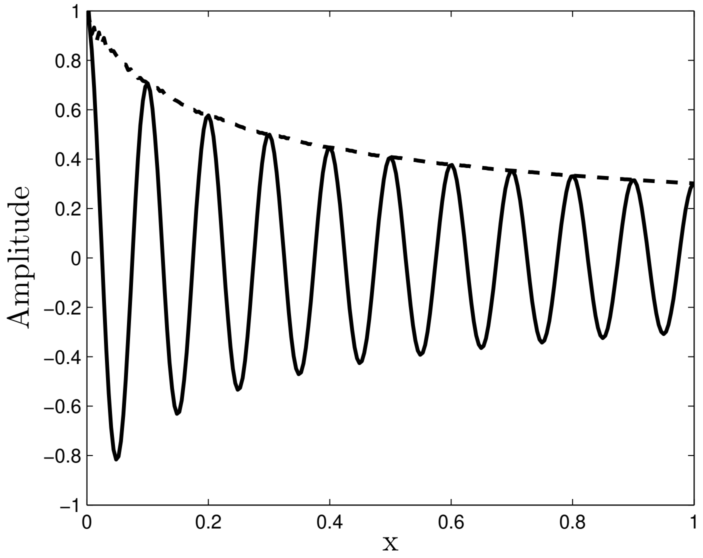

(a)

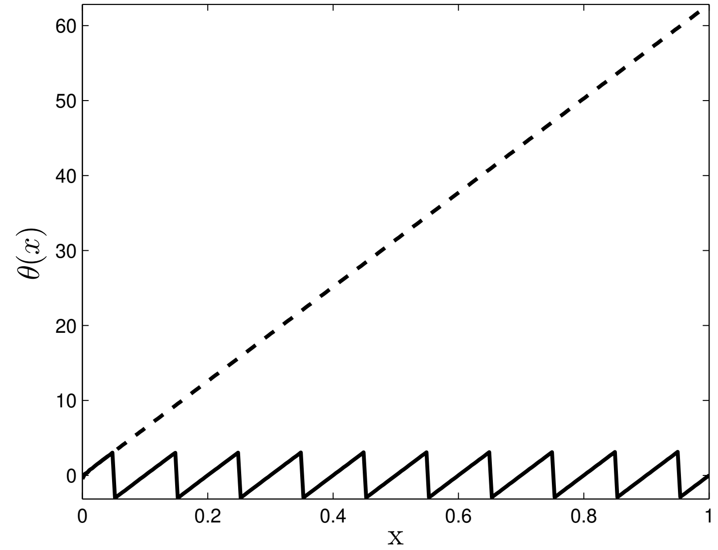

(b)

Figure 4.1: (a) Harmonic signal of decaying amplitude (solid line) and its envelope computed with Equation (4.3) and (b) corresponding wrapped phase $\theta(x)$ (solid line) and unwrapped phase $\theta_u(x)$ (dashed line)

A common practice when dealing with this issue is to unwrap the phase, i.e., shifting the phase of $+2\pi$ every time a discontinuity is detected, as illustrated by the dashed line in Figure 4.1b. The unwrapped phase is denoted $\theta_u(x, y, t)$.

However, unwrapping the phase is not always a straightforward operation, especially in the presence of measurement noise. To avoid the phase unwrapping operation, an alternative computation of $\theta(x, y, t)$ is proposed by Rogge and Parker in [126]. Let the natural logarithm of the analytical signal be:

$$\log(g(x, y, t)) = \log\left(A(x, y, t)\right) + i\theta(x, y, t) \tag{4.8}$$

Then, according to Equations (4.6) and (4.7), the wavenumber k_x can be written as:

$$\begin{aligned} k_x(x, y, t) &= \frac{\partial\theta(x, y, t)}{\partial x} = \mathcal{I}\left(\frac{\partial}{\partial x} ln(g(x, y, t))\right) = \mathcal{I}\left(\frac{1}{g(x, y, t)}\frac{\partial g(x, y, t)}{\partial x}\right) && (4.9) \\ k_y(x, y, t) &= \frac{\partial\theta(x, y, t)}{\partial y} = \mathcal{I}\left(\frac{\partial}{\partial y} ln(g(x, y, t))\right) = \mathcal{I}\left(\frac{1}{g(x, y, t)}\frac{\partial g(x, y, t)}{\partial y}\right) && (4.10) \end{aligned}$$

where $\mathcal{I}$ denotes the imaginary part. Note that, during the calculation of these quantities, the spatial derivative is achieved by a finite different scheme. With this formulation, the denominator $g(x, y, t)$ is not equal to zero as long as the envelope is non-zero, which only happens in regions where no wavepackets are present. In practice, treating the problem this way shifts the numerical difficulty from unwrapping the phase to computing a finite difference.

Finally, the Instantaneous Wavenumber, denoted $IW(x, y, t)$, is given by the magnitude of the wavenumber vector:

$$\begin{aligned} IW(x, y, t) &= \sqrt{k_x(x, y, t)^2 + k_y(x, y, t)^2} \\ &= \mathcal{I}\left(\frac{1}{g(x, y, t)}\left(\left(\frac{\partial g(x, y, t)}{\partial x}\right)^2 + \left(\frac{\partial g(x, y, t)}{\partial y}\right)^2\right)^{\frac{1}{2}}\right) \end{aligned} \tag{4.11}$$

In words, $IW(x, y, t)$ is the value of the wavenumber at the location (x, y) of the wavefield at the time instance t. To smooth the result and attenuate the effect of the measurement noise, a median filter is applied to the IW map. The median filter is a nonlinear filtering filter [132] that mitigates the effect of the noise by smoothing the peak values of a signal.

4.2.2 Results: Analytical wavefield

For illustration purposes, a wavefield is created analytically with two waves of wavenumbers 11 and 5 rad/m. A time snapshot of this wavefield is displayed in Figure 4.2a. The corresponding IW computed using Equation (4.11) is shown in Figure 4.2b. Three regions are clearly visible in the IW map: the light blue and the orange regions show the annular regions characterized by wavenumbers of 5 and 11 rad/m respectively. The third region, located between the other two, exhibits a wavenumber value of zero, meaning that no wave is present in this region. As this data was created numerically, i.e., there is no measurement noise, the value of the IW in the non-illuminated region corresponding to the undetermined case in Equation (4.11), is equal to zero.

4.2.3 Results: Experimental wavefield

The IW process is then applied to an experimental wavefield. The specimen is the glass fiber specimen introduced in Section 2.4. The excitation function is a four-cycle tone burst of center frequency 300 kHz and the size of the inspected region is 112×106 mm centered on the delamination. Two time snapshots of the wavefield are shown in Figure 4.3a and 4.3b, corresponding to $t = 39$ μs and $t = 66$ μs after the excitation. The $S0$ mode interacting with the defect is visible in the first snapshot while the second snapshot includes both modes plus the standing wave in the delaminated area. The corresponding IW maps in Figure 4.4a and 4.4b show the regions with no wave of wavenumber included between 150 to 250 m^{-1}. This is due to the mathematical indetermination in Equation (4.11) and this value has no physical meaning.

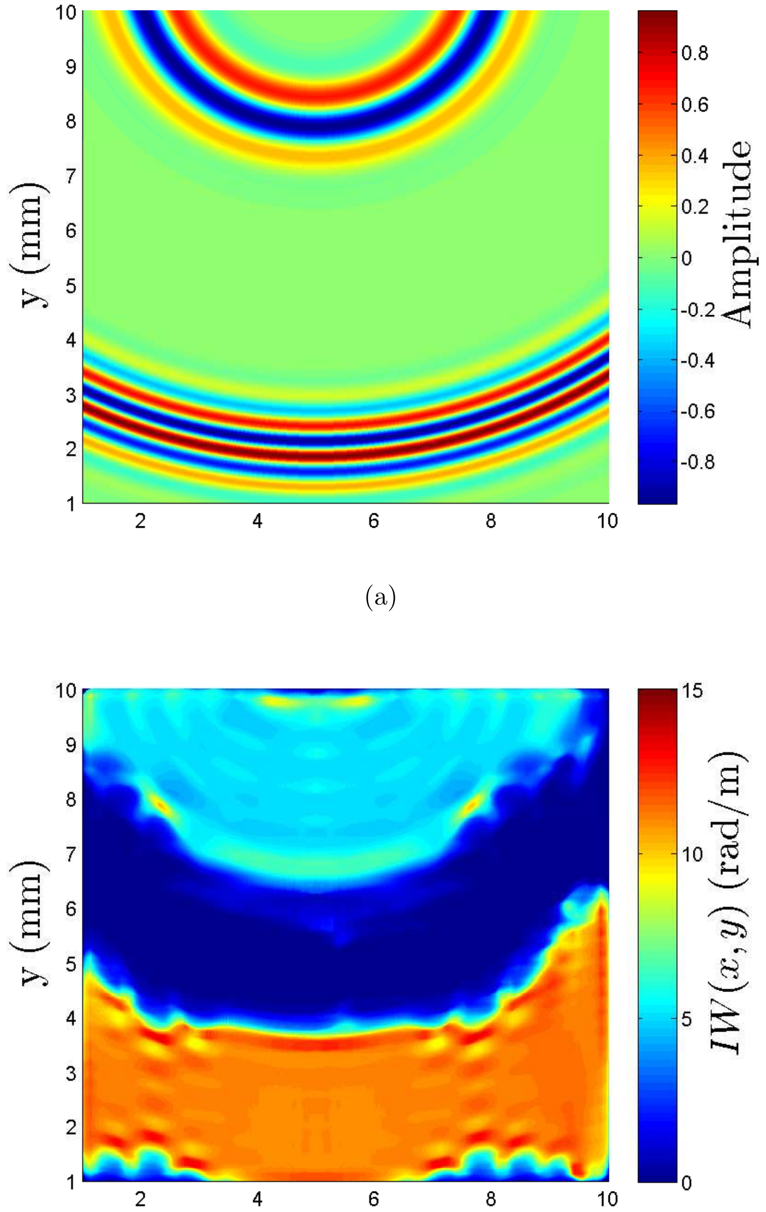

(a)

(b)

Figure 4.2: (a): Snapshot of a wavefield created analytically with wavepackets of 5 and 11 rad/m and (b): Corresponding $IW(x, y)$ at the same time instance highlighting the wavenumbers of the two wavepackets

Furthermore, the wavenumber of the $S0$ is found to be roughly equal to 72 m^{-1} in the top half of Figure 4.4a and the wavenumber of the $A0$ mode to be within 190 and 210 m^{-1}, which is in agreement with the dispersion relations of this specimen shown in Figure 2.5b. Note that the circular defect is characterized in the two IW maps by an area of greater wavenumber values. This is due to the fact that there is a higher wavenumber mode which does not obey the dispersion relation of the pristine specimen in the delaminated region. This confirms the fact that measuring the wavenumber as a function of space can lead to an efficient defect location and shape estimation.

Even though the IW quantifies the wavenumber of a wavefield locally and at every time instant and has the ability to estimate the shape of the defect, it has two majors shortcomings. First, the IW only provides information if a wavepacket is present in the inspected region, as visible in Figures 4.2b, 4.4a and 4.4b. Where no wavepacket is present, no information regarding the health of the specimen is available. Furthermore, if two wavepackets are superimposed, as it is often the case with multi-modal dispersive phenomena such as Lamb waves, the value of the IW fluctuates between the values of the wavenumbers of the modes. This makes the use of IW impractical as multiple time snapshots must be observed simultaneously in order to cover the entire inspected region. Secondly, the wavenumber value computed by IW cannot be analyzed for depth estimation purposes as it is not related to a single frequency. Indeed, as discussed in Section 2.2, the wavenumber is a function of frequency. Hence, besides observing relative local values of the wavenumber in function of time, it is not possible to quantify the depth of a defect using the IW.

4.3 Frequency Domain Instantaneous Wavenumber

Given the intrinsic limitations of the IW described in the previous section, the Frequency Domain Instantaneous Wavenumber (FDIW) is introduced [133] and [134].

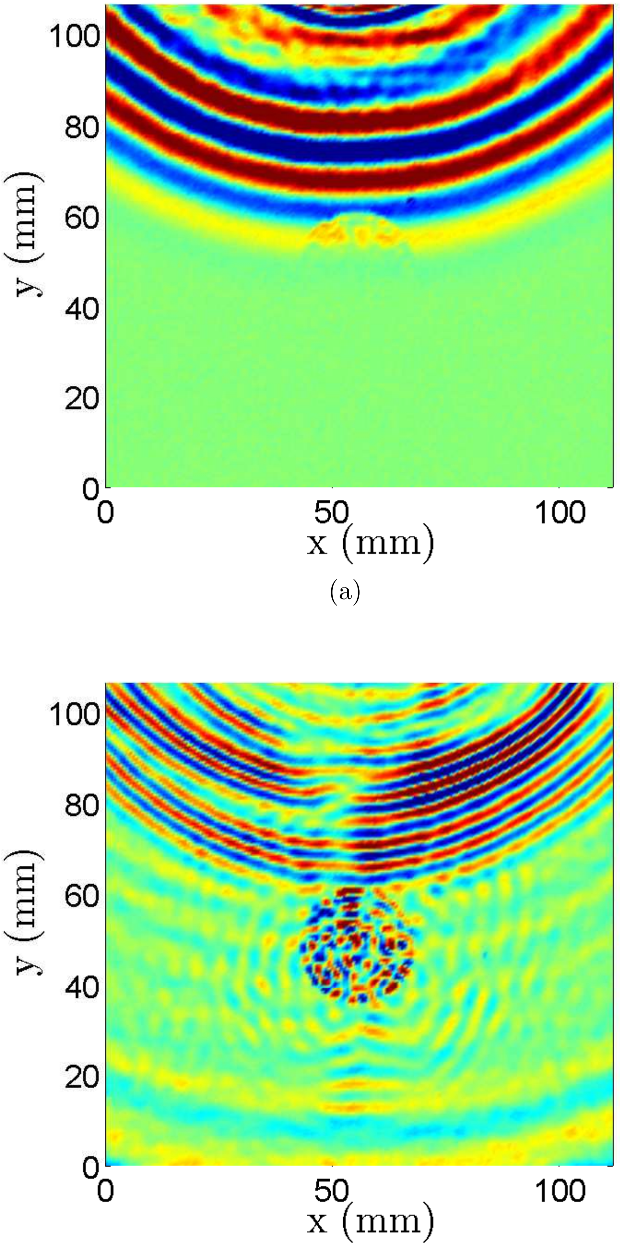

(a)

(b)

Figure 4.3: Application of the IW: (a) and (b): Snapshot of the studied wavefield at $t = 39$ μs and $t = 66$ μ

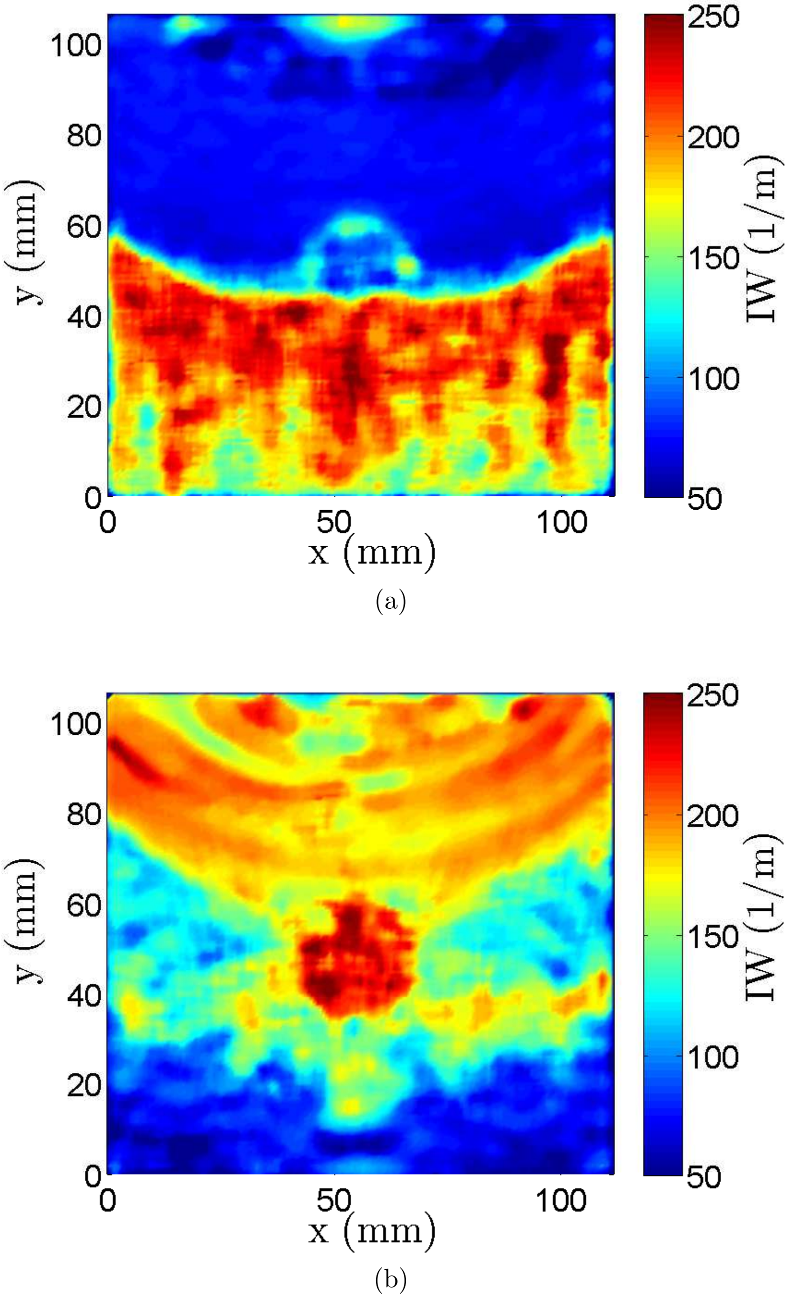

(a)

(b)

Figure 4.4: Application of the IW: (a) and (b): IW maps at $t = 39$ μs and $t = 66$ μs

The idea behind the FDIW is to apply to IW to a single frequency wavefield. Using a single frequency solves the two limitations previously presented: steady state wavepackets cover the entire region of interest and the estimated wavenumber is directly related to a single frequency, thus it is a physically meaningful quantity that can be used for damage quantification. One downside arises when working with steady state datasets however: the measured wavefield is the superposition of all the Lamb wave modes responding to the excitation and their reflections from the edges and the features of the specimen.

Two different manners to obtain single frequency wavefields are presented in this section along with an illustrative result of the FDIW technique.

4.3.1 Single frequency wavefield from a time scan

The most intuitive method to obtain a single frequency wavefield is to extract the single frequency component of a time dependent wavefield. This is achieved by applying a one-dimensional Fourier Transform (FT) in time to the wavefield and extracting a frequency component, typically the excitation frequency. This operation is denoted as:

$$w(x,y,t) \xrightarrow{1D\ FT} \widehat{W}(x,y,f_0) \tag{4.12}$$

This method provides the possibility to remove the edge reflections by truncating the time vector before reflections affects the wavefield in the measurement region. The single frequency wavefield obtained from the time scan presented in the previous section is shown in Figure 4.5a.

4.3.2 Single frequency wavefield from a Fast Scan

A single frequency wavefield can also be obtained by continuously exciting a specimen at a given frequency f_0. The Polytec SLDV PSV-400 has an option called *fast scan* whereby the complex value of the out-of-plane velocity at the frequency of excitation is recorded. Note that even though this method seems similar to the previous

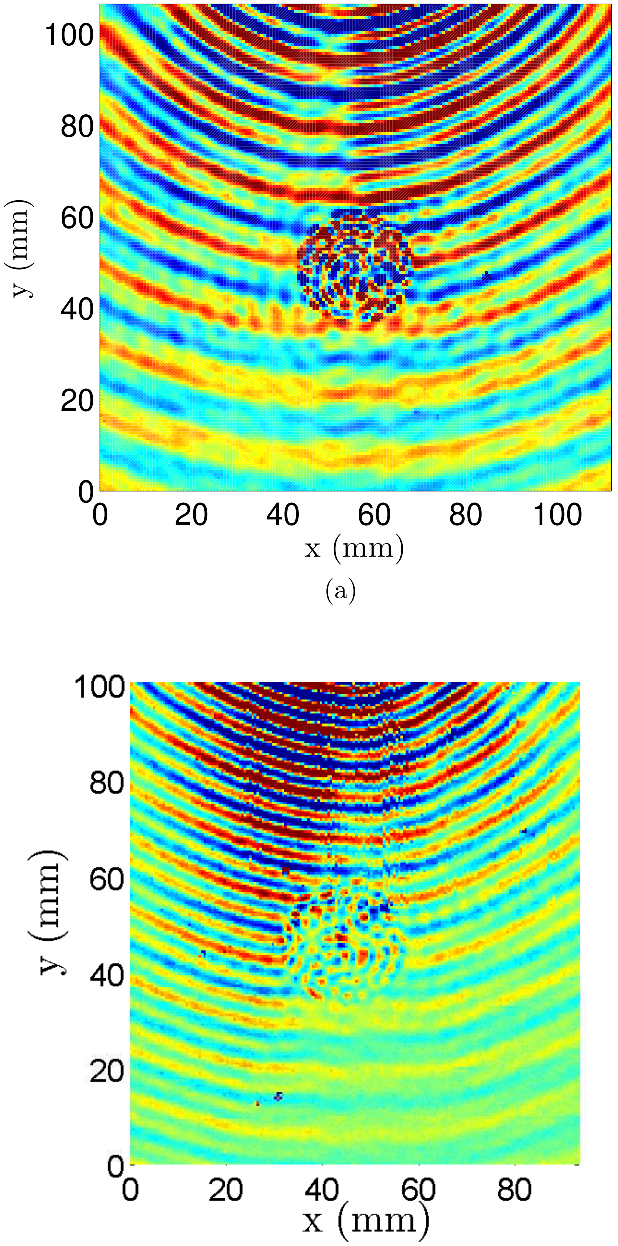

(a)

(b)

Figure 4.5: Single frequency wavefield $W_{300\ kHz}(x, y)$ obtained by (a): time scan and (b): fast scan

one, the two methods are very different in both signal-to-noise ratio and duration of acquisition. Indeed, as the excitation is a continuous sinusoid, there is no need to wait for the plate to be at rest in between measurements, hence the acquisition is much faster. However the measurement is corrupted because of two reasons. First, the steady state response of the specimen contains the superposition of a very high number of reflected modes from the boundaries and the other features of the specimen. Even though these reflected waves are small in amplitude compared to the waves directly incoming from the transducer, they corrupt the interrogating incident wave. Secondly, the risks of overheating the transducer with a continuous excitation is greater than with tone burst excitations, hence the amplitude of the excitation needs to be reduced so the transducer is not damaged. In practice, fast scans acquisitions obtained from traditional PZT transducers are about one order of magnitude faster than regular time scans but the signal-to-noise ratio is also smaller. A single frequency wavefield $W_{300\ kHz}(x, y)$ obtained from a fast scan at 300 kHz on the same region as the time scan presented in the previous section is shown in Figure 4.5b. Note that independently on the method used to obtain it, the single frequency wavefield is always a complex quantity. For simplicity, only the real parts are displayed in Figures 4.5a and 4.5b.

4.3.3 Wavenumber map

Even though the excitation frequency is often kept below the cutoff frequency of the $A1$ mode, it is crucial to separate the $A0$ and $S0$ modes before applying the wavenumber technique. The technique to filter modes is not specific to the applications presented in this chapter, but can be used to separate the modes of any dispersive multi-modal physical phenomena. This mode filtering technique used in this research was developed in [11, 12]. The resulting $A0$-only wavefield $W^{A0}_{300\ kHz}(x, y)$ obtained from the time scan is shown in Figure 4.6.

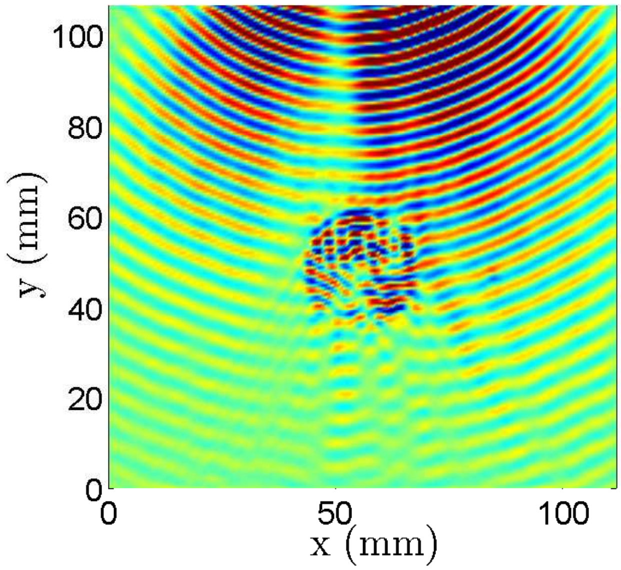

Figure 4.6: Single frequency $A0$-only wavefield $W^{A0}_{300\ kHz}(x, y)$

The Frequency Domain Instantaneous Wavenumber (FDIW) is the IW technique applied to a single frequency wavefield instead of a time dependent wavefield. By analogy with the IW technique, the local value of the wavenumber is estimated by deriving the phase of the signal according to the equation:

$$FDIW(x, y) = \nabla\angle W^{(\mu)}_{f_0}(x, y) \tag{4.13}$$

where ∇ and $\angle$ represent the first order spatial derivative and the phase function, respectively. The single mode single frequency wavefield $W^{(\mu)}_{f_0}(x, y)$ can be obtained either from a time scan or a fast scan. Note that as $W^{(\mu)}_{f_0}(x, y)$ is a complex quantity, therefore there is no need to use the Hilbert transform to compute the phase. The phase can be similarly computed with integrated unwrapping functions or by using the alternative technique presented for the IW in Equation (4.11). As a side comment, 2D phase unwrapping techniques such as the ones developed in [135] and [28] can be used to compute the phase over the region of interest. However, the only advantage of the 2D unwrapping techniques is to translate the phase of each point by a constant value with respect to its neighbors to obtain a continuous 2D phase map. Because in

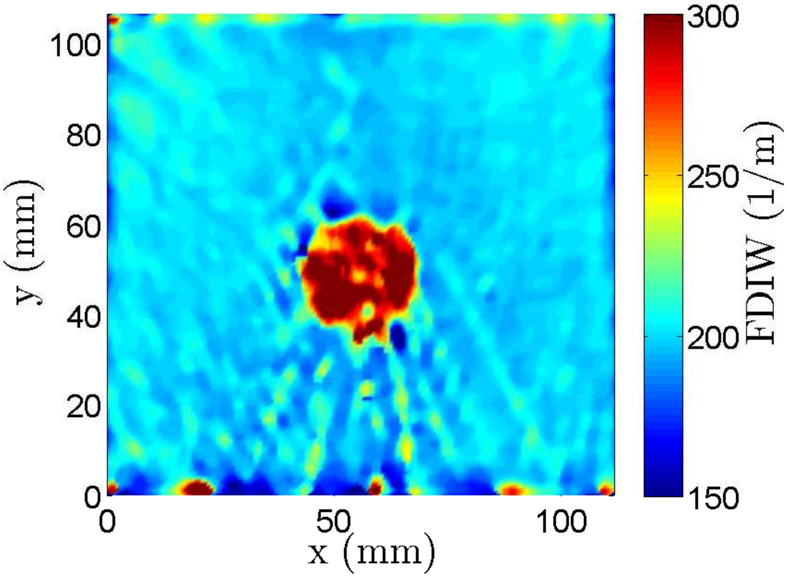

Figure 4.7: FDIW map of the single frequency $A0$-only wavefield at 300 kHz

the FDIW process the phase is immediately derived, it is not necessary to estimate the value of this constant that would be lost in the derivation.

As the derivative operation amplifies the impact of the noise on the quality of the data, it is wise to smooth the phase with an averaging filter window. In practice, a average filter window of five points is used to smooth all the phase vectors before applying the spatial differential.

Figures 4.7 present the application of the FDIW technique to the $A0$-only single frequency wavefield presented in Figures 4.6 thus creating the $A0$ wavenumber map. This map clearly shows a circular region with a greater wavenumber than the background. The size and the area of this region matches nicely the known delamination of the specimen. The FDIW is therefore capable of quantifying the wavenumber of the entire region of interest by transforming a single picture.

4.4 Depth quantification: Effective Thickness

The goal of this section is to relate the local value of the wavenumber to the depth of the defect. This section first develops the model to deduce a depth information from

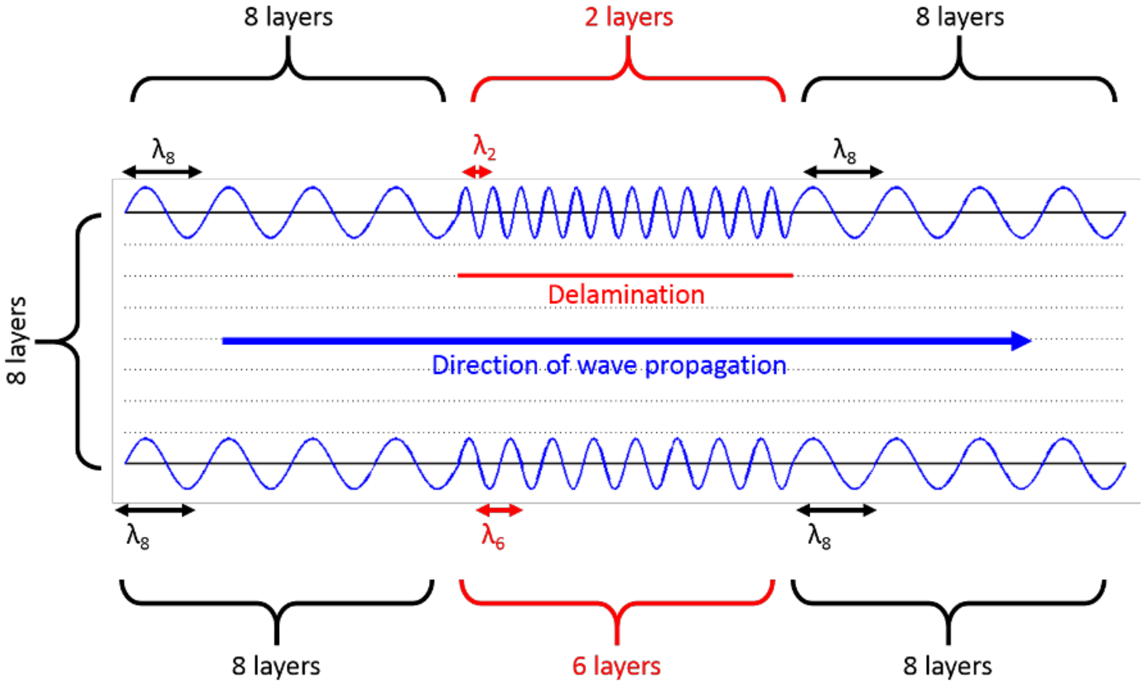

Figure 4.8: Schematic of the Effective Thickness as a function of the depth of the defect

a wavenumber value and then presents the application of the model to the wavefield studied in the previous section.

The model assumes that the delaminated region of a plate obeys the dispersion relations for the group of layers on either side of the delaminated interface. Figure 4.8 shows the 2D schematic of the 8-layer plate with a delamination under the second ply. According to the assumption above, at the location of the delamination, two sub-plates support the propagating wave: a plate made of two layers above and a plate made of six layers below the delamination. The Effective Thickness (ET) is the number of layer in each of the sub-plate. In other words, the ET is the number of ply *seen* by the guided wave. Note that for a pristine area of a plate, the ET is equal to the number layers of the plate. If a delamination is present, the ET takes a local value equal to the number of layers between the delamination and the scanned surface, thus revealing the depth of the defect.

The process to convert the wavenumber to an ET value is the following:

- The dispersion relations are computed for each possible sub-plate. See Figure 4.9a for the dispersion relations of the $A0$ mode of all the sub-plates of the studied layered specimen.
- For each sub-plate, a single scalar value corresponding to the appropriate direction of propagation θ, mode μ and frequency f_0 is extracted, thus creating the function $k^{(\mu)}_{f_0,\theta}(ET)$, which is the unique relationship between the wavenumber and the ET represented in Figure 4.9b.
- Each point of the FDIW map is then mapped to its corresponding ET value by finding the closest match in the $k^{(\mu)}_{f_0,\theta}(ET)$ function.

Figure 4.8 shows which set of ET value would be measured in function of which surface was inspected: if the top surface is inspected, the ET would take the values $[8, 2, 8]$ while the ET values would be [8,6,8] if the inspection was made on the opposite side.

The ET map conversion process is applied to the previous $A0$ wavenumber map obtained using the FDIW method at 300 kHz and yields the ET map of Figure 4.10. Note that as the variation of the $A0$ wavenumber as a function of the ET is much greater than the one of the $S0$ wavenumber (Figure 4.9b). Therefore the $A0$ mode appears better suited for depth quantification. This ET map thus quantifies the in-plane (2D location) and the out-of-plane (depth) of the defect and can also be represented in 3D as shown in Figure 4.11.

The ET map in Figure 4.10 shows a circular damage of approximate diameter between 25 and 26 mm (actual diameter is 25.4 mm) and of average ET 2.7 (actual depth is 2 layers). Note that even if the location and shape of the defect are properly quantified, the depth quantification is not exactly equal to 2 over the whole delamination. In general, the depth quantification provides an estimation of the depth of

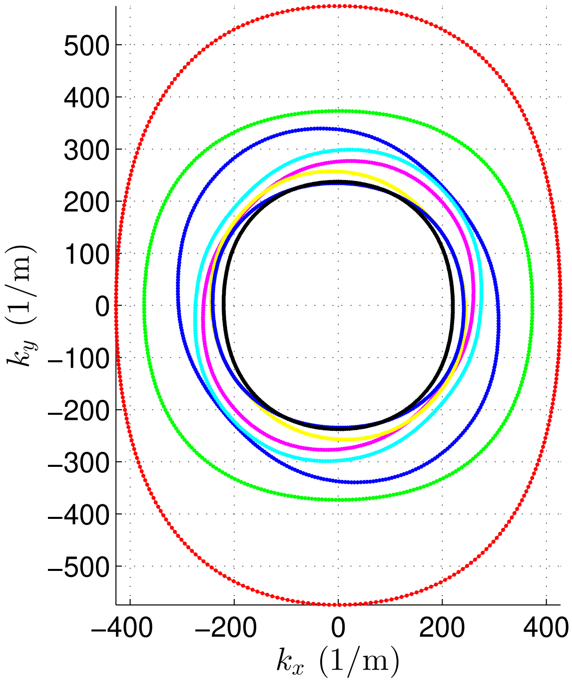

(a)

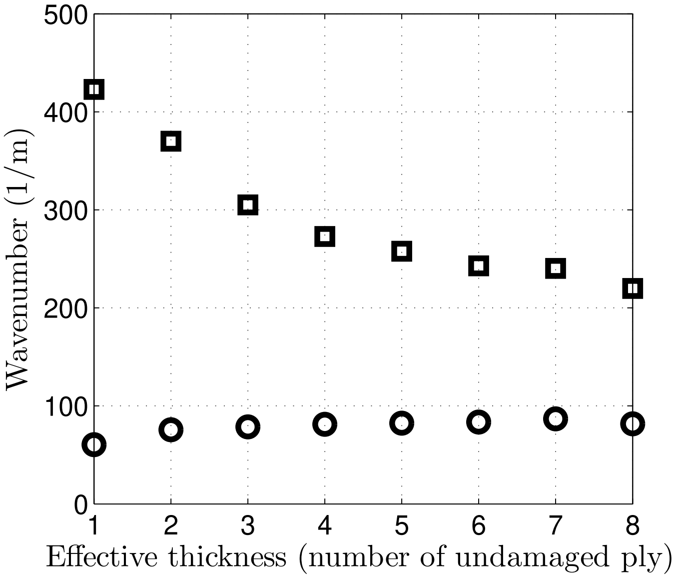

(b)

Figure 4.9: (a) Dispersion relation for the $A0$ mode at 300 kHz ($k_{A0,300\ kHz}$) in the glass fiber specimen for each set of upper layer, red: layer $[0]$, green: layer $[0, 90]$ etc. until black: layer $[0, 90, +45, -45]_s$ and (b) Wavenumber of the $A0$ (squares) and $S0$ (circles) modes at 300 kHz in the vertical direction in the glass fiber specimen as a function of the Effective Thickness

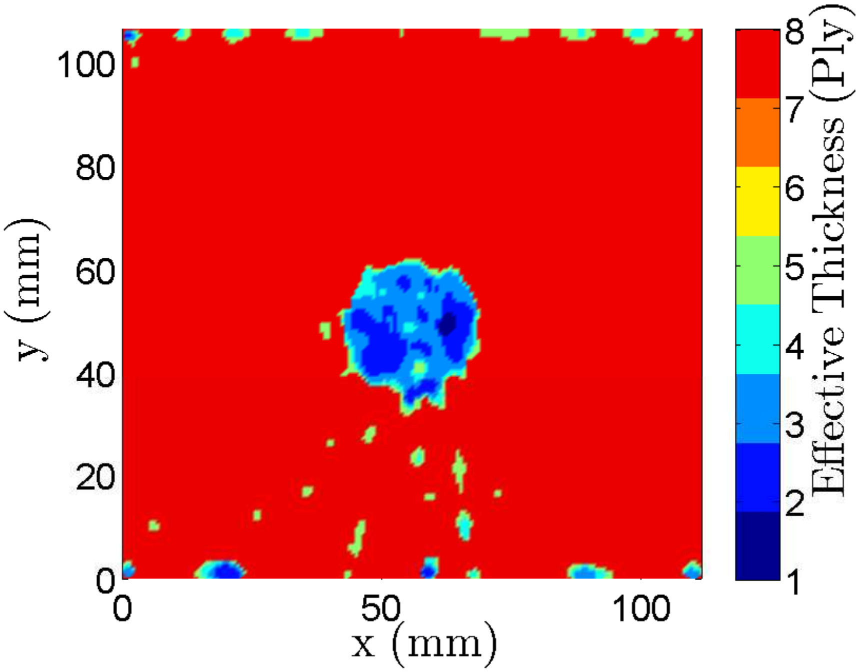

Figure 4.10: Effective thickness map obtained from the $A0$-only wavefield

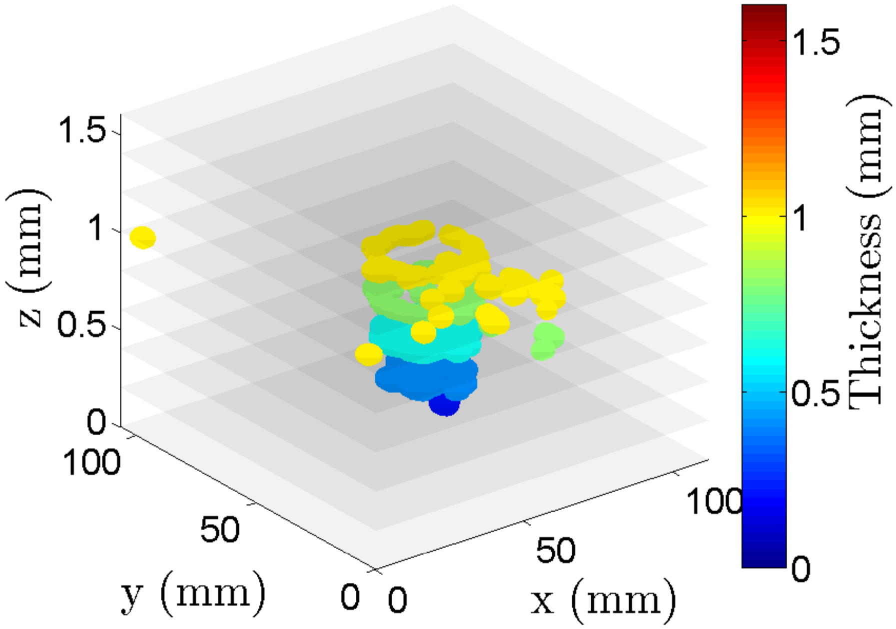

Figure 4.11: 3D representation of the Effective Thickness map obtained from the $A0$-only wavefield

the defect correct at plus or minus one layer. This inexact estimation may be due to two factors: First the physical properties used to generate the dispersion relations are not exact, thus inducing error in the wavenumber versus ET relationship. The second factor is directly related to the model detailed in Figure 4.8. The two sub-plates of 2 and 6 layers separated by a Teflon disk do not behave as true free plates because of the contact with the Teflon disk. This contact potentially changes the boundary conditions thus changing the wavenumber of the modes propagating in the defect area, eventually resulting in an inexact ET estimation. Hence it is concluded that the ET map only provides an approximate value of the depth of the defects.

It is important to note that in parallel to the development of the ET metric by the author, other research groups have obtained similar result such as [136], in which depths of blind holes in aluminum are estimated through a similar process and [137], which refine the concept of ET by using several frequency values to obtain a better depth estimate.

4.5 Validation: Identification of the directional wavenumber

This section validates experimentally the ability of the FDIW to properly measure a wavenumber as a function of the direction in both isotropic and anisotropic materials. To this effect, three wavefields measured on three distinct materials are studied. For each wavefield, the FDIW map is computed and the value of the FDIW at a distance $R = 50$ mm from the transducer is extracted as a function of the direction θ. The result is then compared with the wavenumber estimated by SAFE and the one obtained by applying a FT to the wavefield. In addition this section evaluates the accuracy of the wavenumber obtained by the FDIW technique and its ability to identify potential experimental limitations.

4.5.1 Aluminum plate

First, a 2 mm thick aluminum plate is studied. Lamb waves are generated by a PZT disk bonded on the surface of the plate. The region of inspection is a pristine area of 209×210 mm^2 discretized in 94×97 points. The excitation function is a four-cycle tone burst of center frequency 190 kHz. The representation of the 190 kHz $A0$-only wavefield in the wavenumber domain is shown in Figure 4.12a. As expected, because the material is isotropic, the dispersion relations are represented by a circular contour. The FDIW is then applied to the single frequency $A0$-only wavefield. The value of the FDIW is then extracted along a 50 mm radius circle centered on the transducer, leading to the wavenumber-direction relationship displayed in Figure 4.12b by the solid line. For comparison purposes, the wavenumber obtained by SAFE is shown in Figure 4.12b by the dashed line.

According to Figure 4.12b, the wavenumber calculated by the FDIW technique is very close to the theoretical value predicted by SAFE. However, the FDIW wavenumber oscillates around the theoretical value as a function of the direction, which is mainly due to the experimental noise, but overall, the FDIW accurately predicts the wavenumber within a $\pm 2\%$ accuracy window for this isotropic specimen.

4.5.2 Carbon fiber reinforced polymer panel

Secondly, a $600 \times 600 \times 1$ mm 8-layer Carbon-FiberReinforced Polymer (CFRP) plate is studied. The layup of the plate is $[0^o, 90^o, 0^o, 90^o]_s$. A PZT transducer is bonded at the center of the plate. The region of inspection is a 183×171 mm^2 region centered on the transducer and discretized in 79×79 points. The transducer is excited by a four-cycle sine burst at 200 kHz and each point is measured during 400 μs. The steady state response of the $A0$ mode is then extracted at the excitation frequency. The Fourier representation of the $A0$-wavefield is shown in Figure 4.13a.

The FDIW is then applied to the $A0$-only single frequency wavefield and the

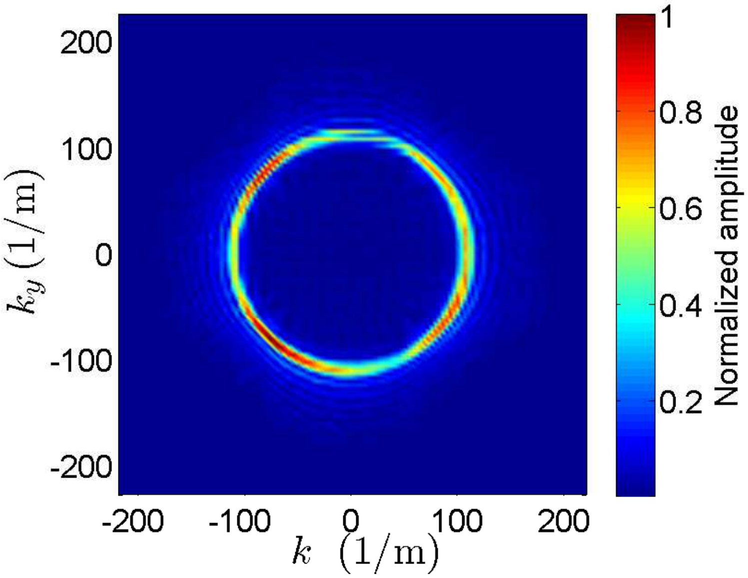

(a)

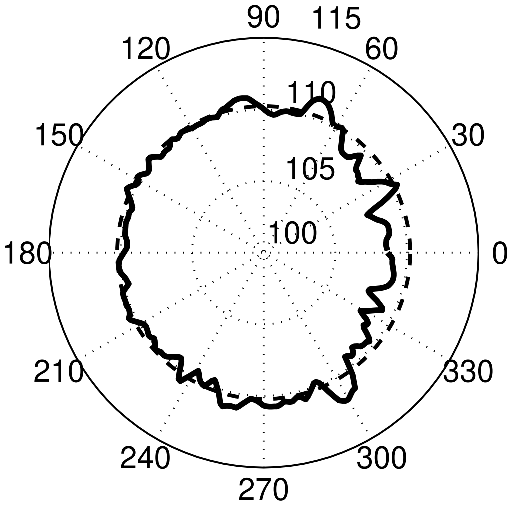

(b)

Figure 4.12: Aluminum specimen (a): Dispersion relations of the 190 kHz $A0$-only wavefield obtained by Fourier Transform and (b): Wavenumber as a function of the direction at 190 kHz computed by the FDIW technique (solid line) and calculated by SAFE (dashed line)

wavenumber values are extracted 50 mm away from the transducer, leading to the solid line representing the wavenumber as a function of the direction in Figure 4.13b. The wavenumber predicted by SAFE is shown in Figure 4.13b by the dashed line. The calculated wavenumber matches properly the SAFE value within an error bounded by ±5%, thus demonstrating the ability of the FDIW to detect directional wavenumber change.

4.5.3 Glass fiber reinforced polymer panel

Finally, a 600 × 600 × 1 mm 8-layer glass fiber plate is studied. For the purpose of this example, the time window is truncated before the $A0$ mode reaches the delamination. This dataset is effectively the one of Section 2.6, truncated in time to prevent reflections from the defect. The transducer is excited by a four-cycle sine burst at 200 kHz and each point is measured during 75 μs. The Fourier representation of the 200 kHz $A0$-only wavefield is shown in Figure 4.14a.

The FDIW value is then computed and extracted on a 50 mm radius circle centered on the transducer. The wavenumbers are then compared in Figure 4.14b. For this dataset, it is important to highlight that even though the illumination is poor in the vertical direction, the measured wavenumber fits satisfyingly the predicted value. Overall, the wavenumber is correctly estimated in every direction within a tolerance of ±5%.

4.5.4 Discussion

This section validates the ability of the FDIW to measure a directional wavenumber and quantifies the accuracy of the calculation of the wavenumber. In the cases presented, the error is bounded by ±5%. In the meantime, the FDIW technique was successfully applied to three distinct materials. Finally, it is good to notice that the FDIW is a purely experimental technique that requires a very little amount of data to compute the wavenumber-direction relationship. In the cases presented here, the

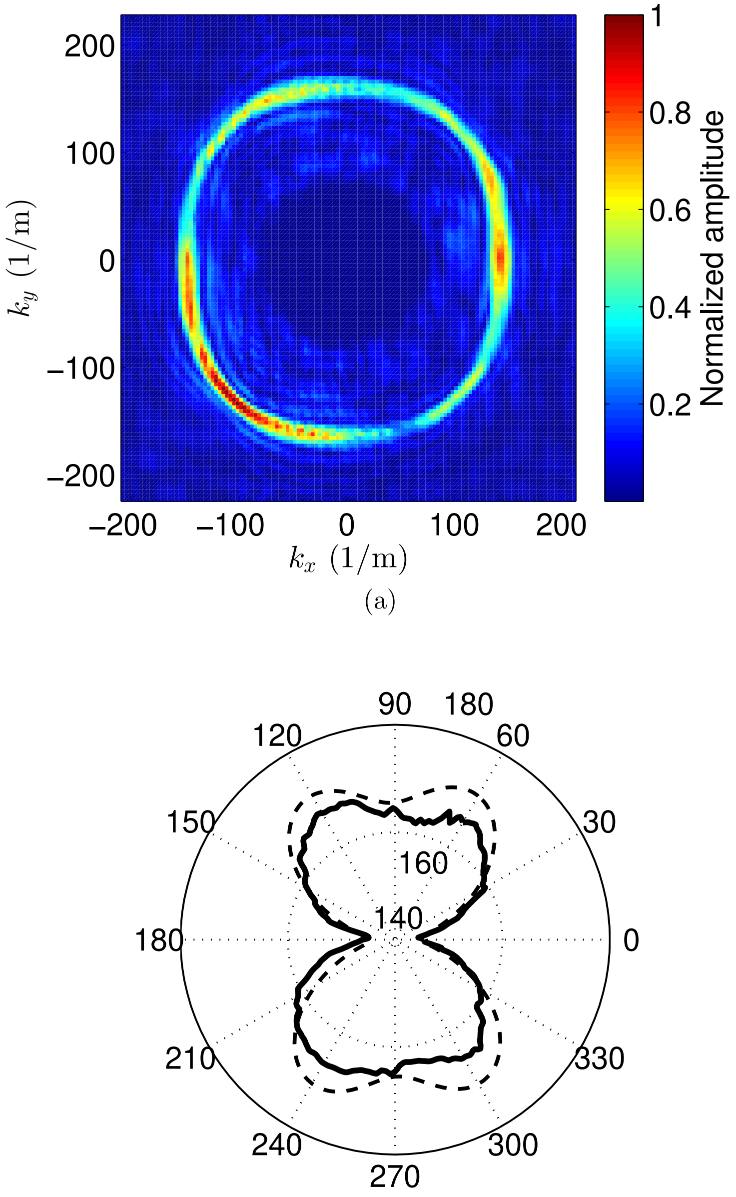

(a)

(b)

Figure 4.13: Carbon fiber reinforced polymer specimen (a): Dispersion relations of the 200 kHz $A0$-only wavefield obtained by Fourier Transform and (b): Wavenumber as a function of the direction at 200 kHz computed by the FDIW technique (solid line) and calculated by SAFE (dashed line)

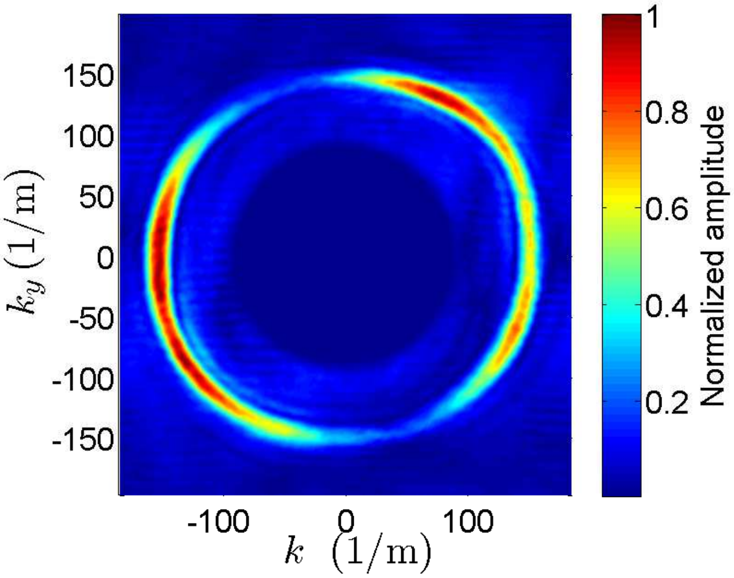

(a)

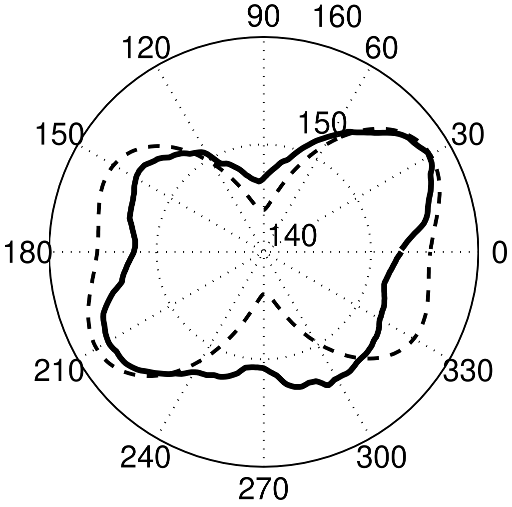

(b)

Figure 4.14: Glass fiber reinforced polymer specimen (a): Dispersion relations of the 200 kHz $A0$-only wavefield obtained by Fourier Transform and (b): Wavenumber as a function of the direction at 200 kHz computed by the FDIW technique (solid line) and calculated by SAFE (dashed line)

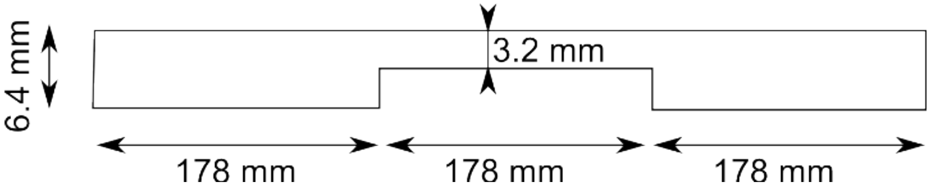

Figure 4.15: Schematic of the aluminum beam of varying thickness

FDIW could have been computed from the measurement of an annular region of space around the source while the FT requires to measure a dense and large regular grid of points.

4.6 Damage quantification results

This section aims at establishing the range of abilities, the functional limitations and the potential shortcomings of the FDIW technique. To this effect, diverse materials and structural defects are studied. Critical parameters for each dataset are presented and conclusions are drawn based on the results shown.

4.6.1 Aluminum beam with varying thickness

The ability of the FDIW technique to measure thickness through the ET metric is demonstrated. To this end, an aluminum beam of dimension 534 × 45 × 6.4 mm is studied experimentally. The beam is separated in three sections and the thickness of the middle section is reduced by a factor of two, as depicted in Figure 4.15. The resulting beam is a waveguide of varying thickness. A PZT transducer is placed at one end of the beam and excited by a four-cycle sine burst centered at 117 kHz. This frequency was selected by interrogating the specimen with a broadband excitation below the first cut-off frequency and selecting the frequency leading to the greater amplitude of excitation. The $A0$-only single frequency wavefield measured at the middle of the beam is displayed in Figure 4.16 where the coordinate y denotes the position along the length of the beam.

The FDIW calculation is then applied to the $A0$-only wavefield leading to the

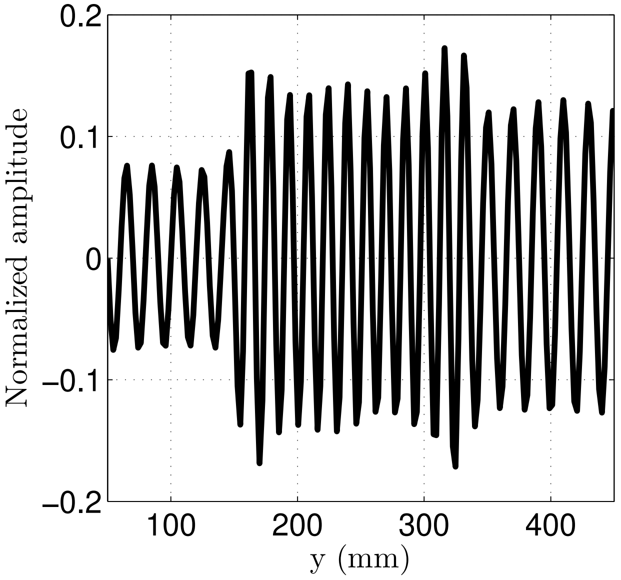

Figure 4.16: $A0$-only wavefield at 117 kHz at the middle of the beam

FDIW plot of Figure 4.17a. The three regions are clearly delimited by different wavenumbers in the FDIW plot, thus highlighting a change in the thickness of the structure. Using the computed aluminum wavenumber-thickness relationship, the FDIW plot is converted to the ET plot in Figure 4.17b to provide an estimate of the thickness of the beam at each point. The three regions of different thicknesses are clearly separated in the ET map and the value match the true thicknesses displayed by the red dashed lines in Figure 4.17b. The ET plot therefore measures the thickness of the beam with high fidelity in both regions.

4.6.2 Aluminum plate with notch

This section demonstrates that beyond its main application, the FDIW is also an effective tool to detect wavefield discontinuities with thickness reduction areas of nearly zero, as in the case of a crack or a thin notch. To this effect, a 10 mm wide, 2 mm long and 1.4 mm deep notch is created in a 2 mm thick aluminum plate. Lamb waves are generated by a PZT transducer bonded 150 mm away from the notch and recorded in a 124×72 mm^2 area discretized in 163×105 points centered on the

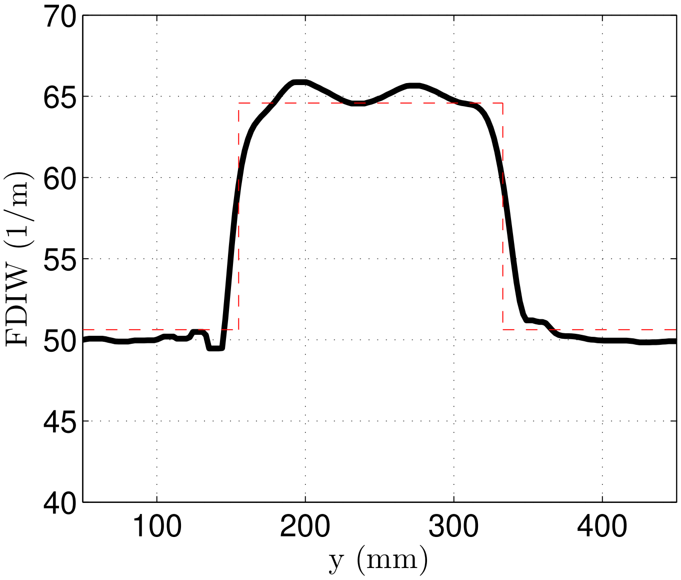

(a)

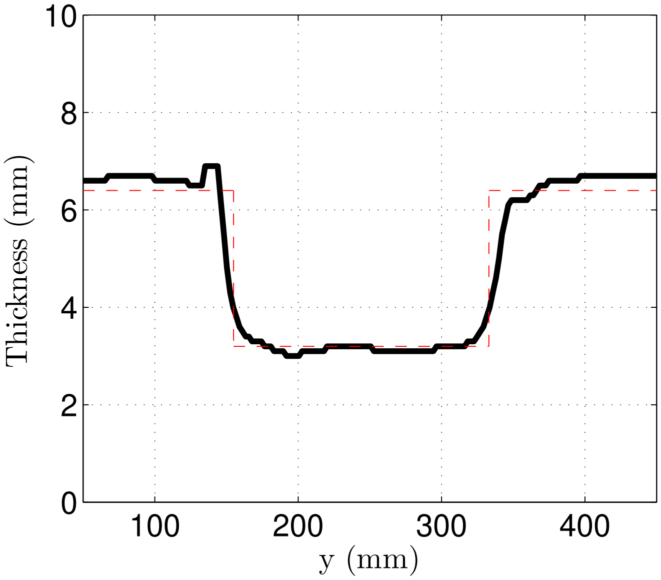

(b)

Figure 4.17: Aluminum beam of varying thickness (a): FDIW plot, red dashed lines: SAFE predictions and (b): ET map, red dashed lines: true thickness

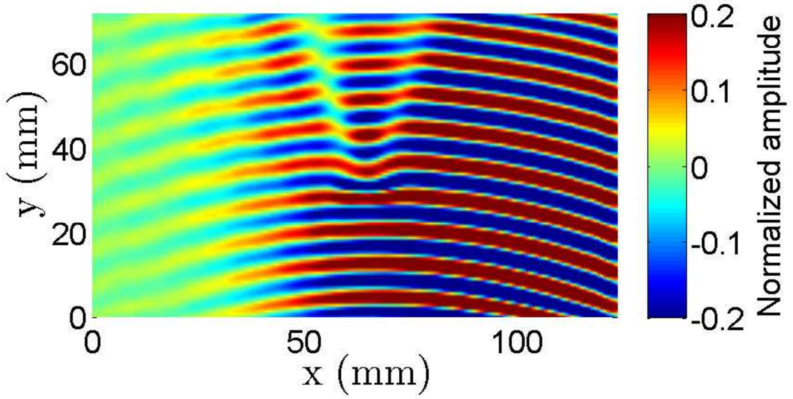

Figure 4.18: Single frequency $A0$-only wavefield

notch. The $A0$-only single frequency wavefield is displayed in Figure 4.18. Even though a change of wavenumber at the location of the notch is not directly visible to the naked eye, the wavepackets are clearly scattered by the notch as two *tails* in the wavefield are observed, characterized by phase discontinuities. The FDIW process is then applied to this wavefield leading to the map of Figure 4.19. There are three characteristic features in the FDIW standing out of the background wavenumber value. First, the notch is represented by a higher wavenumber in an ellipsoidal shape, roughly estimating the dimensions of the notch. The other two features are the two *tails* previously mentioned. These *tails* do not directly identify a defect location, but identify a discontinuity in the phase of the propagating wavepackets. In a more general case, these *tails* are always observed in the FDIW maps when a sharp discontinuity is present, hence lead to the location of the discontinuity by following the *tail* back to its origin.

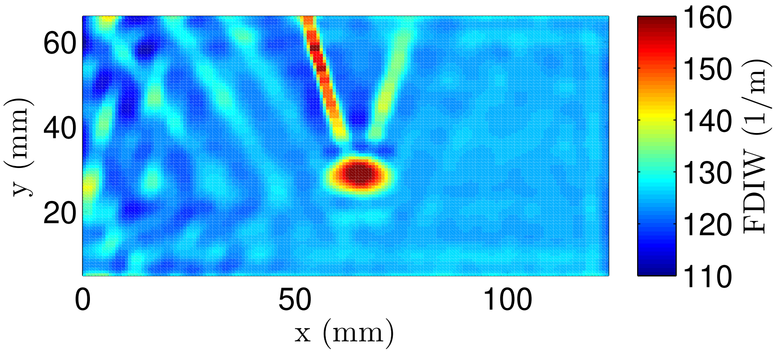

Figure 4.19: FDIW map of an aluminum plate with a notch

4.6.3 Carbon fiber plate with Teflon insert

For the sake of completeness, an anisotropic carbon fiber composite plate made of unidirectional layers of layup $[0^o, 90^o, 0^o, 90^o]_s$ is studied. Teflon inserts were inserted in the plate during the manufacturing. For this plate, Teflon objects with the shape of a peanut were inserted in between all the inner layers aligned with the direction of the fiber at the same location, leading to a single helix-shaped defect of about 20 mm diameter located 100 mm away from the center. A PZT transducer is bonded to the center of the plate and excited by a four-cycle tone burst of center frequency 200 kHz. The wavefield is recorded on a 102×100 mm^2 area discretized in 179×181 points around the defect. The $A0$-only wavefield is displayed in Figure 4.20a along with the corresponding FDIW map in Figure 4.20b. The values of the wavenumber different than the one in the background displayed in blue, show the spatial extend of the defect and an estimate its shape. In order to estimate the depth of the defect, it is necessary to use the wavenumber-ET relationship in the propagation direction (0^o with respect to the scanned layer) computed by SAFE and plotted in Figure 4.21a.

Note that, the vertical error bars in the wavenumber-ET plot show the ±5% FDIW accuracy limit quantified in Section 4.5. From this relationship, it can be seen that the FDIW map has difficulty differentiating some layers. In words, the FDIW may not differentiate properly the layers $6, 7, 8$, the layers $3, 4, 5$ and the layers $1, 2$, because the wavenumber corresponding to these sets of layers are too similar. Finally, the ET map obtained by the application of wavenumber-ET relationship to the FDIW map is shown in Figure 4.21b. Note that the orange and yellow areas, representing an ET value of 7 and 6 are likely undamaged but show a thickness reduction due to the indetermination of the wavenumber-ET relationship previously discussed. Moreover, at its deepest location, the measured ET value is equal to 2, which may also be equal to the ET value of 1 due to the wavenumber-ET indetermination.

4.7 Conclusions

This chapter illustrates the Frequency Domain Instantaneous Wavenumber (FDIW), a technique able to locally quantify the wavenumber of guided waves. Thus provides location and 2D mapping of any feature modifying the wavenumber of the propagating waves. These features may include a delamination, a thickness reduction or a notch. Using the physical properties of the studied specimen, the defect can be entirely mapped in three dimensions by using the Effective Thickness (ET) concept. Even though the full defect mapping is only possible if the defect has a non-zero area in order for the change of wavenumber to be measurable, the FDIW has also been shown to detect and locate notches by detecting phase discontinuities. Note that, it is necessary to know the dispersion relations of the specimen to obtain the three dimensional ET map, but it is not necessary to know the dispersion relations to obtain the two dimensional defect quantification provided by the FDIW map, which may be sufficient for some applications. Overall, the FDIW is an efficient and detailed defect quantification tool for composite inspection, fulfilling the first three objectives

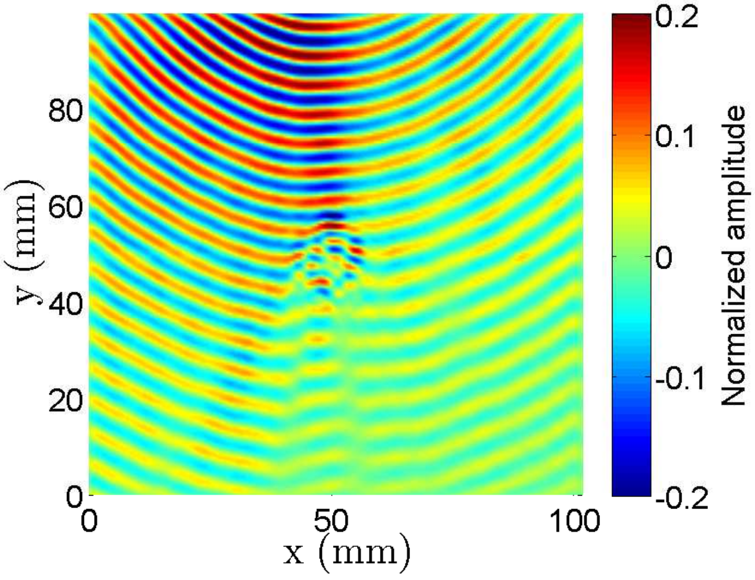

(a)

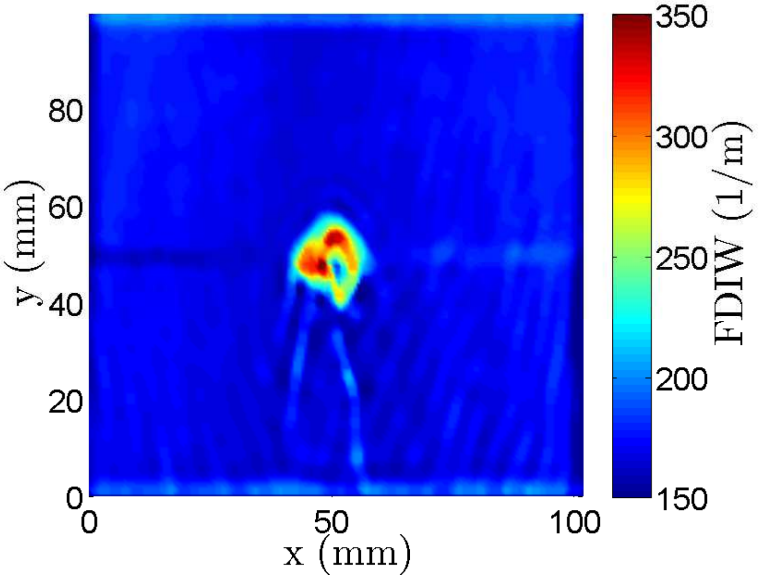

(b)

Figure 4.20: (a): Filtered $A0$-only single frequency wavefield and (b): corresponding wavenumber map

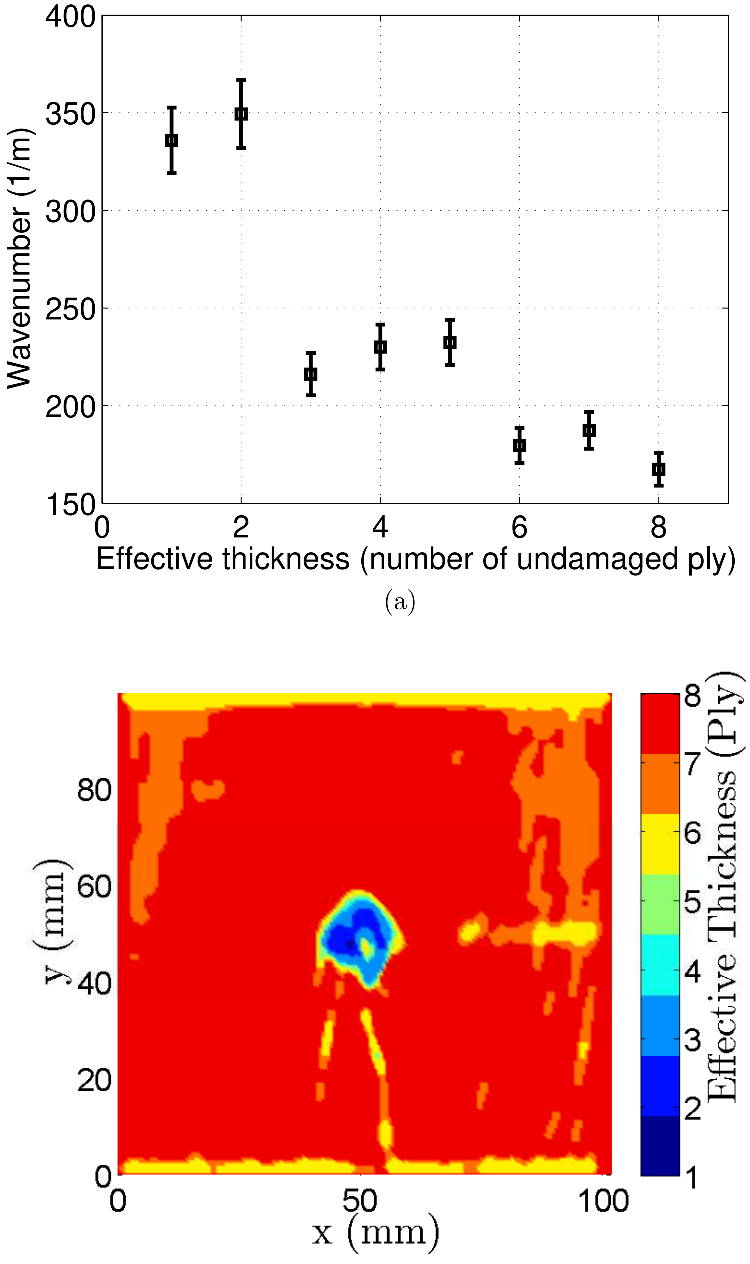

(a)

(b)

Figure 4.21: (a): Wavenumber in the direction 0^o at 200 kHz as a function of the number of undamaged layers and (b): ET map

described in Section 1.5. The following chapter will discuss an integration of the Sparse Wavefield Reconstruction (SWR) and the FDIW.

CHAPTER V

SWR AND FDIW INTEGRATION AND COMPARISON AGAINST NDE TECHNIQUES

5.1 Chapter overview

The SWR has the potential to detect and locate defects from sparse measurements on an entire structure regardless of its size while the FDIW fully maps defects. Even though these techniques are independent, it is natural to attempt to couple them in order to be able to fully quantify defects of unknown locations in large composite specimen. The approach developed in this chapter follows the multiple scans approach proposed in [138].

This chapter presents the integration of the FDIW and the SWR. The basic idea is to first identify the locations of the defects using sparse measurements and the SWR, followed by the application of the FDIW technique in the region of the detected defect with a steady state scan. The study considers realistic defects obtained through an impactor designed to induce impact-like defects in composites panels. NDE techniques, namely Pulse Thermography and Air-Coupled C-scan, are employed to validate the results obtained with the integrated approach.

Another goal to be pursued for increased practicability is to achieve full non-contact capabilities for both generation and detection of guided wavefields. Acquisition by the SLDV is a one-sided contact-free inspection methodology hence this objective is met for the acquisition. However, meeting these requirements for the actuation is less straightforward. So far, PZT disk transducers have been bonded to the surface of the interrogated specimen. Moreover, PZT transducers are excited at non-resonant frequencies, which leads to low excitation amplitudes and the requirement to add a reflective surface, typically a reflective tape, on the surface of the specimen in order to get better signal-to-noise ratios. The next sections discusses options considered to overcome some of these limitations by using a different type of transducer, as well as a proposed implementation of the integration of the FDIW and the SWR.

5.2 Guided waves generation through non-bonded transducers

Stacked PZT disks or power transducers have been introduced in Section 2.3.2. The main advantage of power transducers is the high excitation amplitude achievable. This leads to high signal-to-noise ratios without the need of a reflective coating on the specimen. Furthermore, it is possible to hold the power transducer magnetically on a specimen by inserting a steel set screw in the power transducer and holding it with a neodymium magnet on the other side of the specimen. This setup was initially described in [139] and later implemented in the context of this research. A schematic of the assembly is shown in Figure 5.1a. Shear gel is inserted between the power transducer and the specimen in order to ensure the quality of coupling between the transducer and the specimen. This setup however has the major drawback to require access on both sides of the specimen. The setup in Figure 5.1b is then proposed, in which the magnet is replaced by a simple support, preventing the transducer to fall due to gravity. It was found experimentally that there is no noticeable difference between the two setups in term of results quality because the shear gel ensure the coupling in both configurations. Note that the shear gel is nonabrasive fluid and is easily washable with water.

In order to validate the wave generation setup presented in Figures 5.1a and 5.1b, to find the resonant excitation frequencies and to compare the power transducer to single PZT disks, the following steps are followed: A power transducer tuned to resonate at 120 kHz, i.e., the resonant frequency provided by the manufacturer, is attached to a 2 mm thick aluminum plate using the setup shown in Figure 5.1a. A

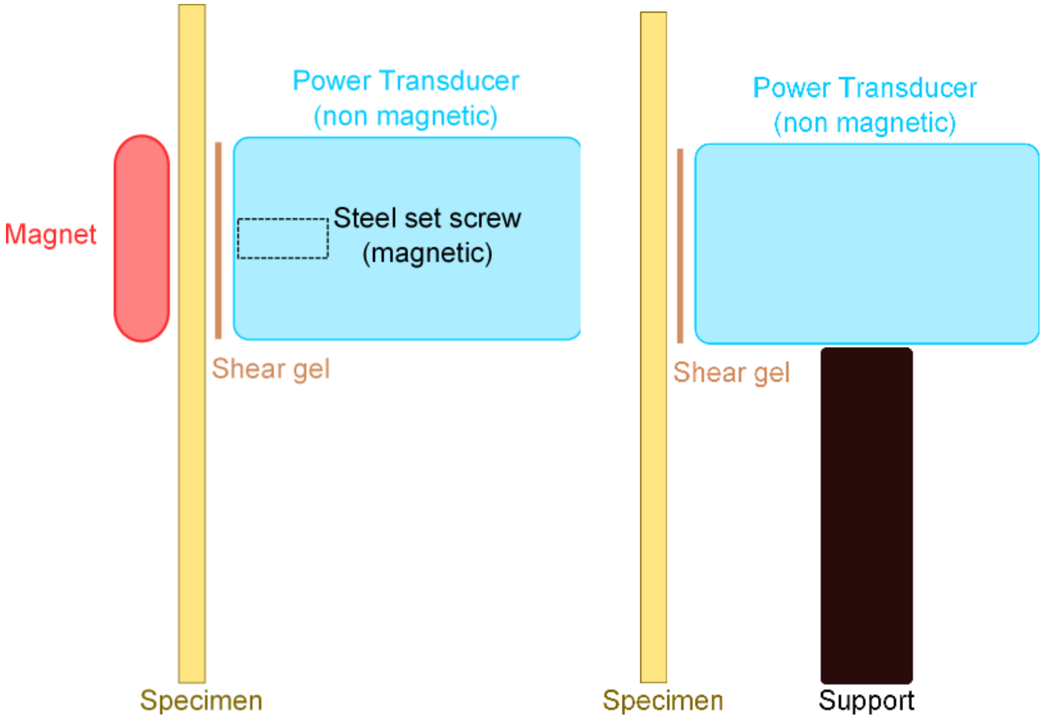

(a) (b)

Figure 5.1: Schematic of the assembly to hold the power transducer (a): magnetically and (b): with a support

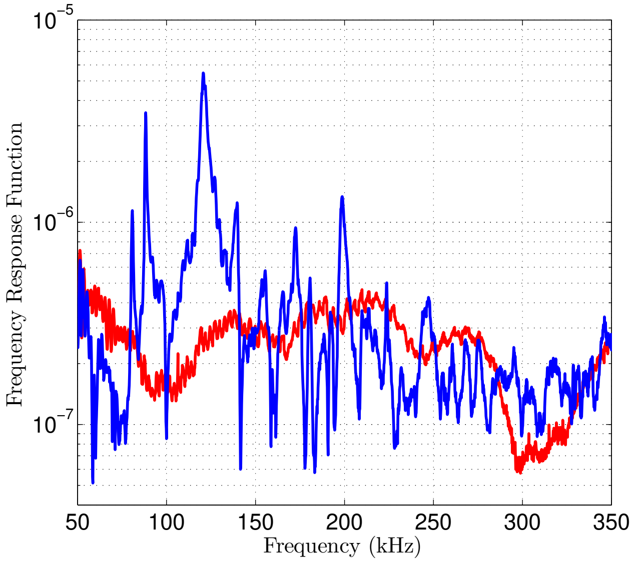

Figure 5.2: Frequency response functions of the power transducer (blue) and the single PZT disk (red) between 50 and 350 kHz

chirp function is then fed to the power transducer in order to inspect a broad frequency range. Guided waves are then measured at a distance of 50 mm from the power transducer, converted to the frequency domain and normalized by the Fourier transform of the excitation function in order to obtain the Frequency Response Function (FRF) of the entire assembly. The same process is repeated with a permanently bonded PZT disk of resonant frequency 3.4 MHz in order to compare the relative FRFs and the response amplitudes. The chirp function used to obtain the FRFs is between $f_0 = 50$ kHz and $f_1 = 350$ kHz, and $t_1 = 0.5$ ms is the duration of the chirp.

The FRF of a material point located 50 mm away from each transducer is displayed in Figure 5.2 as measured by the SLDV. Note that each FRF includes the unknowns transfer functions of all the elements used to generate, propagate and measure the guided waves: signal generator, amplifier, wires, transducer, specimen and SLDV. However the only parameter changing between the two experiments is the transducer, hence it is assumed that comparing these FRFs is an effective way to illustrate how these transducers excite the system. It is observed that the FRF of the single PZT disk (red line) is mostly flat in the inspected frequency range, which is expected since its resonant frequency of 3.4 MHz is far above the studied frequency range. The FRF of the power transducer however shows several resonances and antiresonances frequencies, which is expected as it is tuned to resonate at 120 kHz. For the frequency 122.5 kHz for example, the power transducer provides an excitation amplitude 12 times greater than the one of the PZT disk for the same input power. In addition to providing a greater excitation amplitude, the power transducer has the advantage of being able to handle more power. Indeed it was found experimentally that the PZT disks used for this research would heat up and eventually *blow up* when receiving more than 1 or 2 Watt of power while, according to the manufacturer, the power transducer is capable to handle up to 60 Watt, thus allowing much greater excitation amplitude.

5.3 Fast guided wavefield measurement

Even though the acquisition of a single point measurement is a nearly instantaneous process, a full wavefield acquisition is a relatively slow process due to the number of points to measure. The two techniques presented previously address differently the measurement duration constraint. With the SWR process, the number of points to measure is reduced and with the FDIW technique, acquisition is accelerated by measuring the steady state response of the specimen. However the measurement time is also limited by a physical limitation intrinsic to the SLDV used for this research: the number of measurements per second. This is directly related to the fact that the rotating mirrors orienting the Laser beam have non-negligible inertia. More specifically, the mirrors of the Polytech PSV-400 can only be displaced 30 times per second [29], hence the maximum measurement speed is 30 points per seconds. Any processing improvement requiring scans beyond this limit is non-valuable due to this equipment bottleneck. For example, for a typical fast Scan, i.e., a single frequency continuous scan as described in Section 4.3.2, each point only needs to be measured during approximately 100 μs. Furthermore, there is no waiting time requirement between each measurement, leading to the theoretical capability of fast scan to measure $10,000$ points per seconds. With the current experimental setup, limited at 30 point per second, the measurement time is about 300 times slower than what it could be with if the equipment could scan $10,000$ points per seconds.

A solution to overcome this limitation is to continuously move the test Laser beam in a given direction using continuously rotating mirrors, hence eliminating the stop-and-go problem related to the inertia of the mirrors. This solution is described and implemented in [139] where measurement capabilities of the order of $10,000$ points per seconds are demonstrated. Nevertheless, such system is limited to steady state scans only. The creation of a similar system was not possible in the context of this research.

5.4 Combination of the SWR and the FDIW

The most direct combination of the FDIW and the SWR techniques would be to apply the FDIW technique to a wavefield reconstructed on a dense grid using the SWR process, to conduct both the location and quantification in a single step. Unfortunately, the wavefield reconstructed by the SWR cannot be directly used by the FDIW. This is because the FDIW focuses on local wavenumber quantification while the SWR process attempts to reconstruct wavefields by constraining the wavenumber to a finite set of predefined values. Reconstructions are specifically achieved using the wavenumber values of the pristine specimen, hence applying the FDIW technique to a reconstructed wavefield will only reveal the wavenumbers that were used to reconstruct the wavefield. It is therefore required to acquire two distinct sets of measurements: the first will be used to locate the sources over a large area through the SWR process, while the second will be a refined scan in a reduced area to fully

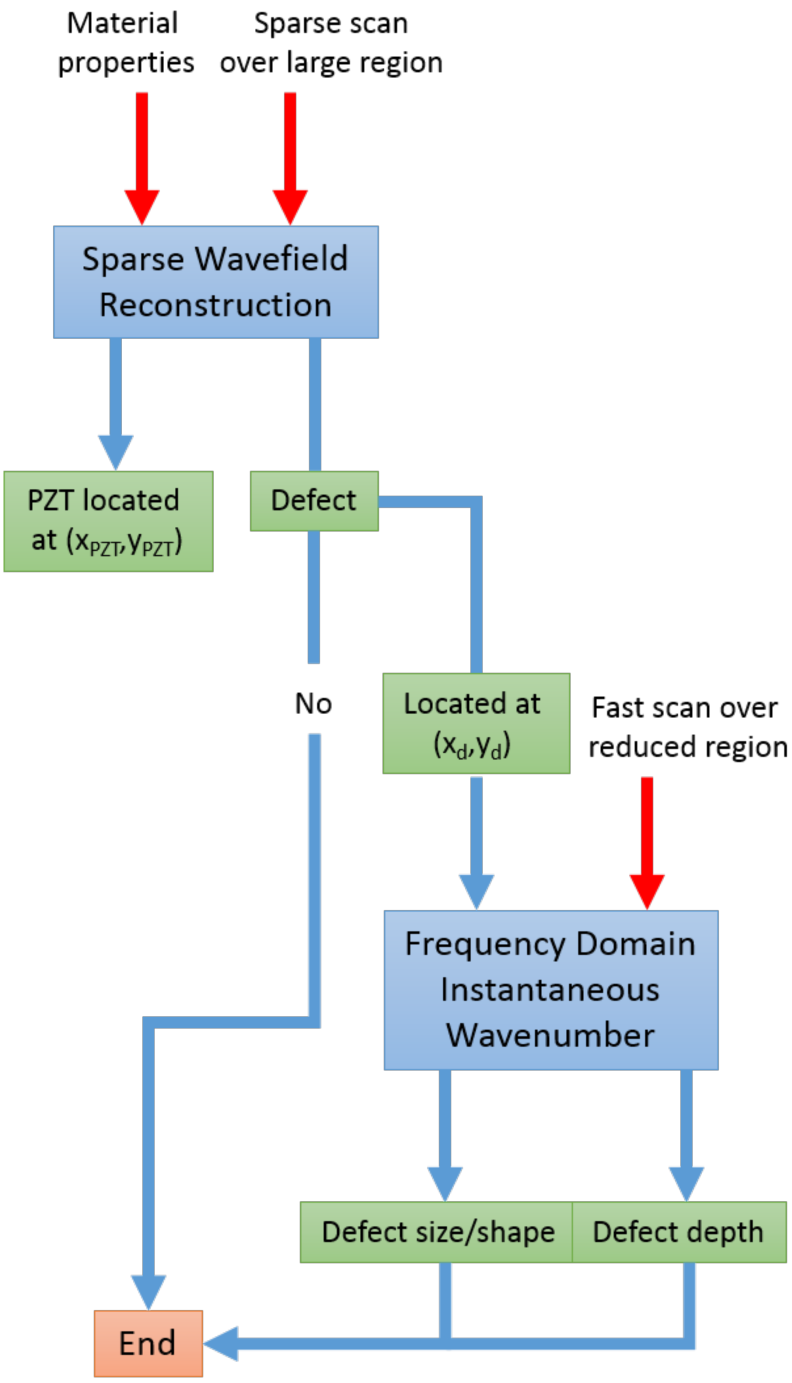

Figure 5.3: Proposed integration of SWR and FDIW

quantify the sources. A flow chart of this integration is shown in Figure 5.3. First, the sparse measurement distributed over a large region are fed to the SWR process. The results of this first step is the location of the transducer and of the potentials defects. If no defect is detected by the SWR, then the specimen is declared pristine. However if a defect is detected, its location is used to define a smaller region on which a fast scan is measured and is then fed to the FDIW technique. This second step has the potential to yield the location, size, shape and depth of the defect. The accuracy of these estimations could be further confirmed by follow-on NDE inspections. Some of these techniques are discussed in the next section along with some results.

5.5 NDE baseline defect imaging

This section presents the generation of impact defects in composites panels. Impact defects are necessary in order to study the application of the integration previously presented to realistic flaws. Thermography and C-scan by air coupled transducers are employed for the purpose of validation.

5.5.1 Creation of defects by weight drop

The impactor depicted in Figure 5.4 was designed especially for the purpose of creating delamination in composite materials. The impactor is made of a cylindrical steel mass of mass $m = 2.15$ kg, dropped from a customizable height $0 < H_{impactor} < 1.5$ m and guided by a PVC pipe. The PVC pipe is slightly larger than the mass to guide it with low friction. Air resistance on the mass is neglected in the energy calculation. The specimen is placed on a cardboard directly placed on the floor of the laboratory. The cardboard is used to allow local omni-directional deformation, which would be difficult to obtain on a rigid floor without promoting a specific direction for the defect creation. Once dropped, the flat bottom of the mass hits a steel sphere prior placed at the desired impact location. Different steel spheres can be used to customize the radius of the impact. For the results presented in this research, a steel sphere of 20

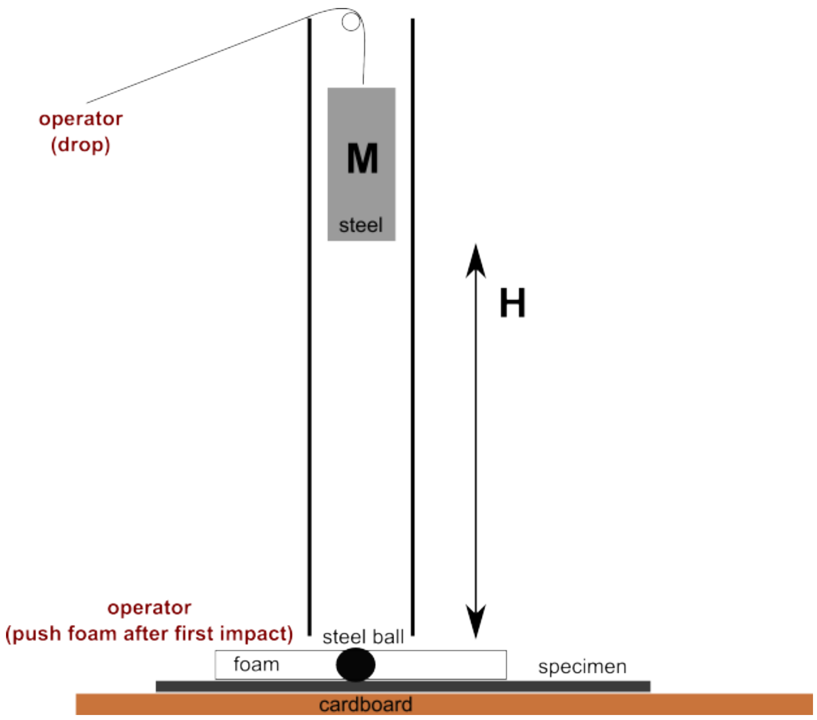

Figure 5.4: Schematic of the impactor used to create impacts in composite materials

mm diameter was used. The steel sphere is embedded in a foam fixture which serves two purposes: an operator holds the foam until the impact so that the steel sphere stays at the desire impact location. After the first impact, the mass bounces back and in order to prevent a second undesired impact, the operator quickly pushes the foam so that the mass falls on the foam and does not damage the specimen any further with a second impact.

Two identical Carbon-FiberReinforced Polymer (CFRP) panels of dimensions

Table 5.1: Properties of the CFRP panels used for impact defect creation

Properties	Unit	Value
Dimension	mm	$600 \times 600 \times 2.54$
Layup	n/a	$[0^o, 45^o, 90^o, -45^o]_s$
Density	kg/m^3	1568
E_1	GPa	137.137
$E_2 = E_3$	GPa	9.308
G_{23}	GPa	4.206
$G_{12} = G_{13}$	GPa	4.551
$\nu_{12} = \nu_{13} = \nu_{23}$	n/a	0.304

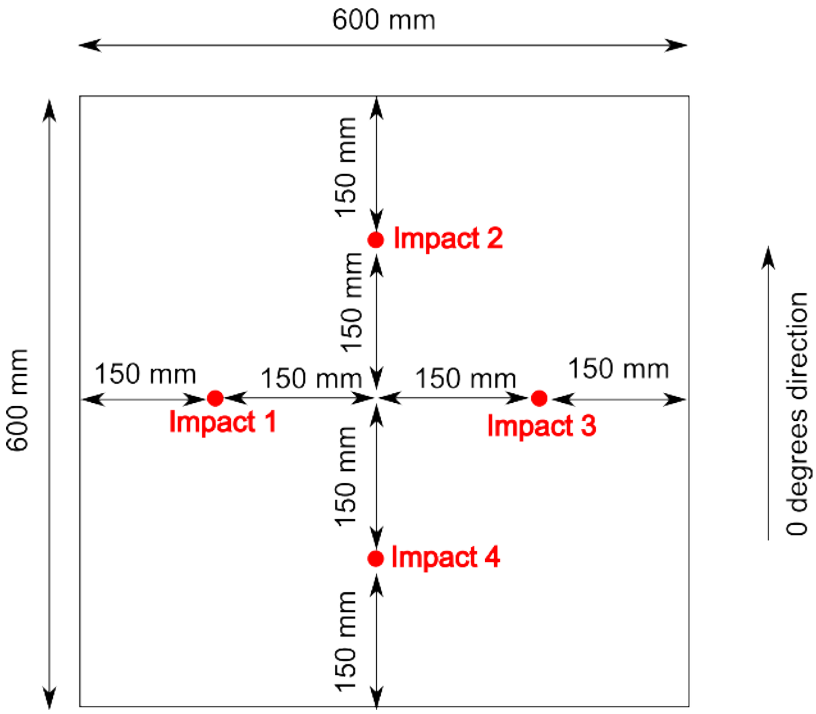

Figure 5.5: Locations of the impacts in the CFRP panels

$600 \times 600 \times 2.54$ mm and layup $[0^o, 45^o, 90^o, -45^o]_s$ were purchased to be impacted. The properties of the panels [140] are listed in Table 5.1. Four impacts of different energies were created in each of the two plates. The energy of the impact was controlled by the height of the impactor. Each impact point is located 150 mm away from the center of the plate in the four cardinal directions as depicted in Picture 5.5. Table 5.2 lists the different impact heights and the corresponding energies of impact. The eight resulting defects are barely visible to the naked eye and would be nearly impossible to detect by visual inspection. Figure 5.6 shows the back side of the panel (with respect to the impact side), for the defect of 25.7 Joules of energy.

5.5.2 Thermography

5.5.2.1 Introduction

Thermography, also known as *thermal imaging* or *infrared thermography*, is an infrared-based technique finding application in NDE [141, 142, 143]. An infrared camera is a device measuring the infrared wavelengths of the radiations emitted by a studied

Table 5.2: Heights and corresponding impact energy for the eight impacts

Plate	# Impact	Height (in)	Height (mm)	E_{impact}(J)
A	1	48	1219	25.7
	2	42	1067	22.5
	3	36	914	19.3
	4	30	762	16.1
B	1	12	305	6.4
	2	18	457	9.6
	3	24	610	12.9
	4	21	533	11.3

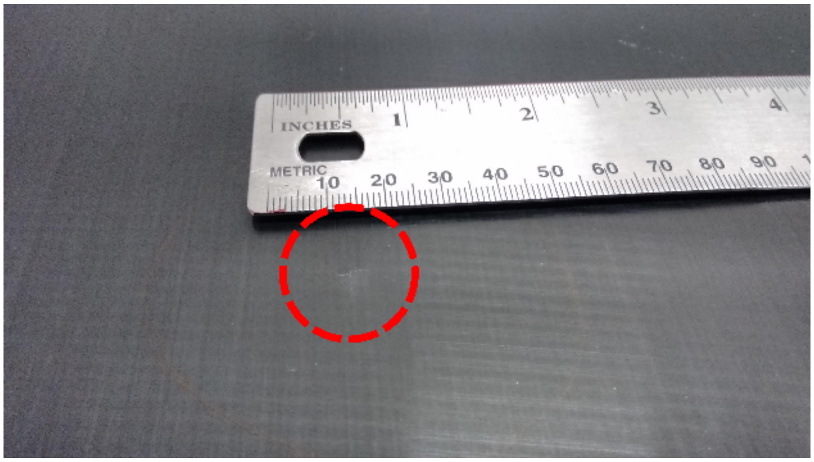

Figure 5.6: Photograph of the resulting surface impact on the back side with respect to the impact for the 25.7 Joules impact

body, which can be converted into an absolute temperature scale through calibration. The source of the temperature gradient separates thermography in two groups: active and passive thermography.

In passive thermography, the measured quantity is the temperature radiated from the body, with no external energy source. Passive thermography relies on the assumption that the region of interest has a different temperature than the background if an anomaly is present. For example, the temperature of any warm-blooded creature is not the same as the one of its surroundings, hence passive thermography finds direct application in the detection of humans or animals. In NDE however, passive thermography has a very limited range of application. Indeed, once created, most structural defects share the temperature of the surrounding structure and are therefore thermally invisible without an external energy input.

In active thermography, an external source illuminates the specimen. The temperature radiation is then recorded over time. The set of pictures corresponding to the time evolution of temperature in the inspected region is called a *thermogram*. Active thermography relies on the assumption that a disturbance would be present in the thermogram if an anomaly exists on or below the surface. The disturbance in the thermogram locates a discontinuity in the thermal conductivity of the specimen, which may be due to an inserted object or locally broken material, such as broken fibers in composites.

Active thermography can be divided into four subcategories: Pulse Thermography (PT), Step-Heating Thermography (SHT), Lock-in Thermography (LT) and VibroThermography (VT). The first three techniques typically use a lamp to heat a specimen during some duration of time and record the evolution of the temperature during and/or after heating. The heating functions are (a) a short pulse for PT, (b) a heavy-side function for SHT and (c) an harmonic function for LT. Figure 5.7 is a schematic of the typical setup used for these three techniques. In VT however,

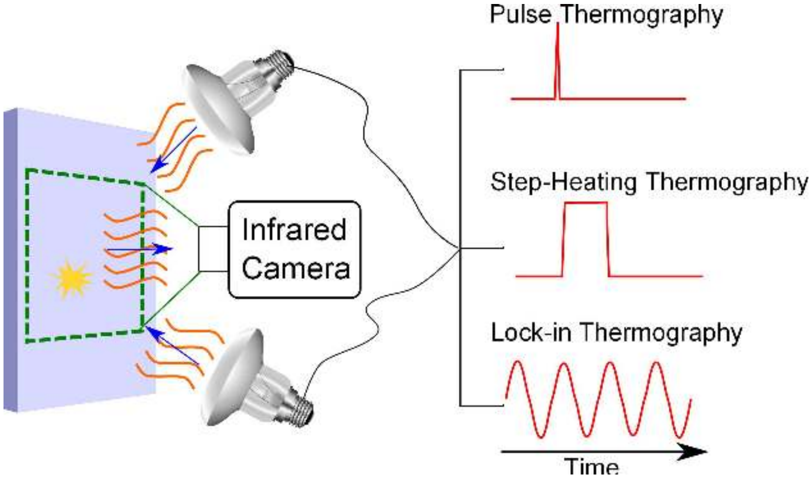

Figure 5.7: Active Thermography

flexural waves are generated by periodically flexing the specimen. The flexural energy is then converted to heat by friction in the specimen at the defects locations, thus highlighting defects such as cracks. Each of this four techniques has major advantages and drawbacks, however, only PT, which is better suited for the desired application, will be presented here.

5.5.2.2 *Pulse Thermography*

Pulse Thermography is characterized by the emission of a very short pulse of energy towards the region of inspection followed by the recording of the temperature radiation resulting of this pulse [144]. Pulse Thermography is effective at detecting and quantifying the depth of flat-bottom holes [145, 146, 147, 148, 149]. Pulse Thermography has even shown the ability to quantify the depths of impact defects in composites [150]. The main limitation of PT is the limited quantity of heat energy penetrating the specimen, leading to a limited ability of PT to detect deep defects, especially in materials with low thermal conductivity. A common practice in PT is therefore to use a very powerful flash light releasing as much energy as possible in a single pulse, and in an homogeneous manner over the region of inspection [151]. For this research, the infrared camera used is a FLIR ThermoVision SC6000 Series, with the ability to acquire up to 126 frames of 640 × 512 points per second, from 0.4 to 9 μm on the electromagnetic spectrum. The flash is emitted by two flash lamp of 1 kJ each and during 10 ms.

The following development presents the equations used to quantify depth of defects using PT [152, 153]. Let us consider the heating of a semi-infinite plate. The evolution of the temperature obeys the unidimensional diffusion equation:

$$\frac{\partial^2 T(z,t)}{\partial z^2} - \frac{1}{\alpha}\frac{\partial T(z,t)}{\partial t} = 0 \tag{5.1}$$

where $T(z,t)$ denotes the temperature, z the spatial variable along the thickness dimension, t denotes the time variable and α denotes the thermal diffusivity of the specimen. The thermal diffusivity α is given by:

$$\alpha = \frac{\epsilon^2}{\rho^2 c^2} \tag{5.2}$$

where q is the energy of the flash pulse per unit area, ϵ is the thermal effusivity and c is the heat capacity per mass. The solution of Equation (5.1) at the surface ($z = 0$) for a semi-infinite sample is:

$$T(z=0,t) = T_0 + \frac{q}{\epsilon\sqrt{(\pi t)}} \tag{5.3}$$

where $T_0 = T(z=0,0)$ is the room temperature before the experiment.

Let ΔT be the difference of the surface temperature with respect to the initial room temperature:

$$\Delta T(t) = T(z=0,t) - T_0 = \frac{q}{\epsilon\sqrt{\pi t}} \tag{5.4}$$

It can now be observed that, in the logarithmic domain, the evolution of the surface temperature evolves linearly:

$$log\left(\Delta T(t)\right) = C - 0.5 log(t) \tag{5.5}$$

where $C = \frac{q}{\epsilon\sqrt{\pi}}$ is a constant.

Therefore in the logarithmic domain, the evolution of the surface temperature evolves linearly, as long as the studied object can be considered semi-infinite, i.e., before the arrival of the first reflection of the heat wave. For a sample of finite depth, the end of the linear regime, called *break time* and denoted t_b, is the instant at which, from a surface measurement perspective, the sample is not semi-infinite. In words, this is the time instant at which the first reflection of the heat diffusion is observable on the surface of the specimen. It was proven in [154] that t_b could be related to the distance from the measurement surface to the object reflecting the heat energy by:

$$\Delta T(t_b) = \frac{q}{\epsilon\sqrt{\pi t}} = \frac{q}{\rho c \times depth} \tag{5.6}$$

where ρ and c are the density and the heat capacity per mass of the specimen, respectively, and *depth* is the distance of the feature reflecting the heat, with respect to the measurement surface. Note that in this equation it is assumed that the object reflecting the heat energy is an adiabatically isolated wall. The combination of Equation (5.2) and Equation (5.6) provides the expression of the depth:

$$depth = \sqrt{t_b \pi \alpha} \tag{5.7}$$

In practice, the scalar *depth* can be computed at every point and represent the distance between the scanned surface and the depth of the main feature reflecting the heat energy, which could either be the back wall of the plate or an internal defect. In this equation, the parameter t_b can be measured experimentally as the first time instant the slope of ΔT is greater than -0.5 in the logarithmic domain, according to Equation (5.5).

The thermal diffusivity α, can be measured experimentally by measuring the *depth* parameter in a pristine region of the specimen which must be equal to the thickness of the specimen as the reflecting feature is the back wall of the specimen. For the CFRP

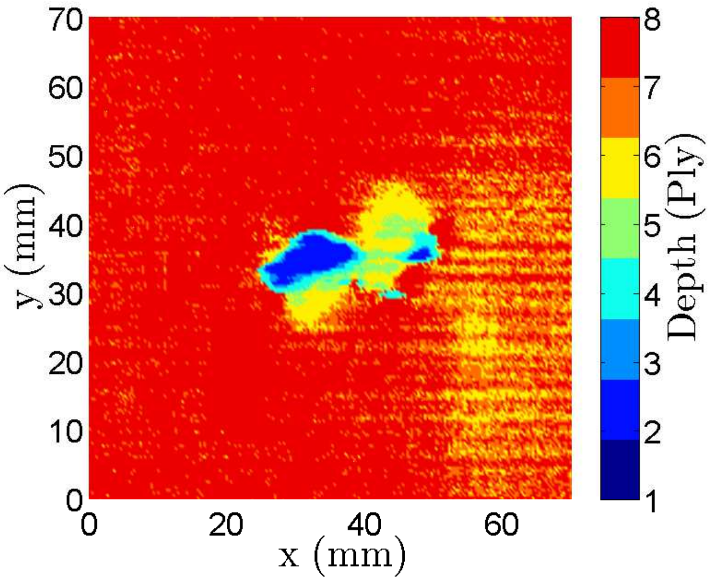

Figure 5.8: Mapping of the 25.7 J impact defect by Pulse Thermography

composites studied in this section, $\alpha = 11.5 \times 10^{-6}$ m^2/s was measured, which is coherent with typical values of thermal diffusivity for carbon fiber specimens [155, 156]. Note that there exist other techniques for depth retrieval from pulse thermography such pulsed phase thermography [157, 158, 159, 160, 161] but require more advanced signal processing and for this reason are not reported herein.

5.5.2.3 Example

For illustration purposes, PT in applied to the defect created by the impact of 25.7 J energy. The evolution of the temperature is recorded on a 204×163 mm area during 2 seconds after the flash. After extraction of the *break time* at each point, the depth plot of Figure 5.8 is obtained. Note that the depth values have been converted to the number of undamaged layer in order to compare it more readily to the FDIW results. In Figure 5.8, beside the pristine regions, two major depths are observed. The first depth of 2 (blue) corresponds to a defect seemingly located between the 2^{nd} and the 3^{rd} layer, and is mainly horizontal, which correspond to the direction 0^o in this picture (the 90^o direction being vertical in this picture). The second depth is between the 5^{th} and 6^{th} layers and is oriented in the direction +45. Because the layup of the plate is $[0, 45, 90, -45, -45, 90, 45, 0]$, it can be observed that the defect is extended mainly across the fiber directions. It is important to highlight that since this depth quantification relies on the measure of a change of slope and on the assumption that the reflecting feature presents an adiabatic surface, some features may not be seen by this process, especially smoother discontinuities (i.e., partially broken lamina). Hence it is expected that the discontinuities resulting of the lower energy impacts may not be visible using this technique. Moreover, the superposition of several discontinuities at a single point cannot be interpreted with this technique.

5.5.3 Air coupled Cscan

5.5.3.1 Introduction

In addition to thermographic imaging, air coupled transducer are used to generate 2D reference maps of the impact defects. The setup and the air coupled transducer equipment presented in this section belong to the QUEST laboratory at Georgia Tech. The schematic of the setup is displayed in Figure 5.9. The setup consists of two air coupled transducers located on either side of the inspected specimen. The transmitter (AS400TI by QMI INC) emits a predefined harmonic signal while the receiver (AS400ARI by QMI INC) measures the signal transmitted through the specimen in the form of displacement. This setup relies on the assumption that the transmitted signal will be somewhat different between a pristine and a damaged region of a specimen [162]. The transducers are essentially membranes vibrating in the ultrasonic range and are similar to regular speakers. The distance from the transducers to the specimen is equal to their focal distances, provided by the manufacturer, so that the area of effect of each transducer is close to a single point.

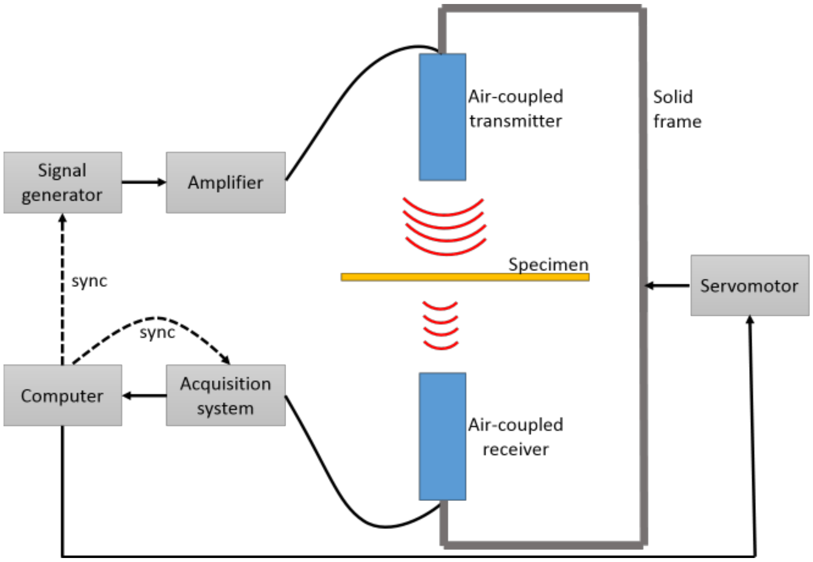

Figure 5.9: Schematic of the air-coupled C-scan measurement setup

5.5.3.2 Example

This setup is now applied to the 25.7 J impact. For each point-measurement, a sine sweep from 50 to 500 kHz is generated and amplified before being sent to the transmitter. The transmitter then excites the plate locally while the receiver measures the transmitted displacement on the other side of the plate. An acquisition system then sends the measurement sampled at 20 MHz to a computer. In addition to handling the synchronization of all the devices, the computers controls the position of the transducer pair, allowed to move in a 2D plane at a fixed distance from the plate at a speed of 50 mm/s. One measurement is taken every 0.76 mm in a 76×76 mm^2 region. The duration of the measurement at each point is from 200 to 900 μs with respect to the beginning of the frequency sweep. The total measurement time is of the order of a few minutes. The root mean square of the transmitted signal over the frequency range is displayed in Figure 5.10.

This C-scan shows that the transmitted energy decreases of several decibels over

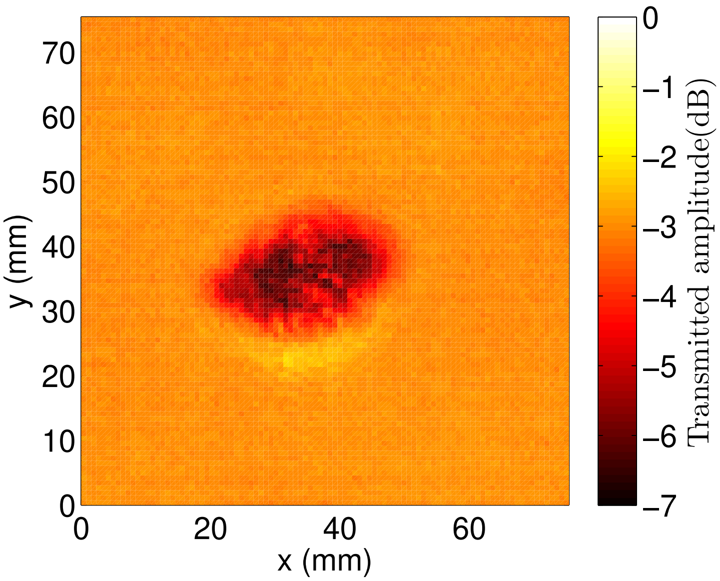

Figure 5.10: Root mean square of the transmitted energy between 50 to 500 kHz through the 25.7 Joules impact

the defect and provides the overall shape and dimensions of the delamination, matching the dimensions and the overall shape of the damage measured by Pulse Thermography in the previous section.

5.6 Application of the integrated approach

This section illustrates the application of the technique shown in Figure 5.3. The goal is to compare the results to C-scan and PT in order to characterize the accuracy of the proposed process when applied to the eight impacts described in previous sections.

5.6.1 Defect detection and localization by SWR

First, a wavefield is measured on plate A (plate with the four impacts of greater energy) over a region including a PZT disk transducer bonded at the center of the plate and the four impact defects. The area is a rectangle of 401×391 mm^2 discretized in $137 \times 141 = 19,317$ points. The surface is not covered with reflective tape, therefore a low signal-to-noise ratio of the measurements is expected. The transducer is excited by 4-cycle tone burst of center frequency equal to 100 kHz. Each point measurement is averaged 10 times. Two snapshots of the wavefield are shown in Figures 5.11a and 5.11b. As visible in these pictures, the signal-to-noise ratio is very low, especially in the lower part of the scanned region. The noise is not constant throughout the region of inspection, which is due to the fact that the amplitude of the measured signal depends on the quality of the reflection of the SLDV Laser beam on the plate, which is a function of the angle between the test beam and the plate. The dispersion relations at 100 kHz, obtained by the application of a Fourier transform, are shown in Figure 5.12. In this picture, the dashed lines represent the wavenumbers used for the reconstruction, derived from SAFE predictions. Note that the $S0$ mode (mode of lower wavenumber) is barely visible in the measurements but nevertheless is used in the reconstruction. Wavefield reconstruction is then conducted with the set of parameters $[M, N_\sigma, N_\lambda] = [5000, 10, 2]$ within the frequency range 50 to 150 kHz. The estimated active sources map for the $A0$ and $S0$ modes are shown in Figure 5.13a and Figure 5.13b respectively.

The transducer, located at the center, is properly located by both modes. Furthermore, the four impact regions are clearly visible in both pictures, which means that even the $S0$ mode that has been barely measured, has the ability to locate the defects. It must be noticed, however, that the $A0$ active source map is very noisy, especially in the North-East and North-West directions. This is mainly due to both wavenumber mismatch in these directions and measurement noise. It is however possible to avoid the false alarms by combining the information from both maps, thus efficiently locating the four impact defects. This results demonstrates both the ability of the SWR process to work with low signal-to-noise ratio data (no reflective tape on the surface) and to detect multiple impact defects.

The same parameters are used to measure and locate the defects using the SWR on plate B (plate with the four impact of lower energy). Two snapshots of the wavefields are visible in Figures 5.14a and 5.14b. Note that, unlike with plate A, the interaction

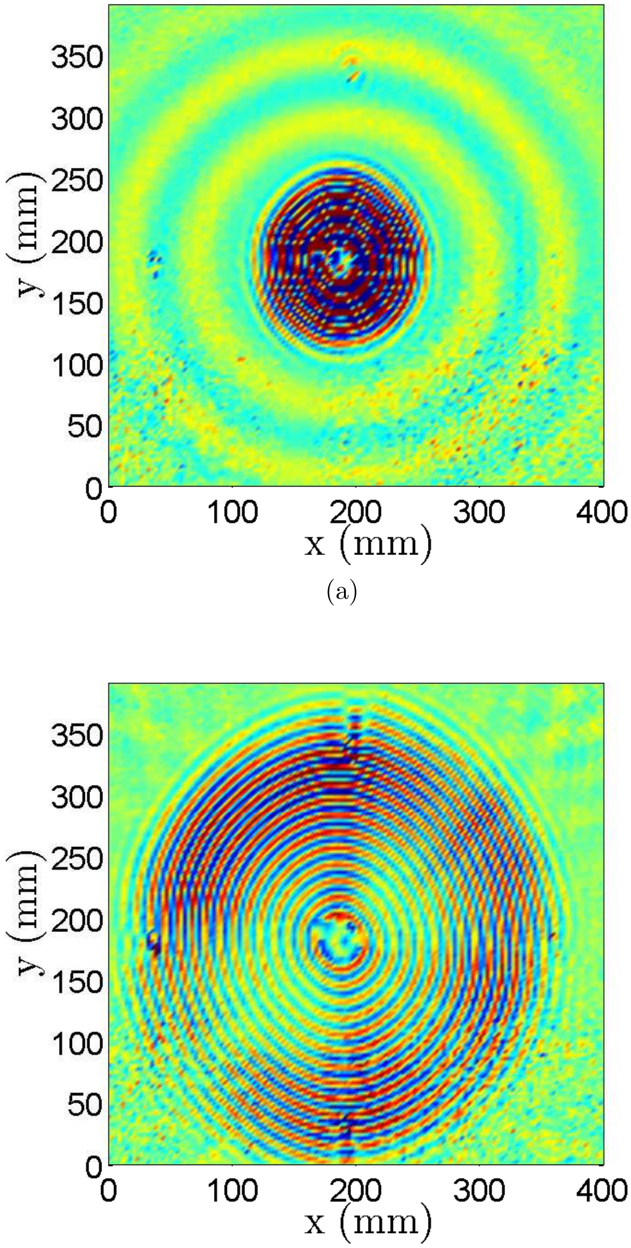

(a)

(b)

Figure 5.11: Snapshots of the wavefield in plate A representing a 4-cycle 100 kHz tone burst interacting with four impact defects (a): at $t = 78$ μs and (b): at $t = 156$ μs

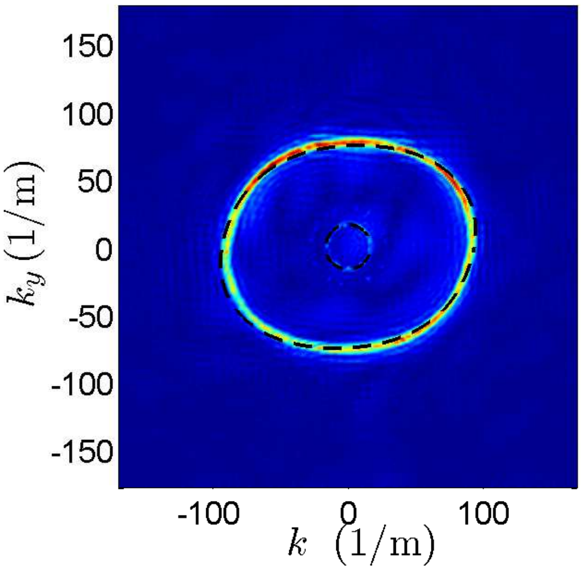

Figure 5.12: Measured dispersion relations on plate A at 100 kHz (dashed lines: SAFE predictions)

of the wavepackets with the defects are not visible in these snapshots, meaning that it is unlikely that the SWR will succeed to locate the defects.

The results of the reconstruction conducted with the parameters $[M, N_\sigma, N_\lambda] = [5000, 10, 2]$ within the frequency range 50 to 150 kHz shown in Figure 5.15a for mode $A0$ and in Figure 5.15b for mode $S0$. As visible in the active sources maps of Figure 5.15, the SWR fails to locate the four impacts of lower energy with both modes.

5.6.2 Defect quantification by FDIW

Next, the FDIW process is applied. The case of the 25.7 J impact is presented here first. A fast scan is measured over the region of the detected defects provided by the SWR process in the preceding section for the 25.7 J impact. The guided wave excitation is a continuous sine function at 122 kHz generated by a power transducer tuned to resonate at this frequency and placed 10 mm away from each impact. Note that because it is allowed by the experimental setup of Figure 5.1b, the position of the power transducer is customized for each defect to ensure proper illumination. There is still no reflective coating on the surface of the specimen. The $A0$ wavenumber -

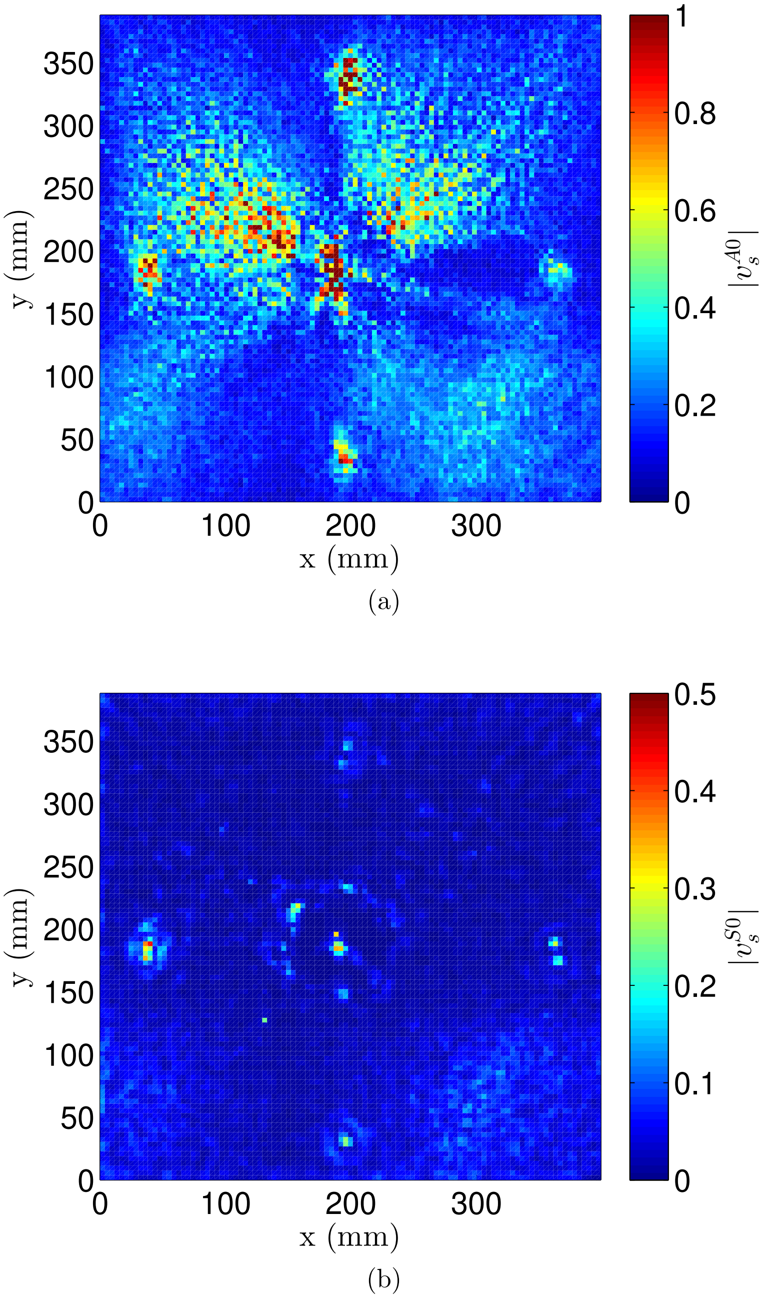

Figure 5.13: Sparse representation of the wavefield on plate A with the set of parameters $[M, N_\sigma, N_\lambda] = [5000, 10, 2]$ (a): $A0$ sources ($|\ \widehat{v}_s^{A0}\ |$) (b): $S0$ sources ($|\ \widehat{v}_s^{S0}\ |$)

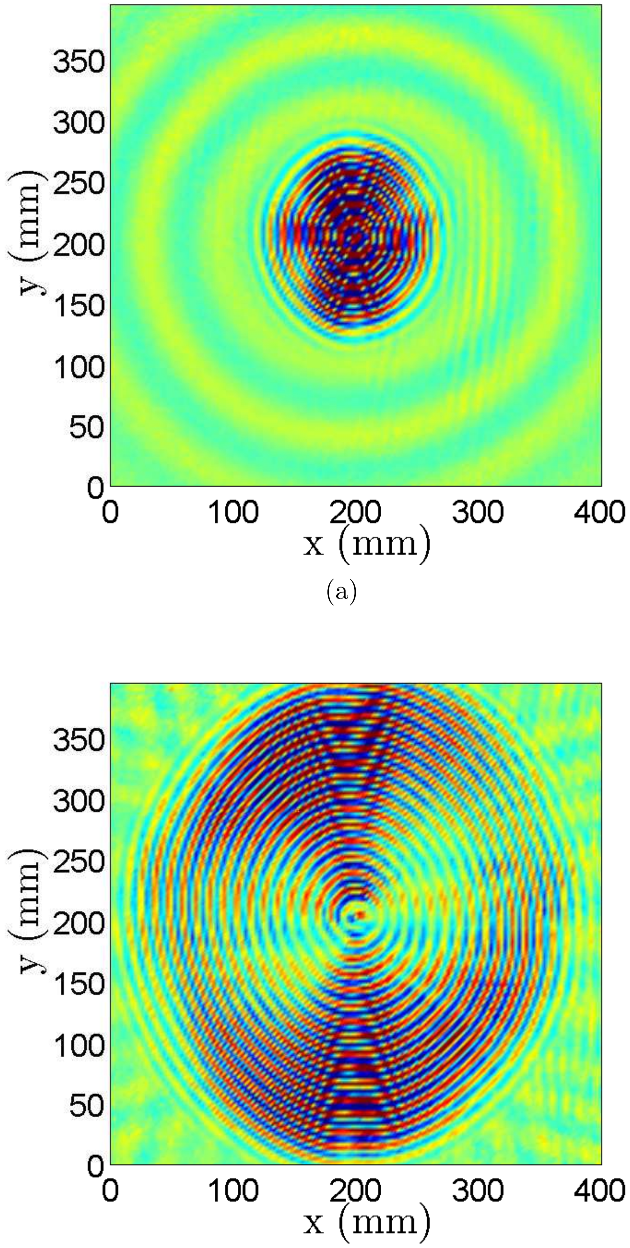

(a)

(b)

Figure 5.14: Snapshots of the wavefield in plate B representing a 4-cycle 100 kHz tone burst interacting with four impact defects (a): at $t = 78$ μs and (b): at $t = 156$ μs

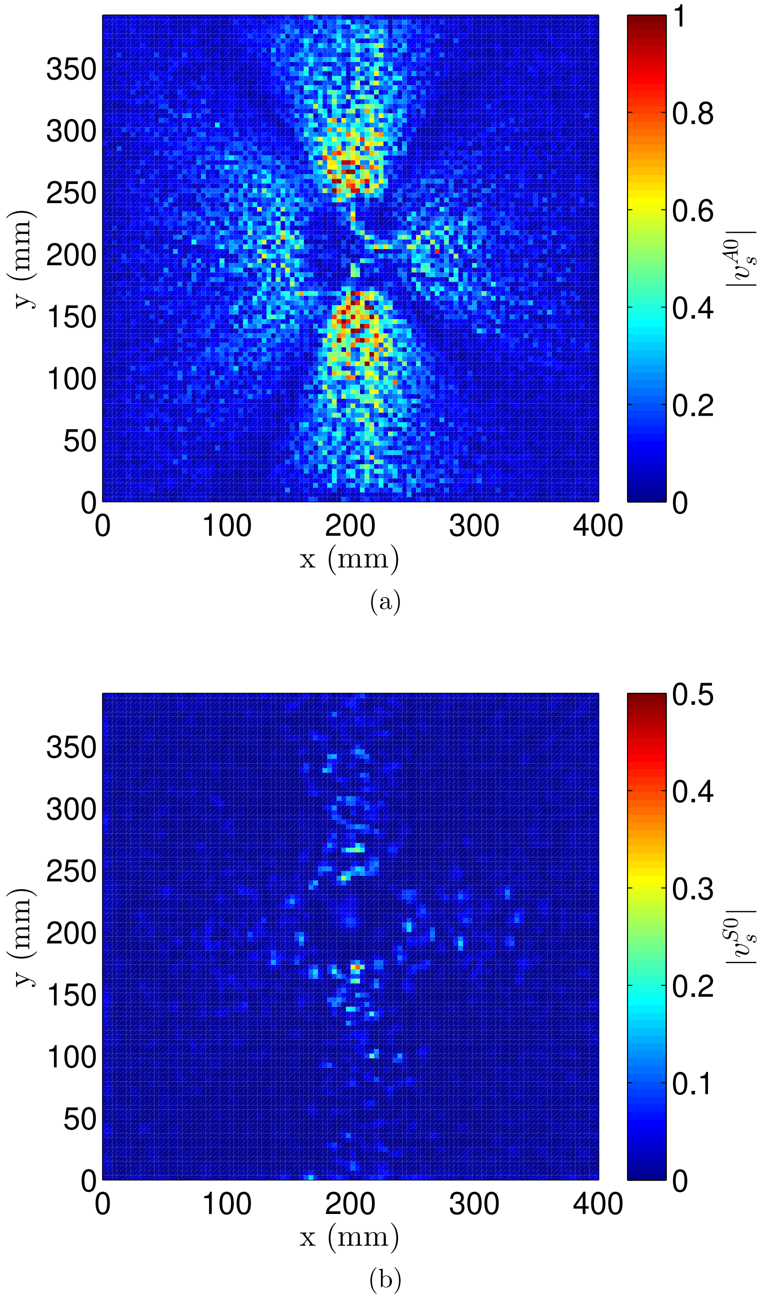

(a)

(b)

Figure 5.15: Sparse representation of the wavefield on plate B with the set of parameters $[M, N_\sigma, N_\lambda] = [5000, 10, 2]$ (a): $A0$ sources $(\mid \widehat{v}_s^{A0} \mid)$ (b): $S0$ sources $(\mid \widehat{v}_s^{S0} \mid)$

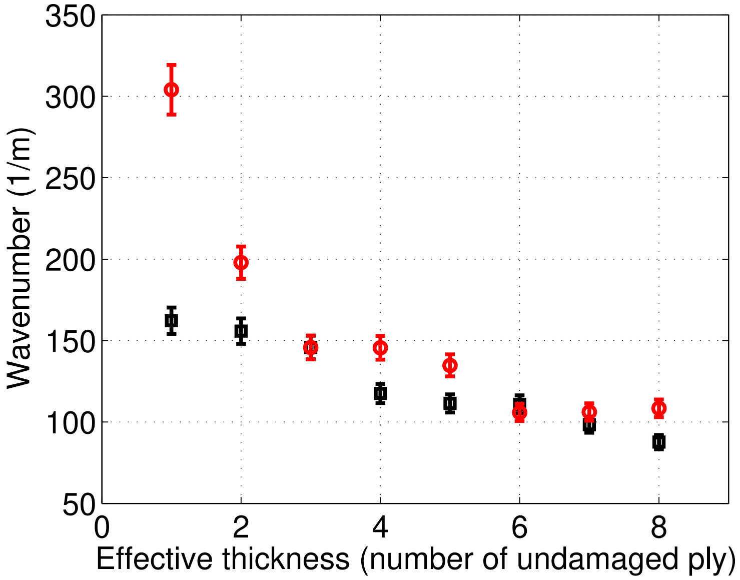

Figure 5.16: Wavenumber and error bars of ±5% of the $A0$ mode at 122 kHz in the CFRP specimen as a function of the Effective Thickness (black squares: direction 0^o, red circles: direction 90^o)

Effective Thickness relationship of the CFRP specimen is plotted in Figure 5.16 in which the black squares represent the evolution of the wavenumber in the direction 0^o and the red circles in the direction 90^o. In addition, error bars shown correspond to the ±5% accuracy of the FDIW technique established in Section 4.5. These error bars show that for some values of the wavenumber, it is not possible to determine precisely the number of undamaged layers. More specifically according to this plot, it is not possible to differentiate the wavenumber for the group of layers $[1, 2, 3]$, $[4, 5, 6]$ and $[7, 8]$ in the direction 0^0 (black square) and between the layers $[3, 4, 5]$ and $[6, 7, 8]$ in the direction 90^o (red circles). Note that this indetermination is an intrinsic property of the specimen and of the accuracy of the technique. Because of this indetermination, the groups of layers previously stated are considered indistinguishable during the conversion of the FDIW map to the ET map.

The FDIW map of the $A0$-only wavefield measured in the region of the 25.7 Joules impact defect and illuminated from the North direction, is shown in Figure

5.17a and then converted into the ET map in Figure 5.17b. In addition to the apparent ellipsoidal shape of the defect that was already observed in both the Pulse thermography (Figure 5.8) and the C-scan (Figure 5.10), three *tails* are observed in both of these plots. As explained in Section 4.6.2, these *tails* are due to a discontinuity of the phase induced by the scattering of the wave, and as expected, are located on the opposite direction of the main source. To ensure that the *tails* observed in Figure 5.17b are not material defects, the same experiment is conducted by placing the power transducer West with respect to the impact location in order to obtain the FDIW map in Figure 5.18a and the ET map of Figure 5.18b of the defect illuminated from the West. Two new *tails* are visible in the ET map illuminated from the West while the three previously described *tails* have disappeared. This proves that the defect is only the ellipsoidal shape visible at the center of both ET maps. Moreover, the indetermination of the layer is not the same in both plots since the direction of the illumination differs. Combining the information from both ET maps, it is concluded that the impact defect is an ellipsoidal delamination between the second and the third layer.

Results of the application of the integrated approach to the remaining seven impacts are discussed next along with comparisons results obtained with Pulse Thermography and air-coupled transmitted C-scan. The application of the SWR successfully located the four defects in plate A (see Figure 5.13). The result of the application of the FDIW process for the 25.7 J impact is shown in Figure 5.19b (same picture as Figure 5.17b, replicated here for comparison), the 22.5 J impact in Figure 5.20b, the 19.3 J impact in Figure 5.21b and the 16.1 J impact in Figure 5.22b. For all these cases, the transducer is located 100 mm away from the impact location in the North direction. Overall for these four impacts, the delamination shape obtained by the FDIW technique matches the one provided by the C-scan but hardly matches the PT results. This is explained by the fact that the PT technique measures changes in the

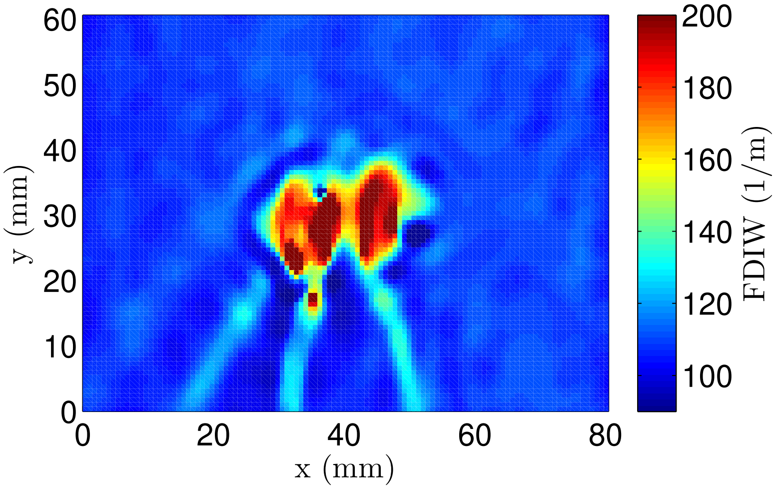

(a)

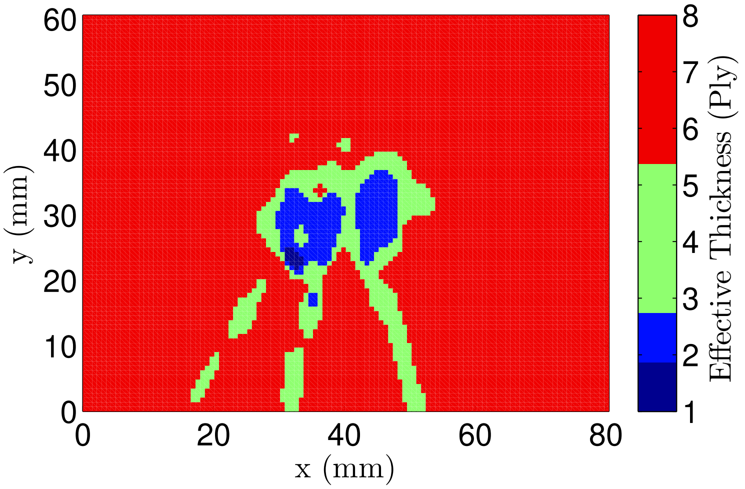

(b)

Figure 5.17: Result for the 25.7 J impact defect illuminated from the North (a): FDIW map and (b): ET map

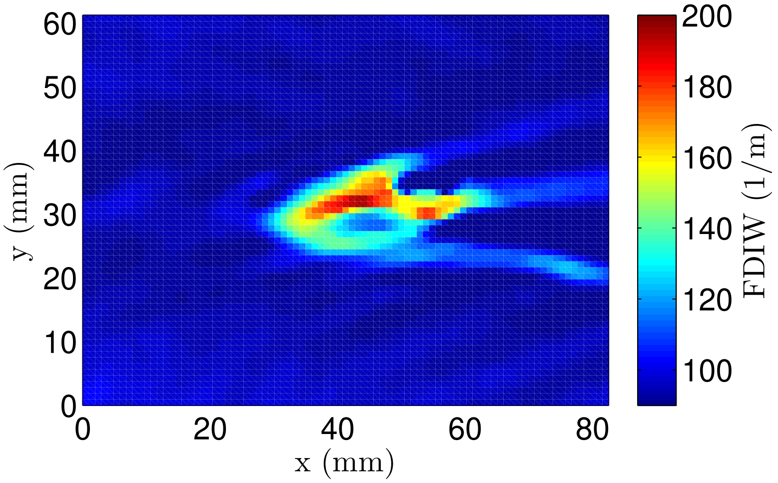

(a)

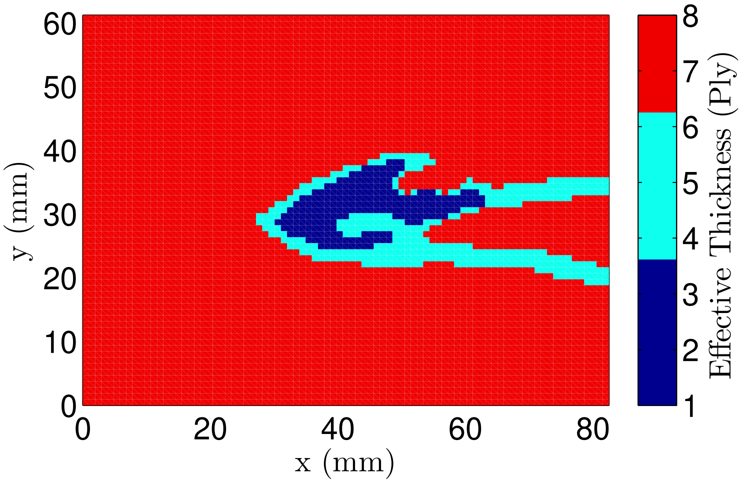

(b)

Figure 5.18: Result for the 25.7 J impact defect illuminated from the West (a): FDIW map and (b): ET map

thermal diffusivity of the material while both the C-scan and the FDIW technique measure a local stiffness loss, which may not overlap with the lower thermal diffusivity regions. However, the orientations of the defects are consistent in the three techniques.

Next, plate *B* with the four impacts of lesser energy is studied. The application of the SWR leads to the Figure 5.15 and as previously explained, does not succeed to locate the defects. Nonetheless, the FDIW technique is applied to four known impact regions, leading to Figures 5.23b, 5.24b, 5.25b and 5.26b. Unlike for the previous plate, both the FDIW technique and the PT fail to detect the defects. However, the defect are slightly visible in the C-scan, leading to the conclusion that there exist some defect at these locations, but these defects are not important enough to be picked up by the FDIW technique.

5.7 Conclusions

This chapter presented a methodology for the integration of the Frequency Domain Instantaneous Wavenumber (FDIW) and the Sparse Wavefield Reconstruction (SWR) technique. The SWR is first used to locate the defects on a large area and the FDIW is used to refine the scan and quantify the detected defects. To judge the effectiveness of the proposed methodology, the process has been compared to Pulse Thermography and air-coupled C-scan. Results were obtained for multiple impact defects of various impact energies in CFRP panels. Results show that the proposed methodology is able to appropriately locate and quantify the defects of higher impact energy. Lower impact energy defects remain nearly invisible to the guided wave techniques leading to the conclusion that the FDIW and the SWR have an accuracy slightly inferior, but comparable to the one of the air-coupled C-scan and the Pulse Thermography.

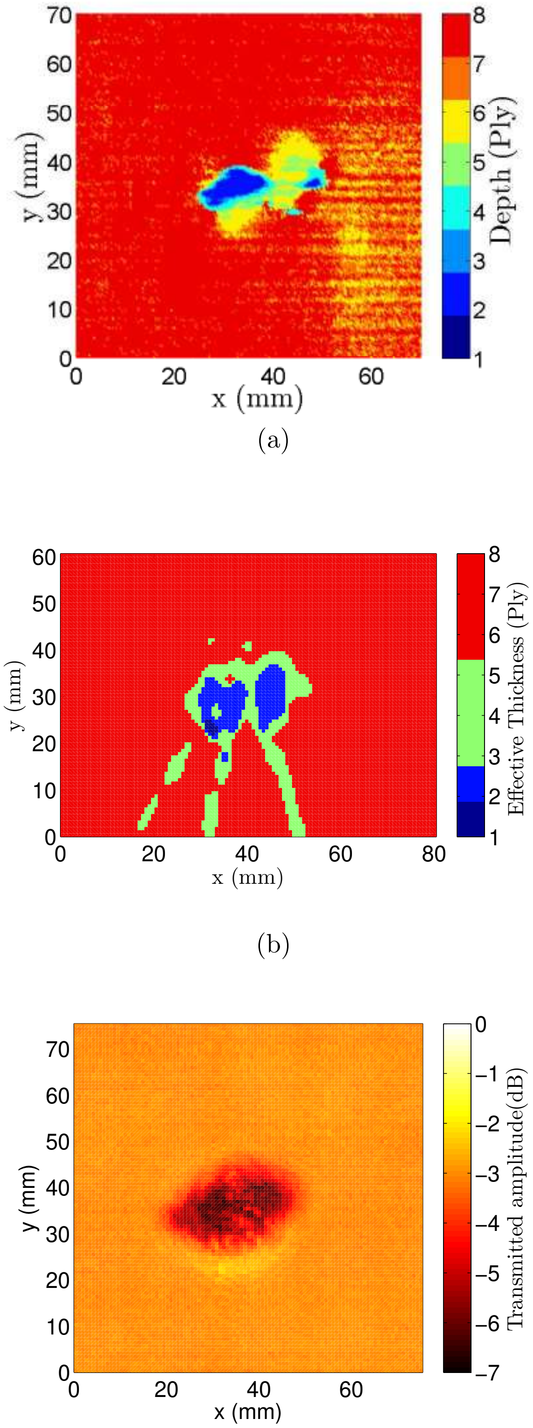

(a)

(b)

(c)

Figure 5.19: Imaging of the 25.7 J impact illuminated from the North (a): Pulse Thermography, (b): FDIW and (b): Air-coupled C-scan

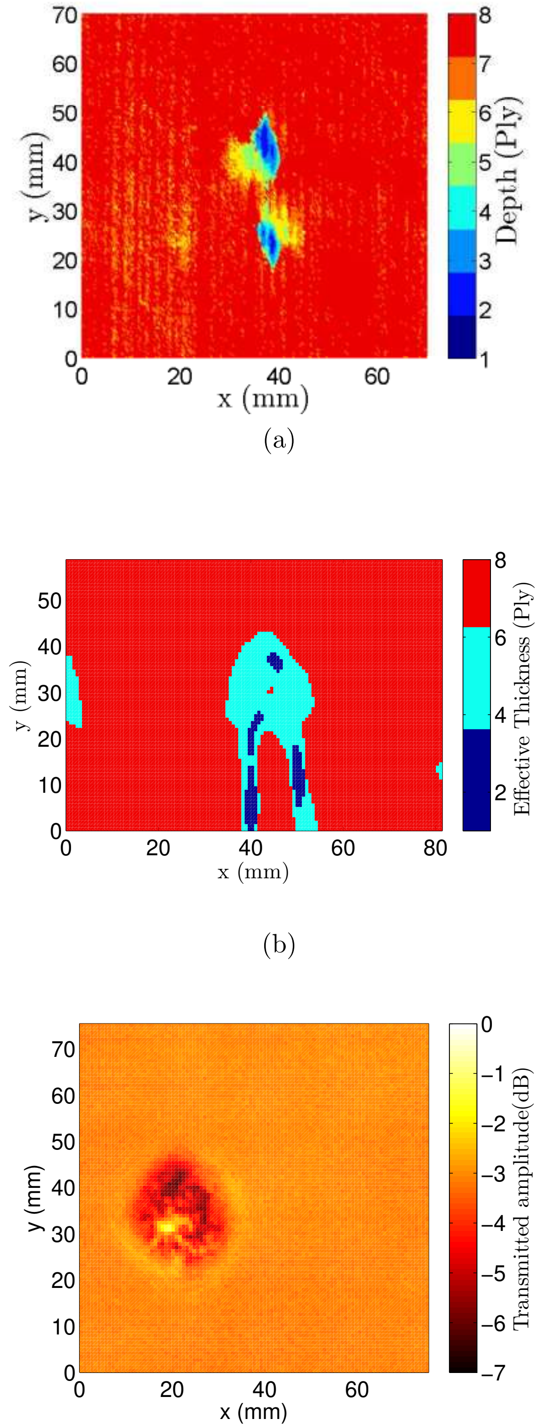

(a)

(b)

(c)

Figure 5.20: Imaging of the 22.5 J impact illuminated from the North (a): Pulse Thermography, (b): FDIW and (b): Air-coupled C-scan

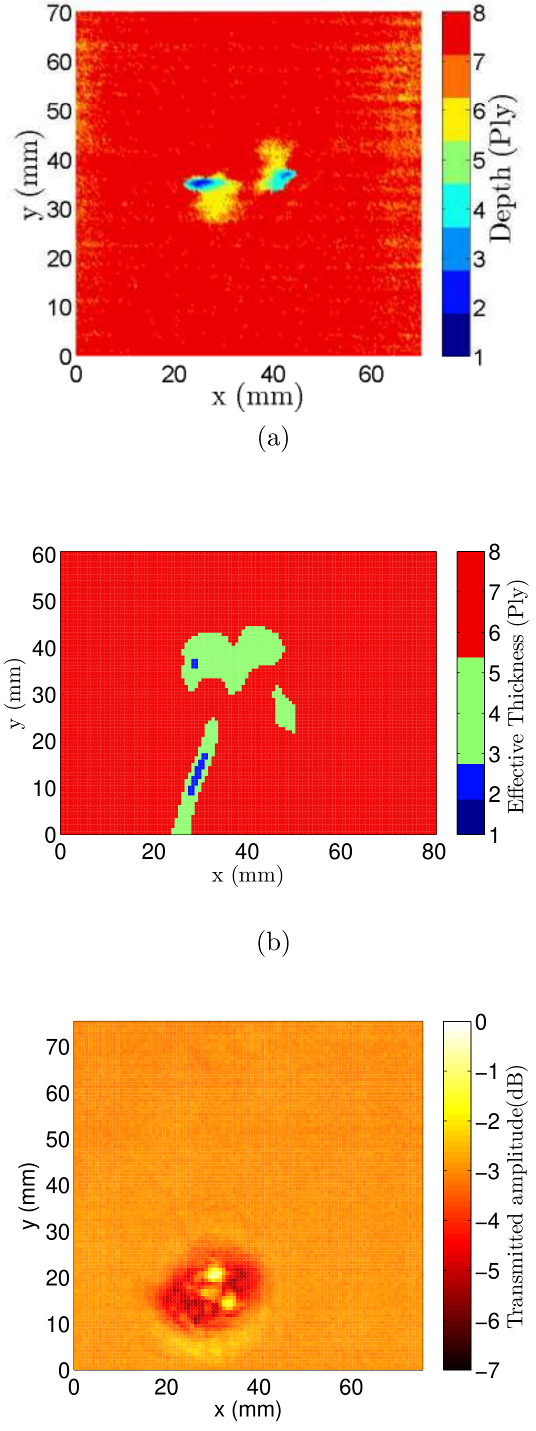

(a)

(b)

(c)

Figure 5.21: Imaging of the 19.3 J impact illuminated from the North (a): Pulse Thermography, (b): FDIW and (b): Air-coupled C-scan

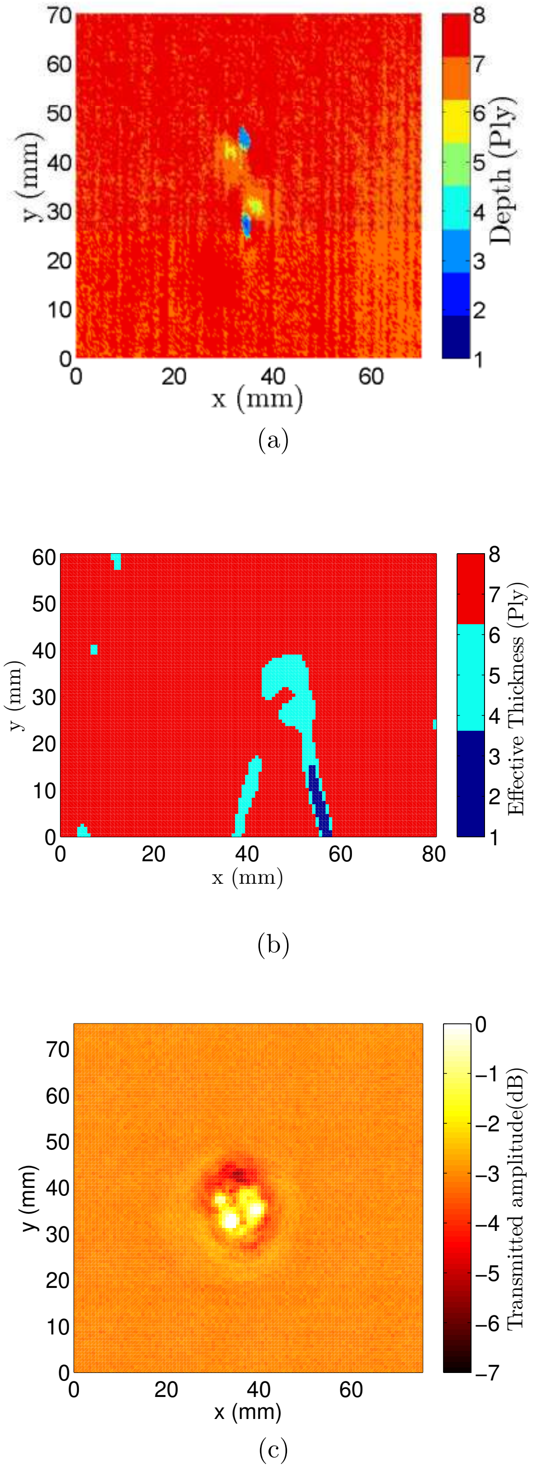

Figure 5.22: Imaging of the 16.1 J impact illuminated from the North (a): Pulse Thermography, (b): FDIW and (b): Air-coupled C-scan

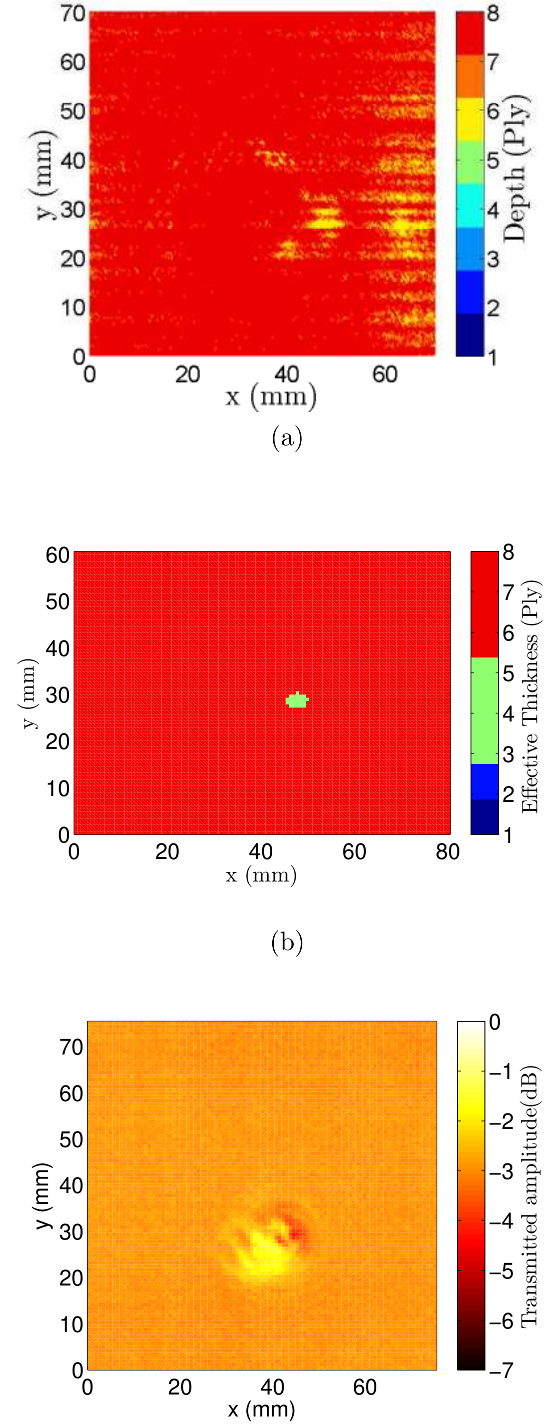

(a)

(b)

(c)

Figure 5.23: Imaging of the 12.9 J impact illuminated from the North (a): Pulse Thermography, (b): FDIW and (b): Air-coupled C-scan

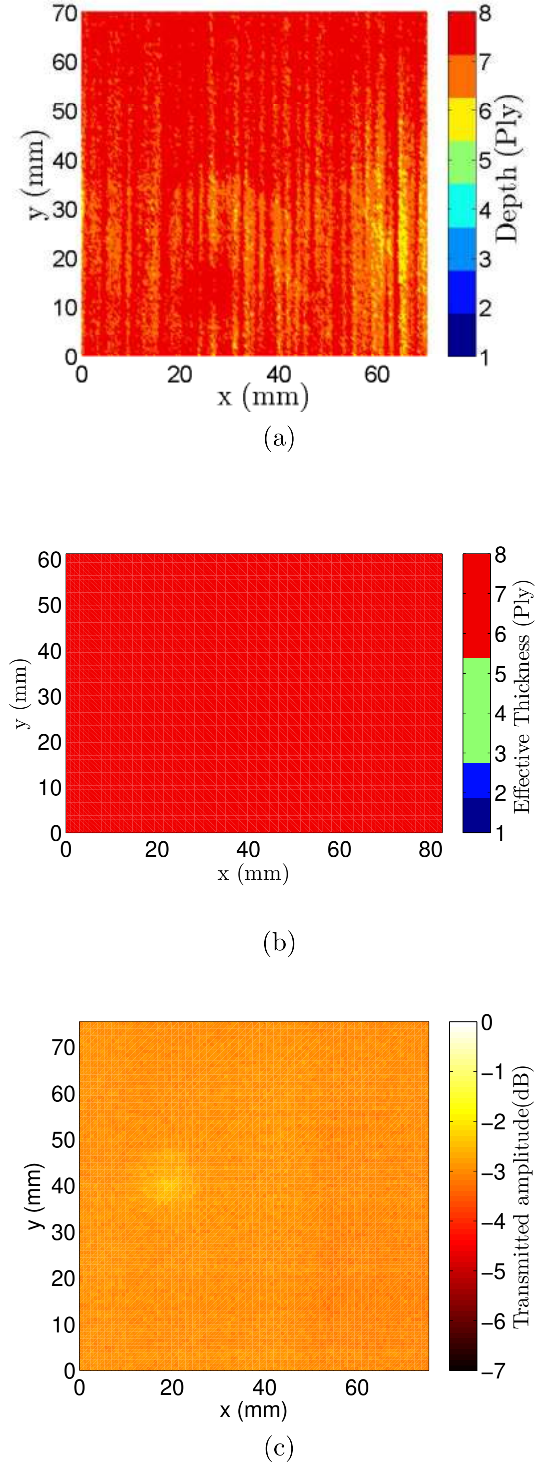

(a)

(b)

(c)

Figure 5.24: Imaging of the 11.3 J impact illuminated from the West (a): Pulse Thermography, (b): FDIW and (b): Air-coupled C-scan

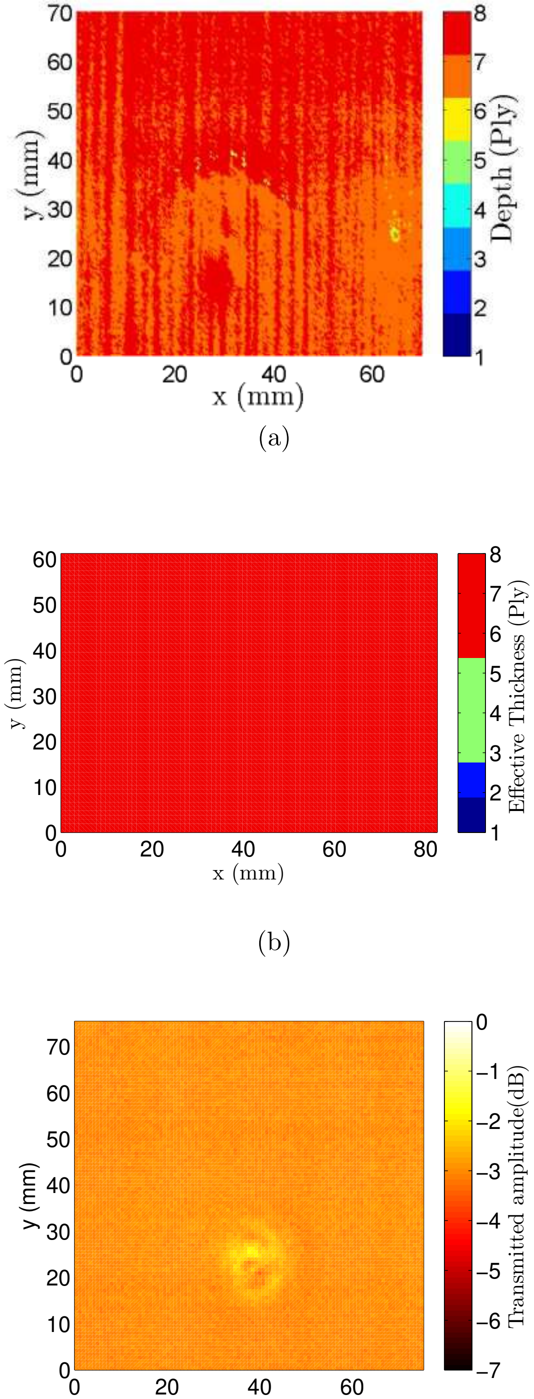

(a)

(b)

(c)

Figure 5.25: Imaging of the 9.6 J impact illuminated from the West (a): Pulse Thermography, (b): FDIW and (b): Air-coupled C-scan

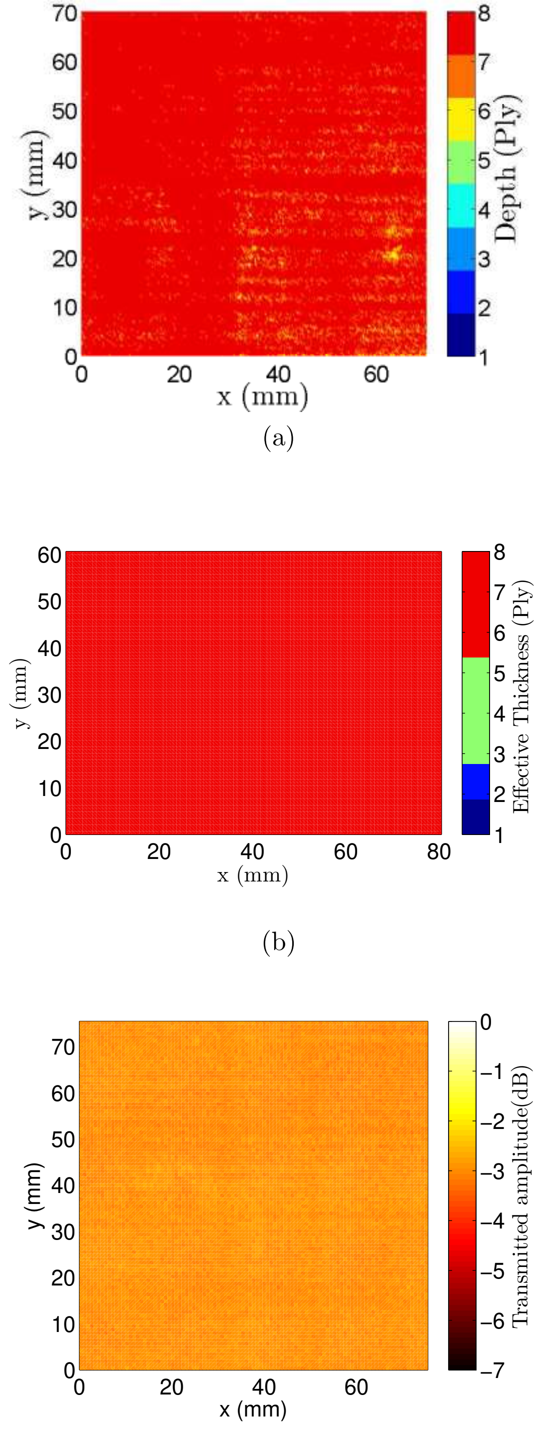

(a)

(b)

(c)

Figure 5.26: Imaging of the 6.4 J impact illuminated from the North (a): Pulse Thermography, (b): FDIW and (b): Air-coupled C-scan

CHAPTER VI

CONSTITUTIVE DAMAGE PARAMETERS DETECTION AND ANALYSIS

6.1 Chapter overview

Assessing the health of a structure is crucial in regular maintenance operations but must be followed by a diagnosis step to facilitate the decision making process. Once a defect has been properly identified and quantified, one must be able to determine whether this defect is critical, or how soon the defect will start being a threat to the operation of the structure. Several approaches have been developed during the past decades to estimate the residual structural properties of a damaged specimen. For example, fracture mechanics theory has a very rich literature, based on theoretical, empirical and phenomenological models [163]. For more than a decade, research groups have attempted to come up with efficient and reliable numerical models able to predict damage onset and growth for all the possible failure modes individually and simultaneously in composite materials [164]. These models require prior knowledge of the initial structural properties of the studied specimen, which often require extensive testing.

Among these techniques, Continuum Damage Mechanics (CDM) is a non-linear fracture mechanics theory whose goal is to estimate the residual structural properties of a composite specimen with minimal experimental testing, privileging numerical methods instead. In CDM, damage modes are represented by a local stiffness reduction [165]. CDM denotes a very mature group of techniques and is implemented in various commercial finite element codes. CDM efficiently predicts the mixed-mode failure characteristics either of a pristine specimen or a standard test specimen, such as the double cantilever beam [166]. However, estimating the initial constitutive damage parameters is a difficult operation for non-standard test samples. To the author's knowledge, no work aiming at estimating the initial constitutive damage parameters of a damaged specimen using guided waves has been attempted.

Combining the defect information obtained with the imaging techniques developed in this dissertation with CDM methods may provide a quantitative estimate of the remaining structural life for a specimen containing a specific defect from a guided wave non-destructive measurement. This work is necessary as it closes the NDE loop by providing the failure characteristics for a specific flawed sample without the need to do multiple failure experiments. Therefore the goal of this chapter is to establish a relationship between guided wave characteristics and the constitutive damage parameters. This relationship will then be used to obtain a mapping of the damage parameters distribution. Because the FDIW technique presented in Chapter 4 is a measure of the wavenumber at every location of space, a relationship between the wavenumber and the damage parameter will be sought.

In this chapter, cohesive zone methods are first presented and illustrated, then the process to estimate the constitutive damage parameters using guided waves is introduced. Finally, the application of the proposed process to simulated specimens is presented. Note that the work presented in this chapter has no intent to provide quantitative results, but instead aims at drawing the guidelines of a process to estimate failure characteristics of a non-pristine composite by using finite elements methods in combination with Guided Wave Imaging techniques.

6.2 Cohesive zone model

Cohesive Zone Model (CZM) is a damage mechanics method widely used to simulate the onset and the growth of defects in materials [167]. The main idea behind CZM is to create a special finite element that is susceptible to deform elasticity until a

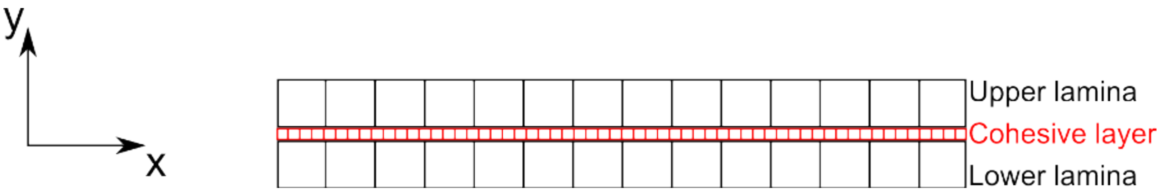

Figure 6.1: Schematic of a cohesive layer between two lamina. The lamina and the cohesive layer are discretized in finite elements to illustrate the relative element sizes.

damage initiation criterion is met, followed by a plastic deformation described by a damage evolution criterion. Cohesive zone methods are commonly used in composites to simulate breakable interfaces between the layers as depicted in Figure 6.1. By using CZM to simulate layer interfaces, the damage initiation and growth is constrained to spread only within the cohesive zones, which is an appropriate assumption in many cases as it is accepted that the interfaces between layers are the more susceptible regions to fail first. Cohesive zones have the advantage to be able predict both the onset and growth of defects, even when starting with an initially pristine geometry. A schematic of the inclusion of a cohesive layer between two lamina is shown in Figure 6.1.

In addition to interface failure, there exist multiple models for lamina failure, such as the Hashin failure criteria for unidirectional composites [168]. For more details regarding the multiple failure methodologies in composites, the reader is invited to refer to [169]. In this chapter and the rest of this dissertation, defects are assumed to exist only at the interface between layers, so only CZM will be presented and used.

6.2.1 Governing equations

The Cohesive Zone Method relies on the assumption that the stress transfer between the two faces of a discontinuity does not immediately plunges to zero at damage initiation. Instead, damage evolution is a progressive event during which the stiffness of the cohesive element decreases as the faces of the discontinuity separate further until the total failure of the element is observed, and the stiffness of the element

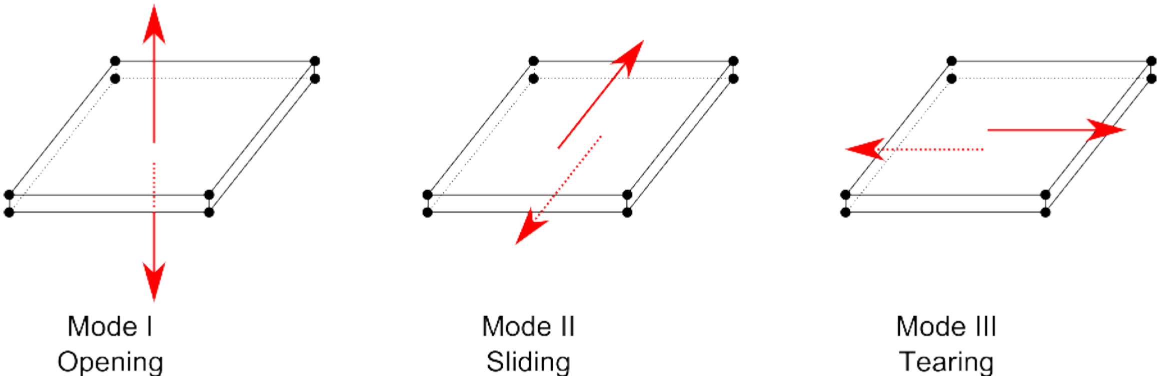

Figure 6.2: Schematic of the eight-node cohesive element of zero thickness for the three failure modes

becomes zero [170]. Unless modeling interfaces of considerable thickness, cohesive elements have a zero thicknesses and are governed by a traction separation behavior.

6.2.1.1 Single mode model

Consider the eight-node rectangular cohesive element of zero thickness depicted in Figure 6.2 obeying the stress-traction law of Figure 6.3. For a single failure mode i, with $i = I, II$ or III, where I, II and III denote the three crack separation modes of fracture mechanics [163], the traction separation rule for the cohesive element is given by:

$$\sigma_i = K_i \delta_i \tag{6.1}$$

where σ_i is the surface traction for mode i, K_i is the stiffness of the element and δ_i is the separation distance between the two faces of the cohesive element. Note that this equation is the analogy of the well-known linear elastic relationship $\sigma = E\epsilon$. However, to model interfaces with cohesive elements, it is required that the thickness of the element is zero at rest, therefore it is necessary to replaces the dimensionless strain ϵ by the traction separation distance δ_i. Because the separation distance δ_i is not dimensionless, the unit of the stiffness K_i is in $[Pa/m]$. The stiffness of the cohesive element is then determined by the following equation:

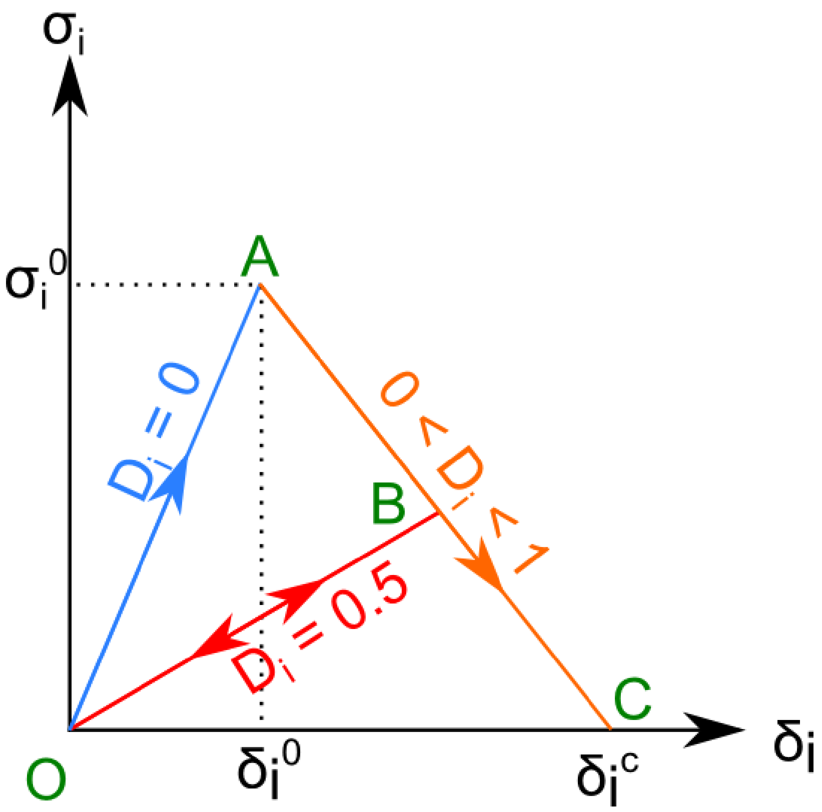

Figure 6.3: Schematic of the bilinear traction separation law for failure mode *i* for a cohesive element.

$$K_i = (1 - D_i)K_i^p \tag{6.2}$$

where K_i^p denotes the pristine value of the stiffness of the cohesive element before damage occurs and D_i is the damage variable. The damage variable D_i is a crucial parameter that assesses the health of the cohesive element.

A common practice to model the evolution of the damage variable is to use a bilinear traction separation law, represented in Figure 6.3. Note that the bilinear traction law, initially defined in [171], is a good compromise between result accuracy and computational costs. However, there exist other laws such as exponential, trapezoidal and linear parabolic [172] with various characteristics, such as degree of accuracy of the results or numerical performance.

According to the bilinear traction law of Figure 6.3, the cohesive element deforms elastically (segment OA) until the damage initiation criteria at point A. When the stress in the cohesive element reaches the maximum value σ_i^0 at point A, the damage variable D_i increases as the element quality degrades, until complete failure is reached when the separation reaches the critical value of δ_i^c. Point A in Figure 6.3 represents the damage onset, while the orange segment AC represents the linear damage evolution. Note that if the element is unloaded during the damage evolution, at point B for example, the separation δ_i returns to zero. The damage state of the element is stored in the damage variable D_i so that the re-loading curve is the segment OB. The damage evolution is then irreversible, even though no permanent deformation remains after unloading.

The slope of the elastic zone (segment OA in Figure 6.3) is fixed by the pristine stiffness K_i^p of the cohesive element. The slope of the damage evolution curve (segment OC) is calculated by imposing that the area under the curve must be equal to the critical energy release rate G_{ic} according to Griffith's principle [173]. The separation fracture is then given by:

$$\delta_i^c = \frac{2G_{ic}}{\sigma_i^0} \tag{6.3}$$

The damage variable is then directly related to the separation of the faces of the cohesive elements by the following equation [170]:

$$D_i = \frac{\delta_i^c(\delta_i - \delta_i^0)}{\delta_i(\delta_i^c - \delta_i^0)} \tag{6.4}$$

At this point, it is important to recall that these equations are valid for the individual failure modes $i = I, II$ or III. However in practice, failure often occurs under mixed-mode conditions. In order to take into account mixed-mode failure, the damage initiation criterion and the damage evolution criterion must be adapted to include the three failure modes.

6.2.1.2 Mixed-mode model

There exist multiple mixed-mode damage initiation and evolution criteria. For simplicity, this paragraph only presents the criteria used in this research which are widely accepted within the research community [174]. First, it is assumed that the properties of the interfaces between the lamina is dominated by the matrix of the composite, which is isotropic, hence the stiffness of the cohesive element is identical along the three failure modes, i.e., $K = K_I = K_{II} = K_{III}$. The quadratic stress criterion is given by:

$$\left(\frac{\sigma_I}{\sigma_I^0}\right)^2 + \left(\frac{\sigma_{II}}{\sigma_{II}^0}\right)^2 + \left(\frac{\sigma_{III}}{\sigma_{III}^0}\right)^2 = 1 \tag{6.5}$$

where σ_i is the stress in the element along mode i and σ_i^0 is the maximum value of the stress in the element along mode i. Equation (6.5) is the damage initiation criteria, represented by point A in Figure 6.3. The mixed mode separation, i.e., the cumulated separation of the three failure modes, is given by the quadratic norm of the separation of the three failure modes:

$$\delta_m = \delta_I^2 + \delta_{II}^2 + \delta_{III}^2 \tag{6.6}$$

where δ_i is the separation of the element along mode i and δ_m is the mixed mode separation. Similarly, δ_m^0, i.e., the mixed mode separation at damage initiation (point A in Figure 6.3) and δ_m^c, i.e., the mixed mode separation at the failure (point C in Figure 6.3) are computed by:

$$\delta_m^0 = (\delta_I^0)^2 + (\delta_{II}^0)^2 + (\delta_{III}^0)^2 \tag{6.7}$$

$$\delta_m^c = (\delta_I^c)^2 + (\delta_{II}^c)^2 + (\delta_{III}^c)^2 \tag{6.8}$$

Finally, the damage variables of each failure mode can be combined in a single mixed-mode variable D_m assessing the health of the structure at a given location of space by:

Table 6.1: Constitutive damage parameters of a cohesive element

Parameters	Unit	Description
K	[Pa/m]	Pristine stiffness of the cohesive elements
$\sigma_I, \sigma_{II}, \sigma_{III}$	[Pa]	Strengths required for the damage initiation
$G_{Ic}, G_{IIc}, G_{IIIc}$	[J/m^2]	Critical energy release rates for the damage evolution
η	[ ]	B-K exponent
D_m	[ ]	Damage variable assessing the current health

$$D_m = \frac{\delta_m^c(\delta_m - \delta_m^0)}{\delta_m(\delta_m^c - \delta_m^0)} \tag{6.9}$$

For the damage evolution, i.e., segment AC in Figure 6.3, the energy based Benzeggagh-Kenane (B-K) [175] is commonly used in practice and implemented in most commercial finite element codes and is given by:

$$G_c = G_{Ic} + (G_{IIc} - G_{Ic}) \left(\frac{G_{II} + G_{III}}{G_I + G_{II} + G_{III}} \right)^{\eta} \tag{6.10}$$

where G_{ic} and G_i denote the critical fracture energies and the energy release rates respectively and G_c is the mixed mode fracture energy of the material. Damage propagation occurs when the sum of the energy release rates is equal to G_c. The dimensionless parameter η is a parameter sets to fit experimental data.

6.2.2 Constitutive damage parameters

Table 6.1 is the list of the constitutive damage parameters required for CZMs. First, the stiffness of the cohesive elements K, also called penalty stiffness, is a numerical parameter that must be carefully chosen to ensure convergence. The penalty stiffness K must be much large enough so that the interface separation at failure initiation is small with respect to the thickness of the individual layer, i.e., the segment OA is nearly vertical in Figure 6.3. However the value of K must remain bounded in order to avoid numerical instabilities. Multiple papers [174, 172, 170, 176, 167] propose guidelines regarding the choice of this parameter within the range of 10^{14} to 10^{15} Pa/m.

Second, the strengths σ_i and fracture toughnesses G_{ic} are parameters that depend on the quality of the bonding at the interfaces. These parameters must be measured experimentally, or estimated by referring to similar materials. The B-K exponent η is also measured experimentally [167].

Finally, the mixed-mode damage variable D_m (simply denoted D from now on), assesses the health of the interfaces of the structure. Unlike the other parameters, D is a state variable and not a material variable. Most commonly in simulations, D will be equal to zero (undamaged) at the beginning configuration of each numerical simulation, except in an area of space to simulate a pre-existing debonding where $D = 1$. To the author's knowledge, no numerical simulation has been conducted with an initial configuration containing a region where $0 < D < 1$.

6.2.3 Length of the cohesive zone

The cohesive zone is the region in which $0 < D < 1$, i.e., this is the region in which the elements are in the damage propagation stage. In order to ensure convergence, it is crucial to have more than one cohesive element inside the cohesive zone. Because there is only one cohesive element across the thickness of the cohesive layer, the number of elements in the cohesive zone is measured along the length of the interface, i.e., along axis x in Figure 6.1. It is demonstrated in [166] that placing 3 to 5 elements inside the cohesive zone is good practice. However, cohesive zones are typically very small, leading to fine meshes and sometimes intractable simulations. Indeed, the length of the cohesive zone is the structural property approximated by [174, 177]:

$$l_{i,cz} \approx E_2 \frac{G_{ic}}{(\sigma_i^0)^2} \tag{6.11}$$

where E_2 is the transverse modulus of the lamina, i.e along axis y in Figure 6.1. Very commonly, the length of the cohesive zone is close to or below one millimeter, leading to a fine meshing of the cohesive regions.

6.2.4 Example - Double Cantilever beam

For illustration purposes, this section presents the case of a Double Cantilever Beam (DCB). This example is greatly inspired from the Chapter 10 of [170], especially, the material and inter-facial properties are directly imported from this book. The commercial software Abaqus 6.14 is used for this simulation with the built-in cohesive elements options. The DCB is made of two beams of layup $[0^o]$ of dimensions $100 \times 20 \times 1.5$ mm whose properties are given in Table 6.2.

Table 6.2: Engineering properties of the laminas of the DCB

Parameters	Unit	Value
E_1	[GPa]	135.5
$E_2 = E_3$	[GPa]	9
ν_{23}	[ ]	0.46
$\nu_{12} = \nu_{13}$	[ ]	0.23
G_{23}	[GPa]	3.3
$G_{12} = G_{13}$	[GPa]	4.5

The direction of the fibers is aligned with the longest dimension of the beams, i.e., direction x as depicted in Figure 6.4. Due to the symmetry of the system, the model is simplified to a 2D problem, in which the beams are modeled by plain strain elements. The right end of the beam is fixed, all the other faces are free. Two initial configurations are considered: (a) the interface between the layers is intact and (b) a pre-existing crack of 30 mm starting from the left extremity is present between the two layers. Note that according to this description, the only difference between the two configurations is the distribution of the damage state variable D in the initial configuration. In both cases, cohesive elements of zero thickness are inserted between the two beams, with the properties presented Table 6.3. However in case (b), the cohesive elements are removed in the initially cracked region to simulate a region in which $D = 1$. According to the properties of Table 6.3 and equation (6.11), the length of the cohesive zone is 0.78 mm. Hence the element size is 0.25 mm in order to ensure three elements in the cohesive zone. Imposed displacements of opposite signs

Table 6.3: Properties of the cohesive zone of the DCB beam

Parameters	Unit	Value
$K_I = K_{II} = K_{III}$	[GPa/m]	57×10^4
$\sigma_I = \sigma_{II} = \sigma_{III}$	[MPa]	57
$G_{Ic} = G_{IIc} = G_{IIIc}$	[J/m^2]	280
η	[ ]	2.284
D	[ ]	(a): $D = 0$ for $0 < x < 100$ mm (b): $D = 1$ for $0 < x < 30$ mm, $D = 0$ otherwise

are applied at the nodes of the free extremity, as displayed in Figures 6.4.

Figure 6.5 shows the vertical displacement computed by Abaqus as well as the corresponding deformed geometry of the initially pre-cracked beam for an imposed displacement of 3 mm for illustration purposes. The evolution of the imposed load as a function of the imposed displacement is then plotted in Figures 6.6a and 6.6b. As expected, the behaviors of the initially pristine and the pre-cracked DCBs are quite different in term of maximum imposed load. Indeed, it appears that the imposed force jumps to its maximum value as soon as a displacement is imposed in configuration (a), while the effect is more progressive for configuration (b), due to the bending of the two separated beams in the pre-cracked region. Damage initiation occurs immediately in configuration (a) and around 1 mm of imposed displacement in configuration (b). The maximum load that can be carried by the pristine beam is nearly 1000 N while the pre-cracked beam can only carry 65 N of load before damage growth. The progress of the crack tip with respect to the left edge of the beams is then represented by studying the number of failed elements, leading to Figure 6.7.

The evolution of the crack tip plotted in Figure 6.7 measures the length of the crack tip starting from the left extremity of the beam. For the pre-cracked configuration, the initial crack length is 30 mm. This plot demonstrates that the same configuration is achieved as soon as both beam started failing (approximately at 1 mm of imposed displacement).

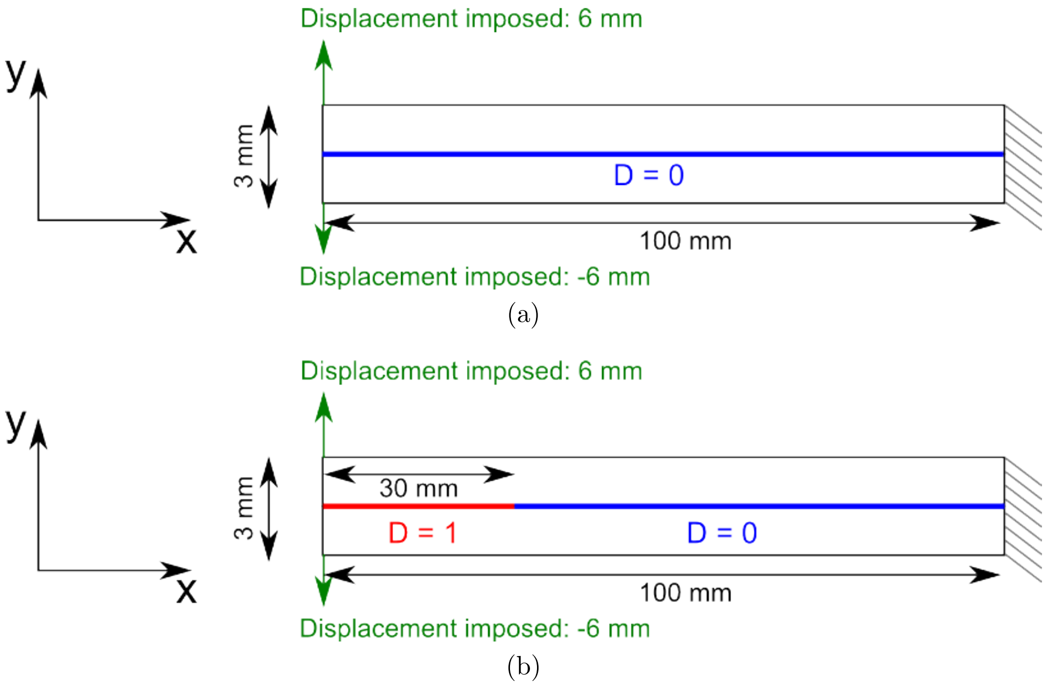

Figure 6.4: Schematic of the pre-cracked double cantilever beam (not to scale) for configuration (a): Initially pristine and (b): pre-cracked. The blue layer represents the pristine ($D = 0$) cohesive layer. The red layer indicate the absence ($D = 1$) of the cohesive layer.

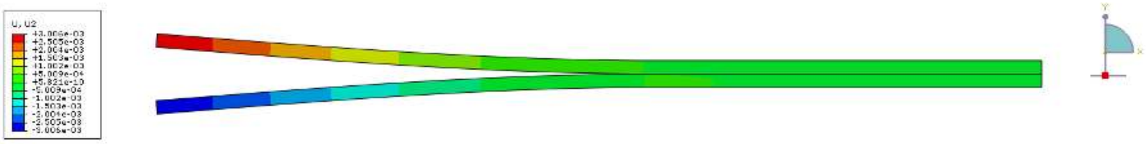

Figure 6.5: Displacement norm distribution in the pre-cracked DCB for an imposed displacement of 3 mm

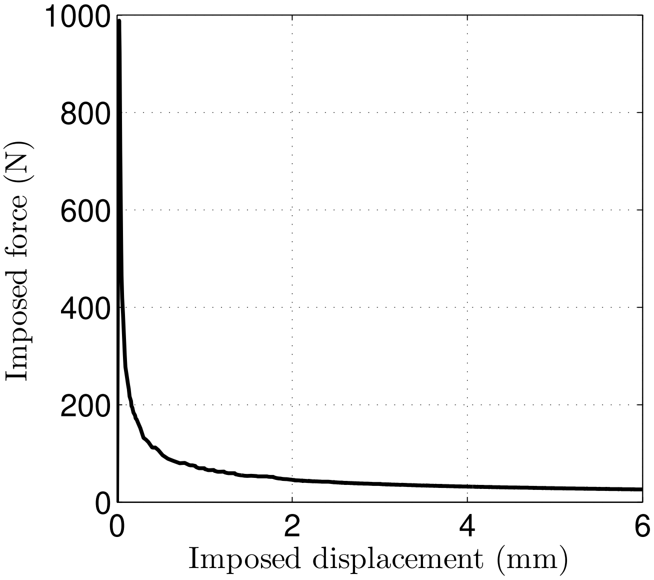

(a)

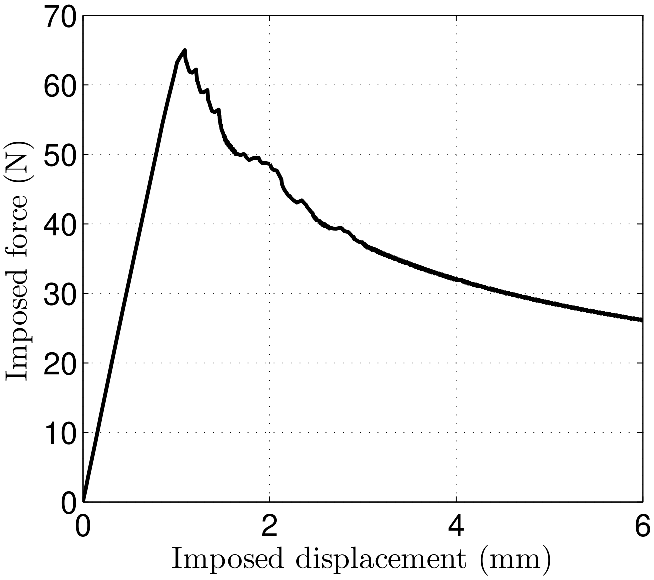

(b)

Figure 6.6: Imposed load versus imposed displacement (a): Initially pristine configuration and (b): Pre-cracked configuration.

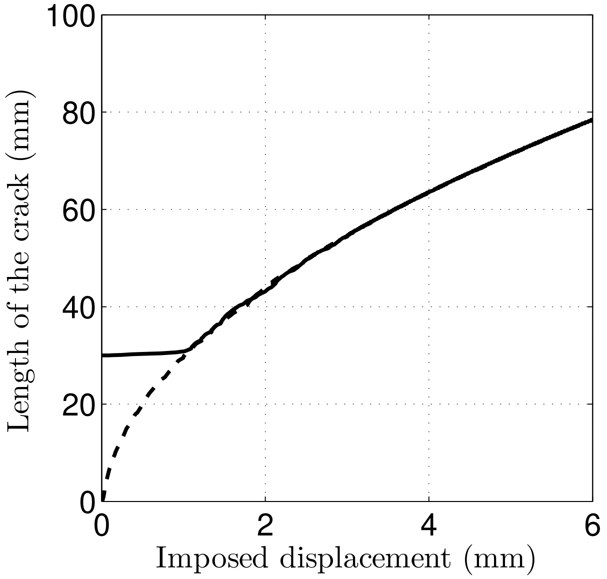

Figure 6.7: Evolution of the length of the crack VS imposed displacement. Dashed line: configuration (a) and solid line: configuration (b)

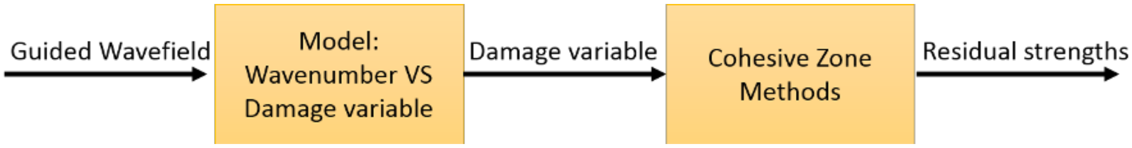

Figure 6.8: Process to estimate the residual strength of a structure based on a Guided Wavefield

6.3 Estimation of the damage variable using guided waves

The distribution of the state variable D assesses the current health of the structure at every point of space. Being able measure the distribution of the damage variable D through an experiment would therefore be a milestone allowing to build customized numerical models of non-pristine real specimen. Figure 6.8 depicts the process that could be used to estimate the residual strengths of a structure based on a guided wavefield. The first step of this process is to convert the guided wavefield into a damage variable distribution estimate. This estimate is then fed to CZMs to calculate the desired residual properties, such as strengths. Being able to achieve these estimates using guided waves provides a fast and reliable bridging technique between experimental defect measurement and numerical properties estimate. This section focuses on numerically establishing a relationship between the guided wave characteristics and the value of the damage variable. In other words, this section defines the model that will be used in the first step of Figure 6.8. All results presented in this section are numerical.

6.3.1 Guided wave propagation in composites with cohesive interfaces

In order to establish the link between guided wave and damage variable corresponding to the first step of Figure 6.8, it is necessary to combine guided wave and CZM. However, current implementations of CZMs are not adapted to numerical wave propagation. This section focuses on adapting current CZM implementation to model guided waves. Indeed, as explained in Section 6.2, cohesive zones are modeled numerically by zero-thickness regions located at the interface between layers. Numerical simulations involving CZM are most often the static response of a test sample to a specific loading. Due to the fine mesh requirement (see Section 6.2.3) and the complicated behavior of the cohesive zones, computational times may be significant even for simple 2D simulations. On the other hand, the numerical propagation of guided waves require a time-dependent simulation with a very fine time step. It is therefore necessary to adapt the CZM in order to model the dynamic wave propagation response while using pristine and non-pristine cohesive zones with reasonable computational duration.

In CZM, zero-thickness cohesive layer are commonly modeled using the cohesive properties of Table 6.3 for example. To combine cohesive zones and guided wave propagation, it is required to replace the cohesive zones by very-thin (but finite thickness) inter-facial layers. The thickness of these layers must be negligible with respect to the thickness of the lamina. In practice, for the results presented herein obtained with

Abaqus, the thickness of the inter-facial layers is two orders of magnitude smaller than the thickness of the lamina. Finer interfaces could be used but are counter-productive as they require finer meshes.

First, the elastic properties of the inter-facial layer are derived from the properties of the zero-thickness cohesive zones. As shown in Table 6.3, the penalty stiffness of the cohesive zones is given in Pa/m. As inter-facial layers of finite thickness are now used to simulate guided wave propagation, the following formula is used to calculate the elastic properties of the inter-facial layer:

$$K_i^{inter-facial\ layer} = K_i^{cohesive\ zone} \times L_0 \tag{6.12}$$

where L_0 is the thickness of the inter-facial layer. Next, because guided wave propagation is a non-destructive phenomenon, it is safe to remove the damage evolution and initiation criteria. In words, because guided waves are harmless for the structures they are propagating into, there is no need to check at each iteration whether the damage initiation criterion is met or not, as it must be done with CZM. It is therefore assumed that the inter-facial layer is linearly elastic for any range of stress or strain value. In other words, the elements constituting the inter-facial layer only follow the segment OA of Figure 6.3. This is an important simplification of the problem as no equivalent value for the maximum strength or energy release rate must be calculated as they are not part of the model anymore. Moreover, not checking these criteria for each element at each iteration speeds up the simulation significantly.

As a summary, the model consists of stacked lamina and isotropic linearly elastic and inter-facial layers of thickness L_0 whose modulus of elasticity is given by Equation (6.12). A schematic of the model is shown for a 3-layer 3-mm thick lamina in Figure 6.9. The model can then be solved in the time domain to study wave propagation or in the frequency domain to study the steady state response of the specimen at a given frequency.

Figure 6.9: Model of a 3-layer 3-mm thick lamina with finite-thickness inter-facial layers. The green layer is kept pristine ($D = 0$) while the damage variable of the red layer takes multiple non-zero values.

6.3.2 Guided wave wavenumber as a function of the damage variable

The goal of this section is to establish the relationship between guided wave characteristics and the damage variable, corresponding to the first step of the process depicted in Figure 6.8. This relationship will then be used in the following sections to obtain a mapping of the damage variable distribution. Because the FDIW technique presented in Chapter 4 is a measure of the wavenumber at every location of space, this section focuses in determining a relationship between the wavenumber and the damage variable. To achieve this, the model presented in the previous section is first modeled with SAFE for the 3-layer 3-mm thick aluminum beam depicted in Figure 6.9.

In SAFE, inter-facial layers of thickness 1 nm are inserted between each aluminum layer. By analogy with the cohesive zone properties of Table 6.3 and according to Equation (6.12), the pristine stiffness of the inter-facial layer is $K^0_{SAFE} = 0.57$ MPa. This value is based on the model presented in the previous section and the value of the penalty stiffness found in the literature. Each layer, including the 2 inter-facial layers are discretized by 3 3-node elements. In order to study the variation of the guided waves characteristics as a function the damage variable, the dispersion relations of the specimen of Figure 6.9 are computed for various initial values of D for the lower inter-facial layer (red layer). By conducting these operations for multiple initial values of D for a single layer, dispersion relations are calculated for non-pristine specimens. Since there exist no damage variable in the SAFE implementation, changing the value of D is done through changing the stiffness of the inter-facial layer through equation

(6.2).

The results displayed by the black dots in Figure 6.10 shows the evolution of the $A0$-wavenumber at 200 kHz as a function of the logarithm of $D' = 1 - D$. Note that $D' = 1$ means that the inter-facial layer is pristine while $D' = 0$ means that the lower layer (red layer in Figure 6.9) has completely failed. It can be seen in Figure 6.10 that the wavenumber of the $A0$ mode is sensitive to D' in the range $D' \in [10^{-4}, 10^{0}]$. It is important to notice that a new mode appears at approximately $D' = 10^{2.7}$. This mode exists due to the debonding between the upper two aluminum layers and the lower aluminum layer that occurs when D' converges to zero. In words, there exist two modes in the region $D' < 10^{2.7}$ because the groups of layers on either side of the damaged interface are not bonded and because of their different thickness, different wavenumbers are present. The red lines in Figure 6.10 shows the theoretical $A0$-wavenumber at 200 kHz of 1, 2 and 3 mm thick pristine aluminum samples. This confirms that for $D' < 10^{2.7}$, the wavenumbers converge towards the wavenumber of a 1 mm and a 2 mm thick aluminum sample. In the region $10^{-4} < D' < 10^{2.7}$ the wavenumber is still a function of D' despite the occurrence of the new mode. This is due to the fact that the upper and lower group of layers still interact through the damaged inter-facial layer.

In order to validate these results, the same model is implemented in Abaqus. The inter-facial layer thickness is fixed at $L_0 = 10^{-5}$ m, leading to $K^0_{Abaqus} = 5.7GPa$ according to Equation (6.12). Frequency analyses at 200 kHz are then conducted for different values of D' for the lower inter-facial interface. The studied beam is 100 mm long and discretized in $2D$ plain strain elements. The wavenumber of the $A0$ mode is then extracted and represented in Figure 6.10 by the blue crosses. This validation demonstrates a good agreement between the wavenumber evolution predicted by SAFE and the results from Abaqus. In addition, the $A0$ mode shapes at 200 kHz are plotted in Figures 6.11, 6.12 and 6.13 for $D' = 10^{0}$ (pristine), $D' = 10^{-2}$ and

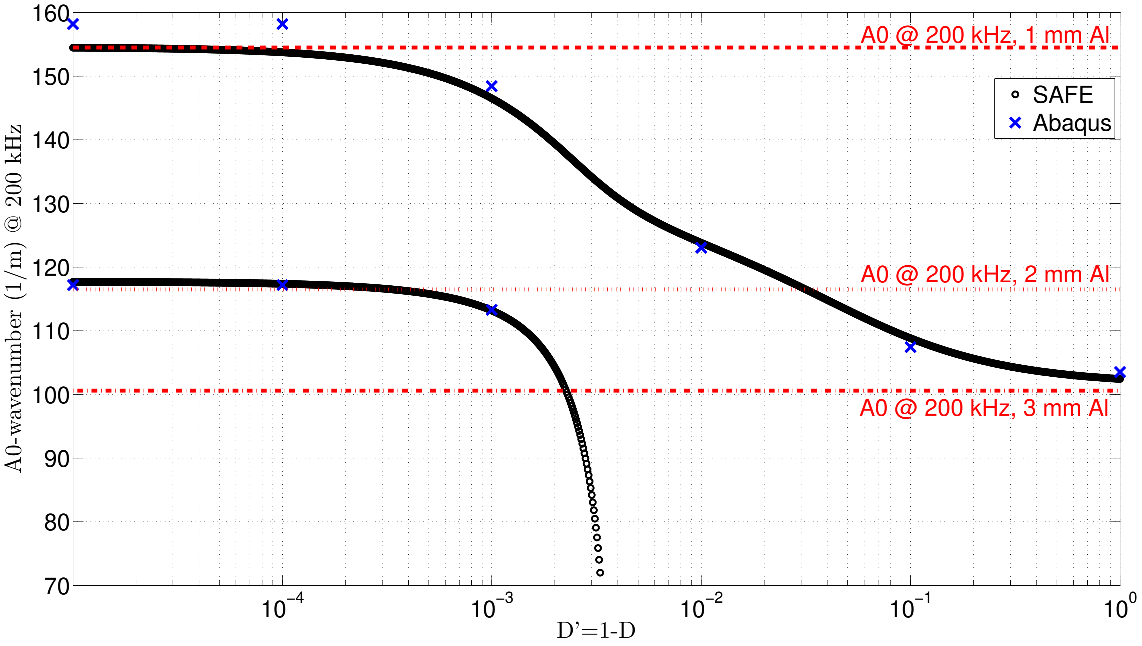

Figure 6.10: Evolution of the $A0$-wavenumber at 200 kHz in the geometry represented in Figure 6.9 as a function of $D' = 1 - D$. Black dots: SAFE prediction, blue crosses: Abaqus verification. Red line show the theoretical wavenumber of 1, 2 and 3 mm thick pristine aluminum samples

$D' = 10^{-4}$. In these figures, the color-scale indicates the normalized value of the vertical deformation.

First in Figure 6.11, only the antisymmetric mode $A0$ of the 3-mm pristine beam is visible as expected. Secondly, in Figure 6.12 it is clear that there is some abnormal interaction between the second and third layer due to the weak bonding at the lower interface. According to Figure 6.10 this interaction leads to an increase of the wavenumber of about 25%. Finally in Figure 6.13, the mode shapes are completely separated due to the failed interface.

6.3.3 Maximum load as a function of the damage variable

The relationship between the wavenumber and the damage variable has been evaluated numerically in Figure 6.10. However from this picture, it is visible that the guided waves are nearly insensitive to a change of the damage variable within $10^{-1} < D' < 10^{0}$ corresponding to $0 < D < 0.9$. More specifically, the wavenumber

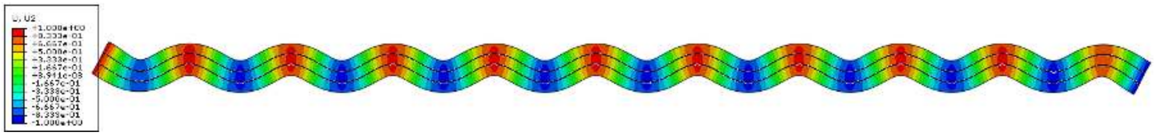

Figure 6.11: Mode shape of the $A0$ mode at 200 kHz for $D' = 10^0$ (pristine) for both interfaces

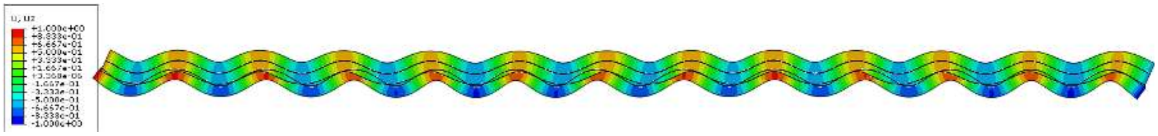

Figure 6.12: Mode shape of the $A0$ mode at 200 kHz for $D' = 10^{-2}$ for the lower interface

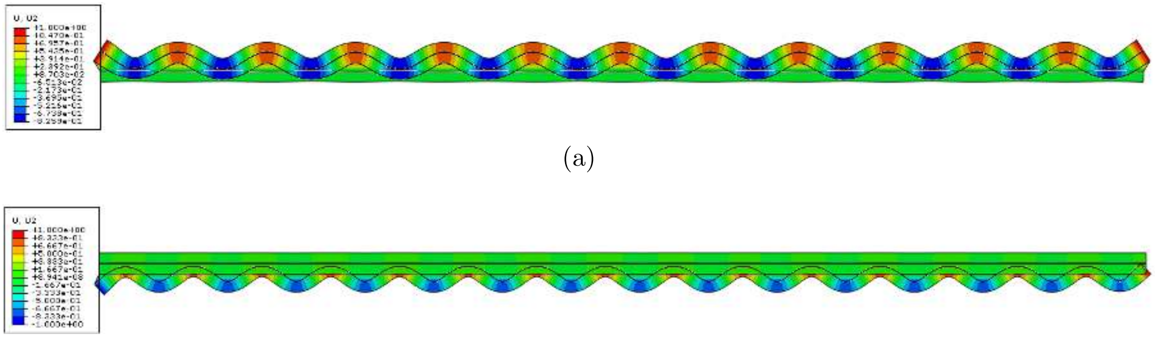

(a)

(b)

Figure 6.13: Mode shape of the $A0$ mode at 200 kHz for $D' = 10^{-4}$ for the lower interface (a): motion of the upper two layers and (b): motion of the lower layer

increase between $D = 0$ and $D = 0.75$ is of the order of 5%. Moreover, it was proven in Section 4.5 that the sensitivity of the FDIW technique is of the order of ±5% meaning that it is impossible with such technique to measure the damage variable accurately in the range $0 < D < 0.75$.

This section focuses on providing an estimate of the evolution of the maximum carrying load of a composite test sample for a damage variable evolving between $D = 0$ and $D = 0.9$. This is an important analysis because, as the FDIW technique is unlikely to be able to accurately map the damage variable in this range, it is necessary to know the maximum carrying load loss that won't be measured by this technique. Even though specific numbers are used in this section, the sole goal of this section is qualitative.

To quantify the loss of maximum carrying load as a function of D, a Double Cantilever Beam (DCB) similar to the one presented in Section 6.2.4 is studied. The beam is made of two 1-mm thick aluminum layers joined by an interface with the properties used in the previous section. Peeling tests are then conducted for different values of the damage variable. For example $D(initial) = 0.5$ corresponds to a reduction of the stiffness $K^{inter-facial\ layer}$ and the strength $\sigma^{inter-facial\ layer}$ of the inter-facial layer by a factor of two prior to loading. The evolution of the imposed force on the DCB as a function of the imposed displacement is plotted in Figure 6.14a for various initial values of the damage variable. For these results, damage initiation occurs when the imposed force reaches its maximum; the rest of the curve represent the damage propagation.

The load at damage initiation, i.e., the maximum carrying load of the structure, is plotted in Figure 6.14b as a function of the initial damage variable. This figure shows that the stress at damage initiation reduces significantly for decreasing values of the damage variable. More specifically for a damage variable of $D = 0.9$, i.e., $D' = 0.1$, the maximum load is reduced by about 50%.

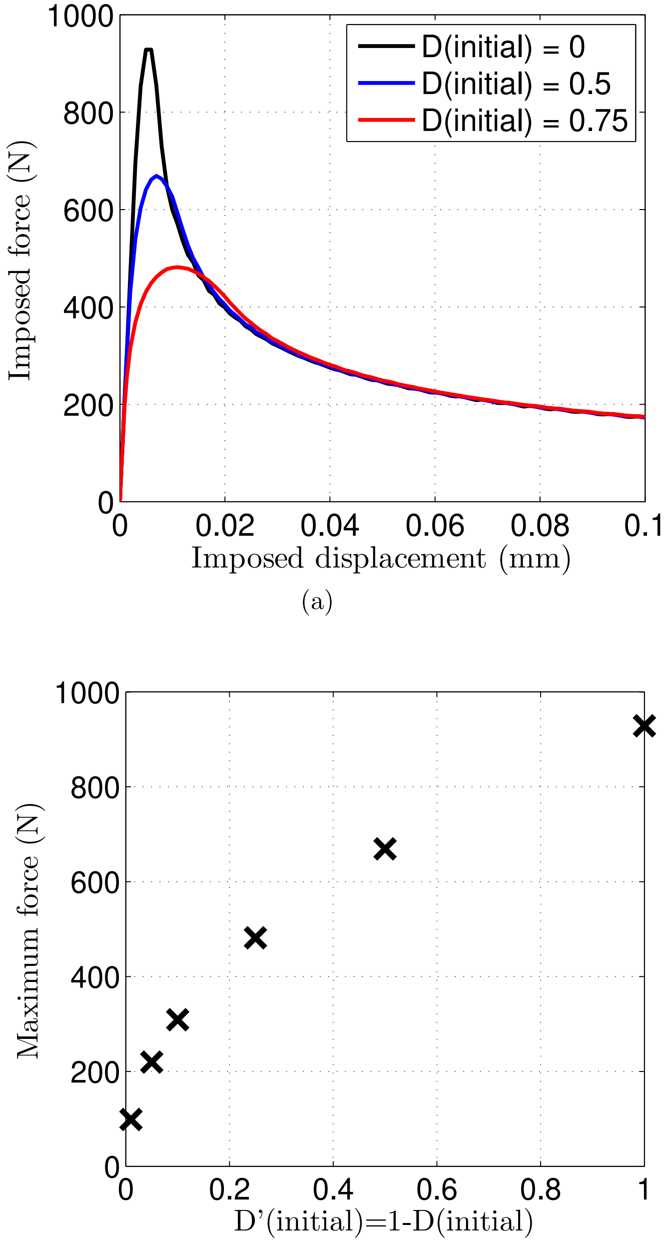

(a)

(b)

Figure 6.14: Result for a DCB made of two 1-mm thick aluminum layers (a): Imposed force VS imposed displacement for various initial value of the damage variable and (b): Maximum force imposed to the DCB before damage propagation as a function of the initial value of the damage variable

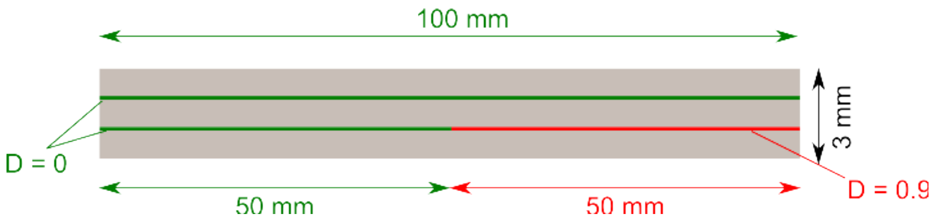

Figure 6.15: Model of a 3-layer 3-mm thick lamina. The green layers are pristine ($D = 0$) while the red layer represents $D = 0.9$.

In conclusion, due to their lack of sensitivity in the range $0 < D < 0.75$, guided waves have a limited ability to measure defect that reduce significantly the maximum carrying load of a structure. However it is important to notice that in the analysis presented in this section, the entire interface was weakened by a constant value of the damage variable. In reality, it is expected that the region in which an interface is weakened is limited in size. Therefore as long as guided waves have the ability to locally quantify the damage variable, minor property losses can be measured.

6.3.4 Application to damage mapping

In this section, guided waves are used to map damages of varying damage variable. First, the geometry with varying damage variables is created in Abaqus. Then guided waves are simulated in the geometry. The FDIW technique is then used to measure the wavenumber at every point of space. Finally, the wavenumber map is converted to a damage variable map using the relationship between the wavenumber and the damage variable showed in Figure 6.10.

First, the two-dimensional model of Figure 6.15 is modeled in Abaqus. This model is a 100-mm long beam made of three 1-mm aluminum layers. The interfaces between the layers are considered pristine, i.e., $D = 0$, except in half of the lower interface, in which the damage variable is $D = 0.9$. The thickness of the inter-facial layer is 10^{-5} m, i.e., two orders of magnitude smaller than the thickness of the aluminum layers.

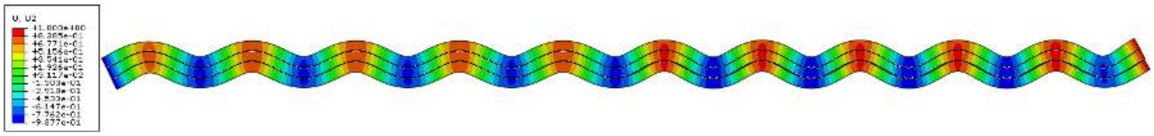

Figure 6.16: Mode shape of the $A0$ mode at 200 kHz for the model of Figure 6.15

A frequency analysis is then conducted at 200 kHz leading to the deformed configuration of Figure 6.16. Note that in this picture, it is nearly impossible to see that the wavenumber is slightly different in the right half with respect to the wavenumber in the left half.

The vertical displacement of the upper layer is then extracted and fed to the FDIW technique leading to the wavenumber map of Figure 6.17a. In this picture, an increase in wavenumber is clearly visible at $x = 50$ mm. The wavenumber is then converted into the damage variable using Figure 6.10 leading to Figure 6.17b.

In Figure 6.17b, the black line represents the damage variable measured using the FDIW and the red line represent the true damage variable of the model. First, it must be noted that the measured damage variable in the pristine region (left) is inaccurate, which is due to the 5% inaccuracy of the FDIW. In the damage region (right) however, the damage variable is appropriately measured. In order to take into account the fact that the accuracy of the FDIW technique is of the order of 5%, the region of wavenumber less than 5% greater than the pristine wavenumber can be replaced by the value of the pristine wavenumber. This artificial filtering leads to the much clearer damage mapping of Figure 6.18.

Even though using the limit of the accuracy of the FDIW technique provides much better damage maps, one must recall that all the features leading to a change of wavenumber of less than 5% with respect to the pristine value will not be detected by this technique. In practice, this means that any damage variable value in the range $0 < D < 0.75$ are automatically mapped to zero, hence weakened interfaces may be missed.

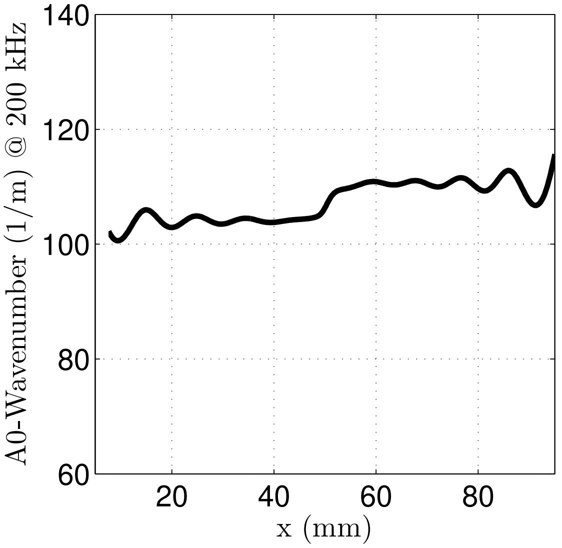

(a)

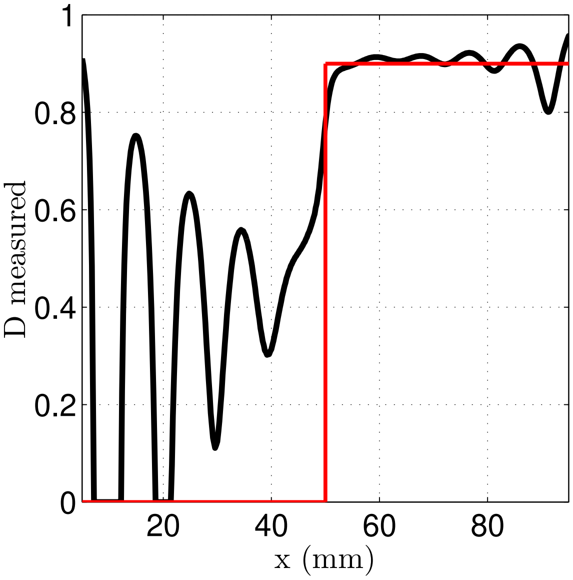

(b)

Figure 6.17: (a) Wavenumber measured by the FDIW technique on the upper layer of Figure 6.16 and (b): Corresponding damage variable measure, black line: measurement and red line: true damage variable

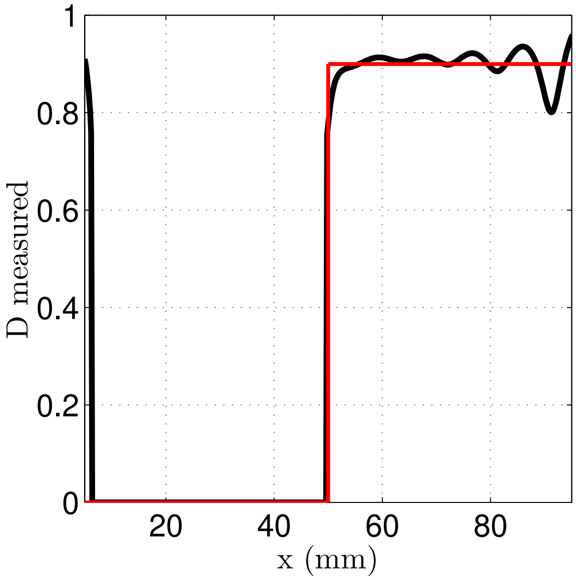

Figure 6.18: Damage variable measured with the FDIW technique with the accuracy threshold of 5%, black line: measurement and red line: true damage variable

Finally, the same process is applied to the three-dimensional model displayed in Figure 6.19. The specimen is a $150 \times 50 \times 3$ mm three layer aluminum beam. One end of the specimen is pinned while an out-of-plane four-cycle tone burst of centered frequency 200 kHz is imposed to the other. Symmetry conditions are imposed to the side of the specimen and the out-of-plane displacement is measured on the upper layer. The interfaces of the lamina are pristine ($D = 0$) except in the circular region of radius 20 mm depicted in red in Figure 6.19 in which $D = 0.9$. After extraction from Abaqus to Matlab, the dataset is mirrored with respect to the plane located at the middle of the defect so that the defect becomes a circle.

The wavenumber map obtained by the FDIW technique is shown in Figure 6.20a in which the circular region corresponding to the defect is clearly visible by an increase of the wavenumber. The wavenumber is then converted to the damage variable of Figure 6.20b using the relationship obtained in Section 6.3.2. The location and the value of the damage variable is correctly measured. Note that an indetermination about the localization of the defect through the thickness remains. In order words,

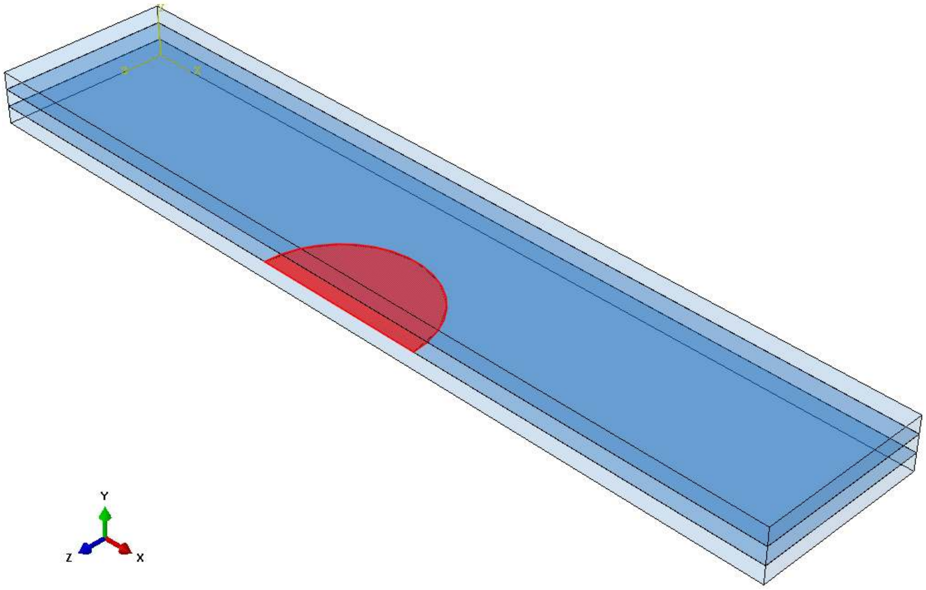

Figure 6.19: Model of a 3-layer $150 \times 50 \times 3$ mm^3 lamina. The interface are pristine ($D = 0$) except in the red region ($D = 0.9$)

it is impossible to determine the depth of the weakened interface with the technique presented in this section.

Based on this measurement, it is possible to implement this geometry and the damage variable distribution in a CZM software to estimate the residual properties.

6.4 Conclusions

This section suggested guidelines for the use of guided waves to quantify the constitutive damage variable of composites samples in order to obtain residual properties estimation with cohesive zone methods. This chapter contributes to the fourth objectives listed in Section 1.5. After an introduction to the cohesive zone methods, the fundamental relationship between guided waves characteristics and the damage variable was presented and then used to measure the damage variable for simple numerical cases. The techniques presented in this chapter are imperfect as they only have the capability to detect severe interface weakening ($D > 0.75$ approximately). This chapter is the foundation of future techniques that would enable the use of CZMs for customized residual properties estimate.

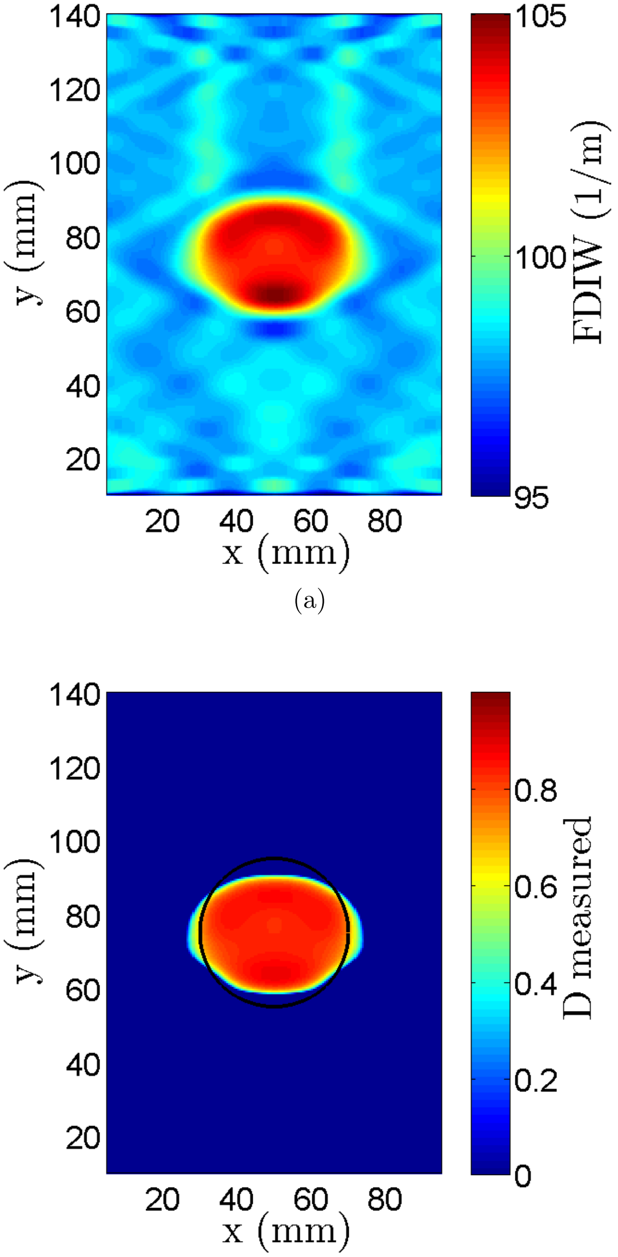

(a)

(b)

Figure 6.20: (a) Wavenumber measured by the FDIW technique on the upper layer of Figure 6.19 and (b): Corresponding damage variable measure, black line: true defect

CHAPTER VII

CONCLUSIONS AND FUTURE WORK

7.1 Summary

This thesis presents the study of novel guided wave-based techniques that locate, quantify and analyze defects in composite materials and metals. These techniques find themselves at the intersection of Structural Health Monitoring (SHM) and Non Destructive Evaluation (NDE) due to their use of both guided wave methods and Guided Wavefield Imaging (GWI) techniques. The primary goals of NDE are limited to the local detection and the evaluation of damages. NDE is often characterized by off-line inspection requiring a cumbersome equipment. On the other hand, SHM generally aims at monitoring the condition of the structure during its regular operating cycle, ideally with embedded sensors. Guided wave methods are commonly considered to be part of SHM methodologies and are widely used for the detection of flaws in plate-like structures. Guided Wavefield Imaging is a technique that relies on the detection of images corresponding to the time evolution guided waves propagation in the structure. Due to the high sensibility of guided waves to internal defects and the amount of information they include, wavefields have the potential to provide extensive information regarding the structural component under consideration. However the main limitation of GWI is the time consuming guided wavefield acquisition process.

The objectives of this dissertation is to develop novel GWI techniques able to detect, locate and quantify defects in metals and composite materials while reducing the acquisition time. In addition, the work attempts to link guided wave signatures to damage parameters in order to provide strength estimates. Two complimentary techniques are developed to achieve the objectives. The first technique, namely the Sparse Wavefield Reconstruction (SWR) reduces the acquisition time required to detect a wavefield. The approach employs sparse measurements, i.e., fewer measurements than required by the traditional sampling criteria, scattered within the region of inspection. The SWR technique is applied for the reconstruction of various experimental wavefields with compression ratios of about 90%, where compression ratio denotes the reduction of point measurement with the SWR technique with respect to traditional sampling criteria. The second technique, namely the Frequency Domain Instantaneous Wavenumber (FDIW), focuses on the quantification of a defect through local measurement of the wavenumber. The FDIW is applied to multiple defects and provides and estimation of the three-dimensional shape of the defects. . The combination of these two techniques provides an inspection methodology that reduces the inspection time and provides detailed defect quantification. Finally, a novel methodology bridging guided wave measurements and residual life prediction is presented. This study measures the constitutive damage parameters of composite panels in order to obtain residual properties estimates through damage mechanics numerical models. This methodology is used to measure the constitutive damage variable of a numerically simulated damage and show promising results for an experimental application.

7.2 Sources of errors, uncertainties and inaccuracies

There exist multiple potential sources of errors, uncertainties and inaccuracies that may affect the detection and quantification of damages with the Sparse Wavefield Reconstruction (SWR) and the Frequency Domain Instantaneous Wavenumber (FDIW).

In the case of the SWR process, the errors on the reconstruction are driven by the quality of the model used to reconstruct the sparse measurements. Section 3.8

quantifies the error induced by multiple model-experiment mismatches in term of reconstruction coherence. First, the dispersion relations used for the reconstruction of sparse measurements are corrupted by a scaling factor in Section 3.8.1. The quality of the reconstruction is then evaluated for multiple values of the scaling parameter. This parametric study concluded that using inaccurate dispersion relations decreases significantly the quality of the reconstruction. In this thesis, the dispersion relations used for the reconstructions were obtained by means of a Semi Analytical Finite Element (SAFE) method [41], leading to an error due to the inaccuracy of the estimate of the material properties. A calibration experiment could be conducted prior to the reconstruction to measure the dispersion relations in a pristine region of the studied specimen to ensure the use of the appropriate dispersion relations and maximize the reconstruction coherence. Second, the influence of the amplitude decay exponent on the reconstruction quality is quantified in Section 3.8.2. This study shows that the impact of the use of an inaccurate amplitude decay exponent is bonded. However, in the model used in the reconstruction, the energy dissipation phenomena are neglected. It would therefore be valuable to use an empirical model to better model the amplitude decay exponent. Finally, the impact of the measurement noise on the quality of the reconstruction was studied in Section 3.8.5 by numerically adding noise to a noise-free numerical dataset. It was concluded that the measurement noise could have a major impact on the quality of the reconstruction. Obtaining a complete parametric study to quantify the effect of each model-experiment mismatch on the quality of the reconstruction could be achieved by attempting reconstruction on various specimens, followed by parametric studies similar to the ones presented in Section 3.8. This process would have to be repeated for a large number of specimens in order to use statistical analysis to quantify the effect of each parameter. In order to isolate each individual parameters, numerical models could be used. The combined effect of multiple parameters could then be studied with the experimental inspection of pristine specimens.

In the case of the FDIW, the inaccuracies on the damage quantification originate primarily from two sources. First, the measurement noise corrupts the measured wavefield, hence decreases the quality of the wavenumber estimate. In order to ensure a sufficient signal-to-noise ratio of the measurements and to reduce the effect of noise, reflective tape is used to increase the quality of the reflection of the SDLV from the specimen. In addition, power transducers are used to increase the amplitude of the excited waves. Second, the estimate of the through-the-thickness defect location is achieved by using the model described in Section 4.4. In this model, it is assumed that the interaction between the sub-plates on either side of a delamination is negligible. This assumption is however a source of uncertainty for the depth estimate. Indeed, the contact between either sides of a delamination may corrupt the wavenumber measured in the delaminated region. Moreover, the disbond in a delaminated region may not be a clear discontinuity. In order to judge the quality of the depth estimation, it is necessary to compare the results obtained with the FDIW technique to truth measurements. Truth measurements could be obtained by NDE X-ray technique for example. The difference between the true defect and the measured defect is detailed in the case of the Teflon disk insert presented in Section 4.4 and is less than one layer. In order to fully assess the impact of the inaccuracies of the damage quantification, the FDIW should be applied to a statistically significant number of specimens for which truth measurements are available. More specifically, the estimation of the size, in-plane coordinates and depth of a large number of known defects should be compared with the true geometry of the corresponding defects. This analysis could be conducted numerically first by designing a set of models with defects of increasing complexity, followed by experimentations by manufacturing samples with known-defects. The variance value of the difference between the true and the measured dimensions would indicate the typical error of the FDIW technique.

7.3 Contributions

The following contributions to Guided Wavefield Imaging (GWI) are made:

1. The Sparse Wavefield Reconstruction (SWR). The methodology employs Compressed Sensing and the physics of Lamb waves to extrapolate the information embedded in sparse measurements to reconstruct a wavefield. The formulation relies on the use of the fundamental propagation equation (Section 3.4) to interpret sparse measurements (Section 3.5). An implementation of the process to reconstruct wavefields, reducing drastically the acquisition time of guided waves is provided (Section 3.6). The proposed methodology is applied to multiple specimens with various defects which demonstrate the ability to resolve complex geometries (Section 3.7). The proposed technique presents the unique feature to use prior knowledge of the inspected specimen, thus allowing damage localization in addition to wavefield reconstruction along with compression ratios up to 90% with respect to Nyquist sampling criteria.

2. The Frequency Domain Instantaneous Wavenumber (FDIW). This is an efficient tool for damage mapping in composite materials (Section 4.3). An approach to relate a wavenumber map to a three-dimensional defect map is introduced (Section 4.4). This approach leads to an efficient 3D damage characterization process in both isotropic and anisotropic materials. The accuracy of the process is quantified (Section 4.5) and results are shown for multiple specimens with various defects (Section 4.6).

3. SWR and FDIW integration and comparison against NDE techniques. An approach integrating the SWR and the FDIW is proposed (Section 5.4), implemented and applied to realistic impact delamination in composites (Section 5.6). Results are compared to existing NDE methodologies (Section 5.5). Discussion to improve the guided waves excitation-measurement setup commonly

used within the GWI research community are proposed with non-bonded excitation (Section 5.2) and continuously scanning Laser vibrometer (Section 5.3).

4. Constitutive damage parameters detection and analysis. The Cohesive Zone Model (CZM) are introduced (Section 6.2). The model to obtain a relationship between GWI and the damage parameter of CZM is presented (Section 6.3.2). This model is then used to map partially weakened bonds using GWI (Section 6.3.4). This study presents the guidelines to obtain residual properties estimate from GWI hence facilitating the decision making process once a defect is detected and quantified.

7.4 Future work

This section lists the proposed avenues to further advance the work presented in this dissertation.

7.4.1 Non-contact excitation

As described in Section 5.1, the use of a contact-free excitation device, such as a pulsed laser or an air-coupled transducer, is highly desirable to improve the feasibility of the presented integrated approach and the quality of the results. Aside from making the experimental setup simpler, it would also remove the need to permanently bond transducers on the structure, which is a concern in the aerospace industry for example. Moreover, a movable source would easily enable the possibility to automatically illuminate a defect from multiple directions.

7.4.2 Improvements of the FDIW and SWR

This section lists three suggestions to improve the FDIW and the SWR techniques presented in this research. First, the inspection of multiple frequencies with the FDIW technique would lead to a more accurate defect size and depth estimate. A process similar to the one presented in [137], which studies the wavenumber at various frequencies to obtain a robust depth estimate, could be considered.

Second, solving of the model-experiment mismatches issues of the SWR process described in Section 3.8 could crucially improve the performances of the reconstruction. The mismatches could be reduced by performing a calibration experiment prior to the sparse measurement of a given group of identical specimen. Another avenue to reduce the influence of these mismatches is to use additional information regarding the expected wavefield represented by the sparse measurements, such as the location of the transducer or the excitation function. Finally, the influence of mismatches could be reduced by letting the parameters driving the reconstruction, such as the wavenumber, to fluctuate within a finite range. Compressed Sensing could then be used to find the optimal set of parameters while reconstructing the wavefield.

Finally, an intelligent sampling scheme could be used to minimize the number of sparse measurements and improve the overall results of the SWR process. An intelligent sampling scheme means that the reconstruction would be attempted with very few sparse measurements at first, leading to an information regarding the optimal area in which further measurements should be measured next. This process could then be iterated until appropriate reconstruction and feature resolution is obtained. To achieve this intelligent sampling scheme, it would be required to resolve the SWR process in real time in parallel to the measurements.

7.4.3 Promising application areas

Chapter 5 presents the integration of the Guided Wavefield Imaging (GWI) techniques developed in this document. This integration minimizes the inspection duration by using sparse measurements to detect and locate defects and dense measurements to quantify the defects. This technique requires the optical access to the inspected structure. Indeed, the area of inspection to be measured by the Scanning Laser

Doppler Vibrometer (SLDV) must be accessible to the laser beam. This limits the application of the technique to external structures only. For example, the inspection of internal human tissue, or the inspection of buried pipes would not be possible using GWI techniques. Similarly, the internal components of a structure would have to be disassembled to be inspected using GWI. The other limitation is related to the thin plate-like assumption required for the application of the GWI techniques. Based on this constraint, thick structure such as load-carrying walls are not good candidates to be inspected with GWI.

Multiple applications of the techniques presented in this document can be found in external structure inspection for example, aircraft or rotorcraft fuselage, the body of a car or the haul of a ship. Defects detected by the techniques presented in this dissertation could include impact defects, corrosion, fatigue cracks, manufacturing defects such as foreign object inserts or external pipe erosion. Other applications includes the monitoring of thin 3D-printed parts. Quality inspection of thin structures with multiple thicknesses could also be achieved with these techniques. Damage quantification obtained with the GWI techniques could be coupled with ultrasonic techniques such as pulse-echo to achieve finer defect resolutions.

7.4.4 Damage variable measurement

Chapter 6 only presents preliminary investigations towards the use of guided waves for strength estimations. The methodology presented in this document has been proven to be efficient for severe defects only. Other guided wave damage quantification techniques such as phase-based techniques [27] for example could be more sensitive to non-severe interface weakening. Moreover, other NDE techniques, such as thermography, may also provide a damage variable assessment by relating the heat radiation reflected by partially weakened interfaces to the damage variable.

REFERENCES

[1] Boris Muravin, Gregory Muravin, and Ludmila Lezvinsky. The fundamentals of structural health monitoring by the acoustic emission method. In *Proceedings of the 20th International Acoustic Emission Symposium*, pages 253–258, 2010.

[2] Hoon Sohn, Charles R Farrar, Francois M Hemez, Devin D Shunk, Daniel W Stinemates, Brett R Nadler, and Jerry J Czarnecki. *A review of structural health monitoring literature: 1996-2001.* Los Alamos National Laboratory Los Alamos, NM, 2004.

[3] Charles R Farrar and Keith Worden. An introduction to structural health monitoring. *Philosophical Transactions of the Royal Society of London A: Mathematical, Physical and Engineering Sciences*, 365(1851):303–315, 2007.

[4] Donald O Thompson and Dale E Chimenti. *Review of progress in quantitative nondestructive evaluation*, volume 18. Springer Science & Business Media, 2012.

[5] NASA; Preferred Reliability Practices. Ultrasonic testing of aerospace materials. *Practice No. PT-TE-1422*, pages 1–6.

[6] David N Alleyne and Peter Cawley. Optimization of lamb wave inspection techniques. *Ndt & E International*, 25(1):11–22, 1992.

[7] P Cawley. The rapid non-destructive inspection of large composite structures. *Composites*, 25(5):351–357, 1994.

[8] Sergio H Diaz Valdes and Costas Soutis. Real-time nondestructive evaluation of fiber composite laminates using low-frequency lamb waves. *The Journal of the Acoustical Society of America*, 111:2026, 2002.

[9] Seth S Kessler, S Mark Spearing, and Constantinos Soutis. Damage detection in composite materials using lamb wave methods. *Smart Materials and Structures*, 11(2):269, 2002.

[10] A Demma, D Alleyne, and B Pavlakovic. Testing of buried pipelines using guided waves. In *3rd Middle East Nondestructive Testing Conference & Exhibition*, 2005.

[11] Massimo Ruzzene. Frequency–wavenumber domain filtering for improved damage visualization. *Smart materials and structures*, 16(6):2116, 2007.

[12] Thomas E Michaels, Jennifer E Michaels, and Massimo Ruzzene. Frequency–wavenumber domain analysis of guided wavefields. *Ultrasonics*, 51(4):452–466, 2011.

[13] Luca de Marchi, Alessandro Marzani, Nicolo Speciale, and Viola E. A passive monitoring technique based on dispersion compensation to locate impacts in plate-like structures. *Smart Materials and Structures*, 20(3), 2011.

[14] AJ Croxford, PD Wilcox, BW Drinkwater, and G Konstantinidis. Strategies for guided-wave structural health monitoring. *Proceedings of the Royal Society A: Mathematical, Physical and Engineering Science*, 463(2087):2961–2981, 2007.

[15] Jennifer E Michaels. Detection, localization and characterization of damage in plates with an in situ array of spatially distributed ultrasonic sensors. *Smart Materials and Structures*, 17(3):035035, 2008.

[16] Thomas Clarke, Peter Cawley, Paul David Wilcox, and Anthony John Croxford. Evaluation of the damage detection capability of a sparse-array guided-wave shm system applied to a complex structure under varying thermal conditions. *Ultrasonics, Ferroelectrics and Frequency Control, IEEE Transactions on*, 56(12):2666–2678, 2009.

[17] Fei Yan, Roger L Royer, and Joseph L Rose. Ultrasonic guided wave imaging techniques in structural health monitoring. *Journal of Intelligent Material Systems and Structures*, 21(3):377–384, 2010.

[18] Z Sharif-Khodaei and MH Aliabadi. Assessment of delay-and-sum algorithms for damage detection in aluminium and composite plates. *Smart Materials and Structures*, 23(7):075007, 2014.

[19] H Sohn, D Dutta, JY Yang, M DeSimio, S Olson, and E Swenson. Automated detection of delamination and disbond from wavefield images obtained using a scanning laser vibrometer. *Smart Materials and Structures*, 20(4):045017, 2011.

[20] MJ Sundaresan, PF Pai, A Ghoshal, MJ Schulz, F Ferguson, and JH Chung. Methods of distributed sensing for health monitoring of composite material structures. *Composites Part A: Applied Science and Manufacturing*, 32:1357–1374, 2001.

[21] WJ Staszewski, BC Lee, and R Traynor. Fatigue crack detection in metallic structures with lamb waves and 3d laser vibrometry. *Measurement Science and Technology*, 18(3):727, 2007.

[22] Lingyu Yu, Cara AC Leckey, and Zhenhua Tian. Study on crack scattering in aluminum plates with lamb wave frequency–wavenumber analysis. *Smart Materials and Structures*, 22(6):065019, 2013.

[23] Yun-Kyu An, Byeongjin Park, and Hoon Sohn. Complete noncontact laser ultrasonic imaging for automated crack visualization in a plate. *Smart Materials and Structures*, 22(2):025022, 2013.

[24] Matthew D Rogge and Cara AC Leckey. Characterization of impact damage in composite laminates using guided wavefield imaging and local wavenumber domain analysis. *Ultrasonics*, 53(7):1217–1226, 2013.

[25] MD Rogge and CAC Leckey. Local guided wavefield analysis for characterization of delaminations in composites. In *REVIEW OF PROGRESS IN QUANTITATIVE NONDESTRUCTIVE EVALUATION: VOLUME 32*, volume 1511, pages 963–970. AIP Publishing, 2013.

[26] Matthew D Rogge and PH Johnston. Wavenumber imaging for damage detection and measurement. 1430:761, 2012.

[27] Aaron Darnton and Massimo Ruzzene. Phase congruency for damage mapping in composites. In *Review of Progress in Quantitative Non-Destructive Engineering*, 2015.

[28] Aaron Darnton and Massimo Ruzzene. Damage mapping in composites with phase gradient. In *ASME 2014 Conference on Smart Materials, Adaptive Structures and Intelligent Systems*. American Society of Mechanical Engineers, 2014.

[29] Polytec. *PSV-400 Scanning Vibrometer*, 2011.

[30] Joseph L Rose. *Ultrasonic guided waves in solid media*. Cambridge university press, 2014.

[31] Zhongqing Su, Lin Ye, and Ye Lu. Guided lamb waves for identification of damage in composite structures: A review. *Journal of sound and vibration*, 295(3):753–780, 2006.

[32] Joseph L Rose. A baseline and vision of ultrasonic guided wave inspection potential. *Journal of pressure vessel technology*, 124(3):273–282, 2002.

[33] Ajay Raghavan and Carlos ES Cesnik. Review of guided-wave structural health monitoring. *Shock and Vibration Digest*, 39(2):91–116, 2007.

[34] Horace Lamb. On waves in an elastic plate. *Proceedings of the Royal Society of London. Series A*, 93(648):114–128, 1917.

[35] DC Worlton. Experimental confirmation of lamb waves at megacycle frequencies. *Journal of Applied Physics*, 32(6):967–971, 1961.

[36] Karl F Graff. *Wave motion in elastic solids*. Courier Corporation, 2012.

[37] F Schöpfer, F Binder, A Wöstehoff, T Schuster, S von Ende, S Föll, and R Lammering. Accurate determination of dispersion curves of guided waves in plates by applying the matrix pencil method to laser vibrometer measurement data. *CEAS Aeronautical Journal*, 4(1):61–68, 2013.

[38] RB Nelson, SB Dong, and RD Kalra. Vibrations and waves in laminated orthotropic circular cylinders. *Journal of Sound and Vibration*, 18(3):429–444, 1971.

[39] SB Dong and Richard B Nelson. On natural vibrations and waves in laminated orthotropic plates. *Journal of applied mechanics*, 39(3):739–745, 1972.

[40] PJ Shorter. Wave propagation and damping in linear viscoelastic laminates. *The Journal of the Acoustical Society of America*, 115(5):1917–1925, 2004.

[41] Ivan Bartoli, Alessandro Marzani, Francesco Lanza di Scalea, and Erasmo Viola. Modeling wave propagation in damped waveguides of arbitrary cross-section. *Journal of Sound and Vibration*, 295(3):685–707, 2006.

[42] Victor Giurgiutiu. Lamb wave generation with piezoelectric wafer active sensors for structural health monitoring. *Smart Structures and Materials 2003*, 5056:111–122, 2003.

[43] Victor Giurgiutiu, Jingjing Bao, and Wei Zhao. Piezoelectric wafer active sensor embedded ultrasonics in beams and plates. *Experimental Mechanics*, 43(4):428–449, 2003.

[44] Amir Manbachi and Richard SC Cobbold. Development and application of piezoelectric materials for ultrasound generation and detection. *Ultrasound*, 19(4):187–196, 2011.

[45] M Gresil and V Giurgiutiu. Guided wave propagation in composite laminates using piezoelectric wafer active sensors. *Aeronautical Journal*, 117(1196):971, 2013.

[46] Ltd APC International. Ultrasonic power transducer, October 2015.

[47] E.A. Neppiras. The pre-stressed piezoelectric sandwich transducer. In *Ultrasonics international 1973*. Ultrasonics International 1973 Conference Proceedings.

[48] Lin Shuyu and Zhang Fucheng. Study of vibrational characteristics for piezoelectric sandwich ultrasonic transducers. *Ultrasonics*, 32(1):39–42, 1994.

[49] Lin Shuyu. Load characteristics of high power sandwich piezoelectric ultrasonic transducers. *Ultrasonics*, 43(5):365–373, 2005.

[50] Amir Abdullah, Mohsen Shahini, and Abbas Pak. An approach to design a high power piezoelectric ultrasonic transducer. *Journal of Electroceramics*, 22(4):369–382, 2009.

[51] R Bruce Thompson. Physical principles of measurements with emat transducers. *Physical acoustics*, 19:157–200, 1990.

[52] J.P Joule. On the effects of magnetism upon the dimension of iron and steel bars. *The London, Edinburgh and Dublin philosophical magazine and journal of science (Taylor & Francis)*, 30:76–87, 1847.

[53] David K Hsu, Kwang-Hee Im, and In-Young Yang. Applications of electromagnetic acoustic transducers in the nde of non-conducting composite materials. *KSME International Journal*, 13(5):403–413, 1999.

[54] M Luukkala and P Meriläinen. Metal plate testing using airborne ultrasound. *Ultrasonics*, 11(5):218–221, 1973.

[55] D Tuzzeo and F Lanza di Scalea. Noncontact air-coupled guided wave ultrasonics for detection of thinning defects in aluminum plates. *Journal of Research in Nondestructive Evaluation*, 13(2):61–77, 2001.

[56] M Castaings and B Hosten. Lamb and sh waves generated and detected by air-coupled ultrasonic transducers in composite material plates. *Ndt & E International*, 34(4):249–258, 2001.

[57] Thomas E Michaels and Jennifer E Michaels. Application of acoustic wavefield imaging to non-contact ultrasonic inspection of bonded components. In *AIP Conference Proceedings*, volume 820, page 1484. IOP INSTITUTE OF PHYSICS PUBLISHING LTD, 2006.

[58] P-Y Le Bas, MC Remillieux, L Pieczonka, JA Ten Cate, BE Anderson, and TJ Ulrich. Damage imaging in a laminated composite plate using an air-coupled time reversal mirror. *Applied Physics Letters*, 107(18):184102, 2015.

[59] Richard M White. Generation of elastic waves by transient surface heating. *Journal of Applied Physics*, 34(12):3559–3567, 1963.

[60] Jong-Ho Park, Joon-Hyun Lee, and Min-Rae Lee. The propagation characteristics of laser-generated guided wave in carbon steel plate with wall-thinning. *Asia-Pacific Conference on NDT, 5th–10th Nov*, 2006.

[61] International Society for Optics and Photonics. *Development of an optic-based guided wave excitation technique*, 2009.

[62] Robert E Green. Non-contact ultrasonic techniques. *Ultrasonics*, 42(1):9–16, 2004.

[63] Dipesh Dhital, Jung Ryul Lee, Chan Yik Park, and Eric Flynn. Laser excitation and fully non-contact sensing ultrasonic propagation imaging system for damage evaluation. In *SPIE Smart Structures and Materials+ Nondestructive Evaluation and Health Monitoring*, pages 83430D–83430D. International Society for Optics and Photonics, 2012.

[64] Christian Doppler. Ueber das farbige licht der doppelsterne und einiger anderer gestirne des himmels: Versuch einer das bradley'sche aberrations-theorem als integrirenden theil in sich schliessenden allgemeineren theorie (about the coloured light of the binary stars and some other stars of the heavens). 1842.

[65] CT Truong, D-H Kang, J-R Lee, and CR Farrar. Comparative study of laser doppler vibrometer and capacitive air-coupled transducer for ultrasonic propagation imager and the new development of an efficient ultrasonic wavenumber imaging algorithm. *Strain*, pages 332–342, 2015.

[66] Harry Nyquist. Certain topics in telegraph transmission theory. *American Institute of Electrical Engineers, Transactions of the*, 47(2):617–644, 1928.

[67] Pierre Duhamel and Martin Vetterli. Fast fourier transforms: a tutorial review and a state of the art. *Signal processing*, 19(4):259–299, 1990.

[68] E Cupido, S Morel, and D Smith. Multipoint laser doppler vibrometer for transient analysis. *Proceedings of IMAC XXI, Orlando, USA*, 2003.

[69] Yu Fu, Min Guo, and Poh Boon Phua. Multipoint laser doppler vibrometry with single detector: principles, implementations, and signal analyses. *Applied optics*, 50(10):1280–1288, 2011.

[70] Eric B. Flynn. Embedded mutli-tone ultrasonic excitation and continuousscanning laser doppler vibrometry for rapid and remote imaging of structural defects. In *7th European Workshop on Structural Health Monitoring*, 2014.

[71] Emmanuel J Candes. Compressive sampling. In *Proceedings oh the International Congress of Mathematicians*, volume 3, pages 1433–1452. Madrid, Spain, 2006.

[72] D.L. Donoho. Compressed sensing. *IEEE Trans. Inform. Theory*, 52:1289–1306, 2006.

[73] Emmanuel J Candes and Michael B Wakin. An introduction to compressive sampling. *Signal Processing Magazine, IEEE*, 25(2):21–30, 2008.

[74] Marco F. Duarte, Mark A. Davenport, Dharmpal Takhar, Jason N. Laska, Ting Sun, Kevin F. Kelly, and Richard G. Baraniuk. Single-pixel imaging via compressive sampling. *IEEE Signal Processing Magazine*, 25(2):83, 2008.

[75] Michael Lustig, David L Donoho, Juan M Santos, and John M Pauly. Compressed sensing mri. *Signal Processing Magazine, IEEE*, 25(2):72–82, 2008.

[76] Dong Liang Haifeng Wang and Leslie Ying. Pseudo 2d random sampling for compressed sensing mri. *Engineering in Medicine and Biology Society, 2009. EMBC 2009. Annual International Conference of the IEEE*, 2009.

[77] Matthew Herman and Thomas Strohmer. Compressed sensing radar. In *Radar Conference, 2008. RADAR'08. IEEE*, pages 1–6. IEEE, 2008.

[78] Gabriel Peyre. Best basis compressed sensing. *Signal Processing, IEEE Transactions on*, 58(5):2613–2622, 2010.

[79] Zaixing HE, Takahiro OGAWA, and Miki HASEYAMA. The simplest measurement matrix for compressed sensing of natural images. In *Proceedings of 2010 IEEE 17th International Conference on Image Processing September 26-29, 2010, Hong Kong*. IEEE, 2010.

[80] Graeme Pope. Compressive sensing: a summary of reconstruction algorithms. Master's thesis, ETH, Swiss Federal Institute of Technology Zurich, Department of Computer Science, 2009.

[81] Stéphane G Mallat and Zhifeng Zhang. Matching pursuits with time-frequency dictionaries. *Signal Processing, IEEE Transactions on*, 41(12):3397–3415, 1993.

[82] Yagyensh Chandra Pati, Ramin Rezaiifar, and PS Krishnaprasad. Orthogonal matching pursuit: Recursive function approximation with applications to wavelet decomposition. In *Signals, Systems and Computers, 1993. 1993 Conference Record of The Twenty-Seventh Asilomar Conference on*, pages 40–44. IEEE, 1993.

[83] Joel A Tropp and Anna C Gilbert. Signal recovery from random measurements via orthogonal matching pursuit. *Information Theory, IEEE Transactions on*, 53(12):4655–4666, 2007.

[84] T. Tony Cai and Lie Wang. Orthogonal matching pursuit for sparse signal recovery with noise. *IEEE Trans. Inform. Theory*, 57(7):4680–4688, July 2011.

[85] Shaobing Chen and David Donoho. Basis pursuit. In *Signals, Systems and Computers, 1994. 1994 Conference Record of the Twenty-Eighth Asilomar Conference on*, volume 1, pages 41–44. IEEE, 1994.

[86] Donoho, Chen, and Saunders. Atomic decomposition by basis pursuit. *SIAM J. Sci. Comput*, 20:33–61, 1998.

[87] Chengbo Li. *An efficient algorithm for total variation regularization with applications to the single pixel camera and compressive sensing*. PhD thesis, Citeseer, 2009.

[88] Leonid I Rudin, Stanley Osher, and Emad Fatemi. Nonlinear total variation based noise removal algorithms. *Physica D: Nonlinear Phenomena*, 60(1):259–268, 1992.

[89] Emmanuel J Candes, Yonina C Eldar, Deanna Needell, and Paige Randall. Compressed sensing with coherent and redundant dictionaries. *Applied and Computational Harmonic Analysis*, 31(1):59–73, 2011.

[90] Afonso S Bandeira, Edgar Dobriban, Dustin G Mixon, and William F Sawin. Certifying the restricted isometry property is hard. *arXiv preprint arXiv:1204.1580*, 2012.

[91] Sara Cohen. Compressive sensing with highly coherent dictionaries. *Undergraduate Senior Thesis, University of California, Davis*, 2012.

[92] Emmanuel J Candès, Yaniv Plan, et al. Near-ideal model selection by l1 minimization. *The Annals of Statistics*, 37(5A):2145–2177, 2009.

[93] Yair Weiss, Hyun Sung Chang, and William T Freeman. Learning compressed sensing. In *Snowbird Learning Workshop, Allerton, CA*. Citeseer, Citeseer, 2007.

[94] E. van den Berg and M. P. Friedlander. Probing the pareto frontier for basis pursuit solutions. *SIAM Journal on Scientific Computing*, 31(2):890–912, 2008.

[95] E. van den Berg and M. P. Friedlander. SPGL1: A solver for large-scale sparse reconstruction, June 2007. http://www.cs.ubc.ca/labs/scl/spgl1.

[96] Robert Tibshirani. Regression shrinkage and selection via the lasso. *Journal of the Royal Statistical Society. Series B (Methodological)*, pages 267–288, 1996.

[97] B WU, Y HUANG, and H LI. Sparse reconstruction of flaw signal from noisy ultrasonic data: A bayesian framework. *Structural Health Monitoring 2015*, 2015.

[98] A GOLATO, S SANTHANAM, F AHMAD, and MG AMIN. Multi-path exploitation in a sparse reconstruction approachto lamb wave based structural health monitoring. *Structural Health Monitoring 2015*, 2015.

[99] Paul D Wilcox. A rapid signal processing technique to remove the effect of dispersion from guided wave signals. *Ultrasonics, Ferroelectrics and Frequency Control, IEEE Transactions on*, 50(4):419–427, 2003.

[100] Emanuele Baravelli, Luca De Marchi, Nicolò Speciale, and Massimo Ruzzene. Bimodal warped frequency transform (bwft) for guided wave mode conversion characterization. *International Society for Optics and Photonics*, 2012.

[101] Luca De Marchi, Alessandro Perelli, and Alessandro Marzani. A signal processing approach to exploit chirp excitation in lamb wave defect detection and localization procedures. *Mechanical Systems and Signal Processing*, 39(1-2):20–31, Aug 2013.

[102] Alessandro Perelli, Luca De Marchi, Alessandro Marzani, and Nicolo Speciale. Frequency warped cross-wavelet multiresolution analysis of guided waves for impact localization. *Signal Processing*, 96:51–62, Mar 2014.

[103] Alessandro Perelli, Luca De Marchi, Luca Flamigni, Alessandro Marzani, and Guido Masetti. Best basis compressive sensing of guided waves in structural health monitoring. *Digital Signal Processing*, 42:35–42, 2015.

[104] Tommaso Di Ianni, Alessandro Perelli, Luca De Marchi, and Alessandro Marzani. Compressive sensing for full wavefield image recovery in structural monitoring applications. In *7th European Workshop on Structural Health Monitoring*, 2014.

[105] Tommaso Di Ianni, Luca De Marchi, Alessandro Perelli, and Alessandro Marzani. Compressive sensing of full wave field data for structural health monitoring applications. *Ultrasonics, Ferroelectrics, and Frequency Control, IEEE Transactions on*, 62(7):1373–1383, 2015.

[106] Amara Graps. An introduction to wavelets. *IEEE Computational Science & Engineering*, 1995.

[107] Joel B Harley and Jose MF Moura. Sparse recovery of the multimodal and dispersive characteristics of lamb waves. *The Journal of the Acoustical Society of America*, 133:2732–2745, 2013.

[108] Joel B. Harley and Jose M. F. Moura. Data-driven matched field processing for lamb wave structural health monitoring. *The Journal of the Acoustical Society of America*, 135(3):1231–1244, Mar 2014.

[109] Joel B. Harley. Characterizing and predicting guided wave eigenmode behavior through sparse representations. *IEEE*, 2015.

[110] Jeffrey M Druce, Jarvis D Haupt, and Stefano Gonella. Anomaly-sensitive dictionary learning for structural diagnostics from ultrasonic wavefields. *Ultrasonics, Ferroelectrics, and Frequency Control, IEEE Transactions on*, 62(7):1384–1396, 2015.

[111] Arno Volker and Paul van Neer. Imaging beyond aliasing. In *Review of Progress in Quantitative Nondestructive Evaluation*. eds. D. E. Chimenti and L. J. Bond, (American Institute of Physics, Melville, NY), 2015.

[112] Olivier Mesnil and Massimo Ruzzene. Sparse wavefield reconstruction and source detection using compressed sensing. *Ultrasonics*, 2016.

[113] Karl F Graff. *Wave motion in elastic solids*. Courier Corporation, 1975.

[114] Jan Achenbach. *Wave propagation in elastic solids*, volume 16. Elsevier, 2012.

[115] Alexander Velichko and Paul D Wilcox. Guided wave arrays for high resolution inspection. *The Journal of the Acoustical Society of America*, 123(1):186–196, 2008.

[116] James S Hall and Jennifer E Michaels. Model-based parameter estimation for characterizing wave propagation in a homogeneous medium. *Inverse Problems*, 27(3):035002, 2011.

[117] Michel Bouchon. A simple method to calculate green's functions for elastic layered media. *Bulletin of the Seismological Society of America*, 71(4):959–971, 1981.

[118] Ross Levine. *Ultrasonic Guided Wave Imaging via Sparse Reconstruction.* PhD thesis, Georgia Institute of Technology, 2014.

[119] Gilles Hennenfent and Felix J Herrmann. Simply denoise: wavefield reconstruction via jittered undersampling. *Geophysics*, 73(3):V19–V28, 2008.

[120] Robert Bridson. Fast poisson disk sampling in arbitrary dimensions. In *SIGGRAPH Sketches*, page 22, 2007.

[121] Yuval Eldar, Michael Lindenbaum, Moshe Porat, and Yehoshua Y Zeevi. The farthest point strategy for progressive image sampling. *Image Processing, IEEE Transactions on*, 6(9):1305–1315, 1997.

[122] PD Wilcox, MJS Lowe, and P Cawley. Mode and transducer selection for long range lamb wave inspection. *Journal of intelligent material systems and structures*, 12(8):553–565, 2001.

[123] Jennifer E. Michaels Westin B. Williams and Thomas E. Michaels. Using scattering information to enhance sparse array imaging of impact damage in composite materials. In *Review of Progress in Quantitative Nondestructive Evaluation.* eds. D. E. Chimenti and L. J. Bond, (American Institute of Physics, Melville, NY), 2015.

[124] Lazarus H Tenek, Edmund G Henneke, and Max D Gunzburger. Vibration of delaminated composite plates and some applications to non-destructive testing. *Composite Structures*, 23(3):253–262, 1993.

[125] Robert G Stockwell, Robert P Lowe, and L Mansinha. Instantaneous wavevector analysis. In *AeroSense'97*, pages 349–358. International Society for Optics and Photonics, 1997.

[126] F. Raymond Parker Matthew D. Rogge. Instantaneous wavenumber estimation of guided wavefield images for characterization of damage in composite structures. 2013. NASA/TM-2013, internal NASA report (received via private communication from author).

[127] Bradley Lee Barnhart. *The Hilbert-Huang Transform: theory, applications, development.* PhD thesis, University of Iowa, 2011.

[128] Norden E Huang and Zhaohua Wu. A review on hilbert-huang transform: Method and its applications to geophysical studies. *Reviews of Geophysics*, 46(2):RG2006, 2008.

[129] Yue Min Zhu, Françoise Peyrin, and Robert Goutte. The use of a two-dimensional hilbert transform for wigner analysis of 2-dimensional real signals. *Signal Processing*, 19(3):205–220, 1990.

[130] Poularikas. *The Hilbert Transform The Handbook of Formulas and Tables for Signal Processing.* CRC Press, 1999.

[131] Ron Bracewell. The fourier transform and iis applications. *New York*, 5, 1965.

[132] Jae S Lim. Two-dimensional signal and image processing. *Englewood Cliffs, NJ, Prentice Hall, 1990, 710 p.*, 1, 1990.

[133] Olivier Mesnil, Cara AC Leckey, and Massimo Ruzzene. Instantaneous and local wavenumber estimations for damage quantification in composites. *Structural Health Monitoring*, 2014.

[134] Olivier Mesnil, Hao Yan, Massimo Ruzzene, Kamran Paynabar, and Jianjun Shi. Fast wavenumber measurement for accurate and automatic location and quantification of defect in composite. *Structural Health Monitoring*, 2016.

[135] Dennis C Ghiglia and Mark D Pritt. *Two-dimensional phase unwrapping: theory, algorithms, and software.* Wiley New York, 1998.

[136] Zhenhua Tian and Lingyu Yu. Damage imaging and quantification using spectral field. In *ASME 2015 Conference on Smart Materials, Adaptive Structures and Intelligent Systems*, pages V002T05A013–V002T05A013. American Society of Mechanical Engineers, 2015.

[137] Peter D Juarez and Cara AC Leckey. Multi-frequency local wavenumber analysis and ply correlation of delamination damage. *Ultrasonics*, 2015.

[138] J.E. Michaels, A.J. Dawson, T.E. Michaels, and M. Ruzzene. Approaches to hybrid shm and nde of composite aerospace structures. *Proc SPIE*, 9064:906427–906427, 2014.

[139] EB FLYNN, AJ HAUGH, and SB LOPEZ. Small defect detection through local analysis of acoustic spatial wavenumber. *Structural Health Monitoring 2015*, 2015.

[140] Walter Lacarbonara. *Nonlinear structural mechanics: theory, dynamical phenomena and modeling.* Springer Science & Business Media, 2013.

[141] Xavier Maldague. *Theory and practice of infrared technology for nondestructive testing.* Wiley, 2001.

[142] S Bagavathiappan, BB Lahiri, T Saravanan, John Philip, and T Jayakumar. Infrared thermography for condition monitoring–a review. *Infrared Physics & Technology*, 60:35–55, 2013.

[143] Clemente Ibarra-Castanedo, Marc Genest, Stéphane Guibert, Jean-Marc Piau, Xavier PV Maldague, and Abdelhakim Bendada. Inspection of aerospace materials by pulsed thermography, lock-in thermography, and vibrothermography: a comparative study. In *Defense and Security Symposium*, pages 654116–654116. International Society for Optics and Photonics, 2007.

[144] Xavier Maldague, François Galmiche, and Adel Ziadi. Advances in pulsed phase thermography. *Infrared physics & technology*, 43(3):175–181, 2002.

[145] Steven M Shepard. Introduction to active thermography for non-destructive evaluation. *Anti-Corrosion Methods and Materials*, 44(4):236–239, 1997.

[146] BB Lahiri, S Bagavathiappan, PR Reshmi, John Philip, T Jayakumar, and B Raj. Quantification of defects in composites and rubber materials using active thermography. *Infrared Physics & Technology*, 55(2):191–199, 2012.

[147] Takahide Sakagami and Shiro Kubo. Applications of pulse heating thermography and lock-in thermography to quantitative nondestructive evaluations. *Infrared Physics & Technology*, 43(3):211–218, 2002.

[148] Liang Cheng and Gui Yun Tian. Comparison of nondestructive testing methods on detection of delaminations in composites. *Journal of sensors*, 2012, 2012.

[149] Adel A Badghaish and David C Fleming. Non-destructive inspection of composites using step heating thermography. *Journal of composite materials*, 42(13):1337–1357, 2008.

[150] YY Hung, Yun Shen Chen, SP Ng, L Liu, YH Huang, BL Luk, RWL Ip, CML Wu, and PS Chung. Review and comparison of shearography and active thermography for nondestructive evaluation. *Materials Science and Engineering: R: Reports*, 64(5):73–112, 2009.

[151] ASTM E2582. Thermgraphy practice for ir flash thermography of composites. 2007.

[152] Inc. Thermal Wave Imaging. *Thermal Equations & Calculations*, 2012.

[153] JG Sun. Analysis of pulsed thermography methods for defect depth prediction. *Journal of Heat Transfer*, 128(4):329–338, 2006.

[154] Steven M Shepard, Julin Hou, James R Lhota, and Joseph M Golden. Automated processing of thermographic derivatives for quality assurance. *Optical Engineering*, 46(5):051008–051008, 2007.

[155] JM Milne and WN Reynolds. The non-destructive evaluation of composites and other materials by thermal pulse video thermography. In *1984 Cambridge Symposium*, pages 119–122. International Society for Optics and Photonics, 1985.

[156] G Wróbel, Z Rdzawski, G Muzia, and S Pawlak. Determination of thermal diffusivity of carbon/epoxy composites with different fiber content using transient thermography. *Journal of Achievements in Materials and Manufacturing Engineering*, 37(2):518–525, 2009.

[157] Clemente Ibarra-Castanedo and Xavier P Maldague. Defect depth retrieval from pulsed phase thermographic data on plexiglas and aluminum samples. In *Defense and Security*, pages 348–356. International Society for Optics and Photonics, 2004.

[158] Clemente Ibarra Castanedo. *Quantitative subsurface defect evaluation by pulsed phase thermography: depth retrieval with the phase.* PhD thesis, Université Laval, 2005.

[159] Ralf W Arndt. Square pulse thermography in frequency domain as adaptation of pulsed phase thermography for qualitative and quantitative applications in cultural heritage and civil engineering. *Infrared Physics & Technology*, 53(4):246–253, 2010.

[160] Roberto Montanini. Quantitative determination of subsurface defects in a reference specimen made of plexiglas by means of lock-in and pulse phase infrared thermography. *Infrared Physics & Technology*, 53(5):363–371, 2010.

[161] JM Roche and DL Balageas. Common tools for quantitative pulse and step-heating thermography-part i: theoretical basis. *The 12th International Conference on Quantitative InfraRed Thermography (QIRT 2014), Jul 2014, BORDEAUX, France.*, 2014.

[162] Vamshi K.R. Kommareddy. *Air-coupled ultrasonic measurements in composites.* PhD thesis, Iowa State University, 2003.

[163] David Broek. *Elementary engineering fracture mechanics.* Springer Science & Business Media, 2012.

[164] Klaus Friedrich. *Application of fracture mechanics to composite materials*, volume 6. Elsevier, 2012.

[165] Cheryl A Rose, Carlos G Dávila, and Frank A Leone. *Analysis methods for progressive damage of composite structures.* Tech. rep. NASA/TM 2013-218024, 2013.

[166] Kyongchan Song, Carlos G Dávila, and Cheryl A Rose. Guidelines and parameter selection for the simulation of progressive delamination. In *ABAQUS Users Conference*, pages 1–15, 2008.

[167] Pedro Ponces Camanho, CG Davila, and MF De Moura. Numerical simulation of mixed-mode progressive delamination in composite materials. *Journal of composite materials*, 37(16):1415–1438, 2003.

[168] Zvi Hashin. Failure criteria for unidirectional fiber composites. *Journal of applied mechanics*, 47(2):329–334, 1980.

[169] AC Orifici, I Herszberg, and RS Thomson. Review of methodologies for composite material modelling incorporating failure. *Composite Structures*, 86(1):194–210, 2008.

[170] Ever J Barbero. *Finite Element Analysis of Composite Materials Using AbaqusTM.* CRC press, 2013.

[171] Y Mi, MA Crisfield, GAO Davies, and HB Hellweg. Progressive delamination using interface elements. *Journal of composite materials*, 32(14):1246–1272, 1998.

[172] Albert Turon Travesa et al. *Simulation of delamination in composites under quasi-static and fatigue loading using cohesive zone models.* Universitat de Girona, 2006.

[173] Alan A Griffith. The phenomena of rupture and flow in solids. *Philosophical transactions of the royal society of london. Series A, containing papers of a mathematical or physical character*, 221:163–198, 1921.

[174] Albert Turon, Carlos G Davila, Pedro Ponces Camanho, and J Costa. An engineering solution for mesh size effects in the simulation of delamination using cohesive zone models. *Engineering fracture mechanics*, 74(10):1665–1682, 2007.

[175] ML Benzeggagh and M Kenane. Measurement of mixed-mode delamination fracture toughness of unidirectional glass/epoxy composites with mixed-mode bending apparatus. *Composites science and technology*, 56(4):439–449, 1996.

[176] Z Zou, SR Reid, S Li, and PD Soden. Modelling interlaminar and intralaminar damage in filament-wound pipes under quasi-static indentation. *Journal of composite materials*, 36(4):477–499, 2002.

[177] Arne Hillerborg, Mats Modéer, and P-E Petersson. Analysis of crack formation and crack growth in concrete by means of fracture mechanics and finite elements. *Cement and concrete research*, 6(6):773–781, 1976.